THESIS 99-003

A SEARCH FOR THE STANDARD MODEL HIGGS BOSON IN FOUR-JET FINAL STATES AT CENTER-OF-MASS ENERGIES NEAR 183 GeV WITH THE ALEPH DETECTOR AT LEP

by

STEPHEN R. ARMSTRONG

A dissertation submitted in partial fulfillment of

the requirements for the degree of

Doctor of Philosophy

(Physics)

at the

UNIVERSITY OF WISCONSIN-MADISON

1998

A Search for the Standard Model Higgs Boson in Four-Jet Final States at Center-of-Mass Energies near 183 GeV with the ALEPH Detector at LEP

Stephen R. Armstrong
Under the supervision of Professor Sau Lan Wu
At the University of Wisconsin-Madison

ABSTRACT

The center-of-mass energies available at the upgraded Large Electron Positron collider (LEP2) at CERN provide an opportunity to search for the Higgs boson, the fundamental scalar boson predicted by the Standard Model of electroweak interactions. A search is performed using data gathered by the ALEPH experiment at LEP during 1997. The data sample consists of an integrated luminosity of 57 pb^{-1} at center-of-mass energies near 183 GeV. Possible signals from production of the Standard Model Higgs boson in the reaction $e^+e^- \rightarrow HZ \rightarrow b\bar{b}q\bar{q}$ are searched for using a cut-based analysis as well as a neural network approach. The main component of this search is a b-tagging algorithm utilizing neural network techniques. Results including other possible final states (*i.e.*, $H\ell^+\ell^-$, $H\nu\overline{\nu}$, $H\tau^+\tau^-$ and $\tau^+\tau^-q\bar{q}$) are also presented. No evidence of a signal is found in the data: seven events are selected, in agreement with the expectation of 7.2 events from standard processes. This results in a lower limit on the mass of the Higgs boson: $m_H > 87.9\,GeV/c^2$ at a 95% confidence level.

Acknowledgements

My thanks and deep gratitude go to my advisor Professor Sau Lan Wu for making this thesis possible. It is hard to describe fully the extent to which she has positively influenced and supported me and my research on many levels over the past six years. Her dedication to the field of high energy physics as well as to the success of her students is extraordinary. I am very fortunate to have benefited from her leadership and vision. Her insight sometimes makes it hard for me to appreciate immediately her point-of-view; I thank her for her patience with and belief in me.

To my parents, Jack and Suzy Armstrong, I owe everything. Without their support and encouragement this all would have been impossible. My sister Joanne Franklin has also constantly supported and encouraged me; the same applies to my brother-in-law Ron, my niece Rachel, and my nephews Mike, Tony, and Adam. I thank them for being a great family, for their love, and for their patience with me.

I am grateful to my friends in the United States: Chester Cooke, Joe and Barbara Elliott, Jim and Carolyn Key, Larry Molinaro, Gary and Ilene Osmundson, and Stephen Schnurr. They have been great friends, and I have benefited greatly from their generosity and advice in spite of my absence from the U.S. The friends I have met in Europe have been very supportive and kind to me: Sam Carmalt, Serge Firioubine, Kristina Gunne, Lesley Hay-Whitton, Hector and Elise (and recently Emma) Munoz, Patrick and

Jean Saint-Dullon, and John and Andrea Yamartino. The stress of graduate school has made it difficult for me to be nearly as good of a friend to them as they have been to me. My fellow graduate students in the Wisconsin group at CERN have been great and supportive friends who have enriched this long experience for me: Douglas Ferguson, Tom Greening, Owen Hayes, Pete McNamara, Jason Nielsen, Bill Orejudos, and Xidong Wu.

It has been a pleasure and a privilege to work closely with members of the Wisconsin Higgs group: Yuanning Gao, Tom Greening, Hongbo Hu, Shan Jin, Pete McNamara, Jason Nielsen, Yibin Pan, Sau Lan Wu, and Xidong Wu. I have benefited greatly from the neural network expertise of Günter Mamier and Michael Vogt. I am very fortunate to have worked with Leo Bellantoni, Ian Scott, and Vivek Sharma on b physics topics during my first years at CERN. Saúl González, Michael Schmitt, and John Yamartino were always willing to help me and to answer my questions.

I would like to acknowledge and thank my colleagues in the ALEPH collaboration who have helped me and provided a great environment in which to learn and to do physics. I have enjoyed membership in and collaboration with the ALEPH Higgs Task Force.

I owe Pedro Teixeira-Dias special thanks for his help with many aspects of this thesis, his being an incredibly nice guy, and his patience with me while we co-edited and wrote the ALEPH Standard Model Higgs paper. My thanks also to another incredibly nice guy, Pete McNamara, for helping me to grasp the complexities of limit setting.

During my undergraduate years at Yale I was fortunate to have guidance

from great scientists who inspired me to pursue physics: Professor Moshe Gai and the late Professor Feza Gürsey. I learned a great deal from working with Dr. Volker Burkert, Dr. Elton Smith, Professor Herbert Funsten, and Dr. Kevin Beard at CEBAF. I would probably not even know what physics is without the early encouragement of Mr. Jim Wirt. Mr. Michael Mitchell and Mr. John Franke at NASA/Langley were also very influential to me.

Dr. Yuanning Gao, Dr. Saúl González, Dr. Shan Jin, Dr. Bill Orejudos, Professor Yibin Pan, Dr. Pedro Teixeira-Dias, Professor Sau Lan Wu, and Professor Tai Tsun Wu have all read rough drafts of this thesis. Mr. Jason Nielsen kindly proofread the final draft. I thank them for their thoughtful comments and suggestions. Any remaining mistakes are my own fault.

I owe Ms. Beth Peo'ch an incredible amount of thanks for the countless times she has helped me, often putting aside her own crushing workload. Her cheerful outlook on life has brightened up our corridor from the first day she joined the group. My thanks also go to the former Wisconsin group administrative assistants who helped me on many occasions: Ms. Patricia van Gene, Ms. Shelly McKenzie, and Ms. Collete Chalier.

The system managers of the Wisconsin group have consistently and professionally maintained the computer systems at an incredibly high level of performance: Dr. Youssef Saadi, Mr. Brian Rathgeber, Mr. Chris Lishka, and Mr. Sloan Looney. I also thank Chris Lishka for sharing with me part of his inhumanly vast knowledge of computers and system management.

Geneva, Switzerland
October 1998

Contents

Abstract i

Acknowledgements ii

1 The Standard Model and the Higgs Boson 1

1.1 The Standard Model 2

1.1.1 Introduction 2

1.1.2 Fundamental Particles and Gauge Symmetries 5

1.1.3 The Higgs Mechanism 7

1.1.4 The Electroweak Interaction 10

1.1.5 Fermion Masses and the CKM Matrix 16

1.1.6 The Strong Interaction 20

1.2 Higgs Boson Phenomenology 21

1.2.1 Higgs Boson Production 21

1.2.2 Higgs Boson Decay 22

1.2.3 Higgs Boson Mass Bounds 24

1.2.4 Experimental Limits on the Mass of the Higgs Boson . 30

1.3 Higgs Boson Production and Background Processes at LEP2 . 32
1.3.1 The Higgsstrahlung Process and Final States 33
1.3.2 Background Processes 39

2 Experimental Apparatus **47**
2.1 The LEP Accelerator 47
2.2 The ALEPH Detector 54
2.2.1 The Vertex Detector (VDET) 56
2.2.2 The Inner Tracking Chamber (ITC) 61
2.2.3 The Time Projection Chamber (TPC) 63
2.2.4 The Electromagnetic Calorimeter (ECAL) 67
2.2.5 The Superconducting Magnet Coil 70
2.2.6 The Hadron Calorimeter (HCAL) 71
2.2.7 The Muon Chambers 73
2.2.8 The Luminosity Subdetectors 75
2.2.9 The Trigger System 77
2.3 Event Reconstruction 78
2.3.1 Track Reconstruction 78
2.3.2 $\mathrm{d}E/\mathrm{d}x$ Measurements 79
2.3.3 The Energy Flow Algorithm 81
2.4 Monte Carlo Simulation 85

3 Identification of b Quark Jets **86**
3.1 Jet Phenomenology 87
3.1.1 Hadronization 87

3.1.2 Jet Clustering 89
3.1.3 Fragmentation Function 90
3.2 Phenomenology of Heavy Flavor Hadrons 92
3.3 b-Tagging Variables 94
3.3.1 Track Impact Parameter 96
3.3.2 Displaced Vertices 104
3.3.3 Lepton Transverse Momentum 108
3.3.4 Jet-shape Variables 117
3.4 A Neural Network b-Tag 124
3.4.1 Motivation 124
3.4.2 Architecture and Training 126
3.4.3 Performance 129
3.4.4 Application to Neutral Higgs Searches 135
3.5 Comparisons between Data and Simulated Events 135

4 Event Selections for the Four-Jet Final State 145

4.1 Event Preselection, Jet Clustering, and Jet Energy Rescaling . 148
4.2 Event Selection with Cuts 157
4.2.1 Four-Jet Quality Cuts 157
4.2.2 b-Tagging and Jet Pairing 161
4.2.3 Performance 169
4.3 Event Selection with Neural Networks 176
4.3.1 The Input Variables 178
4.3.2 The Neural Networks 182

4.3.3 Performance 186
4.4 Systematic Studies 190
4.4.1 b-Tagging 190
4.4.2 Jet Angle 192
4.4.3 Neural Network Variables 193
4.4.4 Summary of Systematics 194

5 Limit Setting Methods and Results **196**
5.1 Limit Setting Method 197
5.1.1 The Confidence Levels 197
5.1.2 Combination of Confidence Levels 201
5.1.3 Working Point Determination 202
5.2 Results from Data 203
5.2.1 Results from the Four-Jet Analyses 206
5.2.2 The Other Final State Analyses 206
5.3 Combined Results and Limits 206

6 Summary, Outlook, and Conclusion **219**
6.1 Summary 219
6.2 Outlook for the Future 220
6.2.1 Future LEP Higgs Boson Searches 220
6.2.2 Future Higgs Searches at the Tevatron 221
6.2.3 Future Higgs Searches at the LHC 222
6.2.4 Future Higgs Searches at e^+e^- Linear Colliders 226
6.3 Conclusion 226

A Other Higgsstrahlung Final State Event Selections **229**

A.1 The Dilepton Final States 230

A.1.1 Selection Criteria 230

A.1.2 Systematic Uncertainties 235

A.2 The Missing Mass Final State 235

A.2.1 Cut-based Event Selection 237

A.2.2 Neural Network Event Selection 238

A.2.3 Results 239

A.2.4 Systematic Uncertainties 242

A.3 Final States with τ Leptons 242

A.3.1 Event Selection 244

A.3.2 The HZ$\rightarrow$H$\tau^+\tau^-$ Final State 246

A.3.3 The HZ$\rightarrow\tau^+\tau^-$q$\bar{\text{q}}$ Final State 248

A.3.4 Systematic Uncertainties 248

List of Figures

1.1 The scalar potential $V(\phi)$ 9
1.2 Diagrams contributing to Higgs boson production in e^+e^- interactions. 23
1.3 Branching ratios for Higgs boson decay as a function of mass. 25
1.4 $\Delta\chi^2$ versus M_H from a fit to precision electroweak measurements. 29
1.5 The Higgsstrahlung cross section versus center-of-mass energy 34
1.6 Cross sections versus Higgs boson mass at $\sqrt{s} = 183\,\text{GeV}$ . . . 35
1.7 Diagrams contributing to Standard Model background processes 45
1.8 Cross sections for Standard Model background processes . . . 46

2.1 The LEP accelerator complex 49
2.2 LEP integrated luminosity delivered to ALEPH during 1997 . 53
2.3 The ALEPH detector 55
2.4 The junction side of a VDET face 59
2.5 The VDET 60
2.6 An $r\phi$ view of a slice of the ITC 62
2.7 A cut-away view of the TPC 64

2.8 A schematic view of a TPC wire chamber sector 66
2.9 The ECAL 68
2.10 Composition of a lead/wire chamber layer of the ECAL 69
2.11 The HCAL 72
2.12 A muon chamber layer 74
2.13 A diagram of the five helix parameters of a track 80
2.14 Measured $\mathrm{d}E/\mathrm{d}x$ versus particle momentum 82
2.15 The average $\mathrm{d}E/\mathrm{d}x$ separation in standard deviations 83

3.1 The stages of an $\mathrm{e^+e^-} \rightarrow$ hadrons event 88
3.2 Diagrams contributing to b hadron decay mechanisms 95
3.3 An illustration of the primary vertex algorithm 99
3.4 An illustration of the impact parameter technique 101
3.5 Impact parameter significance (δ/σ_δ) distributions 103
3.6 The impact parameter-based variable for various jet flavors . . 105
3.7 An illustration of the displaced vertex algorithm 106
3.8 The displaced vertex-based variable for various jet flavors . . . 107
3.9 Electron p_{T} spectra from data and from simulated events . . . 109
3.10 The calorimeter-based electron estimators 112
3.11 An illustration of typical HCAL digital hit patterns 116
3.12 Distributions of $p_{\mathrm{T}\ell}$ 118
3.13 Distributions of boosted sphericity 121
3.14 Distributions of $N_{\mathrm{EF}}/\log E$ 122
3.15 Distributions of Σp_{T}^2 123

3.16 A diagram of the architecture of the neural network b-tag . . . 127
3.17 Neural network b-tag output distributions 131
3.18 Neural network b-tag performance 132
3.19 Neural network b-tag performance differences 133
3.20 Neural network b-tag performance differences 134
3.21 Distributions of $-\log_{10}\mathcal{P}_{\rm jet}$ 138
3.22 Distributions of $\Delta\chi^2_{\rm svx}$ 139
3.23 Distributions of $p_{{\rm T}\ell}$ 140
3.24 Distributions of $S_{\rm b}$ 141
3.25 Distributions of $N_{\rm EF}/\log(E)$ 142
3.26 Distributions of $\Sigma p_{\rm T}^2$ 143
3.27 Distributions of the neural network b-tag output 144

4.1 A simulated four-jet channel Higgs signal event 146
4.2 Charged multiplicity versus energy 150
4.3 Visible mass versus event P_z 151
4.4 Distributions of $-\log_{10} y_{34}$ 153
4.5 Distributions of $(X_\gamma)_{\rm max}$ 154
4.6 An event display of a simulated $q\bar{q}$ background event 158
4.7 Distributions of Θ 159
4.8 Distributions of γ 160
4.9 Distributions of the neural network b-tag outputs 162
4.10 Distributions of M_{12} (Z candidate mass) 165
4.11 Distributions of M_{34} (Higgs boson candidate mass) 166

4.12 Distributions of $\min(\eta_3, \eta_4)$ 167
4.13 Distributions of $-\log_{10}((1-\eta_3)(1-\eta_4))$ 168
4.14 Distributions of $9.5y_{34} + \sum_{i=1}^{4} \eta_i$ 170
4.15 Performance of the cut-based analysis. 172
4.16 Signal efficiency for various Higgs boson mass hypotheses. . . 174
4.17 Distributions of M_{34} and the reconstructed Higgs boson mass . 177
4.18 Distributions of additional topological/kinematic variables . . 183
4.19 Distributions of additional b-tagging variables 184
4.20 Distributions of the four-jet analysis neural network outputs . 187
4.21 Performance of the neural network analysis 189

5.1 The reconstructed Higgs boson mass 205
5.2 An event display of a Higgs boson candidate event 208
5.3 An event display of a Higgs boson candidate event 209
5.4 An event display of a Higgs boson candidate event 210
5.5 An event display of a Higgs boson candidate event 211
5.6 An event display of a Higgs boson candidate event 212
5.7 Confidence levels for the four-jet final state analyses 215
5.8 Confidence levels for the other final state analyses 216
5.9 Observed and expected confidence levels with the ALEPH $\sqrt{s} = 183\,\text{GeV}$ data only 217
5.10 Observed and expected confidence levels with all ALEPH data 218

6.1 Diagrams contributing to Higgs boson production at the LHC 223
6.2 Higgs boson production cross sections at the LHC 224

6.3 Higgs boson production cross sections in high energy e^+e^- collisions 227

A.1 A simulated dilepton channel Higgs signal event 231

A.2 Performance of the $H\ell^+\ell^-$ analysis. 234

A.3 A simulated missing energy channel Higgs signal event 236

A.4 Distributions of the b-tagging sum in the $H\nu\bar{\nu}$ channel 240

A.5 The analysis neural network output in the $H\nu\bar{\nu}$ channel 241

A.6 Performance of the $H\nu\bar{\nu}$ analysis. 243

A.7 A simulated $H\tau^+\tau^-$ signal event 245

A.8 The $H\tau^+\tau^-$ analysis neural network output 247

A.9 The $\tau^+\tau^-q\bar{q}$ analysis neural network output 249

A.10 Performance of the $H\tau^+\tau^-$ and $\tau^+\tau^-q\bar{q}$ analyses. 250

List of Tables

1.1 Properties of quarks and leptons 3

1.2 Gauge bosons of the Standard Model 4

1.3 The Higgsstrahlung final states 36

1.4 Summary of Standard Model background processes 44

2.1 Summary of the 1997 high energy data delivered to ALEPH . 54

3.1 Summary of weakly decaying b and c hadrons 93

4.1 Summary of the simulated event samples 148

4.2 Efficiencies for preselection criteria 156

4.3 Number of events at various analysis stages 161

4.4 Flavor composition of Standard Model background 173

4.5 Breakdown of signal efficiency for the cut-based analysis . . . 175

4.6 Anti-$q\bar{q}$ neural network input variables. 185

4.7 Anti-W^+W^- neural network input variables. 186

4.8 Anti-$q\bar{q}$ neural network training sample composition 188

4.9 Anti-W^+W^- neural network training sample composition . . . 188

4.10 Systematics related to b-tagging 192
4.11 Systematics from reweighting of neural network variables . . . 194

5.1 Summary of all the final state analyses 204
5.2 Summary of Higgs boson candidates in the four-jet final state 207
5.3 Summary of Higgs boson candidates in the dilepton final state 207

6.1 Summary of results of LEP2 Higgs boson searches 220
6.2 Summary of preliminary results of LEP2 Higgs boson searches 221

Chapter 1

The Standard Model and the Higgs Boson

A desire to understand the natural world at a fundamental level has permeated intellectual pursuits throughout history. In the modern era, an extraordinary interplay between theoretical and experimental physics has allowed the establishment of a model describing what are currently believed to be fundamental particles and the interactions they experience. Despite the great success of this *Standard Model*, a crucial component remains unresolved: the origin of the masses of the fundamental particles. Since the inception of the Standard Model, a special particle, the Higgs boson, has been used to address this problem. Unfortunately, direct experimental searches conducted over the past twenty years for the Higgs boson have yielded no evidence of its existence. The upgraded Large Electron Positron collider (LEP2) offers an opportunity to search for this elusive particle.

1.1 The Standard Model

1.1.1 Introduction

The behavior of fundamental particles can be described in terms of Quantum Field Theory (QFT), a synthesis of classical field theory, group theory, and relativistic quantum mechanics. Based on QFT, the heuristic Standard Model was developed by Glashow, Weinberg, and Salam [1] and describes the interactions of fermionic fields that represent what are currently believed to be the fundamental constituents of matter: quarks and leptons. For reasons that are not fully understood, these fundamental fermions are grouped together in families or generations; thus far three generations are known to exist.[1] The fundamental fermions and their properties are summarized in Table 1.1.

The interactions in the Standard Model are based upon the existence of locally invariant gauge symmetries in nature. These gauge symmetries give rise to three forces: the strong, weak, and electromagnetic interactions.[2] Quarks interact through the strong, electromagnetic, and weak interactions. Leptons interact solely either through the electromagnetic and weak interactions (for the charged leptons) or through the weak interaction (for neutrinos). Each of these interactions has a set of gauge boson fields representing the force-carrying particles of nature, the most familiar of which is the photon. These

[1] From measurements of the width of the Z boson at LEP, it has been determined that there are only three generations of matter which have light neutrinos [2].

[2] Gravity, the fourth and weakest interaction which fundamental particles experience, is excluded from the Standard Model and this discussion.

Quarks			
Particle Name	Symbol	Electric Charge (e)	Mass (GeV/c^2) [3]
up	u	$+2/3$	0.0015 to 0.005
down	d	$-1/3$	0.003 to 0.009
charm	c	$+2/3$	1.1 to 1.4
strange	s	$-1/3$	0.060 to 0.170
top	t	$+2/3$	173.8 ± 5.2
bottom	b	$-1/3$	4.1 to 4.4

Leptons			
Particle Name	Symbol	Electric Charge (e)	Mass (MeV/c^2) [3]
electron	e	-1	0.510999
electron neutrino	ν_e	0	< 0.000015
muon	μ	-1	105.658
muon neutrino	ν_μ	0	< 0.17
tau	τ	-1	$1777.05^{+0.29}_{-0.26}$
tau neutrino	ν_τ	0	< 18.2

Table 1.1: A summary of properties of quarks and leptons. Each of the particles in the table has a corresponding antiparticle of opposite charge. The masses of the u,d,s,c, and b quarks are difficult to determine since they exist only in bound hadronic states and not as free particles; however the large top mass permits a direct measurement since it decays before hadronization.

Gauge Bosons				
Force	Particle Name	Symbol	Electric Charge (e)	Mass (GeV/c^2) [3]
Electromagnetism	Photon	γ	0	0
Weak	W boson	$\mathrm{W}^{\pm}$	± 1	80.41 ± 0.10
Weak	Z boson	Z	0	91.187 ± 0.007
Strong	gluon	g	0	0

Table 1.2: A summary of the properties of the gauge bosons of the Standard Model. The uncertainty on the W mass can be expected to improve with additional LEP2 measurements.

are summarized in Table 1.2.

The most impressive achievement of the Standard Model is the partial unification of the electromagnetic and weak interactions which are merged into an *electroweak* force via the gauge group $SU(2) \times U(1)$. However, the model must be augmented somehow in order for this model to remain physical (*i.e.*, renormalizable) while agreeing with experimental evidence (*i.e.*, massive weak gauge bosons). One way to accomplish this is to *spontaneously* break the underlying gauge symmetries and introduce a scalar field, the Higgs boson [4]. Other considerably less simple mechanisms exist which accomplish electroweak symmetry breaking. These include dynamical electroweak symmetry breaking models based upon Technicolor [5] and models which introduce composite Higgs fields such as top quark condensates [6].

While all other features of the Standard Model have been experimentally confirmed, the Higgs boson has thus far eluded detection. It is reasonable to conclude that the Higgs boson mass is larger than existing experimental

sensitivity to it. Thus the search for the Higgs boson is the object of intense research efforts, the prime motivation for the current LEP2 program and the future Large Hadron Collider (LHC), and the topic of this thesis.

The next sections summarize the relevant aspects of gauge symmetries, the Higgs mechanism, and the Standard Model.

1.1.2 Fundamental Particles and Gauge Symmetries

The identification of conserved quantities in the interactions of fundamental particles and the association of these conserved quantities with space-time or internal symmetries forms the basis of the Standard Model. In the context of QFT, fields describing fundamental particles are unitary irreducible representations of the space-time Poincaré group which experience point-like interactions. Fundamental particles may also possess internal symmetries which do not involve space-time but which manifest themselves through interactions. An unmeasurable phase or set of phases correspond to each internal symmetry. A space-time independent transformation of the fermion fields with respect to this unobservable phase is expressed as

$$\psi(x) \rightarrow \psi'(x) = e^{-i\boldsymbol{\tau}\cdot\boldsymbol{\theta}}\psi(x)$$

where $\tau_j (j = 1, 2, ..., N)$ are $n \times n$ matrix representations of N generators of a group G of the internal symmetry, $\theta_j (j = 1, 2, ..., N)$ are a set of arbitrary phases, and $\psi(x)$ is a set of fields $(\psi_1(x), \psi_2(x), ..., \psi_n(x))$ grouped together in a multiplet representation. This is called a global *gauge transformation*, and

it does not affect the Lagrangian $\mathcal{L}(\psi(x), \partial_\mu\psi(x))$ describing the behavior of the fields. Since a conservation law exists for every continuous symmetry of a Lagrangian [7], fundamental particles possess conserved gauge *charges.*

According to the principles of locality, the phase should be allowed to vary locally at different space-time points. A local gauge transformation can be expressed as

$$\psi(x) \rightarrow \psi'(x) = e^{-i\boldsymbol{\tau}\cdot\boldsymbol{\theta}(x)}\psi(x)$$

where $\theta_j(x)$ is now dependent upon space-time coordinates. Unfortunately, the Lagrangian is not locally gauge invariant due to terms involving derivatives of $\psi(x)$. Gauge invariance is recovered by replacing the derivative ∂_μ in the Lagrangian with the gauge-covariant derivative $\mathcal{D}_\mu$. Yang and Mills developed a formalism for local gauge theory which includes non-Abelian as well as Abelian groups [8]. This requires the introduction of a massless vector *gauge boson* field $A^i_\mu(x)$ for each generator of the gauge group and a coupling constant g for each gauge group:

$$\mathcal{D}_\mu \equiv (\partial_\mu + ig\tau_i A^i_\mu(x))\psi(x).$$

A gauge invariant kinetic energy term ($\frac{1}{4}A^j_{\mu\nu}A^{\mu\nu}_j$) associated with these new gauge fields must also be added to the Lagrangian where $A^j_{\mu\nu}$ is a generalized field tensor given as

$$A^j_{\mu\nu} \equiv \partial_\mu A^j_\nu - \partial_\nu A^j_\mu - g f_{jkl} A^k_\mu A^l_\nu$$

where f_{jkl} are the structure constants of the gauge group.

The N massless gauge boson fields interact with fundamental fermion fields. If the gauge group G is non-Abelian (*e.g.*, $SU(2)$ and $SU(3)$), the resulting gauge boson fields are also self-interacting, carry gauge "charges" themselves, and are able to transform one member of a multiplet into another.

1.1.3 The Higgs Mechanism

QFTs based upon local gauge invariance are compelling not only due to their mathematical beauty but also because they are renormalizable theories [9]. However, they accommodate only massless gauge bosons. Explicit mass terms for the gauge boson fields spoil gauge invariance.

The weak gauge bosons (see Table 1.2) must be massive; weak interactions operate on extremely short distance scales, and the $W^{\pm}$ and Z masses have been measured to be large [10]. If gauge invariance is abandoned and mass terms are added by hand to the Lagrangian, the theory becomes unrenormalizable. However, the Higgs mechanism provides a way to generate masses for gauge bosons while retaining local gauge invariance.

A given symmetry is said to be *spontaneously broken* if the vacuum does not possess the same symmetry as the Lagrangian. This can be illustrated with a $U(1)$ locally gauge invariant Lagrangian describing the interaction of

a scalar field $\phi(x)$ with a gauge field $A_\mu(x)$:

$$\mathcal{L} = (\mathcal{D}_\mu\phi)^\dagger(\mathcal{D}^\mu\phi) - V(\phi) - \tfrac{1}{4}A_{\mu\nu}A^{\mu\nu}$$
$$\phi = \tfrac{1}{\sqrt{2}}(\phi_1 + i\phi_2); \quad \mathcal{D}^\mu = \partial^\mu + igA^\mu$$

where the scalar potential $V(\phi)$ is defined as

$$V(\phi) = \mu^2\phi^\dagger\phi + \lambda(\phi^\dagger\phi)^2 \quad (\lambda > 0).$$

There are two possible scenarios for the functional behavior of the scalar potential. There is a minimum at $\phi_1 = \phi_2 = 0$ for the case of $\mu^2 > 0$ as illustrated in Figure 1.1(a). However, when $\mu^2 < 0$, there is a ring of minima at

$$|\phi|^2 = \phi_1^2 + \phi_2^2 = \frac{-\mu^2}{2\lambda} \equiv \frac{v^2}{2}.$$

as illustrated in Figure 1.1(b). The symmetry is broken by Nature's choice of a specific minimum (*e.g.*, $\phi_1 = v/\sqrt{2}, \phi_2 = 0$). In this way, the vacuum is no longer $U(1)$ gauge invariant while the Lagrangian still is. The scalar field can be expanded about this point and substituted into the Lagrangian:

$$\phi(x) = \frac{1}{\sqrt{2}}\exp\left(i\frac{\xi(x)}{v}\right)(v + H(x))\,;$$

$$\begin{aligned}\mathcal{L} = \; & \tfrac{1}{2}(\partial_\mu H)(\partial^\mu H) + \mu^2H^2 + \tfrac{1}{2}(\partial_\mu\xi)(\partial^\mu\xi) \\ & + gvA_\mu(\partial^\mu\xi) + \tfrac{1}{2}g^2v^2A_\mu A^\mu - \tfrac{1}{4}A_{\mu\nu}A^{\mu\nu} + \cdots .\end{aligned}$$

The massless $\xi(x)$ field is referred to as a *Goldstone boson*. In general,

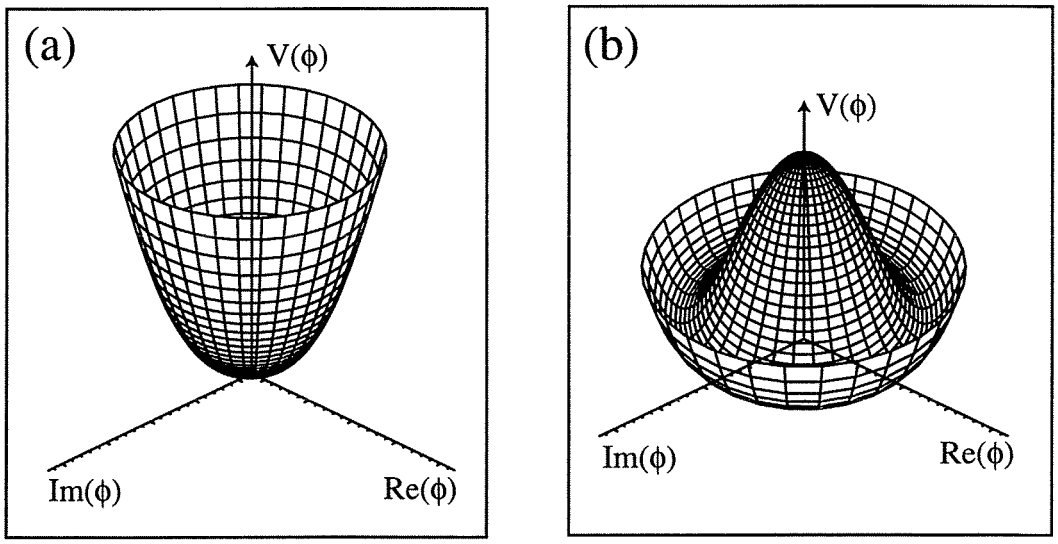

Figure 1.1: The scalar potential $V(\phi) = \mu^2\phi^\dagger\phi + \lambda(\phi^\dagger\phi)^2$ for (a) $\mu^2 > 0$ and (b) $\mu^2 < 0$. In case (a) there is a single minimum at Reϕ =Imϕ=0; in case (b) there is a ring of minima at $|\phi| = \sqrt{-\mu^2/2\lambda}$.

a Goldstone boson appears for each generator of the gauge group that is spontaneously broken [11, 12]. However, in the case of a local gauge invariant Lagrangian, the Goldstone boson does not correspond to a physical particle. This can be shown with a special choice of a local $U(1)$ gauge transformation: $\theta(x) = -\xi(x)/gv$. This choice is referred to as the Unitary Gauge. The resulting transformed vector and scalar fields are

$$A_\mu(x) \rightarrow A'_\mu(x) = A_\mu(x) - \frac{1}{gv}\partial_\mu\xi(x)$$
$$\phi(x) \rightarrow \phi'(x) = \phi(x)\exp\left(i\tfrac{\xi(x)}{v}\right) = \frac{1}{\sqrt{2}}(v + H(x))$$

Terms in the Lagrangian involving $\xi(x)$ and $\partial_\mu\xi(x)$ fortuitously cancel, and

the resulting Lagrangian is

$$\mathcal{L} = \frac{1}{2}(\partial_\mu H)(\partial^\mu H) + \mu^2 H^2 + \frac{1}{2}g^2 v^2 A_\mu A^\mu - \frac{1}{4}A_{\mu\nu}A^{\mu\nu}.$$

The Goldstone boson can be interpreted as the longitudinal polarization degree of freedom for the massive gauge field $A_\mu(x)$. Thus, this Lagrangian now describes a massive real scalar field $H(x)$ with a mass $\sqrt{-2\mu^2}$, and, most importantly, a massive gauge field $A_\mu(x)$ with mass gv.

The above formalism of spontaneously breaking a local gauge symmetry to yield a massive gauge boson is known as the *Higgs mechanism* [4]. The surviving massive scalar field $H(x)$ is the *Higgs boson*. The parameters which appear in the scalar potential are important for determining the phenomenology of the Higgs boson: μ is the tree-level Higgs boson mass, and λ is the quartic Higgs self-coupling. The quantity $v/\sqrt{2}$ is the Higgs vacuum expectation value.

1.1.4 The Electroweak Interaction

The current understanding of electroweak phenomena has evolved from the Fermi theory of weak interactions [13], quantum electrodynamics, and more than a century of detailed study of weak phenomena originating with Becquerel's discovery of radioactivity in 1896 [14]. Between 1961 and 1968, Glashow, Weinberg, and Salam developed the electroweak portion of the Standard Model: a locally invariant gauge field theory based on the group $SU(2) \times U(1)$ which provided a unified treatment of electromagnetic and

weak phenomena [1] and accommodated massive gauge bosons via the Higgs mechanism [4].

The construction of the Standard Model begins with a local $SU(2)$ gauge symmetry associated with a conserved gauge charge, weak isospin (T). Another local $U(1)_Y$ gauge symmetry is associated with another conserved gauge charge: hypercharge (Y). The Yang-Mills formalism discussed in Section 1.1.2 requires the introduction of a massless weak isospin triplet of gauge bosons $\boldsymbol{W}_\mu$=(W^1_μ, W^2_μ, W^3_μ) and a single massless hypercharge singlet gauge boson B_μ. Hence the covariant derivative is

$$\mathcal{D}_\mu = \partial_\mu + i\frac{g}{2}\boldsymbol{\tau}\cdot\boldsymbol{W}_\mu + ig'\frac{Y}{2}B_\mu.$$

The normal electric charge Q is a linear combination of the third component of weak isospin and hypercharge: $Q = T_3 + Y/2$; this anticipates electroweak symmetry breaking where a $U(1)_Q$ group remains unbroken yielding electromagnetism with a massless photon.

In 1956, Lee and Yang proposed parity violation in weak interactions as a solution to an outstanding problem involving kaon decays [15]. Parity violation in weak decays was definitively determined in a series of astounding experiments [16]. To accommodate this observation, the Standard Model allows the electroweak $SU(2)$ gauge bosons to operate only on left-handed particles.[3] Thus, fundamental fermions interact differently depending upon

[3]Right-handed particles have helicity $+1/2$ with their spin oriented parallel to their direction of motion; left-handed particles have helicity $-1/2$ with their spin oriented antiparallel to their direction of motion.

their handedness and are correspondingly grouped into different $SU(2)$ multiplet representations. Left-handed fermions are grouped into weak isospin doublets; there are two isospin doublets in each generation, one for quarks and the other for leptons:

$$T = 1/2, Y = \tfrac{1}{3} \quad \begin{cases} T_3 = +1/2 \\ T_3 = -1/2 \end{cases} \quad \begin{pmatrix} u \\ d' \end{pmatrix}_{\mathrm{L}} \quad \begin{pmatrix} c \\ s' \end{pmatrix}_{\mathrm{L}} \quad \begin{pmatrix} t \\ b' \end{pmatrix}_{\mathrm{L}}$$

$$T = 1/2, Y = -1 \quad \begin{cases} T_3 = +1/2 \\ T_3 = -1/2 \end{cases} \quad \begin{pmatrix} \nu_e \\ e^- \end{pmatrix}_{\mathrm{L}} \quad \begin{pmatrix} \nu_\mu \\ \mu^- \end{pmatrix}_{\mathrm{L}} \quad \begin{pmatrix} \nu_\tau \\ \tau^- \end{pmatrix}_{\mathrm{L}} .$$

Right-handed particles[4] can be grouped into weak isospin singlets:

$$T = 0 \quad \begin{cases} (e^-)_{\mathrm{R}} & (\mu^-)_{\mathrm{R}} & (\tau^-)_{\mathrm{R}} & \} Y = -2 \\ (u)_{\mathrm{R}} & (c)_{\mathrm{R}} & (t)_{\mathrm{R}} & \} Y = \frac{4}{3} \\ (d)_{\mathrm{R}} & (s)_{\mathrm{R}} & (b)_{\mathrm{R}} & \} Y = -\frac{2}{3} \end{cases} .$$

The primes on the left-handed down sector quarks in the $SU(2)$ doublets indicate that these are weak eigenstates and not mass eigenstates; this is discussed further in Section 1.1.5.

To accommodate massive gauge bosons by the Higgs mechanism, a complex weak isospin scalar doublet Φ is introduced along with the scalar poten-

[4]Neutrinos are assumed to be massless. Recent Kamiokande results may indicate the contrary [17], in which case right-handed neutrinos could be added to the collection of Standard Model right-handed singlet particles.

tial $V(\Phi)$ discussed in the previous section:

$$\Phi = \begin{pmatrix} \phi^+ \\ \phi^0 \end{pmatrix} = \frac{1}{\sqrt{2}} \begin{pmatrix} \phi_1 + i\phi_2 \\ \phi_3 + i\phi_4 \end{pmatrix}; \quad V(\Phi) = \mu^2 \Phi^\dagger \Phi + \lambda (\Phi^\dagger \Phi)^2 \quad (\lambda > 0).$$

With these elements in place, the Lagrangian of electroweak interactions can be written as

$$\mathcal{L}_{\rm EW} = \underbrace{-\tfrac{1}{4} \boldsymbol{W}_{\mu\nu} \cdot \boldsymbol{W}^{\mu\nu} - \tfrac{1}{4} B_{\mu\nu} B^{\mu\nu}}_{\left\{\begin{array}{l}\text{kinetic energy and}\\ \text{self-interactions of}\\ \text{the gauge bosons}\end{array}\right.}$$

$$\underbrace{+ (\mathcal{D}_\mu \Phi)^\dagger (\mathcal{D}^\mu \Phi) - V(\Phi)}_{\left\{\begin{array}{l}\text{gauge and scalar}\\ \text{boson couplings and}\\ \text{gauge kinetic terms}\end{array}\right.}$$

$$\underbrace{\begin{array}{l} +\bar{\psi}_{\rm L} \gamma^\mu \left(i\partial_\mu - g' \frac{Y}{2} B_\mu - g \frac{1}{2} \boldsymbol{\tau} \cdot \boldsymbol{W}_\mu \right) \psi_{\rm L} \\ +\bar{\psi}_{\rm R} \gamma^\mu \left(i\partial_\mu - g' \frac{Y}{2} B_\mu \right) \psi_{\rm R} \end{array}}_{\left\{\begin{array}{l}\text{fermion kinetic}\\ \text{energies and}\\ \text{electroweak}\\ \text{interaction terms}\end{array}\right.}$$

where g is the coupling constant of the weak isospin group $SU(2)$ and g' is the coupling constant of the hypercharge group $U(1)_Y$. Terms for the fermion masses are discussed in Section 1.1.5.

To spontaneously break the $SU(2) \times U(1)_Y$ symmetry, μ^2 is required to

be negative and $|\Phi|^2$ must acquire a non-zero vacuum expectation value lying upon the hypersphere of global minima of the scalar potential $V(\Phi)$ at

$$|\Phi|^2 = \Phi^\dagger\Phi = \frac{1}{2}\left(\phi_1^2 + \phi_2^2 + \phi_3^2 + \phi_4^2\right) = -\frac{\mu^2}{2\lambda} = \frac{v^2}{2}.$$

To do this in a manner which yields an unbroken $U(1)_Q$ gauge group for electromagnetism, ϕ_3 is chosen to acquire a non-zero vacuum expectation value:

$$\phi_3 = v, \phi_{1,2,4} = 0: \quad \Phi = \begin{pmatrix} \phi^+ \\ \phi^0 \end{pmatrix} \longrightarrow \frac{1}{\sqrt{2}}\begin{pmatrix} 0 \\ v \end{pmatrix}$$

As illustrated in Section 1.1.3, the resulting particle spectrum becomes apparent upon expansion around the vacuum expectation value:

$$\Phi(x) = \frac{1}{\sqrt{2}}\exp\left(i\frac{\boldsymbol{\xi}\cdot\boldsymbol{\tau}}{2v}\right)\begin{pmatrix} 0 \\ v + H(x) \end{pmatrix}.$$

The components of the field $\boldsymbol{\xi}(x)$ are three Goldstone bosons which are absorbed into longitudinal polarization states of three massive gauge bosons; $H(x)$ is the massive neutral scalar field. After substituting the above expansion and gauge transforming the resulting the Lagrangian, the apparent gauge boson spectrum emerges from the $(\mathcal{D}_\mu\Phi)^\dagger(\mathcal{D}^\mu\Phi)$ term:

$$(\mathcal{D}_\mu\Phi)^\dagger(\mathcal{D}^\mu\Phi) = \frac{v^2}{8}\left[g^2\left(W_{1\mu}^2 + W_{2\mu}^2\right) + \left(gW_{3\mu} - g'B_\mu\right)^2\right].$$

The covariant derivative can be rewritten in terms of physical fields:

$$\mathcal{D}_\mu = \partial_\mu + i\frac{g}{\sqrt{2}}\left(\tau_+ W_\mu^+ + \tau_- W_\mu^-\right) - i\frac{g}{\cos\theta_{\rm W}}\left(\tau_3 - Q\sin^2\theta_{\rm W}\right) + ieQA_\mu$$

where the Weinberg electroweak mixing angle $\theta_{\rm W}$ has been introduced:

$$\tan\theta_{\rm W} = \frac{g'}{g}.$$

The physical gauge fields and their masses are thus

$$\begin{aligned}
W_\mu^\pm &= \tfrac{1}{\sqrt{2}}\left(W_\mu^1 \mp iW_\mu^2\right), & M_{\rm W} &= \frac{gv}{2};\\
Z_\mu &= -B_\mu\sin\theta_{\rm W} + W_\mu^3\cos\theta_{\rm W}, & M_{\rm Z} &= \frac{M_{\rm W}}{\cos\theta_{\rm W}};\\
A_\mu &= B_\mu\cos\theta_{\rm W} + W_\mu^3\sin\theta_{\rm W}, & M_\gamma &= 0.
\end{aligned}$$

Thus, the Z boson and the photon emerge as orthogonal combinations of the W_μ^3 and B_μ fields.

The following has been achieved with the Higgs mechanism within the context of the electroweak Standard Model:

- Three massless Goldstone bosons disappear from the particle spectrum and are reinterpreted as longitudinal polarization states of three massive weak gauge bosons; the charged gauge boson fields $W_\mu^\pm$ have acquired a mass; the neutral gauge boson field Z_μ has acquired a different mass;

- The neutral gauge boson field A_μ corresponding to the $U(1)_Q$ group

(*i.e.*, electromagnetism) remains massless; this is the photon γ;

- A neutral massive scalar field $H(x)$ is predicted; this is the Higgs boson.

While all other aspects of the Standard Model have been confirmed by experiment, the Higgs boson remains unobserved. The Higgs boson is dependent upon the parameters v and λ from the scalar potential discussed in Section 1.1.3. The $SU(2)$ coupling strength determines v:

$$M_{\mathrm{W}}^2 = \frac{g^2 v^2}{4} = \sqrt{2} G_{\mathrm{F}} M_{\mathrm{W}}^2 v^2 \rightarrow v = \left(\frac{1}{\sqrt{2}\, G_{\mathrm{F}}} \right)^{\frac{1}{2}} = 246\,\mathrm{GeV}$$

where G_{F} is the Fermi coupling constant. However, λ cannot be determined *a priori*. Hence, the Higgs boson mass remains a free parameter in the Standard Model and must be experimentally measured, once the Higgs boson is discovered.

1.1.5 Fermion Masses and the CKM Matrix

Although the Higgs mechanism provides masses for the weak gauge bosons, it is naturally extendable to generate masses of the fundamental fermions listed in Table 1.1. Normally, fermion mass terms of the form $m\overline{\psi}\psi$ could be added to the Lagrangian without encountering problems related to gauge symmetry. However, such a mass term in terms of chiral fields is

$$m\overline{\psi}\psi = m\overline{\psi}_{\mathrm{L}}\psi_{\mathrm{R}} + m\overline{\psi}_{\mathrm{R}}\psi_{\mathrm{L}}.$$

Particles of different chiralities are placed into different $SU(2)$ multiplets (ψ_{L} is an $SU(2)$ doublet while ψ_{R} is an $SU(2)$ singlet). Therefore in this case the fermion mass term $m\overline{\psi}\psi$ is not gauge invariant.

Fortunately, the masses of the fundamental fermions can be generated via Yukawa couplings of the Higgs to the fermions. Mass terms are the form

$$g_f \left[\overline{\psi}_{\mathrm{L}}\Phi\psi_{\mathrm{R}} + \overline{\psi}_{\mathrm{R}}\Phi^{\dagger}\psi_{\mathrm{L}}\right]$$

where g_f is the Yukawa coupling of the fermion f represented by the field ψ to the Higgs field. This term can be inserted into the Lagrangian since the inner product of the Higgs and left-handed fermion $SU(2)$ doublets yield a gauge invariant singlet. This is straightforward for the lepton sector if neutrinos are assumed to be massless:

$$g_{\mathrm{e}}\left[(\bar{\nu}_{\mathrm{e}},\ \bar{\mathrm{e}}\,)_{\mathrm{L}}\begin{pmatrix}0\\ v/\sqrt{2}\end{pmatrix}\mathrm{e}_{\mathrm{R}} + \bar{\mathrm{e}}_{\mathrm{R}}\left(0,\ v/\sqrt{2}\right)\begin{pmatrix}\bar{\nu}_{\mathrm{e}}\\ \bar{\mathrm{e}}\end{pmatrix}_{\mathrm{L}}\right] = \frac{g_{\mathrm{e}}v}{\sqrt{2}}\bar{\mathrm{e}}\mathrm{e}.$$

From this it follows that fermion masses are proportional to their Yukawa coupling to the Higgs field.

The situation for generating quark masses is more interesting. Since both components of the $SU(2)$ doublet for quarks have mass, the lepton mass generation mechanism must be modified. This is accomplished by using the

conjugate of the Higgs doublet:

$$\tilde{\Phi} = \begin{pmatrix} \phi^{0\dagger} \\ -\phi^{-} \end{pmatrix} \longrightarrow \begin{pmatrix} v/\sqrt{2} \\ 0 \end{pmatrix}.$$

Thus the quark mass terms may be written as

$$\sum_{i=1}^{3}\sum_{j=1}^{3}\left\{g^{u}_{ij}\left(\bar{u}_i,\ \bar{d}_i\right)_{\mathrm{L}}\tilde{\Phi}\left(u_j\right)_{\mathrm{R}} + g^{d}_{ij}\left(\bar{u}_i,\ \bar{d}_i\right)_{\mathrm{L}}\Phi\left(d_j\right)_{\mathrm{R}}\right\} + h.c.$$

$$\rightarrow \frac{v}{\sqrt{2}}\left(\bar{u}_1,\ \bar{u}_2,\ \bar{u}_3\right)\boldsymbol{g}^{u}\begin{pmatrix} u_1 \\ u_2 \\ u_3 \end{pmatrix} + \frac{v}{\sqrt{2}}\left(\bar{d}_1,\ \bar{d}_2,\ \bar{d}_3\right)\boldsymbol{g}^{d}\begin{pmatrix} d_1 \\ d_2 \\ d_3 \end{pmatrix} + h.c.$$

where indices i and j run over the three generations, u_i are the three up-sector weak eigenstates, and d_i are the three down-sector weak eigenstates. The matrices $\boldsymbol{g}^u$ and $\boldsymbol{g}^d$ each contain nine arbitrary complex Yukawa couplings of the quarks to the Higgs field. Two complex quark mass matrices are defined as $\boldsymbol{M}^u \equiv (v/\sqrt{2})\boldsymbol{g}^u$ and $\boldsymbol{M}^d \equiv (v/\sqrt{2})\boldsymbol{g}^d$. To obtain the physical quark states (*i.e.*, u,d,c,s,t,b quarks), these matrices must be diagonalized by multiplying on the left and right by appropriate separate unitary matrices $\boldsymbol{U}^u$ and $\boldsymbol{U}^d$. This is made clearer if the weak charged current terms coupling the left-handed weak eigenstates of the up- and down-sector quarks are expressed

in terms of the mass eigenstates using $\boldsymbol{U}^u$ and $\boldsymbol{U}^d$:

$$(\bar{u}_1, \bar{u}_2, \bar{u}_3)_{\mathrm{L}}\, \gamma^\mu \begin{pmatrix} d_1 \\ d_2 \\ d_3 \end{pmatrix}_{\mathrm{L}} = (\bar{u}, \bar{c}, \bar{t})_{\mathrm{L}}\, \boldsymbol{U}_{\mathrm{L}}^{u\dagger} \gamma^\mu \boldsymbol{U}_{\mathrm{L}}^{d} \begin{pmatrix} d \\ s \\ b \end{pmatrix}_{\mathrm{L}} = (\bar{u}, \bar{c}, \bar{t})_{\mathrm{L}}\, \gamma^\mu \boldsymbol{V} \begin{pmatrix} d \\ s \\ b \end{pmatrix}_{\mathrm{L}} .$$

The weak eigenstates of the down-sector quarks can be interpreted to be mixed by the matrix $\boldsymbol{V} \equiv \boldsymbol{U}_{\mathrm{L}}^{u\dagger} \boldsymbol{U}_{\mathrm{L}}^{d}$. The matrix $\boldsymbol{V}$ is the Cabbibo-Kobayashi-Maskawa (CKM) matrix [18, 19]. This complex unitary matrix is most often written as

$$\boldsymbol{V} = \begin{pmatrix} V_{\mathrm{ud}} & V_{\mathrm{us}} & V_{\mathrm{ub}} \\ V_{\mathrm{cd}} & V_{\mathrm{cs}} & V_{\mathrm{cb}} \\ V_{\mathrm{td}} & V_{\mathrm{ts}} & V_{\mathrm{tb}} \end{pmatrix} .$$

From the unitarity requirement (which removes nine free parameters) and the fact that gauge invariance allows the redefinition of the phases of the quark fields (which further removes five unphysical phases), the matrix itself possesses three real parameters and one phase angle. The phase is a possible source of CP violation and would not exist if there were only two generations. This was Kobayashi and Maskawa's prime motivation for their proposal of the above 3×3 unitary mixing matrix [19]. Terms such as V_{cb}, V_{cs}, and V_{ub} play a central role in discussions of the decay dynamics of heavy quark hadrons (see Section 3.2).

1.1.6 The Strong Interaction

Quarks experience strong interactions while leptons do not. The part of the Standard Model describing strong interactions is a gauge field theory known as *quantum chromodynamics* (QCD) based on the non-Abelian group $SU(3)$. The corresponding strong gauge charge is referred to as *color* and comes in three varieties (e.g., red, green, and blue). Hence, for each quark flavor, there are three possible colors it may possess. The gauge bosons for the strong interaction are the gluons (see Table 1.2).

The first direct evidence for the gluon was found in three-jet events interpreted as hard gluon bremsstrahlung from one of the quarks leading to two quark jets and a gluon jet (*i.e.*, $e^+e^- \rightarrow q\bar{q}g$) [20]. However, there is no evidence of free single quarks or gluons in nature [3]. This observation supports a central feature of QCD called *confinement*. Confinement refers to the fact that at small values of momentum transfer Q^2 the QCD running coupling constant $\alpha_s(Q^2)$ becomes large. The complementary case is referred to as asymptotic freedom; at large values of Q^2, $\alpha_s(Q^2)$ tends to zero, QCD processes can be treated perturbatively, and quarks behave as quasi-free particles. This leads to the existence of only color-singlet objects in nature (*e.g.*, qqq or $q\bar{q}$ hadronic states), and the fact that a non-color singlet configuration of quarks will polarize the vacuum creating $q\bar{q}$ pairs until a system of color-singlet objects is obtained. This is described further within the context of jets and multi-hadronic final states from e^+e^- annihilations in Section 3.1.

1.2 Higgs Boson Phenomenology

This section summarizes phenomenological issues relevant to Standard Model Higgs boson searches at LEP2. As discussed in Section 1.1.4, until the Higgs boson is discovered, its mass is unknown and remains a free parameter in the Standard Model. However, for a given mass, the relevant properties (*e.g.*, the production cross section) of the Higgs boson can be unambiguously determined. The range of masses relevant to LEP2 searches is from 60 to $105\,\mathrm{GeV}/c^2$.[5]

Section 1.2.1 describes production mechanisms while Section 1.2.2 summarizes Higgs boson decays. Section 1.2.3 discusses arguments for constraining the Higgs boson mass bounds derived from theory and precision measurements of electroweak observables. Section 1.2.4 discusses existing experimental limits on the mass of the Higgs boson.

1.2.1 Higgs Boson Production

The Higgs boson couples to massive fermions and the $W^{\pm}$ and Z bosons. It is possible for Higgs bosons to be produced radiatively from these particles. Alternatively, it can be produced via W^+W^- and ZZ fusion. The s-channel production of Higgs bosons from the annihilation of fermion/anti-fermion pairs is possible, but this process is negligible in e^+e^- collisions since the

[5]This assumes center-of-mass energies near $\sqrt{s} = 196\,\mathrm{GeV}$ are ultimately obtained at LEP2. There is the possibility that, in the year 2000, an upgraded cryogenic system will support running near or above $\sqrt{s} = 200\,\mathrm{GeV}$. In this case, the upper value on the relevant range of Higgs boson masses should increase accordingly.

electron mass (and hence the Higgs-electron coupling) is very small. A Higgs boson and a photon can be produced via higher-order processes involving virtual intermediate massive fermion loops or $W^{\pm}$ loops (*e.g.*, $Z \rightarrow H\gamma$), but this process is not relevant to LEP2 searches [21]. A *gluon fusion* production mechanism exists where two gluons couple to a massive fermion loop which produces a Higgs boson; this is only relevant for searches at $p\bar{p}$ and pp colliders.

Figure 1.2 shows diagrams contributing to Higgs boson production in the context of e^+e^- interactions relevant to LEP2 searches. Radiative Higgs boson production from virtual Z bosons is the dominant process at LEP2 and is referred to as *Higgsstrahlung*. This process is discussed in more detail in Section 1.3.

1.2.2 Higgs Boson Decay

The Higgs boson decays to massive fermions or gauge bosons. The Higgs-fermion coupling is proportional to the fermion mass, while the couplings to the $W^{\pm}$ and Z are proportional to the boson mass squared. Decays to gluons are possible through intermediate massive quark loops, and decays to $\gamma\gamma$ and $Z\gamma$ are possible through intermediate $W^{\pm}$ loops or massive fermion loops [21].

At tree level, the partial width for Higgs bosons decaying into fermions is

$$\Gamma(H \rightarrow f\bar{f}) = N_c \frac{G_F M_f^2 M_H}{4\pi\sqrt{2}} \left(1 - \frac{4M_f^2}{M_H^2}\right)^{3/2}$$

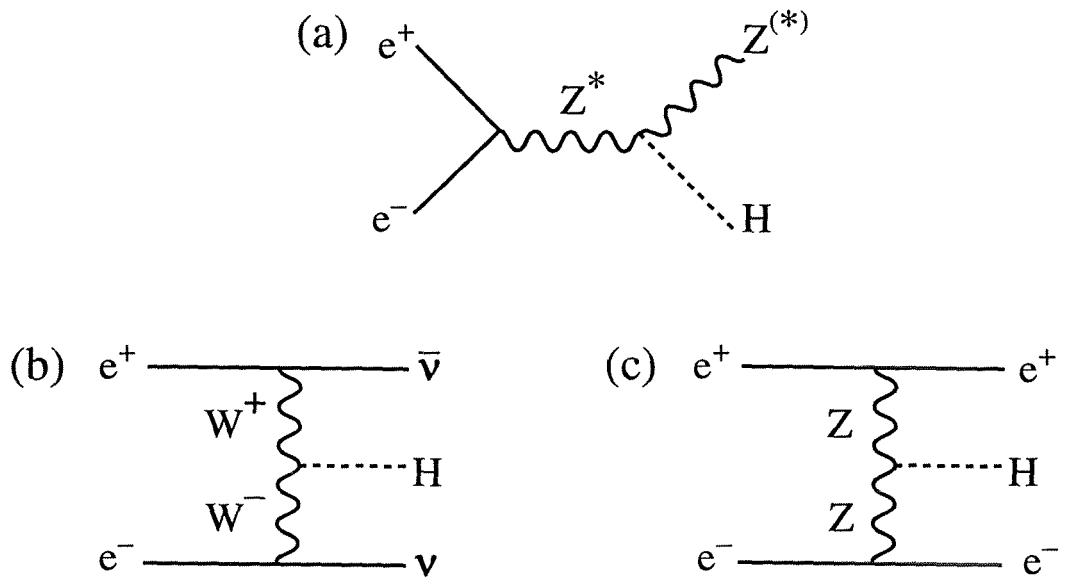

Figure 1.2: Diagrams contributing to Higgs boson production in e^+e^- interactions at LEP2: (a) Higgsstrahlung, (b) W^+W^- fusion, and (c) ZZ fusion.

where N_c is 1 for leptons and 3 for quarks [21].

Within the relevant Higgs boson mass range for LEP2, the Higgs boson decays predominantly to b quark/anti-quark pairs with a branching ratio ranging from roughly 87% to 80% with increasing Higgs boson mass. The next most prevalent decays are to $\tau^+\tau^-$ and c quark/anti-quark pairs with branching ratios of roughly 7% and 3% respectively. The branching ratio for decays to gluons ranges from roughly 2% to 4%. Decays to $W^{(*)+}W^{(*)-}$ and $Z^{(*)}Z^{(*)}$ are very rare, becoming dominant only at larger Higgs boson masses ($M_H > 150\,\mathrm{GeV}/c^2$). Figure 1.3 shows the Higgs boson branching ratios over a large mass range.

The width of the Higgs boson for a mass between 60 and $105\,\mathrm{GeV}/c^2$ ranges between roughly 1.5 and $3\,\mathrm{MeV}/c^2$ (*i.e.*, the lifetime is on the order of 10^{-22} s). However, the typical experimental resolution for reconstructing the Higgs boson mass is on the order of a few GeV/c^2.

1.2.3 Higgs Boson Mass Bounds

Various theoretical arguments have been used to constrain the mass of the Higgs boson. Precision electroweak measurements can also be used to determine the most consistent Higgs boson mass and to derive an upper limit. However, the final arbiter will be the direct experimental observation of the Higgs boson and the measurement of its mass.

An upper limit on the Higgs boson mass can be determined from "unitarity" arguments. In the absence of a fundamental scalar field, the amplitude

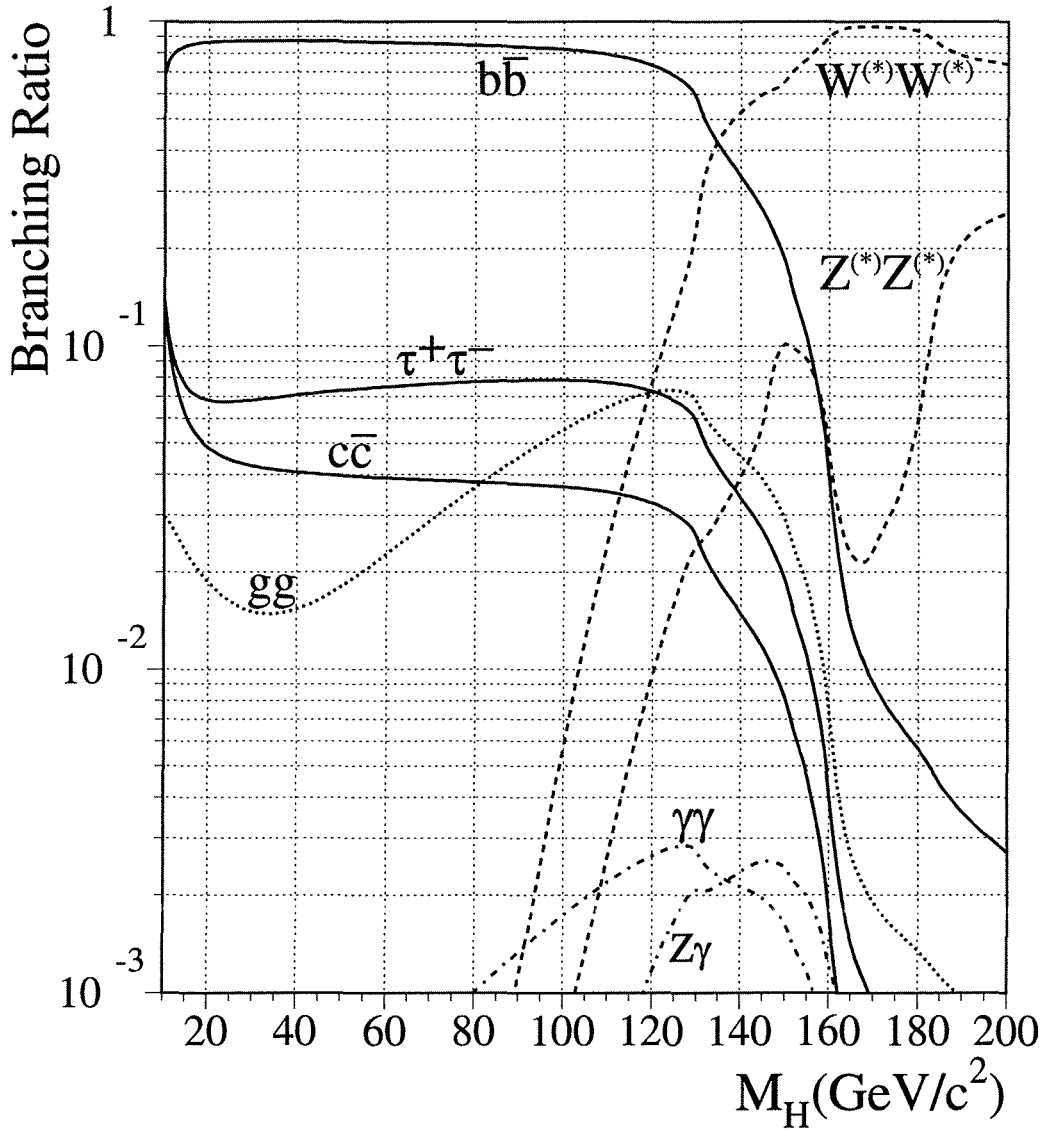

Figure 1.3: Branching ratios for Higgs boson decay as a function of the Higgs mass (calculated by the HZHA generator [22]). Decays to $b\bar{b}$ dominate for Higgs boson masses relevant to LEP2 searches ($60 < M_{\mathrm{H}} < 105\,\mathrm{GeV}/c^2$).

for elastic scattering of longitudinally polarized massive gauge bosons (*i.e.*, $W_L^+W_L^- \rightarrow W_L^+W_L^-$) diverges quadratically in energy when calculated in a perturbation expansion. At an energy above 1.2 TeV, this process would violate unitarity. This problem is solved once diagrams including the exchange of the Higgs boson are included. However, unitarity would again be violated if the Higgs boson mass is too large [23]:

$$M_H^2 > \frac{2\sqrt{2}\pi}{G_F} \approx (850\,\mathrm{GeV}/c^2)^2.$$

Hence this indicates that the Higgs boson mass should be below roughly $850\,\mathrm{GeV}/c^2$ in order to retain perturbative unitarity and renormalizability [24]. However, this is not a strict upper bound, it is only a measure of the scale up to which perturbation theory is reliable (*i.e.* the $W^{\pm}$,Z, and Higgs bosons would become strongly interacting above 1.2 TeV, and the Standard Model would need to be modified in some more complex way) [25].

Another theoretical upper bound on the Higgs boson mass is related to the quartic self-coupling of the Higgs boson, $\lambda(v^2) = M_H^2/2v^2$ (see Section 1.1.3), and the energy scale Λ up to which the Standard Model remains valid. This self-coupling grows logarithmically with energy: $\partial\lambda/\partial \log \mu^2 \approx \lambda^2$, where μ is the renormalization scale. This behavior of λ from the electroweak symmetry breaking scale ($v = 246\,\mathrm{GeV}$) to μ can be approximated as [23]

$$\lambda(\mu^2) = \frac{\lambda(v^2)}{1 - \frac{3\lambda(v^2)}{8\pi^2} \log \frac{\mu^2}{v^2}}.$$

With the condition that $\lambda(\mu^2) < \infty$ for all $\mu < \Lambda$, this translates into an upper bound on the Higgs boson mass [23]:

$$M_{\mathrm{H}}^2 \leq \frac{8\pi^2 v^2}{3 \log \frac{\Lambda^2}{v^2}} \approx (750\,\mathrm{GeV}/c^2)^2 \quad \text{for } \Lambda \approx 1\ \mathrm{TeV}.$$

The upper bound decreases for increasing values of Λ, becoming roughly $200\,\mathrm{GeV}/c^2$ for $\Lambda \approx 10^{19}\,\mathrm{GeV}$ [23].

Lower bounds can be derived from theoretical arguments based on the stability of the electroweak vacuum. Radiative corrections from massive fermions modify the scalar potential given in Section 1.1.3 with terms of the form $-g_f^4 \phi^4 \log \phi$. For the case of the top quark, the shape of the Higgs potential changes if λ is too small. In this case, the Higgs vacuum expectation value $v^2/2$ is a local minima, and the vacuum might not be stable [26]. The requirement that this situation not occur translates into a lower limit on the Higgs boson mass which is dependent upon Λ and the top quark mass. Lower limits are obtained [27]:

$$M_{\mathrm{H}} > 55\,\mathrm{GeV}/c^2 \quad \text{for } \Lambda \approx 1\,\mathrm{TeV};$$
$$M_{\mathrm{H}} > 130\,\mathrm{GeV}/c^2 \quad \text{for } \Lambda \approx 10^{19}\,\mathrm{GeV}$$

with a top quark mass of $175\,\mathrm{GeV}/c^2$. The former limit is consistent with existing LEP2 limits on the mass of the Higgs boson discussed in Section 1.2.4; the latter would not bode well for a Higgs boson discovery at LEP2.

The Higgs boson influences observed electroweak processes via higher-order processes beyond tree-level. Hence, if electroweak observables are pre-

cisely measured, it is possible to determine the Higgs boson mass via the radiative corrections. To demonstrate this, the Fermi coupling constant G_{F} can be rewritten with radiative correction terms (Δr_X) included [23]:

$$\frac{G_{\mathrm{F}}}{\sqrt{2}} = \frac{2\pi\alpha}{\sin^2 2\theta_{\mathrm{W}} M_{\mathrm{Z}}^2}\left(1 + \Delta r_\alpha + \Delta r_{\mathrm{t}} + \Delta r_{\mathrm{H}}\right)$$

where α is the electromagnetic coupling, Δr_α represents the difference between $\alpha(M_{\mathrm{Z}}^2)$ and $\alpha(0)$, and Δr_{t} represents the top radiative corrections to the $\mathrm{W}^{\pm}$ and Z masses. The Δr_{H} term represents the radiative corrections to the $\mathrm{W}^{\pm}$ and Z masses from the Higgs boson; this term is proportional to $\log(M_{\mathrm{H}}^2)$. Measurements of electroweak observables from the four LEP experiments (ALEPH, DELPHI, L3, and OPAL), SLD, CDF, and D0 are combined, and a fit to these data is performed. The Higgs boson mass is determined from the minimum χ^2 of the fit [28]:

$$M_{\mathrm{H}} = \left(76\,^{+85}_{-47} \pm 10\right)\mathrm{GeV}/c^2$$

where the second error is due to theoretical uncertainties. Figure 1.4 shows the value of $\Delta\chi^2 = \chi^2 - \chi^2_{\mathrm{min}}$ as a function of M_{H}. A 95% confidence level upper limit on the Higgs boson mass is also determined [28]:

$$M_{\mathrm{H}} < 260\,\mathrm{GeV}/c^2.$$

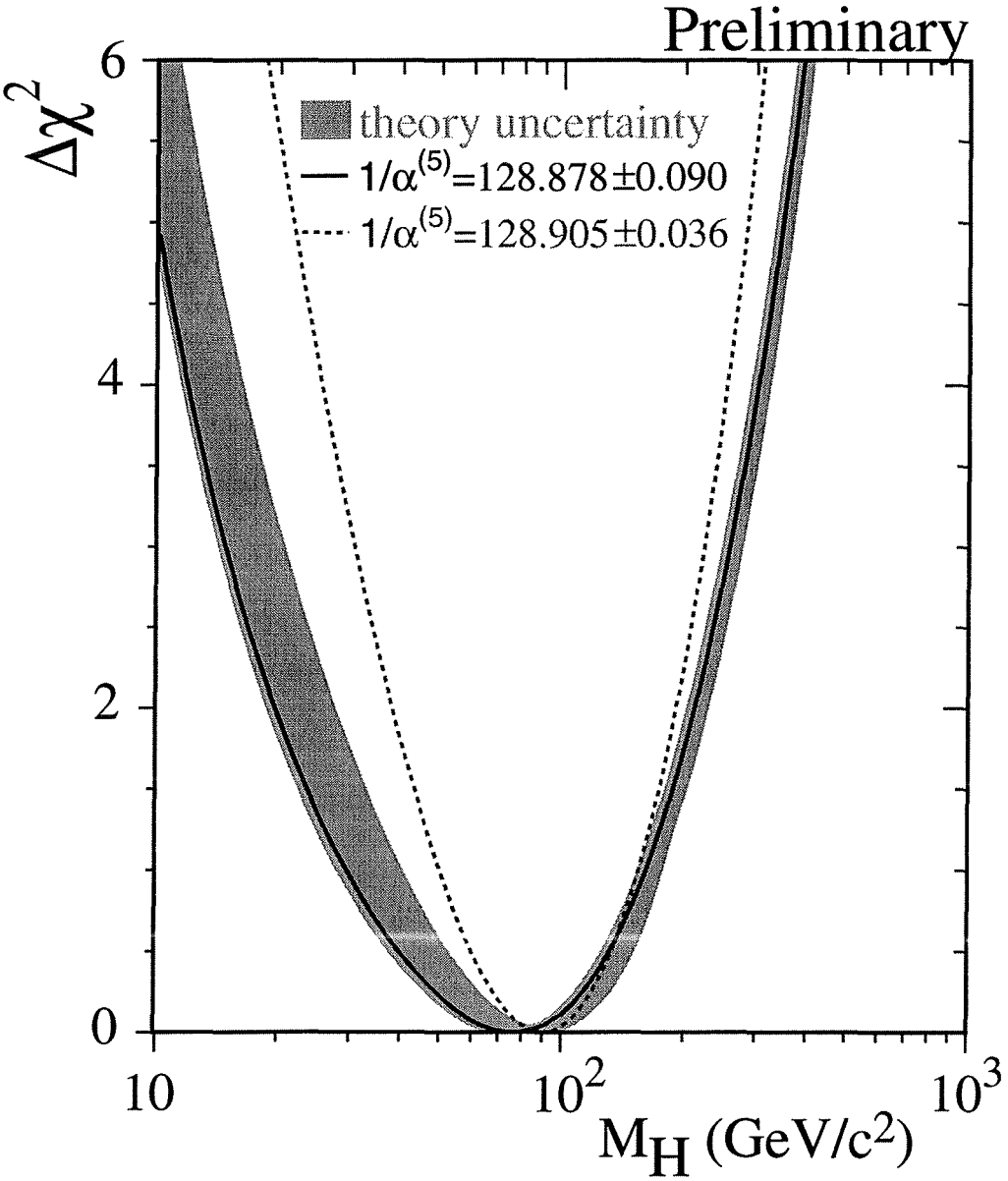

Figure 1.4: $\Delta\chi^2 = \chi^2 - \chi^2_{\text{min}}$ versus M_{H} from a fit to precision electroweak measurements from Ref. [29]. The shaded band around the curve indicates an estimate of theoretical uncertainty.

1.2.4 Experimental Limits on the Mass of the Higgs Boson

A variety of searches have been conducted for Higgs boson over the last 25 years in a variety of quantum mechanical systems. The evolution of the searches from extremely low energies to the highest energy regimes that are currently experimentally accessible reflects the fact that the Higgs boson mass is a free parameter in the Standard Model.

An extremely light Higgs boson ($M_{\mathrm{H}} < 15\,\mathrm{MeV}/c^2$) has been excluded by experiments searching for indirect evidence in atomic and nuclear systems via a Higgs-nucleon coupling [30]. Other searches have excluded a very light Higgs boson ($M_{\mathrm{H}} < 50\,\mathrm{MeV}/c^2$) [31]. In these cases, the mass would be light enough for the Higgs boson to have significant lifetime and the only possible decays would be to $\mathrm{e}^+\mathrm{e}^-$ or $\gamma\gamma$. Searches for unexpected decays of pions [32], kaons [33], B mesons [34], and Υ [35] have excluded a light Higgs boson ($M_{\mathrm{H}} < 5\,\mathrm{GeV}/c^2$).[6]

From 1989 to 1995, the four LEP experiments searched for direct evidence of Higgs boson production via the Higgsstrahlung process in $\mathrm{e}^+\mathrm{e}^-$ collisions at a center-of-mass energy of 91.2 GeV (*i.e.*, LEP1). Due to enormous background from Z→hadrons, only the final states where the Z decays to $\nu\bar{\nu}$ and $\ell^+\ell^-$ (where $\ell^\pm$ denotes either $\mathrm{e}^\pm$ or $\mu^\pm$) were considered. ALEPH used the full LEP1 data sample, observed three candidate events with 2.7 events expected from Standard Model background processes, and set a 95%

[6]Most of these results have a model dependence as summarized in Ref. [25].

confidence level limit of $M_{\mathrm{H}} > 63.9\,\mathrm{GeV}/c^2$ [36]. DELPHI, L3, and OPAL also conducted similar Higgs boson searches and set 95% confidence level lower limits on the mass of the Higgs boson of 55.7, 60.2, and $59.6\,\mathrm{GeV}/c^2$ respectively [37, 38, 39].

With the advent of LEP2 and initial center-of-mass energies of 161 and 172 GeV, the four LEP experiments again searched for direct evidence of Higgs boson production via the Higgsstrahlung process. The total integrated luminosities of the data samples at 161 and 172 GeV were 41.7 and $41.2\,\mathrm{pb}^{-1}$ respectively. Due to the different background conditions at LEP2, all major final states of the Higgsstrahlung process were covered; this is discussed further in Section 1.3. Four (six) candidate events were observed at 161 (172) GeV with expectation from Standard Model background processes of 5.3 (11.1) events. A combined 95% confidence level lower limit of $M_{\mathrm{H}} > 77.5\,\mathrm{GeV}/c^2$ was set [40].

A search for the Standard Model Higgs boson in $\mathrm{p\bar{p}}$ collisions at a center-of-mass energy of 1.8 TeV has been conducted with the CDF and D0 experiments at the Tevatron. The integrated luminosities of the data samples ($110\,\mathrm{pb}^{-1}$ for CDF and $100\,\mathrm{pb}^{-1}$ for D0) are insufficient to set any significant lower limits on the Higgs boson mass since cross sections and signal detection efficiencies are very small; however, in the absence of evidence of an unexpected signal, upper limits on the Higgs boson production cross section can be determined [41]. The Higgs boson production process $\mathrm{q\bar{q}} \rightarrow (\mathrm{W}^{\pm},\ \mathrm{Z})\mathrm{H}$ with $\mathrm{H} \rightarrow \mathrm{b\bar{b}}$ was investigated. CDF concentrated on modes in which $\mathrm{Z} \rightarrow \mathrm{q\bar{q}}$, $\mathrm{W}^{\pm} \rightarrow \mathrm{q\bar{q}}'$, and $\mathrm{W}^{\pm} \rightarrow \mathrm{e}\nu_{\mathrm{e}}$ or $\mu\nu_{\mu}$. D0 concentrated on the modes in which

$Z \rightarrow \nu\bar{\nu}$ and $W^{\pm} \rightarrow e\nu_e$ or $\mu\nu_\mu$. The Standard Model expectation for the cross section is less than 1 pb for Higgs boson masses above $70\,\mathrm{GeV}/c^2$ [41]. No evidence of a signal was detected. CDF set a 95% confidence level upper limit on the cross section for a Higgs boson with mass between 70 and $120\,\mathrm{GeV}/c^2$ in the range from 14 to 19 pb [42]. Limits in the range from 50 to 20 pb are set by D0 [43]. The sensitivity of Tevatron Higgs boson searches is expected to improve after the main injector upgrade is completed [41].

1.3 Higgs Boson Production and Background Processes at LEP2

The Higgsstrahlung process $e^+e^- \rightarrow HZ$ is the dominant Higgs boson production mechanism at LEP2 and constitutes the signal process for the discussions presented in this thesis.

A variety of Higgsstrahlung final states exist when specific decays modes of the Higgs boson and the Z are considered; these are described in Section 1.3.1. These final states have characteristic topologies for which specific sets of event selection criteria (referred to as *analyses*) are designed.

The challenge when designing an analysis for each final state is to detect the Higgs boson signal while rejecting the Standard Model processes which do not involve Higgs boson production but can mimic it in different respects. These Standard Model background processes are described in Section 1.3.2.

After all event selection criteria are applied, the number of events ex-

pected to be observed in data due to Standard Model background processes can be determined from samples of simulated events. If no significant excess events are observed, a lower limit on the Higgs boson mass can be set.

1.3.1 The Higgsstrahlung Process and Final States

At tree-level, the cross section for the Higgsstrahlung process (with a final state Z which is real) is

$$\sigma(\mathrm{e^+e^-} \to \mathrm{HZ}) = \frac{g^4}{3072\pi \cos^4\theta_\mathrm{W}} \frac{1}{s} \left[1 + (1 - 4\sin^2\theta_\mathrm{W})^2\right] \lambda^{\frac{1}{2}} \frac{\lambda + 12M_\mathrm{Z}^2/s}{(1 - M_\mathrm{Z}^2/s)^2}$$

where λ is a two-particle phase space factor: $\lambda = (1 - M_\mathrm{H}^2/s - M_\mathrm{Z}^2/s)^2 - 4M_\mathrm{H}^2 M_\mathrm{Z}^2/s^2$ [44]. The Higgsstrahlung cross section as obtained from the HZHA event generator [22] is shown in Figure 1.5 as a function of center-of-mass energy for various Higgs boson masses. Figure 1.6 shows cross sections for Higgsstrahlung as well as $\mathrm{W^+W^-}$ and ZZ fusion Higgs boson production processes at a fixed center-of-mass energy ($\sqrt{s} = 183\,\mathrm{GeV}$) and as a function of the Higgs boson mass as obtained from the HZHA event generator [22].

At a center-of-mass energy of 183 GeV, the cross section ranges from 1.0 to 0.01 pb for Higgs boson masses between 60 and 100 GeV/c^2. As shown in Figure 1.6, the Higgsstrahlung cross section is roughly two orders of magnitude greater than the cross section for $\mathrm{W^+W^-}$ fusion and roughly three orders of magnitude greater than ZZ fusion for a Higgs boson mass of 85 GeV/c^2.

There exist a variety of Higgsstrahlung final states when specific decay modes of the Higgs and the Z are considered. Table 1.3 summarizes

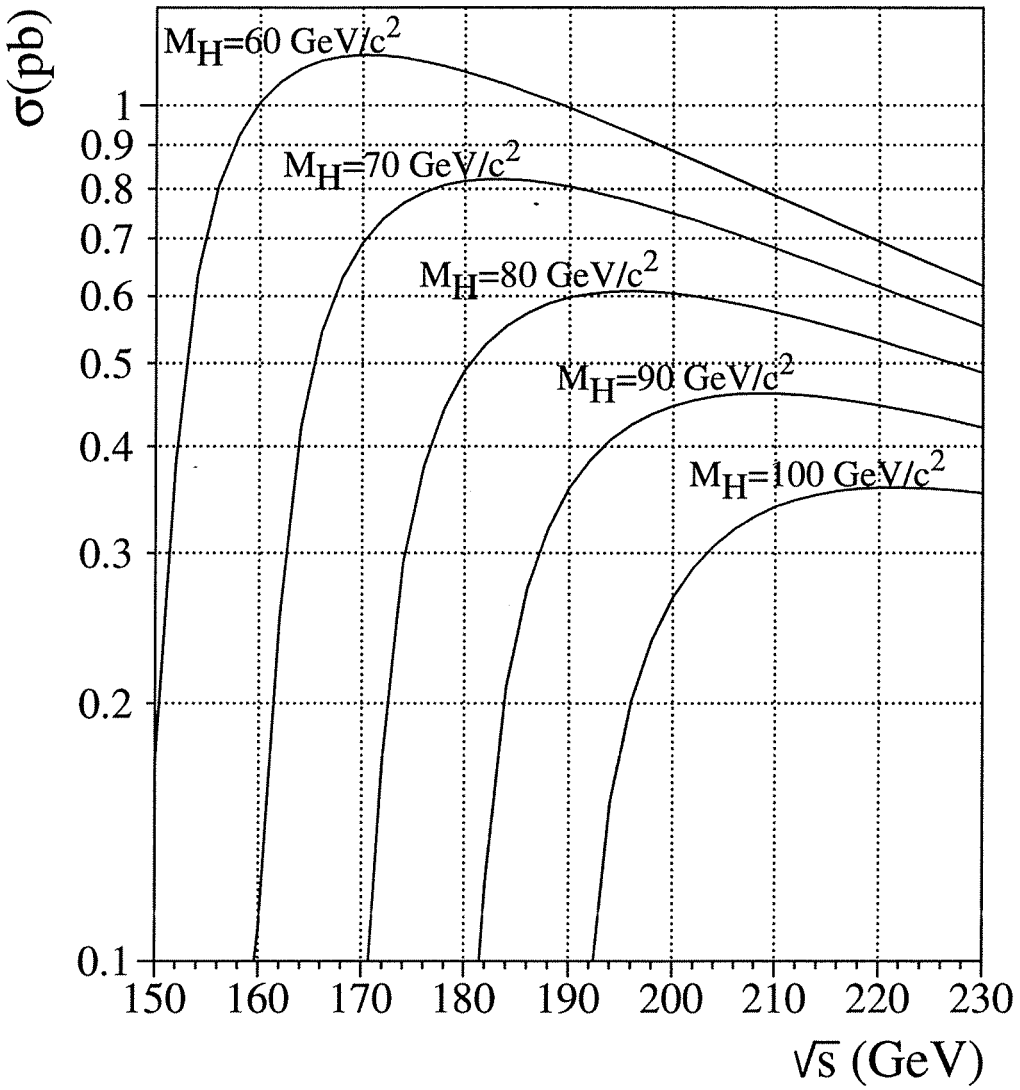

Figure 1.5: The cross section for the Higgsstrahlung process in e^+e^- collisions as a function of center-of-mass energy for various Higgs boson masses as calculated by the HZHA event generator [22].

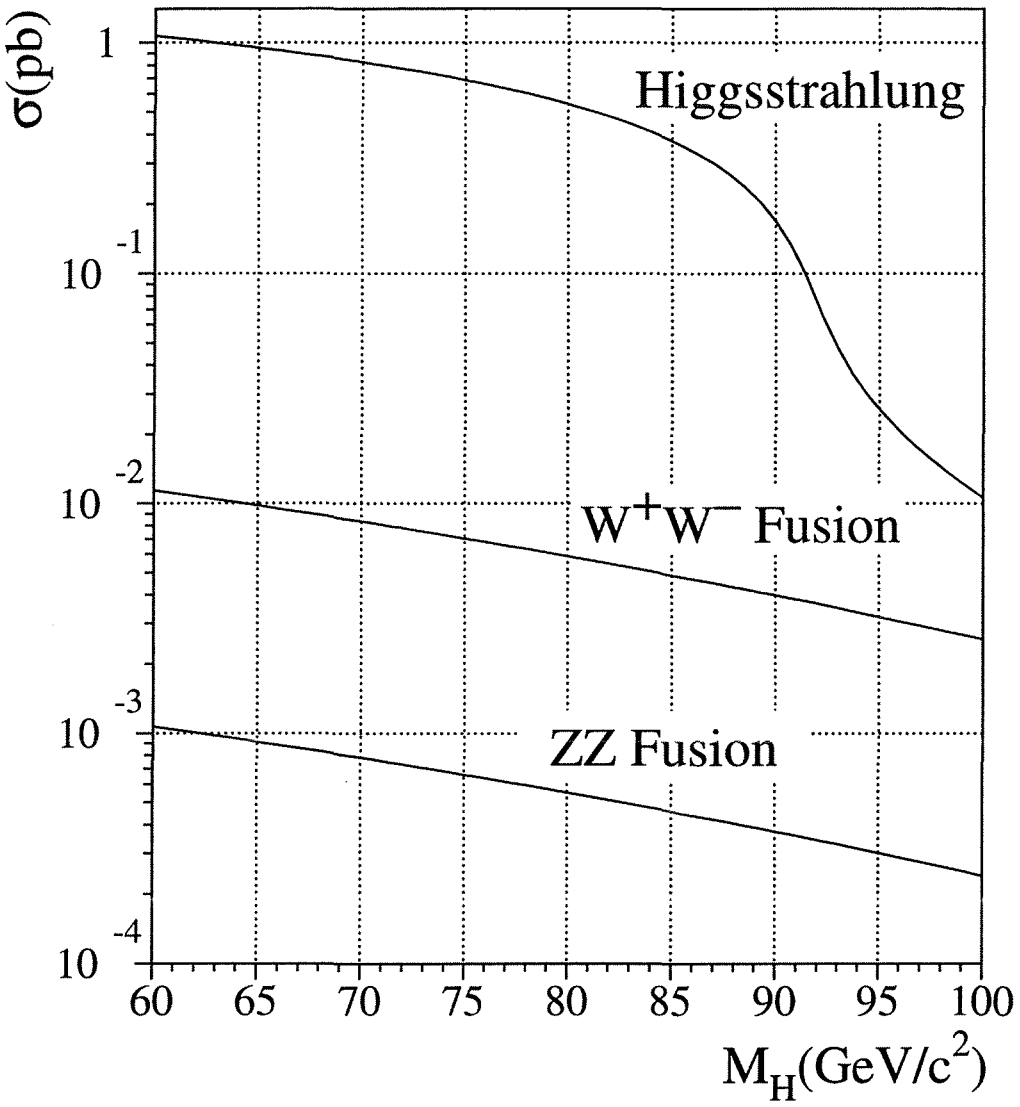

Figure 1.6: The cross section at $\sqrt{s} = 183\,\mathrm{GeV}$ for the Higgsstrahlung, W^+W^- fusion, and ZZ fusion processes in e^+e^- interactions as a function of the Higgs boson mass as calculated by the HZHA event generator [22].

the possible decay modes and the fraction of the total Higgsstrahlung process they represent. This thesis concentrates on the dominant four-jet final state described below. Analyses designed for this final state are described in Chapter 4. As mentioned in Section 1.2.4, this final state was inaccessible in the LEP1 environment due to the large resonant background from $e^+e^- \rightarrow Z \rightarrow$hadrons. Analyses designed to search for the other final states are summarized in Appendix A.

Higgsstrahlung Final States			
$b\bar{b}(q\bar{q},\ b\bar{b})$	$b\bar{b}\nu\bar{\nu}$	$b\bar{b}\ell^+\ell^-$	$b\bar{b}\tau^+\tau^-$
59%	17%	5.6%	2.9%
$\tau^+\tau^-(q\bar{q},\ b\bar{b})$	$\tau^+\tau^-\nu\bar{\nu}$	$\tau^+\tau^-\ell^+\ell^-$	$\tau^+\tau^-\tau^+\tau^-$
5.5%	1.5%	0.5%	0.3%
$(q\bar{q},\ gg)(q\bar{q},\ b\bar{b})$	$(q\bar{q},\ gg)\nu\bar{\nu}$	$(q\bar{q},\ gg)\ell^+\ell^-$	$(q\bar{q},\ gg)\tau^+\tau^-$
5.5%	1.5%	0.5%	0.3%

Table 1.3: A summary of the fraction of various final states with respect to the total Higgsstrahlung cross section for a Higgs boson mass of 85 GeV/c^2. The first fermion pair denotes the decay products of the Higgs boson. The second denotes the decay products of the Z. Non-b quark pairs are denoted as $q\bar{q}$. Electrons and muons are denoted as $\ell^{\pm}$.

The Four-Jet Final State

The dominant Higgsstrahlung final state consists of the Z decaying to $q\bar{q}$ and the Higgs boson decaying to $b\bar{b}$: $e^+e^- \rightarrow HZ \rightarrow b\bar{b}q\bar{q}$. This accounts for between 60 and 57% of the total Higgsstrahlung cross section for Higgs boson masses between 60 and 100 GeV/c^2 respectively. If Higgs boson decays to non-b quark pairs and gg are included, the fraction of the total increases

to between 65 and 64% for Higgs boson masses between 60 and 100 GeV/c^2 respectively. Each of the quarks or gluons manifests itself as jets of hadrons; the phenomenology of jets is described in detail in Section 3.1. Hence, this final state is referred to as the *four-jet* final state

This four-jet final state is characterized by events with a low amount of missing energy. The two jets from the Higgs boson decay are typically b quark jets. If the Z decays to $b\bar{b}$, then the event will have four b jets. In both cases, the experimental identification of b quark jets is crucial to distinguish signal events from the background processes discussed in Section 1.3.2.

The Missing Mass Final State

The next most prevalent Higgsstrahlung final state consists of the Z decaying to neutrinos and the Higgs boson decaying to $b\bar{b}$: $e^+e^- \rightarrow HZ \rightarrow b\bar{b}\nu\bar{\nu}$. This accounts for roughly 17% of the total Higgsstrahlung cross section for Higgs boson masses between 60 and 100 GeV/c^2. If Higgs boson decays to $q\bar{q}$ and gg are included, the fraction of the total Higgsstrahlung cross section increases to roughly 18%. This final state is referred to as the *missing mass* final state.

This final state is characterized by two acoplanar jets with respect to the direction of the incident e^+e^- beams and missing mass close to M_Z due to the neutrinos escaping undetected. Again, the two jets from the Higgs boson are predominantly b quark jets, and the experimental identification of b quark jets is of crucial importance to search for this final state.

The Dilepton Final States

The Higgsstrahlung final state with the Z decaying to e^+e^- or $\mu^+\mu^-$ and the Higgs boson decaying to $b\bar{b}$, $q\bar{q}$ or gg is referred to as the *dilepton* final state and accounts for roughly 6% of the total Higgsstrahlung cross section for Higgs boson masses between 60 and 100 GeV/c^2. Although this is a small percentage of the total, the events have a distinctive signature: two energetic leptons from the Z and typically two b jets from the Higgs boson.

Final States with τ Leptons

The Higgsstrahlung final state involving two oppositely charged τ leptons and a quark/anti-quark pair, e^+e^-, or $\mu^+\mu^-$ accounts for between 8.6% and 8.8% of the total cross section for Higgs boson masses between 60 and 100 GeV/c^2. These final states include the three cases: $H \rightarrow \tau^+\tau^-$ and $Z \rightarrow q\bar{q}$ constituting 5.2 to 5.5% of the total; $H \rightarrow b\bar{b}$ and $Z \rightarrow \tau^+\tau^-$ constituting 2.9 to 2.7% of the total; $H \rightarrow \tau^+\tau^-$ and $Z \rightarrow \ell^+\ell^-$ constituting 0.50 to 0.53% of the total.[7] These final states are characterized by two jets and two oppositely charged τ leptons, typically two b jets and two oppositely charged τ leptons, and two oppositely charged τ leptons and two energetic oppositely charged electron or muon pairs.

[7]The $\tau^+\tau^-\ell^+\ell^-$ final state is dealt with in the context of the analyses designed for the dilepton final state described in Appendix A.

1.3.2 Background Processes

Several Standard Model processes which do not involve Higgs boson production can mimic a potential Higgs signal. Hence, these processes are referred to as *Standard Model background processes* or simply as *background*. These background processes can be classified into two groups: two-fermion and various four-fermion processes. Since the Higgs signal processes considered in this thesis involve at least two quark jets (with the exception of the $\tau^+\tau^-\ell^+\ell^-$ final state), only background processes which could result in a multi-hadronic final state are relevant.

The Two-Fermion Process

The relevant two-fermion background process is the production of a quark/anti-quark pair from a Z or virtual photon: $e^+e^- \rightarrow Z^{(*)}/\gamma^* \rightarrow q\bar{q}(\gamma)$. A diagram contributing to this process is shown in Figure 1.7(b). The (γ) denotes any initial state radiation (ISR) photons from the electron or positron. One of the quarks can bremsstrahlung a hard gluon, leading to events with more than two jets (*e.g.*, $q\bar{q}g$, $q\bar{q}gg$, $q\bar{q}q\bar{q}$, etc...). This process was the dominant physics process at LEP1 with a large cross section of roughly 30 nb due to the center-of-mass energies being near M_Z. As the center-of-mass energy increases towards the LEP2 regime, this cross section falls rapidly. At a center-of-mass energy of 183 GeV, it is 102 pb.[8]

[8]The cross sections for the Standard Model background processes are calculated with the PYTHIA event generator [45] with the exception of the W^+W^- cross section which is calculated with the KORALW event generator [46], the two-photon hadronic cross section which is calculated with the PHOT02 generator [47], and the $Z\nu\bar{\nu}$ cross section which is calculated with the ZNNB01 generator [48].

Roughly 65% of the $e^+e^- \rightarrow Z^{(*)}/\gamma^* \rightarrow q\bar{q}(\gamma)$ process at 183 GeV consists of *radiative Z returns*. This refers to the case when a hard ISR photon from the electron or positron boosts the effective center-of-mass energy of the colliding system back to near M_Z (denoted as $q\bar{q}\gamma$). The ISR photon typically has low transverse momentum; it can escape undetected down the beam pipe and the resulting event will have missing energy, or it could be detected as an isolated energy deposit in a detector and the resulting event will have little missing energy. In either case, the quark jets in $q\bar{q}\gamma$ events recoil against the ISR photon and are not collinear.

The smaller component of the total cross section consists of hard e^+e^- annihilation to $q\bar{q}$. In this case the visible mass of the event is near the center-of-mass energy. Since the total two-fermion cross section consists of radiative Z returns and hard annihilations, it is denoted as $q\bar{q}(\gamma)$. Figure 1.8(a) shows the total $q\bar{q}(\gamma)$ and hard annihilation component cross sections as a function of energy for energies near 183 GeV.

This process and experimental measurements based upon it are described in detail elsewhere [49].

The Two-Photon Process

The process in which virtual photons from the incoming electron and positron form a fermion/anti-fermion pair is referred to as the *two-photon* or $\gamma\gamma$ process, although it is actually a four-fermion process. A lowest-order diagram contributing to this process is shown in Figure 1.7(a). A $\gamma\gamma$ event is referred to as being *untagged* if both the electron and positron escape down the beam

pipe undetected. The majority of the $\gamma\gamma$ events are untagged.

Only the case when the produced fermion/anti-fermion pair are quarks is relevant to Standard Model Higgs searches. The hadronic cross section is highly dependent upon assumed kinematic features; it is roughly 10 nb with a generator level requirement that the invariant mass of the hadronic system W_{had} be greater than $2.5\,\mathrm{GeV}/c^2$. Although this cross section is large, these events are characterized by extremely low visible energy and particle multiplicity. Hence they are easily eliminated at early stages of the event selection criteria designed to search for the Higgs boson, and they do not constitute a significant source of background events.

This process as well as experimental measurements based upon it are described in detail elsewhere [50].

The $\mathrm{W^+W^-}$ Process

The pair-production of $\mathrm{W}^{\pm}$ bosons has a cross section of 15.8 pb at a center-of-mass energy of 183 GeV.[9] This process has two s-channel (γ^* and Z^*) and one t-channel production mechanisms; Figure 1.7(c) shows diagrams contributing to these processes. At energies near the $2M_{\mathrm{W}}$ threshold, the t-channel diagram dominates [44]. This process and experimental measurements based upon it are described in detail elsewhere [51].

For searches for neutral Higgs bosons, this background process represents a source of c jets which can be misidentified as b jets. Figure 1.8(c) shows

[9]The value of M_{W} used in the KORALW event generator [46] for this cross section calculation is $80.35\,\mathrm{GeV}/c^2$.

the W^+W^- cross section as a function of energy for energies near 183 GeV.

The ZZ Process

The four-fermion process involving the pair-production of Z bosons shown in Figure 1.7(d) includes the processes $e^+e^- \to \gamma^*\gamma^*, Z^{(*)}\gamma^*$, and $Z^{(*)}Z^{(*)}$; this process is referred to as ZZ; hence "Z" denotes either an on-shell Z boson, Z*, or a γ^*. Below $2M_Z$, the process results in only one on-shell Z; thus it can resemble the two-fermion $q\bar{q}\gamma$ process.

At a center-of-mass energy of 183 GeV, which is just above $2M_Z$, the production of two on-shell Z bosons begins to turn-on. If a definition of two "on-shell" Z bosons is taken as $\{(M_{Z_1} - 91.2)^2 + (M_{Z_2} - 91.2)^2\} < (10\,\mathrm{GeV}/c^2)^2$, roughly 9% of the 2.9 pb cross section at 183 GeV is due to the production of two on-shell Z bosons.[10] This fraction increases to roughly 22% at 189 GeV. Figure 1.8(b) shows the ZZ cross section as a function of energy for the total and on-shell component as defined above.

This background process is especially problematic for analyses designed to search for the Higgs boson at LEP2. If one Z decays to $b\bar{b}$ or $\tau^+\tau^-$, the resulting final state is indistinguishable from a Higgsstrahlung final state for a Higgs boson mass near M_Z; hence ZZ is referred to as an *irreducible* background in searches for the Standard Model Higgs boson.

This process and experimental measurements based upon it are described in detail elsewhere [52].

[10] A requirement that the mass of each $Z^{(*)}/\gamma^*$ be greater than $200\,\mathrm{MeV}/c^2$ is used for calculating the ZZ cross section.

Single W and Z Processes

The lowest-order dominant t-channel diagrams contributing to the four-fermion processes involving the production of single $W^{\pm}$ bosons ($e^+e^- \rightarrow W^{\pm}e\nu_e$, denoted as We$\nu$) and single Z bosons ($e^+e^- \rightarrow Ze^+e^-$, denoted as Zee) are shown in Figures 1.7(e) and (f). As is the case with the ZZ process, the "Z" denotes a $Z^{(*)}$ or γ^*. The cross sections at 183 GeV are 0.6 and 6.8 pb for Weν and Zee respectively.[11] The Weν process and experimental measurements based upon it are described in detail elsewhere [53].

Both of these processes have events which are characterized by a "spectator" electron or positron escaping down the beam pipe undetected. Hence, these events will have a large component of missing momentum in the z direction. Events from the Weν process have visible masses near M_W. Events from Zee process will often have visible masses near M_Z; the production of low mass virtual photons is possible, but these events have very low particle multiplicity and visible energy.

A second mechanism for single Z boson production exists: $e^+e^- \rightarrow Z\nu\bar{\nu}$. This process is identical to the Higgs production via W^+W^- fusion illustrated in Figure 1.2 except that the product of the W^+W^- fusion is a Z boson instead of a Higgs boson. This process has an extremely low cross section of 0.013 pb at a center-of-mass energy of 183 GeV (calculated with the ZNNB01 generator [48]).

[11] A requirement that the mass of the $Z^{(*)}/\gamma^*$ be greater than $12\,\mathrm{GeV}/c^2$ is used when calculating the Zee cross section.

Summary of Background Processes

Table 1.4 gives a summary of Standard Model background processes and their cross sections at $\sqrt{s} = 183\,\text{GeV}$.

Cross section (pb)					
$q\bar{q}(\gamma)$	W^+W^-	ZZ	Zee	Weν	Z$\nu\bar{\nu}$
102	15.8	2.9	6.8	0.61	0.013

Table 1.4: A summary of the cross sections for Standard Model background processes at $\sqrt{s} = 183\,\text{GeV}$.

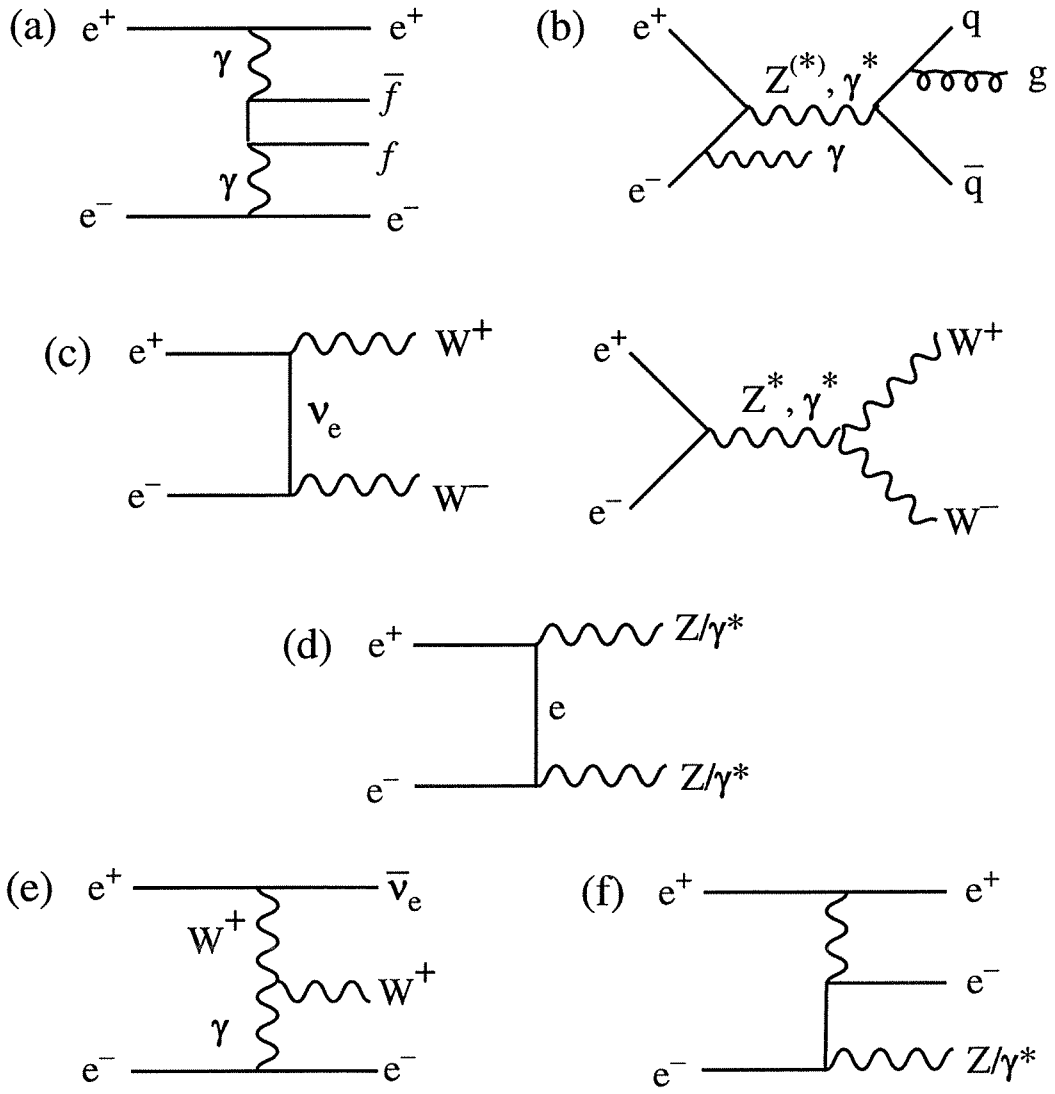

Figure 1.7: Diagrams contributing to Standard Model background processes: (a) two-photon, (b) $q\bar{q}(\gamma)$, (c) W pair production (W^+W^-), (d) $Z^{(*)}/\gamma^*$ pair production (ZZ), (e) single W production ($We\nu$), and (f) single Z production (Zee).

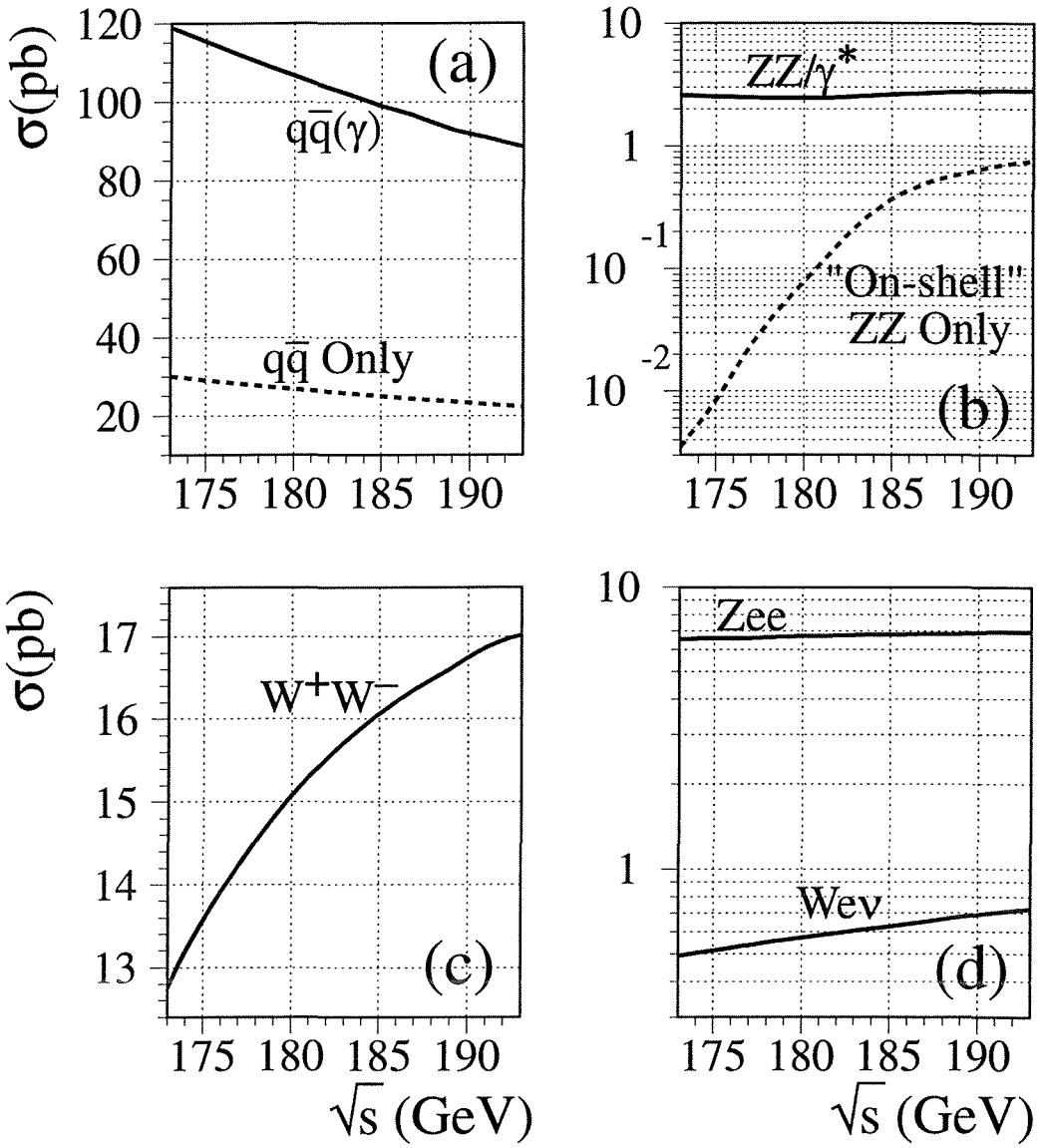

Figure 1.8: Cross sections for Standard Model background processes as a function of center-of-mass energy: (a) $q\bar{q}(\gamma)$ (solid line) and the component without ISR (dashed line), (b) ZZ/γ^* production (solid line) and the component having two "on-shell" Z bosons (dashed line), (c) W^+W^- production, (d) single $W^{\pm}$ ($We\nu$) and single Z (Zee) production.

Chapter 2

Experimental Apparatus

2.1 The LEP Accelerator

Located in the region of the border between France and Switzerland at an average depth of 100 m below the surface, the Large Electron Positron (LEP) storage ring accumulates, accelerates, and collides counter-rotating high energy beams of electrons and positrons. LEP consists of four straight and four curved sections which together form a ring measuring 26.6 km in circumference. The beams circulate in a pipe with a vacuum of the order of 10^{-9} Torr and are guided and focused by 3304 dipole and 496 quadrapole magnets. Radio frequency (RF) cavities accelerate the beams and compensate for energy losses due to synchrotron radiation. Collisions occur at four equidistant interaction points along the ring each of which is the site of a large detector experiment (ALEPH, DELPHI, L3, or OPAL). The LEP storage ring is described in more detail elsewhere [54].

A series of smaller accelerators and storage rings accelerate and inject electrons and positrons into LEP. The LEP Injector Linacs (LIL) produce and accelerate electrons to 600 MeV. A high-current 200 MeV electron beam from the first LIL strikes a tungsten target and produces positrons which are accelerated by the second LIL to 600 MeV. Both electrons and positrons are injected into the Electron/Positron Accumulator (EPA) which serves as a buffer between the dedicated LEP pre-injection facilities and the multi-purpose CERN Proton Synchrotron (PS). The PS receives these leptons and accelerates them to an energy of 3.5 GeV before injection into the CERN Super Proton Synchrotron (SPS) which accelerates them to a final pre-LEP-injection energy of 22 GeV. The accelerator complex is shown in Figure 2.1.

From 1989 to 1995, LEP accelerated e^+e^- beams to an energy of roughly 45 GeV, allowing collisions with center-of-mass energies at or near the Z peak. This first phase of LEP (LEP1) delivered a total of 200 pb^{-1} to each detector experiment and permitted the study of a variety of topics such as precision measurements of electroweak parameters and investigations into production and decay of hadrons containing the heavy b and c quarks.

The second phase of LEP (LEP2) involves increasing the center-of-mass energy to nearly 200 GeV. The most notable and technologically challenging obstacle to this upgrade is the higher accelerating gradients needed to compensate the energy losses due to synchrotron radiation (SR). Since the SR energy loss scales as the fourth power of the beam energy, attaining increasingly higher beam energies in a storage ring such as LEP is a formidable challenge. At the LEP1 beam energy of 45 GeV, the average energy loss due

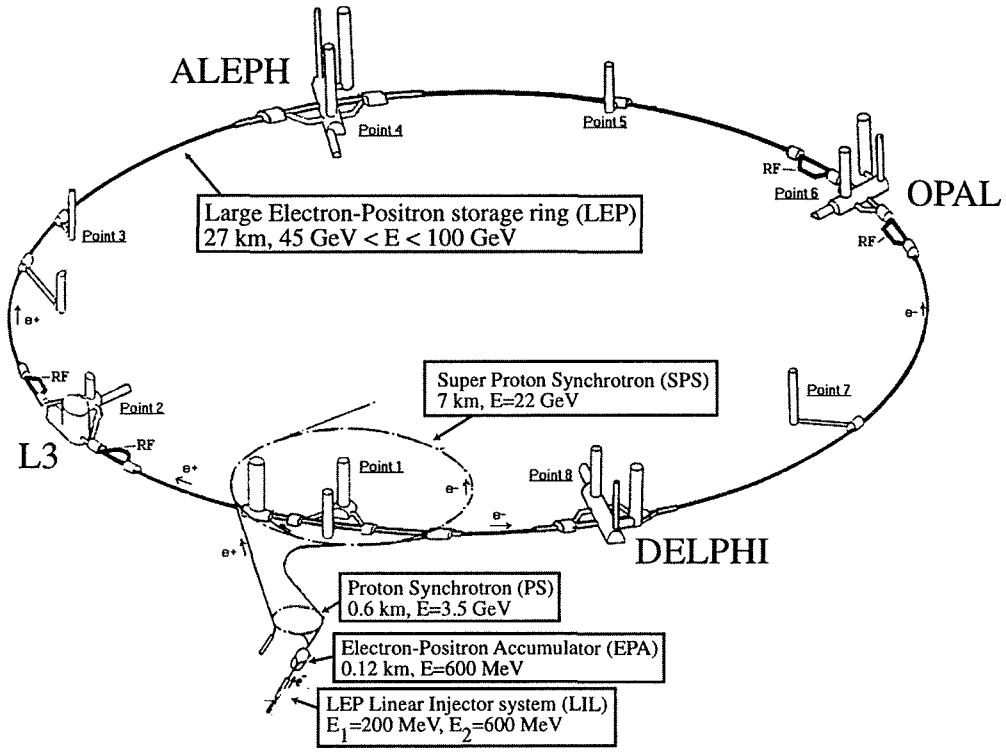

Figure 2.1: The LEP accelerator complex. The LEP Linear Injector system (LIL), Electron Positron Accumulator (EPA), Proton Synchrotron (PS), and Super Proton Synchrotron (SPS) are the injector system for the main LEP storage ring. Electron-positron collisions occur at four experimental areas ALEPH, DELPHI, L3, and OPAL.

to SR was a modest 116 MeV per turn per electron/positron, and normal-conducting copper RF cavities could be used. At a beam energy of 100 GeV this energy loss increases to more than 2800 MeV per turn and superconducting (SC) copper/niobium RF cavities operating near 4.5 K must be used. In November of 1995, following the installation of 56 new SC RF cavities [55], LEP attained center-of-mass energies between 130 and 136 GeV. Another 84 SC RF cavities were installed during the first part of 1996, and LEP was able to increase its energies to 161 GeV and 172 GeV during 1996 [56]. An additional 84 SC RF cavities have since been installed enabling LEP to reach 183 GeV starting in May 1997.

With the advent of LEP2, a new operational method was adopted with respect to the configuration of the circulating beams in order to boost luminosity and to strive towards a goal of a total LEP2 integrated luminosity of $500\,\mathrm{pb}^{-1}$. Prior to 1995, LEP operated in either a *bunch* mode with four equidistant bunches of electrons or positrons in each beam or a *pretzel* scheme which allowed eight bunches per beam [57]. Due to a maximum bunch current limitation of 0.5 mA and intrinsic problems arising from the pretzel mode, these schemes were abandoned in favor of a new *bunch train* configuration in which beams contain four equidistant trains each consisting of up to four bunches [58]. This scheme has been used since November 1995.

LEP strives to deliver the highest possible instantaneous luminosities to each of the four detector experiments. The luminosity $\mathcal{L}$ for LEP is defined

as

$$\mathcal{L} = \frac{N_{e^+} N_{e^-} N_{\text{bunch}} N_{\text{trains}} f}{4\pi\sigma_x\sigma_y}$$

where $N_{e^\pm}$ is the number of $e^\pm$ per bunch, N_{bunch} is the number of bunches in a train, N_{trains} is the number of trains, f is the revolution frequency, and σ_x and σ_y are the RMS beam sizes in the x and y directions at the interaction point of an experiment. The luminosity at each experimental point is determined with dedicated luminosity subdetectors and monitors. Typical luminosities during the 1997 running period were roughly $10^{31}\,\text{cm}^{-2}\text{s}^{-1}$.

An accurate determination of the LEP beam energy is essential for a majority of physics analyses. At LEP1, a method of determining the beam energy through resonant spin depolarization of the circulating beams was developed and had an accuracy of better than 1 MeV [59]. This method relies upon the natural build-up of transverse polarization [60]. An oscillating radial field from an RF-magnet is used to determine the spin precession frequency of electrons. This frequency is directly proportional to the beam energy [61]. However, the strength of depolarizing effects in the accelerator increases as the square of beam energy [62], and it has proved impossible to achieve any significant amount of transverse polarization at LEP2 energies. Hence, energy measurements at LEP2 must be done with a new extrapolation method. Partially polarized 45 or 50 GeV beams are first circulated in LEP to allow an energy calibration via the depolarization scheme. The beams are accelerated to LEP2 energies, and a measurement of the new field strength of the dipole magnets is done with NMR probes. This method gives a beam

energy uncertainty of roughly 30 MeV [63].

It is interesting to note that a variety of environmental phenomena contribute to the energy measurement uncertainty. These include radial deformations of the ring due to lunar and solar tides [61], the amount of rainfall in the region, the water level in Lake Geneva [64], parasitic currents carried by the LEP beam pipe caused by the passage of TGV trains near Geneva [65], and changes in the dipole magnetic fields due to temperature and humidity variations [63].

During 1997, LEP operated in three different energy regimes: $\sqrt{s} = 91.3$, 130 and 136, and 181−184 GeV. The data sample collected at $\sqrt{s} = 91.3$ GeV consists of an integrated luminosity of $2.2\,\mathrm{pb}^{-1}$ and is referred to as the Z *peak data*. This Z peak data sample is used for calibration purposes and systematic studies. The data collected at $\sqrt{s} = 130\,\mathrm{GeV}$ $(3.8\,\mathrm{pb}^{-1})$ and $\sqrt{s} = 136\,\mathrm{GeV}$ $(3.6\,\mathrm{pb}^{-1})$ were used to investigate possible anomalous four-jet production observed by ALEPH in 1995 [66]. The data taken at center-of-mass energies between 181 and 184 GeV are referred to as the *high energy data* and constitute the data sample used for the analysis presented in this thesis. Figure 2.2 shows the LEP integrated luminosity delivered to ALEPH as a function of time. Table 2.1 summarizes the center-of-mass energies and luminosities for the high energy data.

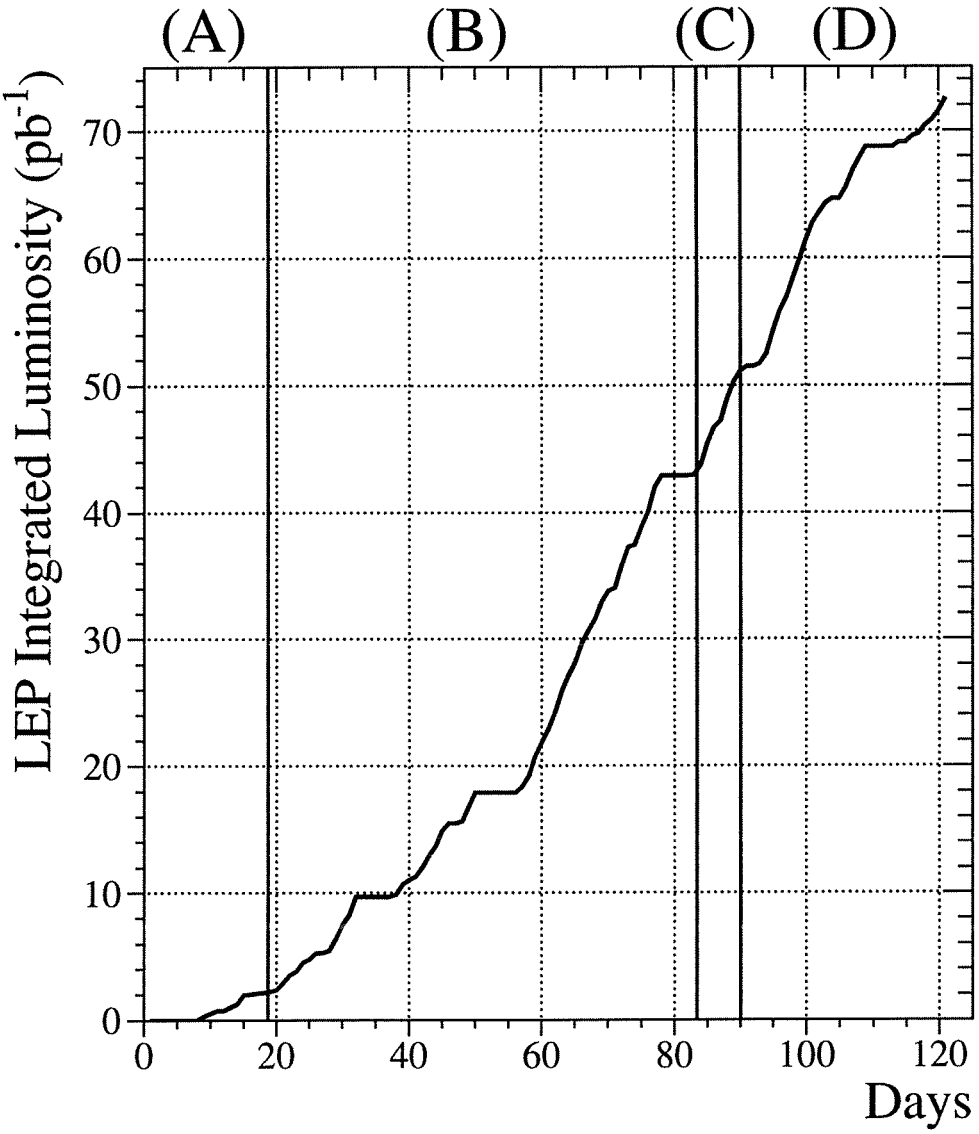

Figure 2.2: LEP integrated luminosity delivered to ALEPH in 1997 as a function of time [67]. The run is divided into four parts of three different center-of-mass energy ranges: (A) $\sqrt{s} = 91.3\,\text{GeV}$, (B) $\sqrt{s} = 181 - 184\,\text{GeV}$, (C) $\sqrt{s} = 130$ and $136\,\text{GeV}$, and (D) return to $\sqrt{s} = 181 - 184\,\text{GeV}$.

Energy (GeV)	Integrated Luminosity (pb^{-1})
180.834	0.16
181.711	3.94
182.714	51.0
183.766	1.93
182.675	57.0

Table 2.1: Summary of the 1997 LEP high energy data delivered to ALEPH. The last row is the luminosity-weighted average. The uncertainty on the energy measurements is 29 MeV [68]. The uncertainty on the total luminosity is 0.54% as discussed in Section 2.2.8.

2.2 The ALEPH Detector

ALEPH (Apparatus for LEP pHysics), one of four large detector experiments on the LEP storage ring, consists of groups of finely segmented cylindrical subdetectors. The detector is large, about 1 000 m^3, and has a high degree of hermeticity. A cut-away view of the detector is shown in Figure 2.3. All subdetectors are coaxial with respect to a central beryllium/aluminum beam pipe with a 5.41 cm outer radius which holds the LEP vacuum and the e^+ and e^- beams.

The origin of the ALEPH coordinate system is a fixed point close to the interaction point where e^+e^- beams collide. The actual interaction point varies according to LEP beam parameters and is determined on an event-by-event basis (see Section 3.3.1). The nominal direction of the e^- beam is defined to be the z direction; the x direction is a horizontal line pointing towards the center of LEP; the y direction points upwards, orthogonal to x

and z. A polar angle θ is defined with respect to the z axis, and an azimuthal angle ϕ is defined circling around the detector in a right-handed sense with respect to the z axis.

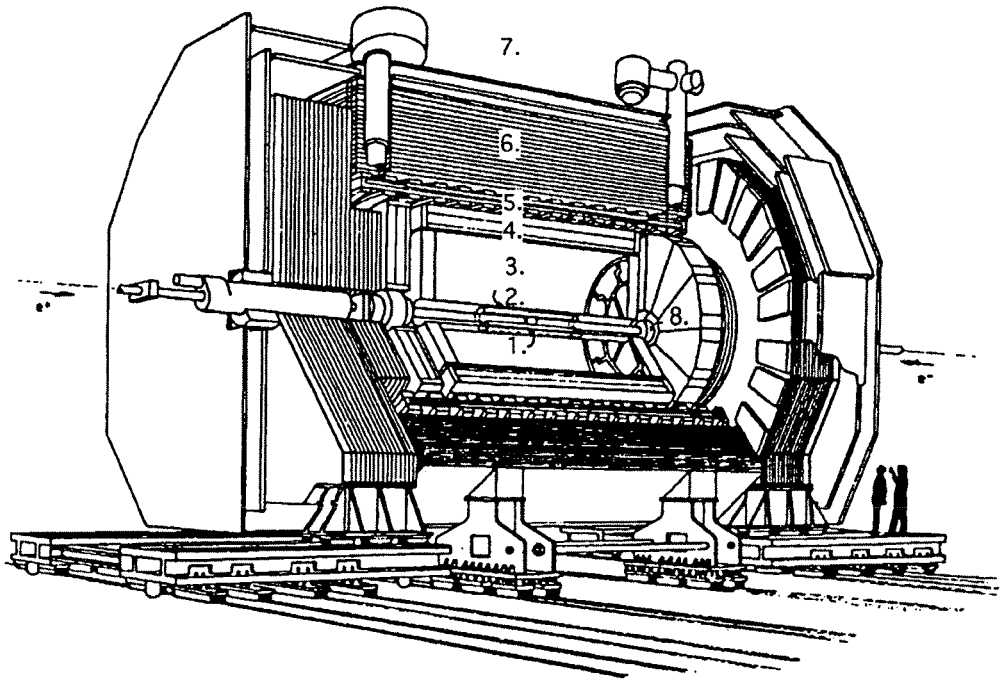

Figure 2.3: The ALEPH detector shown in a cut-away view. The various subdetector components are numbered: (1) silicon microstrip vertex detector (VDET), (2) inner tracking chamber (ITC), (3) time projection chamber (TPC), (4) electromagnetic calorimeter (ECAL), (5) superconducting solenoidal magnet coil, (6) hadron calorimeter (HCAL), (7) muon chambers, (8) luminosity subdetectors.

A large time projection drift chamber (TPC), a multi-wire drift chamber (ITC), and a double-sided silicon microstrip vertex detector (VDET) comprise the central tracking system of the detector and are immersed in an uniform 1.5 T magnetic field created by a superconducting solenoidal coil

coaxial with the beam line. A lead/wire chamber sampling electromagnetic calorimeter (ECAL) and an iron/streamer tube hadron calorimeter (HCAL) provide energy measurements of charged and neutral particles traversing the detector. Outside the HCAL, two double layers of streamer tubes (muon chambers) detect and provide position information for muons. Measurements of absolute luminosity are obtained from specialized low-angle subdetectors, the LCAL and the SiCAL.

The ALEPH detector is described in detail elsewhere [69, 70, 71, 72]. Relevant aspects of the detector components are described in the subsections below.

2.2.1 The Vertex Detector (VDET)

The silicon microstrip vertex detector (VDET) complements tracking information obtained from the ITC and TPC by providing precise measurements of charged particle trajectories close to the interaction point. High-precision position measurements are crucial for identifying and studying properties of short-lived hadrons containing the heavy b and c quarks.

The use of silicon detectors in high energy physics has numerous benefits. Advanced techniques such as photolithography developed in the commercial semiconductor industry permit silicon detectors to be designed and fabricated with relative ease and a high degree of accuracy and reproducibility. Thin and compact detectors can be constructed due to the low average energy (3.6 eV per electron-hole pair) needed to ionize silicon compared to gas chamber gases

(26 eV for argon). The large lattice mobility of charge carriers liberated by ionization and the small readout electrode pitch give fast charge collection and signal response times on the order of 10 ns. A disadvantage of silicon detectors is their susceptibility to radiation damage. The nature of this damage is either bulk damage to sites in the crystal lattice or surface damage to the Si/SiO_2 layer [73, 74]. For this reason, a dedicated subsystem of the ALEPH online data acquisition system, the ALEPH Radiation Beam Loss Interlock System (ARBLIS), monitors radiation levels near the VDET and is able to safely and swiftly dump LEP beams in the event of unacceptably high levels.

In the fall of 1995, the ALEPH VDET was upgraded in order to improve the identification of b jets for neutral Higgs boson searches at LEP2. The completely new VDET described below is twice as long as the previous VDET, has roughly half of the passive material in the active region, and uses new radiation-hard readout chips. More complete descriptions of the upgrade as well as the initial ALEPH VDET program are available elsewhere [75].

The VDET has two concentric cylindrical layers of double-sided silicon wafers. Each silicon wafer is rectangular, measuring 52.6 mm by 65.4 mm, and consists of n-type 300 μm thick silicon. The wafers function as segmented reverse-biased p-n junction diodes. On the *junction* side of each wafer, 2 041 12 μm strips of p^+ material running parallel to the beam direction are implanted every 25 μm. On the *Ohmic* side of each wafer, 1 280 12 μm n^+ strips running perpendicular to the beam direction are implanted every 50 μm interspersed with p^+ blocking strips. The p^+ blocking strips

electrically isolate the n^+ strips from an electron accumulation layer in the Si/SiO_2 interface near the wafer surface. The wafers are reverse-biased with a voltage of between 20 and 62 V, creating a depletion region devoid of mobile charge carriers. Charged particles traversing this depletion zone ionize the material liberating electron-hole pairs which drift to the orthogonal p^+ and n^+ strips and generate measurable signal pulses. The junction side p^+ strips provide an $r\phi$ coordinate for particles while the Ohmic side n^+ strips provide the z coordinate. Only every second p^+ and n^+ strip is connected to readout electronics, hence the readout pitch is 50 μm and 100 μm for the $r\phi$ and z sides respectively. Using charge interpolation techniques, a spatial resolution of 10 μm in $r\phi$ and 15 μm in z can be obtained. The $r\phi$ and z measurements are independent; they are paired together to form true three-dimensional space points during offline event reconstruction.

Three silicon wafers mounted end-to-end create a single readout unit in terms of data acquisition called a module. Readout electronics are mounted at the end of each module in order to minimize material in the active region. Two modules are combined to create a face with an active length of 40 cm shown in Figure 2.4. The entire VDET has 24 faces arranged in two layers shown in Figure 2.5. The inner layer has nine faces with an average radius of 6.3 cm from the beam axis; the outer layer has 15 faces with an average radius of 11 cm from the beam axis. These radii are constrained by the 5.5 cm outer radius of the LEP beam pipe and the inner 12.8 cm radius of the ITC support tube. Adjacent faces are arranged to overlap 0.2 cm in the $r\phi$ view.

Intrinsic limitations to the VDET spatial resolution include strip readout

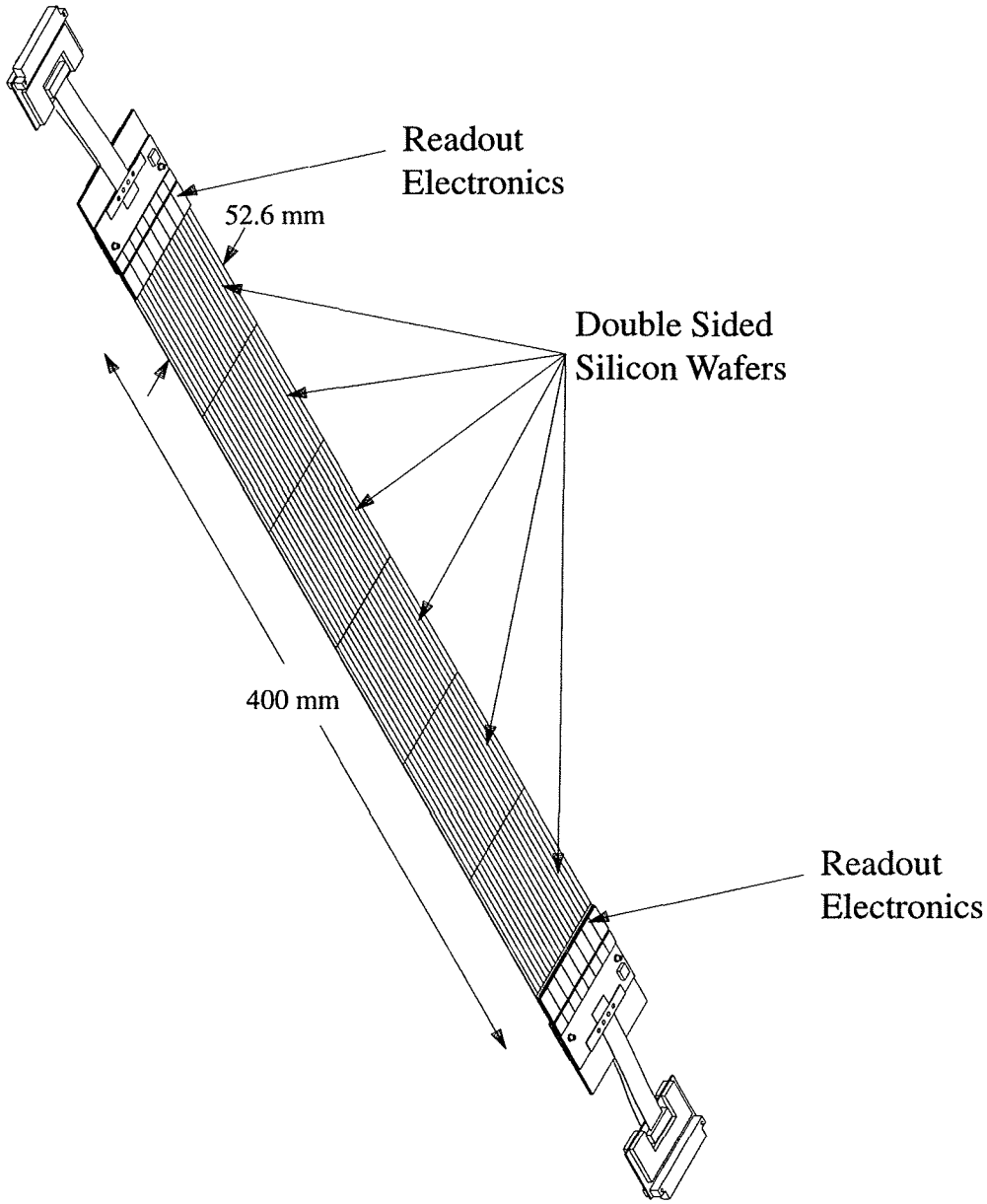

Figure 2.4: A view of the junction side of a VDET face. Each face consists of six wafers (two modules of three wafers) and associated readout electronics and cabling at both ends of the face.

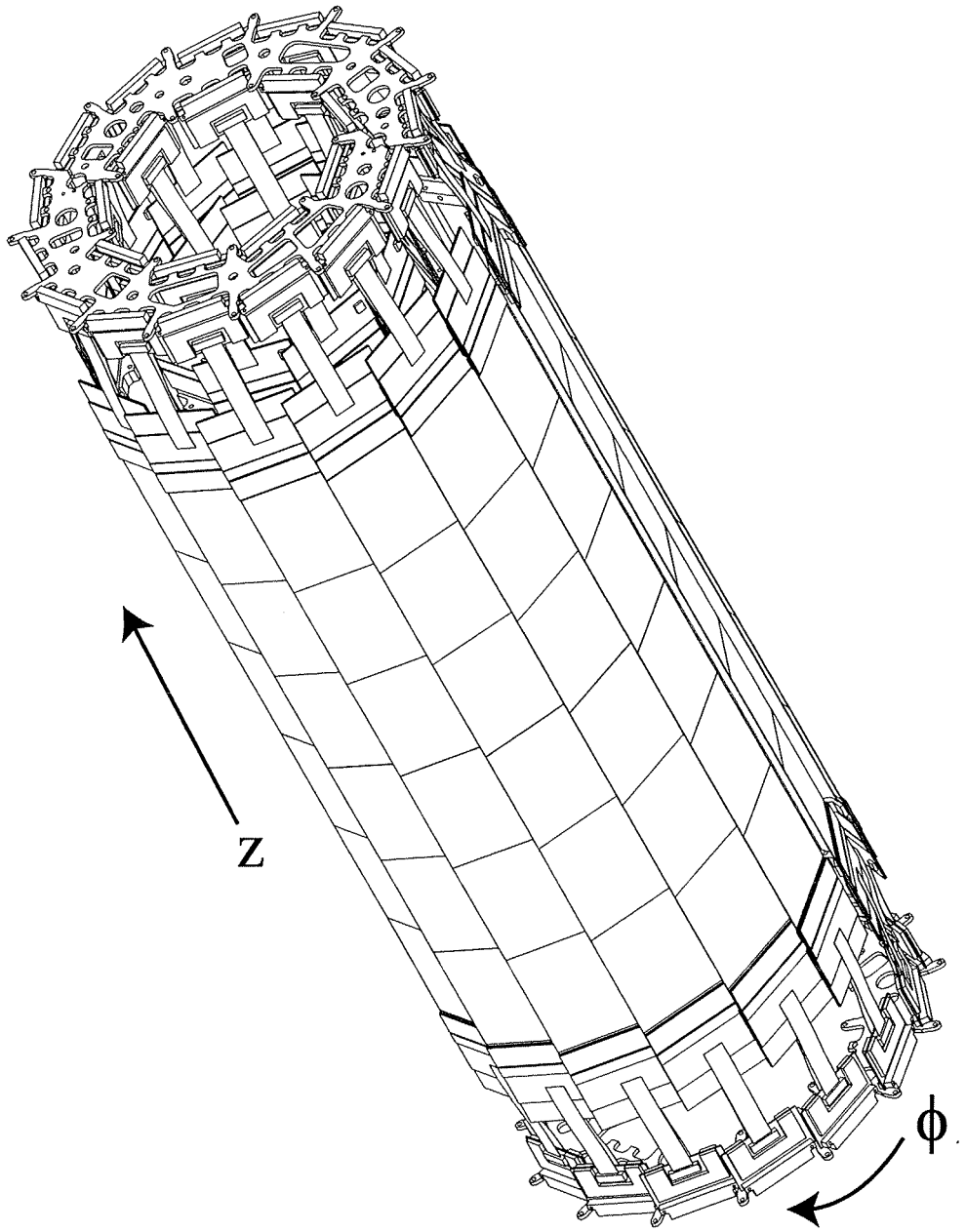

Figure 2.5: A diagram of the assembled VDET consisting of 15 outer faces and nine inner faces.

pitch, Landau energy loss fluctuations of the particles traversing the silicon, electron-hole drift distortions due to the magnetic field, and noise in the readout electronics [73]. Knowledge of the position of the silicon strip detectors relative to one another and the other tracking devices is crucial and represents an additional source of degradation in the performance of the VDET. Ideally, the position of each wafer is known with the same precision as the intrinsic 10 μm resolution. This is challenging since there are a total of 864 alignment parameters: three rotations and three translations for each of the 144 wafers. Fortunately, tracks from data can be used to align the VDET [76]. Alignment parameters and corrections can be determined using tracks from multi-hadronic events obtained during dedicated alignment runs taken at $\sqrt{s} = 91$ GeV as well as from the higher energy runs. A laser system monitors time-dependent mechanical instabilities caused by distortions of the faces. Laser beams shine on 44 light spots; typically three spots are positioned on each outer layer face [77].

2.2.2 The Inner Tracking Chamber (ITC)

The ITC, a cylindrical multi-wire drift chamber, has inner and outer radii of 12.8 cm and 28.8 cm, and a 2 m active length. The chamber is filled with a mixture of 80% argon and 20% CO_2 at atmospheric pressure. Running parallel to the beam direction, 30 μm diameter gold-plated tungsten sense wires are arranged in eight concentric layers. There are 96 wires in each of the four inner layers and 144 wires in each of the four outer layers. Gold-plated

147 μm diameter aluminum field wires are arranged hexagonally around each of the sense wires creating close-packed drift cells. The sense wires carry a positive potential between 1.8 kV and 2.0 kV while the field wires are held at ground, giving a gas gain of between 1.2×10^4 and 4.9×10^4. The drift cells in adjacent layers are offset by half cell-widths allowing left-right track ambiguities to be resolved. Between every two drift cell layers 100 μm diameter copper/beryllium guard wires and aluminum hoops form guard cages to catch any broken wires. Figure 2.6 shows an end-on view of the wire configuration for a slice of the ITC.

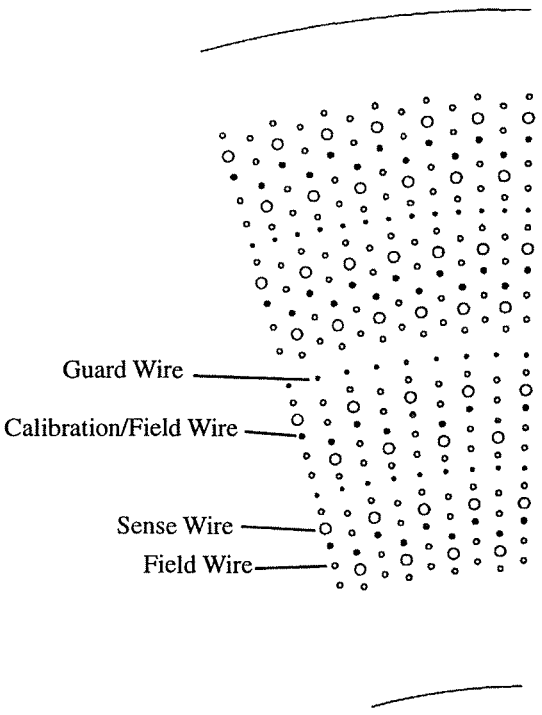

Figure 2.6: An $r\phi$ view of a slice of the ITC. There are eight layers of sense wires together with associated field wires and calibration wires.

Tracks with $|\cos\theta| < 0.97$ will traverse all eight drift cell layers. The drift time in cells determines the $r\phi$ coordinates with an average resolution of $150\,\mu$m. By measuring the difference between the arrival times of pulses at opposite ends of sense wires, the z coordinate can be determined with an average resolution of 5 cm.

The ITC provides the only tracking information for the Level-1 trigger (discussed in Section 2.2.9). The drift cell size has been minimized to be between 4.7 mm and 6.5 mm to provide fast trigger response time. A decision based upon $r\phi$ coordinates is available within $1\,\mu$s of a beam crossing. A three-dimensional $r\phi z$ trigger decision is available within $2\,\mu$s to $3\,\mu$s. These times are less than the successive bunch crossing time at LEP2 of $22\,\mu$s.

2.2.3 The Time Projection Chamber (TPC)

The TPC (shown in Figure 2.7) is a 4.4 m long cylindrical annulus coaxial to the beam direction having inner and outer radii of 0.31 m and 1.80 m. The $43\,\text{m}^3$ gas volume is filled with a mixture of argon (91%) and methane (9%) at a pressure between 8 mbar and 12 mbar above atmospheric pressure. A disc-shaped membrane made from $25\,\mu$m thick Mylar coated with conducting graphite paint is placed at the midpoint of the TPC. A potential of $-27\,$kV is placed on this central membrane while each end of the TPC is held at a potential near ground. This creates an electric drift field of 11.5 kV/m pointing from each end of the TPC towards the central membrane. The surfaces of the inner and outer cylinders which define the TPC volume are referred

to as *field cages*. The field cages contain copper ring-shaped electrodes with a thickness of 10.2 mm spaced 1.5 mm apart. These electrodes are connected in series by resistor chains to the central membrane and shape the electric drift field.

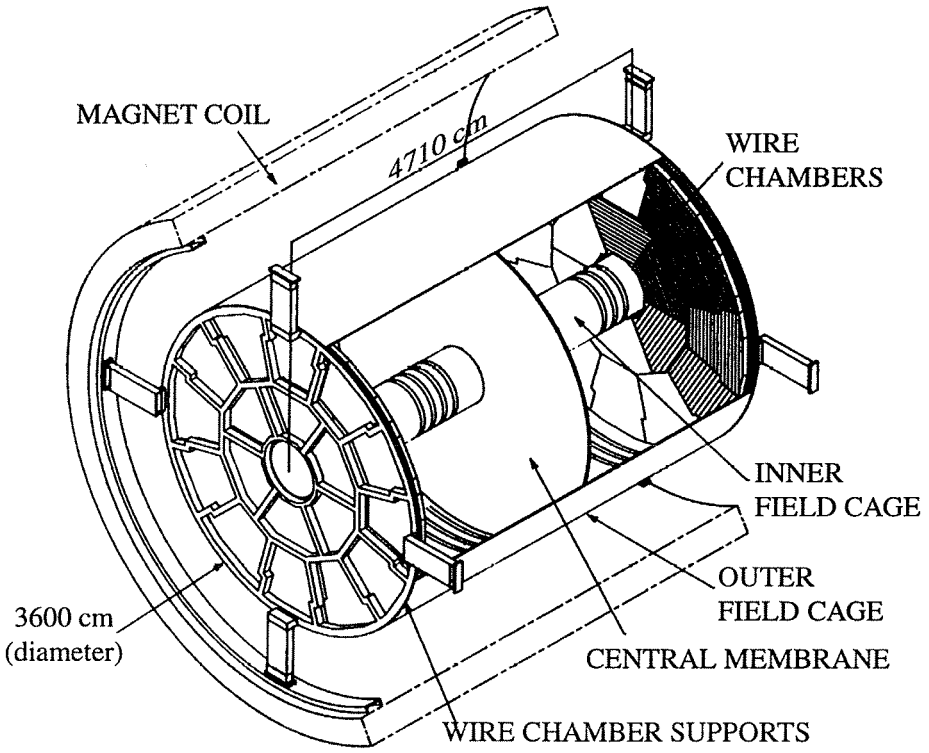

Figure 2.7: A cut-away view of the TPC showing the central membrane, inner and outer field cages, and the 18 wire chamber sectors with their supports at each end.

Charged particles traversing the TPC volume leave ionization trails in the gas. Due to the uniform axial magnetic field, these particle trajectories are helical. Ionization electrons drift towards an end plate with a velocity

of $5.2\,\mathrm{cm}/\mu\mathrm{s}$. Each of the end plates contain 18 sectors of multi-wire proportional chambers. In each sector, three planes of wires are strung over a cathode pad plane as shown in Figure 2.8.

The build-up of charge in the drift volume from positive ions produced in the wire chamber gas amplification avalanches would alter the electric drift field and cause track distortions. This motivates the use of a *gating* grid. The first wire plane over each sector consists of $76\,\mu\mathrm{m}$ diameter copper wires at 2 mm intervals. In its closed state the gating grid blocks the passage of charged particles by holding alternate wires at a potential of $-67 \pm 100\,\mathrm{V}$. Roughly $3\,\mu\mathrm{s}$ before a LEP beam crossing, the grid wires are switched to a potential of $-67\,\mathrm{V}$, permitting the passage of charged particles. When the Level-1 trigger decision is positive, the gate is held in this open state for the $45\,\mu\mathrm{s}$ maximum drift time of ionization electrons in the TPC.

In order to define the potential boundaries of the drift cells and to isolate the drift volume from the wire chamber electric field, a cathode wire plane of $76\,\mu\mathrm{m}$ diameter copper wires is situated 6 mm behind the gating grid in each sector. Four millimeters behind this grid a plane of gold-plated $127\,\mu\mathrm{m}$ diameter copper field wires are interleaved with gold-plated $20\,\mu\mathrm{m}$ tungsten sense wires with a spacing of 2 mm. Ionization electrons from the drift volume cause avalanches around the sense wires and induce signals on a segmented copper cathode pad plane 4 mm from the sense-field wire plane. The size of each cathode pad is $6.2\,\mathrm{mm} \times 30\,\mathrm{mm}$ ($\delta r\phi \times \delta r$) with an azimuthal pitch of 6.7 mm. In each sector there are between 148 and 196 sense wires and 909 and 1326 cathode pads. Between cathode pad rows, 32 trigger pads

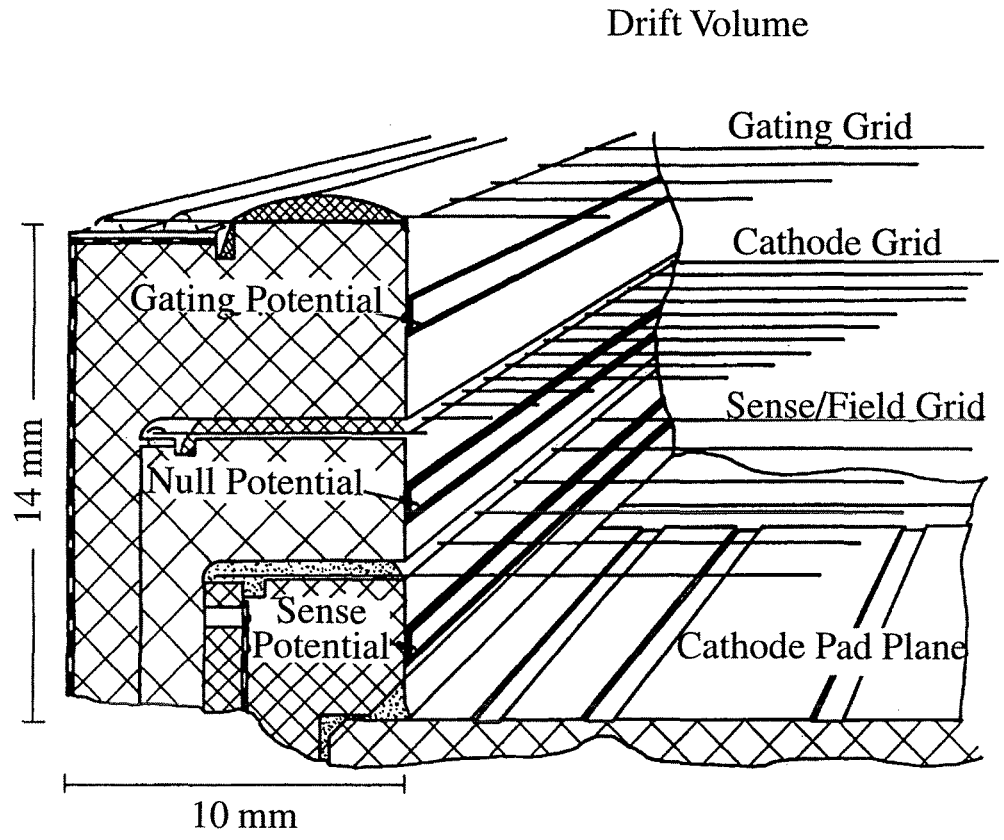

Figure 2.8: A schematic view of a TPC wire chamber sector. Three layers of wires form a cathode wire plane, a gating plane, and a sense/field wire plane. These wires are strung over a plane containing copper cathode readout pads.

measuring 6.3 mm radially and subtending 15° in azimuth are used for the Level-2 trigger discussed in Section 2.2.9.

Charged particle trajectories in the TPC can traverse a maximum of 21 pad rows and 338 sense wires. The ϕ coordinate is determined by charge interpolation from signals induced on the cathode pads. The r coordinate is determined from the known radial position of the pads involved in the measurement. An $r\phi$ point resolution of 180 μm can be obtained. The z coordinate is determined from the measured drift time from the cathode pad signals[1] with a point resolution of 0.8 mm. The pulse heights on the sense wires provide $\mathrm{d}E/\mathrm{d}x$ information which is used for particle identification (see Section 2.3.2).

A calibration system of frequency-quadrupled Nd-YAG lasers provides thirty straight ionization tracks which can be used to measure track distortions and drift velocities. The lasers are fired between beam crossings in order to monitor time-dependent effects present during data taking periods.

2.2.4 The Electromagnetic Calorimeter (ECAL)

Outside the TPC but inside the magnet solenoid is the ECAL, a highly granular lead/wire chamber sampling calorimeter with a thickness of 22 radiation lengths (X_0). Twelve modules surround the TPC cylinder and comprise the central barrel while twelve petal-shaped modules form each of the two endcap

[1]Starting in 1997, modifications and improvements to the ALEPH offline track reconstruction algorithms permit the use of both pad and wire information to determine the z coordinate. This results in an improvement in the z coordinate resolution for high angle tracks by roughly 30%.

modules closing both ends. The ECAL covers 98% (3.9π) of the total solid angle excluding cracks between adjacent active module areas which account for 2% of the barrel surface and 6% of the endcap surfaces. The barrel has inner and outer radii of 185 cm and 225 cm. The endcaps are 251 cm on either side of the interaction point and have active inner and outer radii of 57 and 228 cm and a depth of 41 cm. The barrel and endcap modules are shown in Figure 2.9.

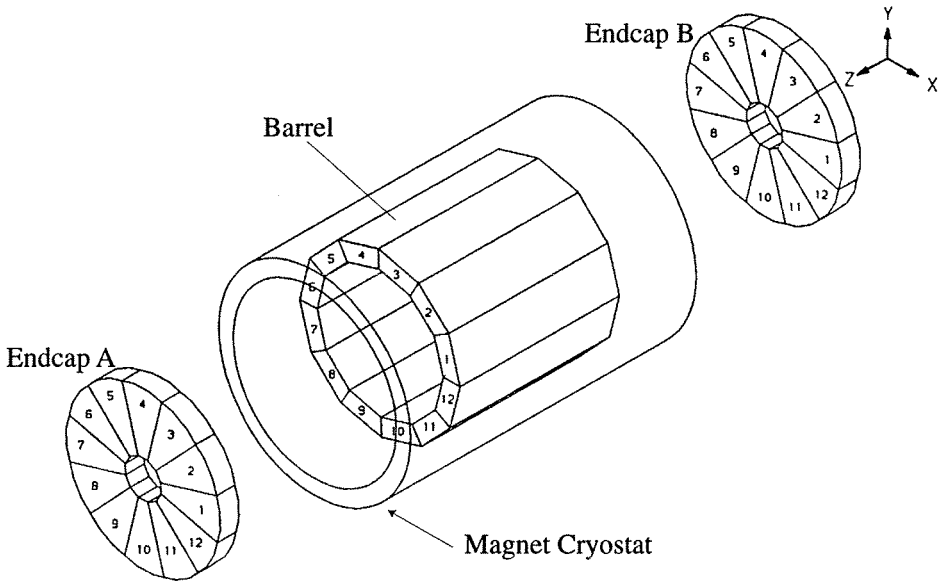

Figure 2.9: An overall view of the ECAL barrel and endcaps surrounded by the cryostat for the magnet coil.

Each module has 45 lead and proportional wire chamber layers. A single layer (see Figure 2.10) consists of a 2 mm or 4 mm thick lead sheet, an aluminum sheet with open extrusions on one side, a plane of 25 μm diameter gold-plated tungsten anode wires with a 5 mm pitch, a thin highly resistive

graphite-coated Mylar window, and a plane of cathode pads. A gas mixture of 80% xenon and 20% CO_2 at 60 mbar above atmospheric pressure is used in the modules.

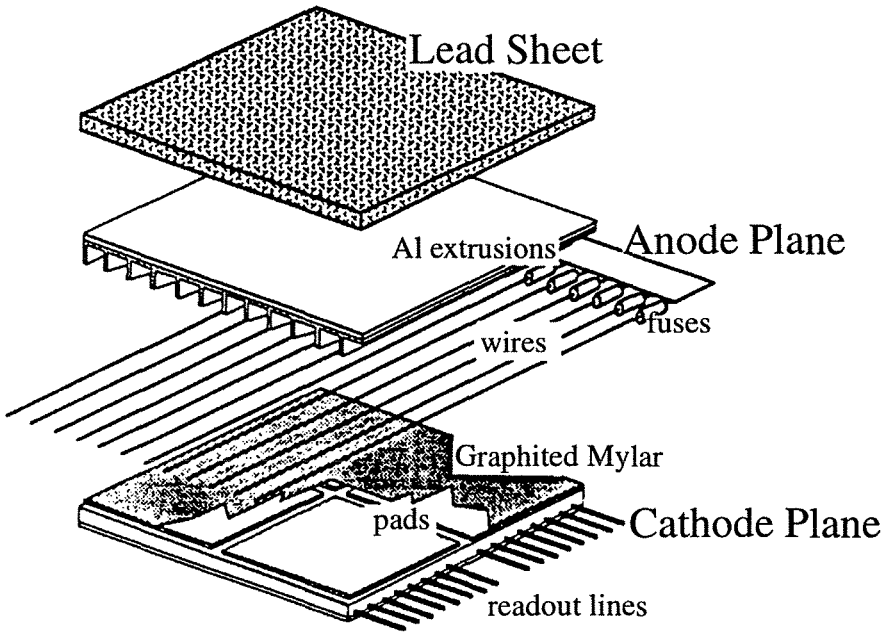

Figure 2.10: Composition of a lead/wire chamber layer of the ECAL: lead sheet, aluminum extrusion layer, anode wire plane, and cathode readout pad plane.

Electromagnetic showers develop in the lead sheets and cause ionization avalanches near the anode wires. These avalanches induce signals on cathode pads which are connected internally to form towers pointing towards the interaction point. The towers are divided into three sections or storeys corre-

sponding to three ECAL stacks: the first four (10 layers of 2 mm lead sheet), the middle nine (23 layers of 2 mm lead sheet), and the last nine radiation lengths (12 layers of 4 mm lead sheet). There are a total of 49 152 towers and 115 404 wires in the barrel and 24 576 towers and 226 800 wires in both endcaps.

The tower storeys and the anode wires planes provide energy measurements with a resolution $\sigma_E/E = 0.18/\sqrt{E} + 0.009$ with E in GeV. The longitudinal evolution of showers can be determined from separate tower storey readouts. The position of a shower centroid can be determined with a resolution of $(6.8\,\text{mm}\,\text{GeV}^{1/2})/\sqrt{E}$ with E in GeV.

2.2.5 The Superconducting Magnet Coil

The solenoidal superconducting coil, positioned between the ECAL and the HCAL, is a continuous winding of a NbTi/Cu conductor along a length of 6.35 m and is cooled by liquid helium to a temperature near 4.4 K. Near both ends of the main coil there are 40 cm long compensating coils. The coils are housed in an annular cryostat with inner and outer radii of 2.48 m and 2.92 m. When the main coil is brought to its full nominal current of 5 000 A, it produces a 1.5 T uniform axial field. With the compensating coils operating, the field within the tracking volume has a homogeneity $\Delta B_z/B_z < 0.2\%$ and radial and azimuthal field components of $B_r/B_z < 0.4\%$ and $B_\phi/B_z < 0.04\%$ respectively. The HCAL serves as the return yoke for the magnetic field.

2.2.6 The Hadron Calorimeter (HCAL)

Consisting of iron slabs interspersed with layers of Iarocci streamer tubes [78], the hadron calorimeter (HCAL) measures the energy of hadrons. It also is the magnet return yoke, the absorbing material for the muon chambers, and the main support for the ALEPH detector. Shown in Figure 2.11, the central barrel and two endcaps encase the superconducting coil and ECAL endcaps, covering 99% of 4π. The barrel has inner and outer radii of 3.0 m and 4.7 m and consists of twelve 70 ton modules 7.24 m in length. Each barrel module has twenty-two 5 cm thick iron slabs and a final 10 cm thick iron slab. The 22 layers correspond to 7.16 interaction lengths at a normal incidence. Each endcap extends from a 0.45 m inner radius to 4.35 m outer radius and consists of six 75 ton petal-shaped modules situated 3.15 m from the interaction point. The narrow end of each endcap petal has twenty-two 5 cm thick iron slab layers with a 10 cm thick final layer and touches the outer edge of the ECAL endcap; the wide end has sixteen 5 cm thick iron slab layers and touches the end of the HCAL barrel. The 1.5 T axial magnetic field pushes the endcaps inwards against the barrel with a force of about 4 000 tons. Both the barrel and endcap modules are rotated by 32.7 mrad with respect to the ECAL so that the cracks in the calorimeters do not overlap.

Between the iron slabs, graphite-coated PVC extrusions create streamer tube cells with square 9 mm $\times$ 9 mm cross sections separated by 1 mm thick walls. Running along the length of each cell there are 100 μm thick beryllium-copper anode wires. The tube cells contain a gas mixture of 22.5% argon,

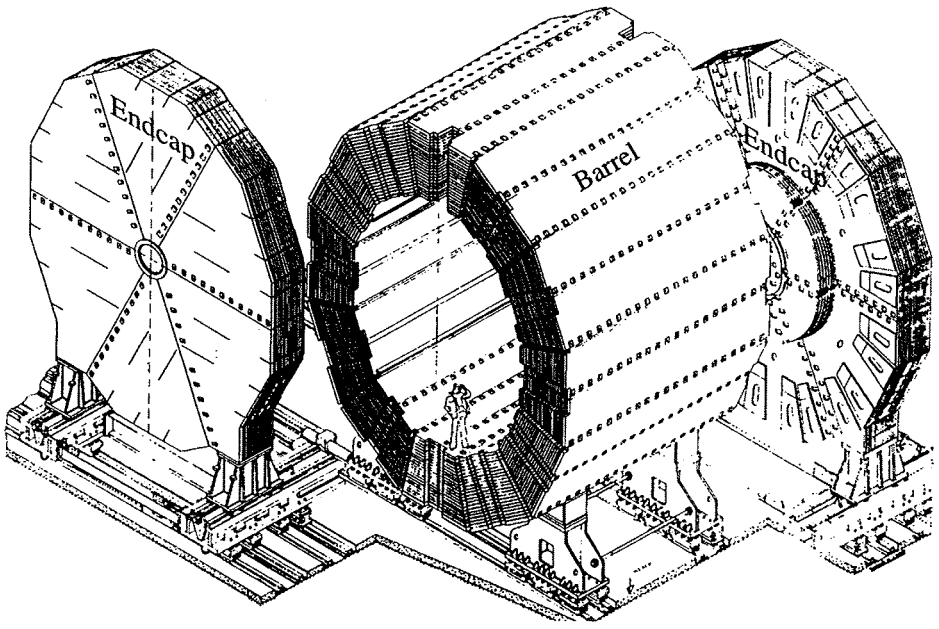

Figure 2.11: The HCAL barrel and endcaps which serve as an absorber to measure the energy of hadrons, a support for the entire detector, and a return yoke for the magnet.

47.5% CO_2, and 30% isobutane. There are 0.4 cm wide aluminum strips running the length of each streamer tube as well as pads over the streamer tubes on the opposite side of the tube plane. Ionizing particles from hadronic showers produce avalanches around the central wire of the tube and induce signals on the strips and pads. The pads are arranged in projective towers with angular segmentation $\Delta\phi \times \Delta\theta$ of $3.7° \times 3.0°$ in the barrel and either $7.5° \times 2.7°$ or $15° \times 2.5°$ in the endcaps. The tower pad readout provides energy measurements of hadronic showers with a resolution of $\sigma_E/E = 84\%/\sqrt{E}$. Strip readout provides projective two-dimensional digital patterns. These digital hit patterns, although only two-dimensional, give a picture of a particle's behavior as it traverses the iron slabs and are used for muon identification.

2.2.7 The Muon Chambers

Outside the HCAL there are two double layers of streamer tubes, the muon chambers. The separation of the two double layers is between 40 and 50 cm. The gas and the streamer tube construction of the muon chambers is the same as the HCAL. Each layer of tubes has 4 mm wide aluminum strips with 10 mm pitch that are parallel to the streamer tube wires (x-strips) as well as 10 mm wide strips with 12 mm pitch that are perpendicular to the wires (y-strips); there are no pads. This configuration is shown in Figure 2.12. Particles traversing the muon chambers leave up to four two-dimensional hits; track directions can be measured with an accuracy of between 10 and 15 mrad.

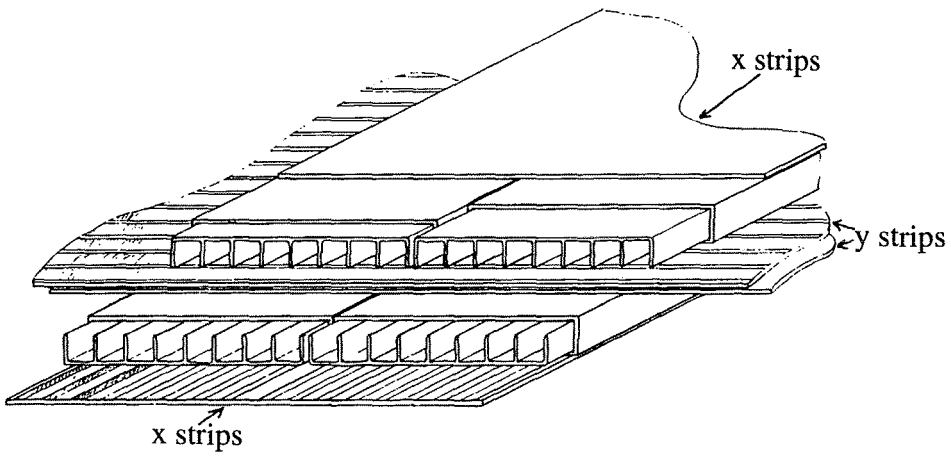

Figure 2.12: A diagram of a single double muon chamber layer. Orthogonal planes of readout strips over streamer tube cells provide up to four two-dimensional coordinates.

2.2.8 The Luminosity Subdetectors

An accurate determination of the integrated luminosity delivered by LEP to ALEPH is essential for physics analyses. This can be accomplished by measuring the number of low-angle Bhabha scatterings, $e^+e^- \rightarrow \gamma^* \rightarrow e^+e^-$. The cross section for this process is inversely proportional to the fourth power of the scattering angle and has a small theoretical uncertainty. Furthermore, interference from the less well known electroweak process $e^+e^- \rightarrow Z \rightarrow e^+e^-$ is small at low angles. Luminosity subdetectors positioned near the beam pipe at both ends of the detector provide position and energy measurements of scattered electrons and positrons and can be used to detect and count Bhabha events. These subdetectors are also treated as extensions of endcap calorimetry, extending ALEPH hermeticity to very low angles.

The Silicon Calorimeter (SiCAL) is a sampling electromagnetic calorimeter consisting of 12 layers of tungsten alternating with layers of silicon pad detectors, 23 radiation lengths in depth. Two identical cylindrical SiCAL detectors are situated 2.5 m on either side of the interaction point with a thickness of 12 cm, and inner and outer radii of 6 and 15 cm. They can detect Bhabha electrons and positrons with scattering angles between 24 and 57 mrad and have an energy resolution of $\sigma_E/E = 34\%/\sqrt{E}$, a 150 μm radial position resolution, and an 3.8 mrad azimuthal resolution. Luminosity measurements with the SiCAL typically have an uncertainty of 0.09%.

An additional luminosity subdetector, the Luminosity Calorimeter (LCAL), consists of two 38 layer lead/wire chamber sampling calorimeters

similar in construction and operation to the ECAL, each having 24.6 radiation lengths of material. The dual LCAL components are positioned 2.7 m on either side of the interaction point and have a thickness of 45 cm, a 10 cm inner radius, and a 52 cm outer radius. They can detect Bhabha electrons and positrons with scattering angles between 45 and 160 mrad and have an energy resolution of roughly $\sigma_E/E = 15\%/\sqrt{E}$ and a position resolution in x and y of $0.43\,\text{mm} + 6.5\,\text{mm}/\sqrt{E}$. Luminosity measurements with the LCAL have an uncertainty of roughly 0.5%.

From 1993 until the end of the LEP1 era in 1995, ALEPH luminosity was determined using the SiCAL only [79]. However, the possibility of higher backgrounds at extremely low angles in the LEP2 accelerator environment motivated the installation of a tungsten mask inside the beam pipe to shield the inner ALEPH detectors from possible synchrotron radiation. To shield the detectors from possible secondary emission from this tungsten mask, a tungsten cone was added around the beam pipe. This cone shadows the SiCAL, reducing the acceptance from 24 to 34 mrad. An unrelated problem at LEP2 is associated with the SiCAL readout electronics which were designed specifically for LEP pretzel operation. With the advent of the LEP2 bunch train mode operation, the SiCAL can only be held open for one bunch out of each train, effectively downscaling the number of bunches in a train [80, 81]. Hence, ALEPH luminosities at LEP2 are determined using the LCAL only.

At center-of-mass energies of 183 GeV, the total systematic error on the luminosity determination is 0.5% including the theoretical error associated with the Bhabha cross-section [82]. The statistical error is 0.2% [83], yielding

a total error on the luminosity of 0.54%.

2.2.9 The Trigger System

It is impractical to record all information from the subdetectors at every beam crossing. Full detector readout not only represents a non-trivial amount of storage space on tape or disk, but also results in a certain amount of detector dead time. Therefore, a trigger system is needed to filter events resulting from genuine e^+e^- reactions from background events caused by cosmic rays or the LEP beam interactions with residual gas molecules in the beam pipe or material upstream of the detector. The fine-structure of the trigger configuration varies between various data-taking periods depending upon background rates and LEP beam configurations.

The ALEPH trigger system has three levels; the first two levels are hardware-based while the third level is software-based. The Level-1 trigger decision is formed from tracking information from the ITC and total energy deposition in the ECAL, HCAL, and LCAL. A *yes* or *no* Level-1 decision is available within 5 μs. Since the time between bunch trains is 22 μs, no events are lost while this decision is made.

If the Level-1 trigger decision is positive, the TPC gate is held open for the full 45 μs drift time. The Level-2 trigger is identical to Level-1 with the exception that TPC trigger pads replace the ITC information. A decision is reached within 50 μs after the beam crossing, and, if positive, initiates full data acquisition readout.

The final software-based Level-3 trigger uses raw digitized information from the whole event and takes advantage of correlations in subdetectors. If positive, the event is written to tape.

The trigger efficiency for multi-hadronic events is essentially 100%.

2.3 Event Reconstruction

2.3.1 Track Reconstruction

A typical hadronic event may have several dozen charged tracks which together may leave several hundred coordinate hits in the tracking system (VDET, ITC, and TPC). Pattern recognition algorithms attempt to group these coordinates together to form track candidates. The results of these track finding procedures are passed on to algorithms based upon Kalman filtering techniques to perform a final global track fit [84].

Charged particles traversing the central tracking systems have helical trajectories due to the uniform 1.5 T magnetic field. The radius of a track helix is inversely proportional to the charged particle's p_{T} (*i.e.*, the component of its momentum perpendicular to the field). ALEPH uses the following five parameters (illustrated in Figure 2.13) to describe track helices:

- ω is the inverse radius of curvature (positive if the helix bends counter-clockwise, turning around the z axis in a left-handed sense);
- $\tan\lambda$ is the tangent of the angle the helix makes with the xy plane;

- ϕ_0 is the emission angle in the xy plane at the point of closest approach to the z axis;
- d_0 is the distance of closest approach to the nominal ALEPH origin in the xy plane;
- z_0 is the z position of the distance of closest approach to the nominal ALEPH origin.

A $1/p_{\mathrm{T}}$ tracking resolution of $10^{-4}\,(\mathrm{GeV}/c)^{-1} \oplus 5 \times 10^{-3}/p_{\mathrm{T}}$ is achieved, and a three-dimensional impact parameter resolution can be parameterized as $(34 + 70/p) \times (1 + 1.6\cos^4\theta)\,\mu\mathrm{m}$, with p in GeV/c [85].

Most analyses rely upon well-measured tracks which satisfy the following criteria

$$|\cos\theta| < 0.95, N_{\mathrm{TPC\ hits}} \geq 4,$$
$$|d_0| < 2.0\,\mathrm{cm}, |z_0| < 10.0\,\mathrm{cm}.$$

Tracks passing these criteria are referred to as *good charged tracks.*

2.3.2 $\mathrm{d}E/\mathrm{d}x$ Measurements

The specific energy loss by ionization $\mathrm{d}E/\mathrm{d}x$ of charged particles can be determined from TPC wire measurements. Wire signals are associated with reconstructed tracks. Tracks must be separated by at least 3 cm in z for a $\mathrm{d}E/\mathrm{d}x$ measurement to be resolved. Signals which are compatible with more than one track are discarded. The resolution on $\mathrm{d}E/\mathrm{d}x$ measurements is

$$\sigma_I/I = \sigma_0 N^{p_1} (\Delta x/\Delta r)^{p_2} (I/I_0)^{p_3}$$

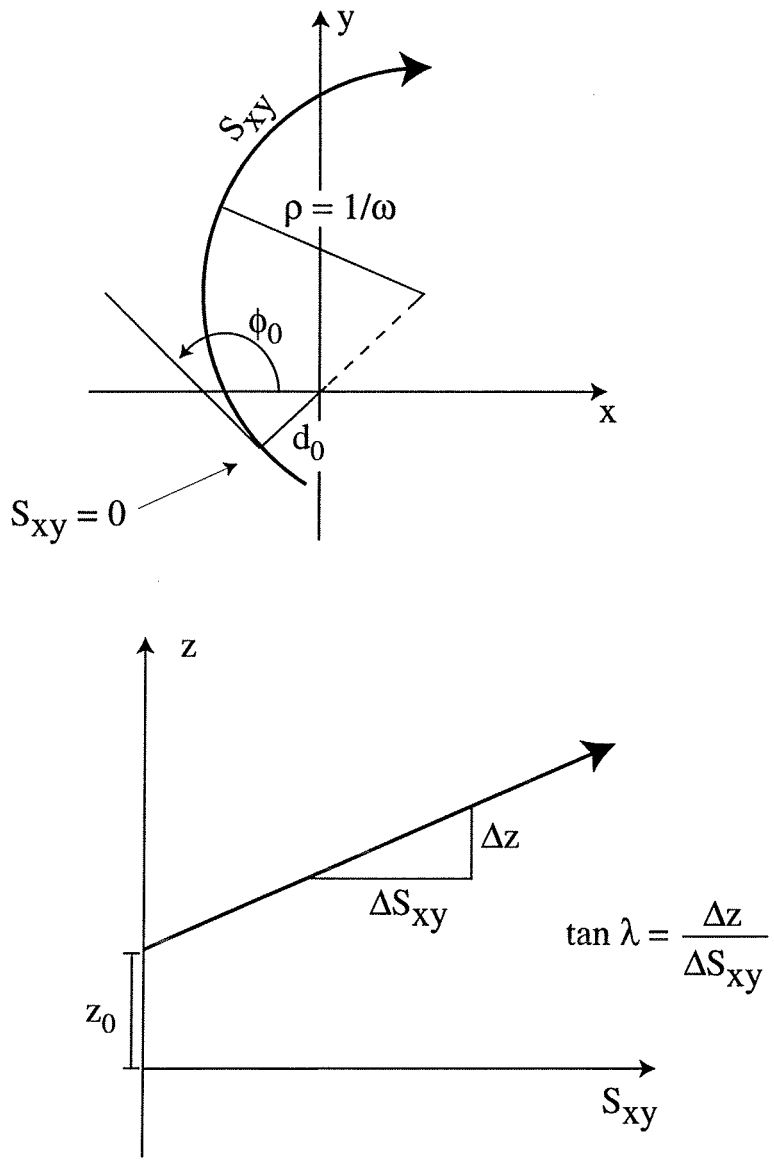

Figure 2.13: A diagram illustrating the five helix parameters: ω, $\tan\lambda$, ϕ_0, d_0, z_0. In the upper diagram, the arc length of the track in the rϕ plane is denoted as S_{xy}.

where N is the number of wire hits, I is the measured $\mathrm{d}E/\mathrm{d}x$, and I_0 is defined to be 1.0 for minimum-ionizing particles. The remaining parameters are determined from data: $\sigma_0 = 1.19$, $p_1 = -0.5$, $p_2 = p_3 \approx -0.4$. For minimally ionizing pions with more than 150 wire measurements, the $\mathrm{d}E/\mathrm{d}x$ resolution is 5.5%.

Figure 2.14 shows $\mathrm{d}E/\mathrm{d}x$ measurements for a given track sample; Figure 2.15 shows the average separation between particle types versus track momenta.

2.3.3 The Energy Flow Algorithm

Energy flow refers to a series of algorithms which determine and classify detected signatures from charged and neutral particle energy in an event. These algorithms properly deal with the multiple energy and momentum signatures of single tracks to avoid double-counting. The excellent momentum resolution of the TPC is combined with calorimetry and particle identification techniques. Energy deposited in the luminosity subdetectors is also used, extending the solid angle calorimetry coverage down to 34 mrad in polar angle [72].

An initial event *cleaning* procedure is performed on charged tracks and calorimeter clusters. Charged particle tracks must meet one of the following sets of criteria:

1. The track must have at least four hits in the TPC and originate from a cylinder of length 20 cm and radius 2 cm coaxial with the beam and

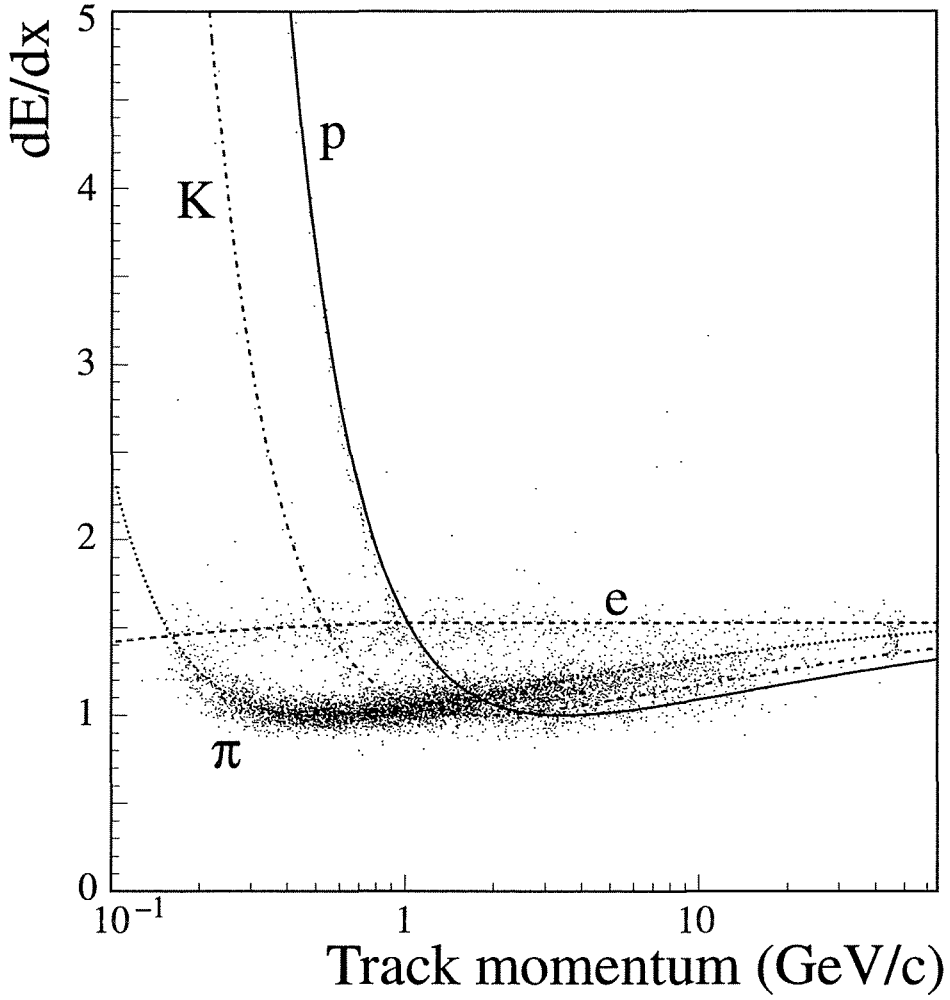

Figure 2.14: The measured $\mathrm{d}E/\mathrm{d}x$ versus particle momentum for tracks having at least 150 $\mathrm{d}E/\mathrm{d}x$ measurements. Fitted parameterizations for electrons, muons, pions, kaons, and protons are superimposed on the data. The measurements have been normalized such that minimum-ionizing particles have an average $\mathrm{d}E/\mathrm{d}x$ equal to 1.0.

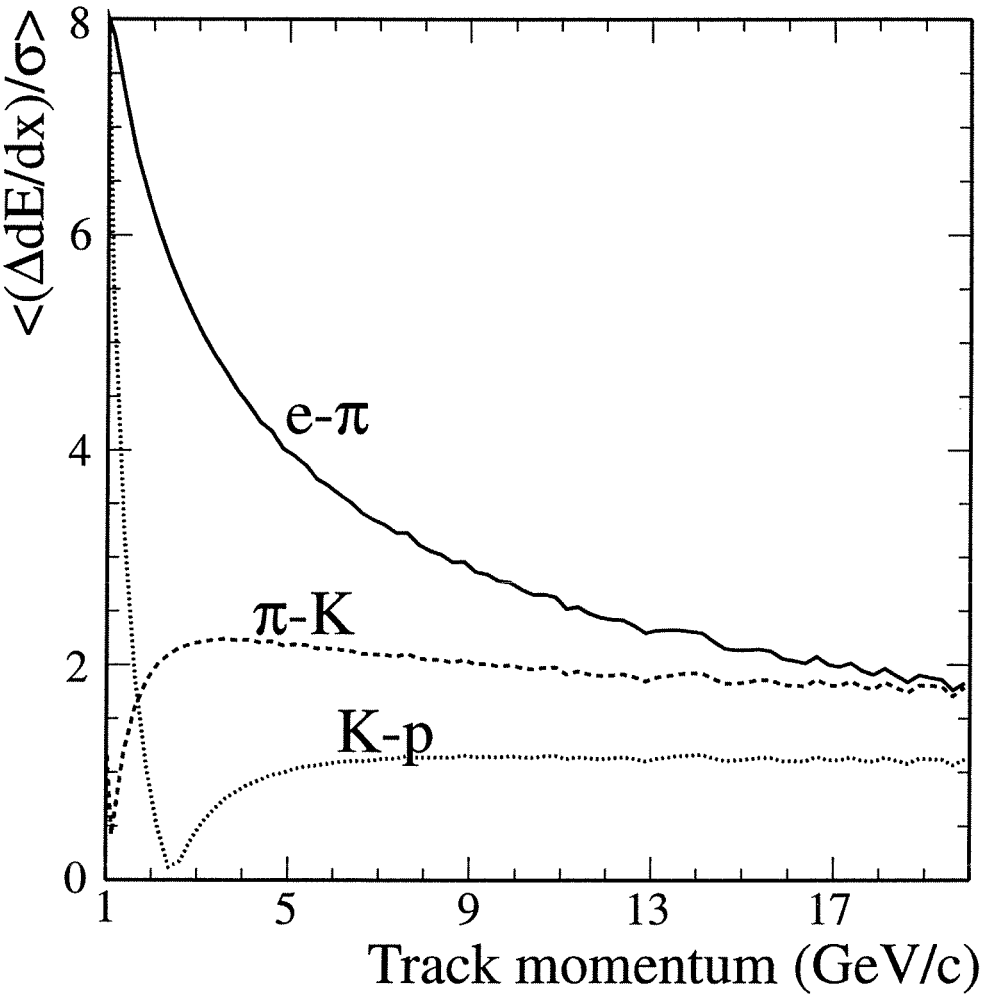

Figure 2.15: The average $\mathrm{d}E/\mathrm{d}x$ separation in standard deviations between particle types for tracks having at least 50 $\mathrm{d}E/\mathrm{d}x$ measurements versus particle momentum.

centered at the nominal interaction point;

2. Charged particle tracks rejected by the criteria above are recovered if they belong to a reconstructed V^0 (refer to Section 3.3.1) which is compatible with originating from the nominal interaction point within a cylinder of length 30 cm and radius of 5 cm coaxial with the beam.

The cleaning procedure also identifies noisy ECAL and HCAL channels and does not use them for calorimeter cluster finding. Fake energy deposits due to occasional calorimeter noise are found and removed when the corresponding signal is incompatible with the signal measured independently on the ECAL wire planes or HCAL streamer tubes.

Charged particle tracks are extrapolated from the tracking chambers to the calorimeters. Topologically connected tracks and calorimeter clusters are used to compose calorimeter objects. The calorimeter objects are processed via a series of particle identification algorithms which classify electrons, muons, photons, and neutral pions. Any remaining calorimeter objects which cannot be associated with charged tracks are classified as neutral hadronic objects. Hence, for each event a set of classified *energy flow objects* is built which is used in the offline analysis of events.

This energy flow algorithm allows jets to be reconstructed with a typical angular resolution of 20 mrad both for the polar and azimuthal angles, and a relatively uniform energy resolution over the whole detector acceptance parameterized as $\sigma_E = (0.60\sqrt{E} + 0.6) \times (1 + \cos^2\theta)$ where E is the jet energy in GeV and θ is the jet polar angle [85].

2.4 Monte Carlo Simulation

In order to develop analyses and design selection criteria, it is necessary to generate large samples of events which simulate the occurrence of physics processes in the ALEPH detector. This relies upon an event generator using Monte Carlo techniques to provide four-vectors of final state hadrons, leptons, and photons. These four-vectors are processed through a detector simulation and then through the same event reconstruction programs used for data.

A multitude of event generators for producing Monte Carlo simulations of processes relevant to e^+e^- annihilations exist [86]. Two event generators are primarily used for the samples of simulated events upon which the results of this thesis are based. The PYTHIA 5.7 generator [45] is used to generate most of the samples for the main Standard Model background processes discussed in Section 1.3.2. The HZHA02 generator [22] is used for all Higgs signal processes.

The ALEPH detector simulation program is called GALEPH. It uses the known position of material and responses of subdetector components in conjunction with the GEANT3 [87] and GHEISHA [88] packages to simulate the passage and possible interactions of charged and neutral particles through the ALEPH detector. The output of GALEPH is in a format identical to the raw data from the detector with additional information relating the detector signals to event generator-level particles (referred to as *Monte Carlo truth* information).

Chapter 3

Identification of b Quark Jets

A Higgs boson with a mass relevant to LEP2 searches decays predominantly to a $b\bar{b}$ quark pair. Quark pairs produced in high energy e^+e^- annihilations manifest themselves as jets of particles; this is described in Section 3.1. Jets originating from b quarks contain b hadrons which have characteristic features summarized in Section 3.2.

The properties of b quarks and b hadrons give b jets characteristic features with respect to jets from lighter quark flavors (*i.e.*, u,d,s, and c quarks) and gluon jets. The identification of b jets and rejection of non-b jets is referred to as *b-tagging* and is the most important selection criterion in most analyses designed to search for the neutral Higgs boson. Section 3.3 describes a variety of b-tagging variables based upon the properties of b jets.

A single b-tagging variable could be used alone in an analysis designed to search for the Higgs boson; however, greater discrimination power between signal and background processes can be obtained by combining mul-

tiple variables together using multivariate techniques. Section 3.4 describes a technique which combines six b-tagging variables using a neural network (NN) which dramatically improves the discrimination power compared to any single b-tagging variable.

3.1 Jet Phenomenology

The primary quarks produced from e^+e^- annihilations manifest themselves as collimated jets of hadrons at high energies; this was first observed at center-of-mass energies near 7 GeV [89]. Gluons may bremsstrahlung from a quark and create additional jets in an hadronic event; this was first observed by Wu and Zobernig at PETRA [20].

3.1.1 Hadronization

Primary quarks and any gluons they may radiate are referred to as *initial partons.* Initial partons carry color charges and cannot exist in isolation since Nature apparently permits only color singlets to exist freely. Non-perturbative QCD processes convert the colored initial partons into color singlet hadrons. This is referred to as *hadronization.* Figure 3.1 illustrates processes involved in a hadronic event from e^+e^- annihilation.

Although the hadronization process is not well understood, phenomenological models exist. Examples of these models are the string model [90] (implemented in the JETSET Monte Carlo program [91]) and the cluster model [92] (implemented in the HERWIG Monte Carlo program [93]). In

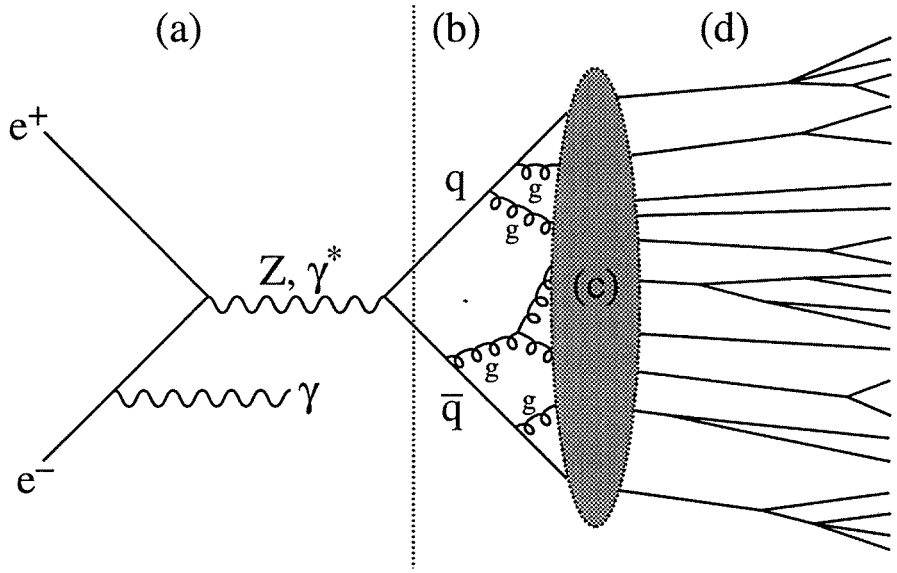

Figure 3.1: A schematic illustration of the stages of an $e^+e^- \rightarrow$ hadrons event: (a) electroweak processes involving the e^+e^- annihilation to a virtual photon or a Z which may be accompanied by a bremsstrahlung photon, (b) Perturbative QCD parton shower processes involving gluon bremsstrahlung of the primary quarks from the virtual photon or Z decay, (c) Non-perturbative QCD processes (hadronization) transforming quarks and gluons into color-neutral hadrons, (d) Strong or electroweak decay of the hadrons into detectable particles.

the string model, for example, the confining nature of the strong interaction dictates that the color potential of the initial partons becomes proportional to their separation at large distances. As the initial partons fly apart from the interaction point, it becomes energetically favorable for additional quark pairs to be produced from the vacuum. Ultimately the initial colored partons are transformed into bound color singlet hadronic states.

Jet originating from quarks are qualitatively different than jets from glu-

ons. In QCD, the gluon self-interaction coupling is proportional to the color factor C_A while the quark-gluon coupling is proportional to the color factor C_F. The values of the color factors are determined by the structure of the color gauge group $SU(3)$. The ratio C_A/C_F is predicted to be $9/4 = 2.25$; this is in good agreement with experimental measurements [94]. Hence gluons are more likely to radiate softer gluons in the hadronization process, and a gluon jet is consequently broader with a higher particle multiplicity than a light quark jet of the same energy. These features of gluon jets have been observed in hadronic events at LEP1 [95].

3.1.2 Jet Clustering

Algorithms exist which cluster charged and neutral particles in an event together to form jets. These algorithms form the basis of most analyses dealing with hadronic events which rely upon the clustered jets to approximate the direction and energies of the initial partons in an event.

Most jet clustering schemes used in ALEPH are based upon the JADE algorithm [96]. This recursive algorithm begins by considering each energy flow object in an event to be a pseudo-jet. Pairs of pseudo-jets are then combined according to a metric defined as

$$y_{ij} = \frac{2E_iE_j(1-\cos\theta_{ij})}{E_{\text{vis}}^2}$$

where i and j are two pseudo-jets, and E_{vis} is the visible energy in the event (*i.e.*, the sum of the energy of all energy flow objects). The numerator is

essentially the invariant mass squared of the two pseudo-jets. The energy and three-momentum of the new pseudo-jets are determined according to a combination scheme from the energy and three-momenta of a previous pseudo-jet and an energy flow object, yielding a new set of pseudo-jets. In the *E scheme* the simple sum of three-momenta and of energy is used. The combination procedure is iterated until all y_{ij} are larger than a specified threshold which is referred to as y_{cut}.

Several variants of the JADE scheme exist and have been extensively studied in the context of QCD-related measurements and predictions [97]. Durham, one of the JADE variants, has several advantages (*e.g.*, reduced sensitivity to soft gluon radiation) [98]. In this scheme, the JADE clustering metric is replaced by

$$y_{ij} = \frac{2\min(E_i, E_j)^2(1-\cos\theta_{ij})}{E_{\text{vis}}^2}.$$

The numerator is essentially the square of the lower-energy particle's transverse momentum $k_{\text{T}ij}^2$ with respect to the higher-energy particle. Unless otherwise indicated, the Durham E scheme is used in the analyses presented in this thesis.

3.1.3 Fragmentation Function

The energy spectrum of hadrons within a jet which contains a primary quark depends upon a convolution of perturbative QCD processes with the non-perturbative hadronization process. It is impossible to predict the expected

energy spectrum exactly, but it is possible to model and parameterize. This energy spectrum becomes relevant when considering heavy quark hadrons since analysis efficiencies are often dependent upon the momenta of decay products from heavy quark hadrons. A *fragmentation function* $D_Q^H(z)$ is defined as the probability to observe a hadron of type H from the fragmentation of an initial heavy quark Q, which carries an energy-momentum fraction z of the initial quark. A parameterization describing heavy quark fragmentation was developed by Peterson *et al.* and is given by [99]

$$D_Q^H \propto z^{-1}\left(1-\frac{1}{z}-\frac{\epsilon_Q}{1-z}\right)^{-2}$$

where z is defined as

$$z=\frac{(E+p_\parallel)_H}{(E+p)_Q}$$

and with $p_\parallel$ representing the component of momentum along the direction of the primary quark. The only free parameter in this parameterization, ϵ_Q, is a function of the heavy quark mass. Due to the high b quark mass, b hadrons are expected to have a harder momentum spectrum than c hadrons. In fact, b hadrons carry on average roughly 70% of the initial b quark momentum [100, 101, 102], and b hadron decay products tend to have high momenta even for high multiplicity b hadron decays.

In the Monte Carlo event generators used in this thesis, the Peterson fragmentation model is used for b and c quarks. The LUND symmetric fragmentation model is used for uds quarks [45].

3.2 Phenomenology of Heavy Flavor Hadrons

This section briefly reviews properties of heavy flavor hadrons (*i.e.*, hadrons containing the heavy b or c quarks) relevant to the design of b-tagging algorithms. It is natural to include c hadrons in this discussion since b hadrons decay predominantly to c hadrons, and c hadrons and b hadrons have similar properties (*e.g.*, lifetime). In fact, W^+W^- events containing c jets constitute a major source of background for the analyses designed to search for the Higgs boson.

Since the discovery of the J/ψ in 1974 [103] and the Υ in 1977 [104], heavy flavor hadrons have been the subject of intense study in high energy physics. Table 3.1 summarizes the properties of weakly decaying heavy quark hadrons. The relatively long lifetime of these hadrons combined with the Lorentz boost they acquire at LEP gives events containing these hadrons a characteristic displaced vertex topology. The sizeable fraction of hadronic Z decays to c and b quark pairs ($R_c \approx 16\%$ and $R_b \approx 22\%$ [3]) permitted the investigation of a wide variety of heavy flavor physics topics at LEP1.

The simplest model describing heavy flavor hadron decay is the *spectator* model [105] where the decay dynamics are governed only by the electroweak behavior of the heavy quark, and the lighter quark or di-quark (the spectator) plays no rôle. This is illustrated in Figure 3.2(a). Any interactions between the spectator and heavy quarks are ignored, and the decay rates of heavy quark hadrons can be calculated in a manner similar to muon decay. The

b hadrons			
Hadron	Quark Content	Mass (MeV/c^2)	Lifetime (ps)
B^-	$b\bar{u}$	5278.9 ± 1.8	1.65 ± 0.04
B^0	$b\bar{d}$	5279.2 ± 1.8	1.56 ± 0.04
B_s^0	$b\bar{s}$	5369.3 ± 2.0	1.54 ± 0.07
Λ_b^0	bud	5624 ± 9	1.24 ± 0.08

c hadrons			
Hadron	Quark Content	Mass (MeV/c^2)	Lifetime (ps)
D^+	$c\bar{d}$	1869.3 ± 0.5	1.057 ± 0.015
D^0	$c\bar{u}$	1864.6 ± 0.5	0.415 ± 0.004
D_s^+	$c\bar{s}$	1968.5 ± 0.6	0.467 ± 0.017
Λ_c^+	cud	2284.9 ± 0.6	0.206 ± 0.012

Table 3.1: A summary of weakly decaying b and c hadrons and their properties[3]. Charge-conjugate states are implied.

hadronic and leptonic widths in the spectator model are roughly given as [106]

$$\Gamma_{\rm had}(Q \to q_1 q_2 \bar{q}_3) \propto m_Q^5 \cdot |V_{q_1 Q}|^2 \cdot |V_{q_3 q_2}|^2 ,$$

$$\Gamma_{\rm lept}(Q \to q \ell \bar{\nu}_\ell) \propto m_Q^5 \cdot |V_{qQ}|^2$$

where $V_{qq'}$ is a CKM matrix element and m_Q is the mass of a heavy quark Q. For b hadron decay, the very small value of $|V_{\rm cb}|$ and the extremely small value of $|V_{\rm ub}|$ lead to long lifetimes. However, it is apparent from the different heavy flavor hadron lifetimes alone that the first-order spectator model does not give a complete or entirely accurate picture of heavy flavor decays. QCD corrections and non-spectator decay mechanisms must also be considered.

Non-spectator diagrams are illustrated in Figures 3.2(b) and (c).

An interesting and relevant class of heavy flavor hadron decay is semileptonic decay. In this case, the $W^{\pm}$ from the $Q \rightarrow q$ transition decays to a charged lepton and a neutrino. For b hadrons, the inclusive semileptonic branching ratio Br(b$\rightarrow X\ell^{-}\bar{\nu}_{\ell}$) has been measured to be $10.95 \pm 0.32\%$ [3]. These semileptonic decays of b hadrons are distinctive: the high mass of b hadrons causes the leptons to have high transverse momentum relative to the b hadron trajectory. Hence the transverse momentum of identified leptons relative to the jet axis (approximating the b hadron trajectory) is an excellent b-tagging variable.

The decays of b hadrons are characterized by a high particle multiplicity. Measurements of the average charge multiplicity of weakly decaying b hadrons have been conducted [100, 101, 102, 107, 108, 109]. A weighted mean of these results yields $\langle n_{\mathrm{b}} \rangle = 4.99 \pm 0.05$, where contributions from K^0 and Λ decay have been excluded. At the Z peak, the difference in the average charged particle multiplicity between b events and uds events has been measured [100, 108]. The weighted mean of these measurements yields $\delta_{\mathrm{b-uds}} = 3.08 \pm 0.51$. Hence, variables incorporating multiplicity information have discriminating power between b jets and light quark jets.

3.3 b-Tagging Variables

Variables which identify b jets can be grouped into different categories. Lifetime-based variables use track impact parameter information and evi-

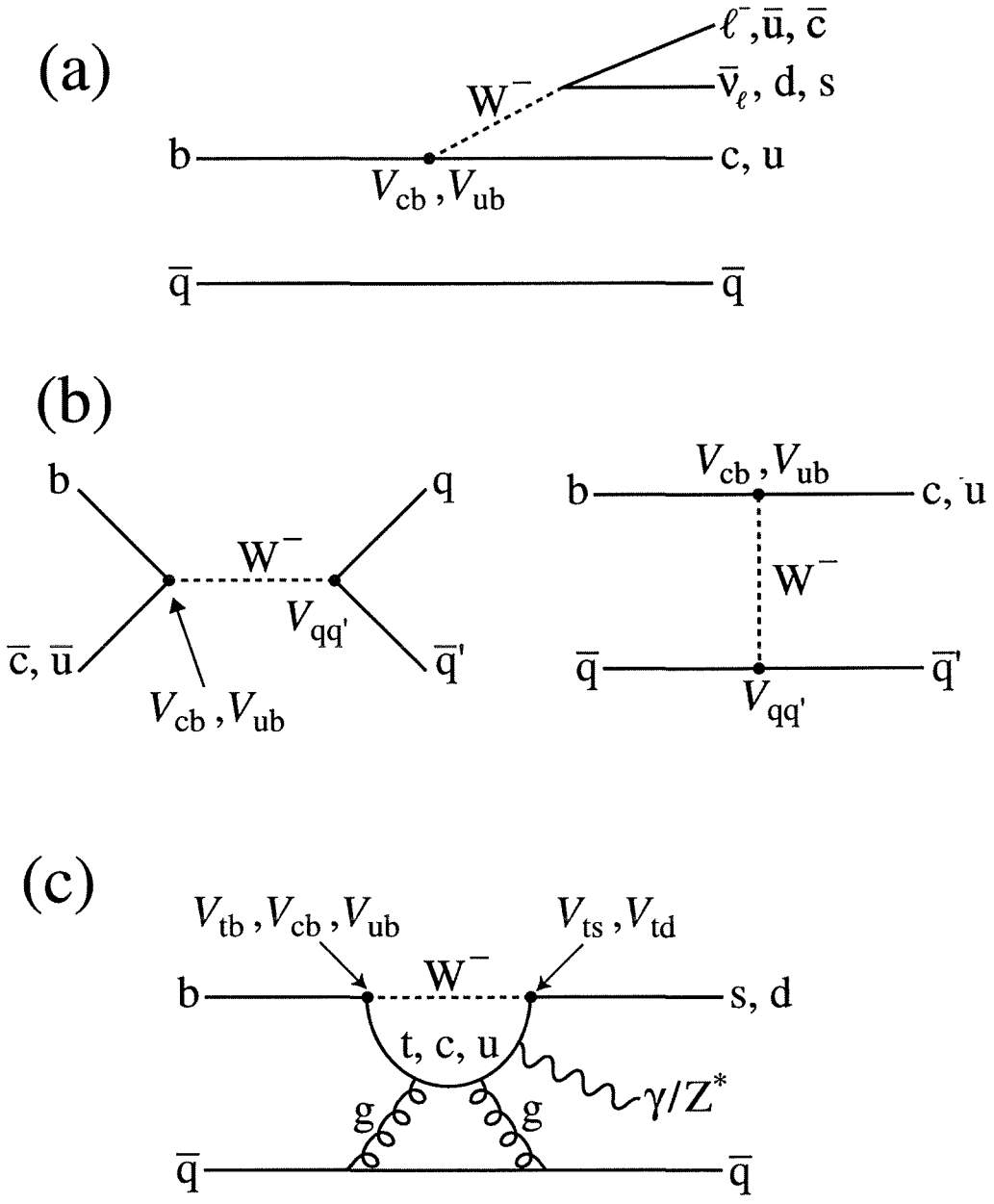

Figure 3.2: Diagrams contributing to different b hadron decay mechanisms: (a) spectator, (b) non-spectator, (c) non-spectator penguin. Relevant CKM matrix elements are indicated at various vertices in each diagram

dence of displaced secondary vertices. Variables can also be based upon the presence of energetic high p_{T} leptons from semileptonic b decay. Finally, it is possible to design variables that are sensitive to topological features of jets, referred to as *jet-shape* variables.

3.3.1 Track Impact Parameter

Compared to tracks produced in the fragmentation process and other long-lived or stable light quark hadrons produced at the primary vertex, b hadron decay products tend to have sizeable impact parameters with respect to the primary vertex due to the lifetime and mass of b hadrons. If the mass of the b hadron were small, its decay products would have small transverse momenta and would tend to point towards the primary vertex. If the lifetime of the b hadron were small, decays would occur at or near the primary vertex.

This section describes a b-tag variable based on the impact parameters relative to the primary vertex of charged tracks in a jet. This method was developed for ALEPH b physics analyses at LEP1 [110] and has been modified for use at LEP2 [111].

Primary Vertex Determination

An accurate determination of the primary vertex is essential for lifetime-based b-tagging. Displaced vertices as well as impact parameters resulting from the decay of b hadrons are all measured with respect to the primary vertex. However, the primary vertex is not a fixed point in space. It depends

on the size of the luminous region (*i.e.*, the size of the region where the LEP beams interact), and the position of the LEP beams. The beam position varies between fills as LEP operators adjust and tune accelerator parameters for optimal performance, and between events due to time-dependent effects in the accelerator. Thus, when dealing with measurements on the scale of $10\,\mu$m, an event-by-event primary vertex determination is required. A method developed for ALEPH b physics analyses at LEP1 [112] uses an average *beam spot* position (*i.e.*, x and y coordinates of the centroid of the luminous region) and energy flow objects in an event.

The average beam spot is determined from a set of 120 charged tracks from a chunk of consecutive events. These charged tracks must have at least one VDET $r\phi$ hit and satisfy several track quality criteria which are looser than those used for LEP1 due to the lower event rate at LEP2 energies [113]. The beam spot position is determined with average accuracies of roughly $27\,\mu$m in the x direction and $25\,\mu$m in y direction. The RMS dimensions of the beam luminous region were measured to be roughly $140\,\mu$m in the x-direction and 7.9 mm along the z-direction during the 1997 run period [114]; the size of the luminous region is small in the y direction, roughly $5\,\mu$m.

Energy flow objects in an event are clustered into jets using the JADE algorithm with a $y_{\rm cut} = 0.01$, and jets with momenta less than $10\,{\rm GeV}/c$ are discarded. Charged tracks are considered to be well-measured if they have

momenta greater than $0.2\,\mathrm{GeV}/c$ and satisfy

$$\begin{aligned} N_{\text{TPC hits}} > 4, \qquad & \chi^2 < 4, \\ \left|d_0^{\mathrm{BP}}\right| < 0.5\,\mathrm{cm}, \quad & \sigma_{d_0^{\mathrm{BP}}} < 0.1\,\mathrm{cm}, \\ \left|z_0^{\mathrm{BP}}\right| < 8.0\,\mathrm{cm}, \quad & \sigma_{z_0^{\mathrm{BP}}} < 0.5\,\mathrm{cm}, \end{aligned}$$

where d_0^{BP} and z_0^{BP} are the d_0 and z_0 relative to the beam spot, and χ^2 refers to the global track helix fit. Well-measured tracks are associated to their nearest jet and are projected into the plane perpendicular to the jet axis (see Figure 3.3). This projection technique reduces bias due to displaced secondary vertices; however, it obviously results in a loss of information along the jet axes.

Using the projected tracks from a given event and the average beam spot information the interaction point is found in each event with typical resolutions of 40, 20, and 40 μm in the x, y, and z directions respectively.

V^0 Identification

The symbol V^0 denotes neutral particles which convert or decay into a pair of oppositely charged particles in the tracking volume (*e.g.*, a photon conversion into an electron-positron pair, or the decay of a K_s^0 or Λ). These represent a source of tracks with high impact parameters which are not necessarily from b hadron decay.

Each candidate V^0 is found by considering all possible pairs of oppositely charged well-measured tracks. The point where the two tracks have minimal separation must be displaced from the primary vertex by more than twice the

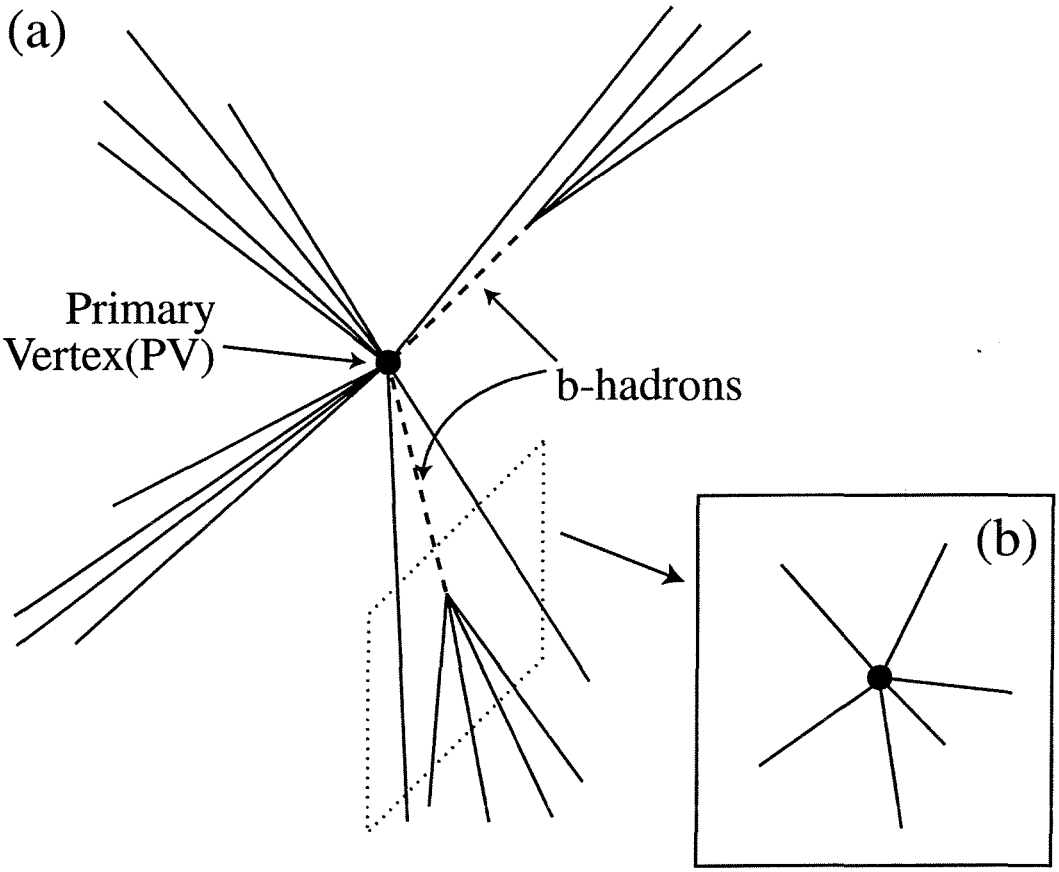

Figure 3.3: An illustration of the algorithm used for primary vertex determination: (a) well-measured charged tracks are associated to their nearest jet; some tracks may originate from a displaced vertex (e.g., due to the decay of a b hadron). (b) tracks in each jet are projected onto a plane perpendicular to the jet axis.

uncertainty on the distance. Three V^0 hypotheses are considered ($\gamma \rightarrow e^+e^-$, $K^0_s \rightarrow \pi^+\pi^-$, and $\Lambda \rightarrow p\pi^-$) based upon available dE/dx measurements and the invariant mass of the charged track pair. Track pairs which pass V^0 selection criteria are flagged and not used in impact parameter calculations.

Impact Parameter

A signed three-dimensional impact parameter, δ, is calculated for each track in an event belonging to jets having momenta greater than $10\,\mathrm{GeV}/c$ and having an angle with respect to the jet axis of less than 45°. The tracks must have momenta greater than $400\,\mathrm{MeV}/c$ and less than $40\,\mathrm{GeV}/c$, at least four TPC hits and four ITC hits, and satisfy criteria on their distance of closest approach to the primary vertex.

Figure 3.4 illustrates the impact parameter method. The primary vertex is denoted by $\vec{V}$; $\hat{J}$ denotes the jet axis approximating the direction of the b hadron. The point of closest approach $\vec{S}_t$ of each track to $\hat{J}$ is determined; $\vec{S}_j$ is the corresponding point along $\hat{J}$. A tangent $\hat{T}$ is calculated at the point $\vec{S}_t$. The impact parameter δ is the distance of closest approach between $\hat{T}$ and $\vec{V}$. The impact parameter is signed according to the position of $\vec{S}_j$ relative to $\vec{V}$ and $\hat{J}$:

$$\delta = \mathrm{sign}((\vec{S}_j - \vec{V}) \cdot \hat{J}, \delta).$$

A track has a positive (negative) impact parameter if its point of closest approach to the jet axis is in front of (behind) the primary vertex in terms of the direction of the jet axis. Negative impact parameter tracks are due to the

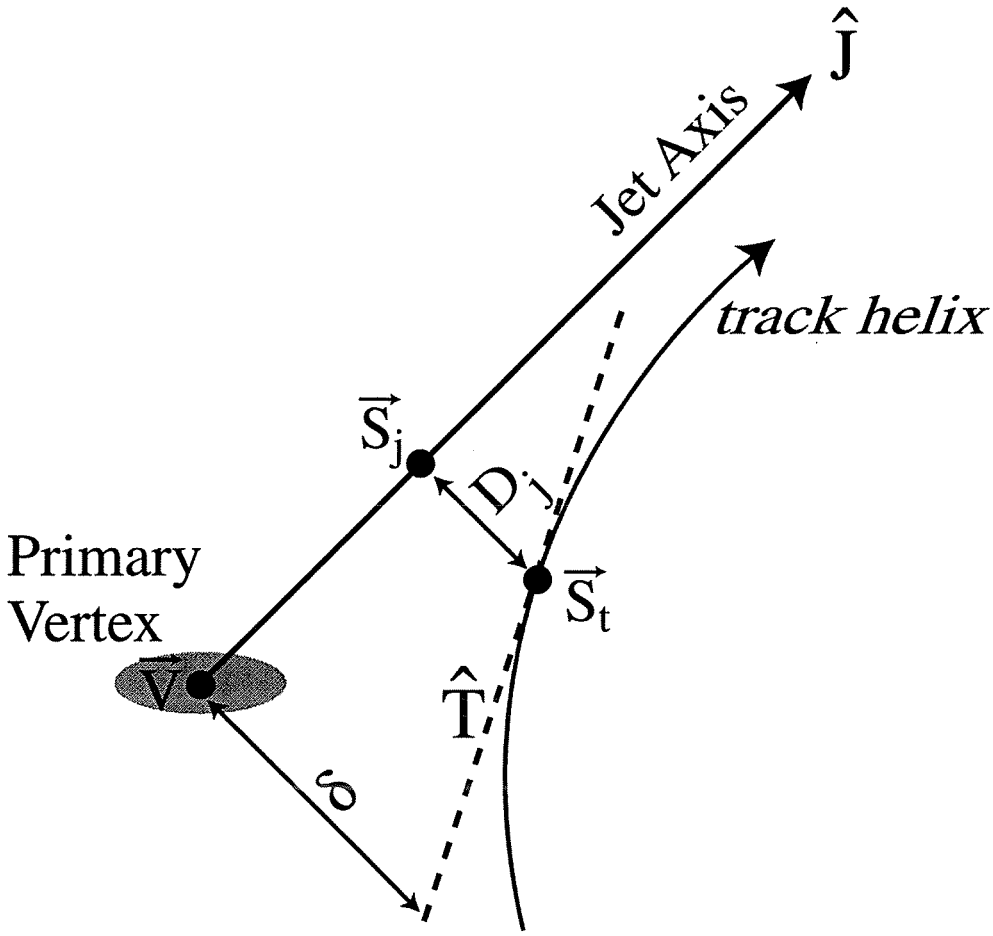

Figure 3.4: An illustration of the impact parameter technique described in the text.

tracking resolution. The uncertainty on the impact parameter measurement σ_δ is determined from the track fit error matrix, the error on the primary vertex, and their correlation. The quantity most often used for b-tagging is not the impact parameter itself, but the impact parameter *significance* defined as the impact parameter divided by its uncertainty. In this manner, a poorly-measured track with a large impact parameter has a small significance while a well-measured track with a small impact parameter may have a large significance.

Figure 3.5 shows impact parameter significance distributions for tracks from various sources in simulated events. Tracks from uds jets and tracks from weakly decaying c hadrons have smaller impact parameter significances than tracks from b hadron decays. Tracks from the decay of a c hadron which itself is from the decay of a b hadron typically have larger impact parameter significances than tracks from other sources. Furthermore, tracks from uds jets are equally likely to have negative impact parameters as positive impact parameters. Hence, a sample of negative impact parameter significance tracks from data can to a good approximation be considered to belong to uds jets.

Tracks are categorized into nine different *track types* on the basis of their VDET hit multiplicity. Tracks in data with negative impact parameter significance are used as a calibration sample; the distributions of track impact parameter significance are fit to a Gaussian resolution function plus two independent exponentially decreasing tail terms. A track probability $\mathcal{P}_{\mathrm{T}}$ is based upon the resolution function and gives the probability that a measurement of a track impact parameter significance give a value greater than or equal to

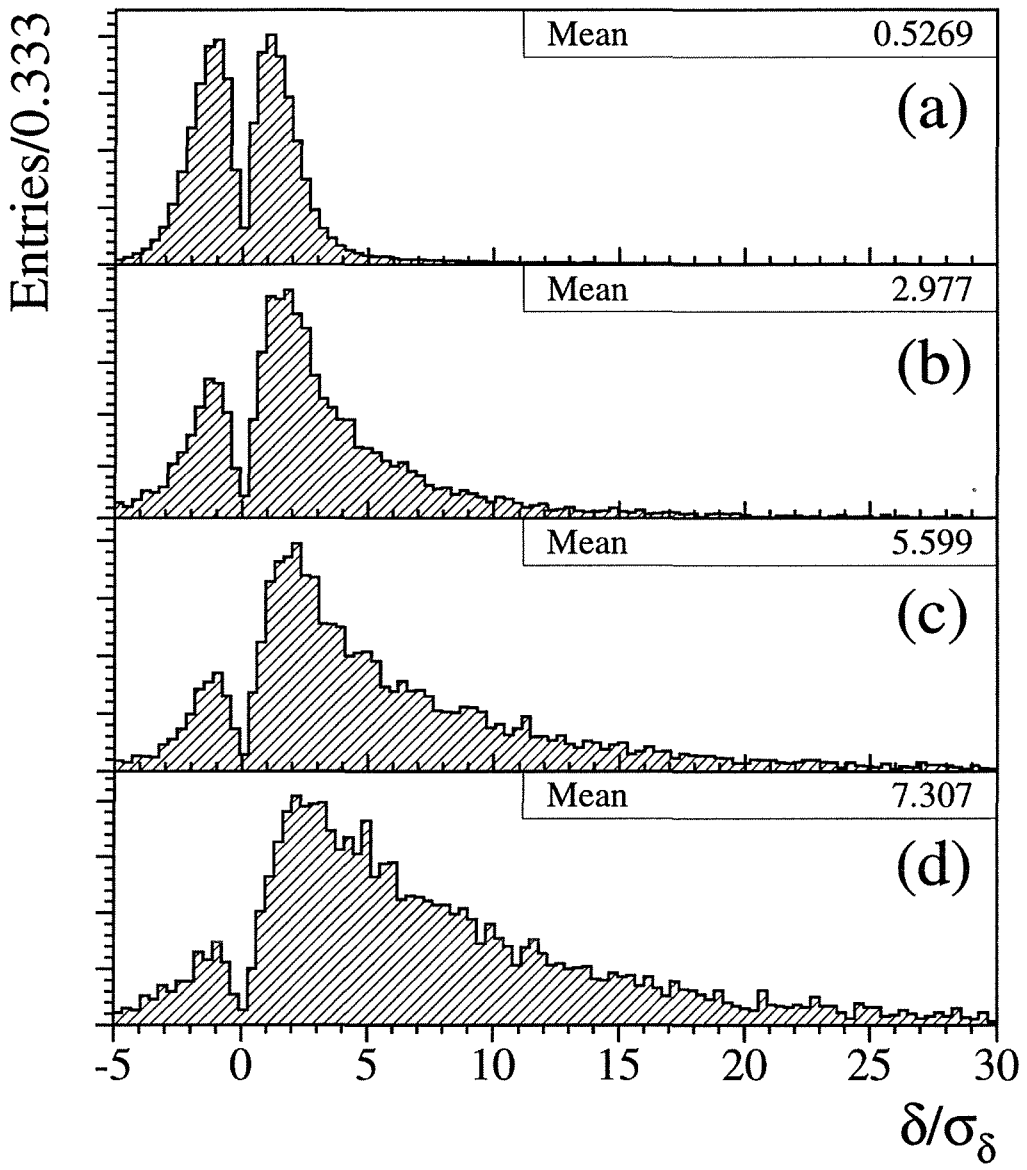

Figure 3.5: Impact parameter significance (δ/σ_δ) distributions for (a) fragmentation or tracks from uds events, (b) tracks from weakly decaying c hadrons, (c) tracks directly from b hadron decay, (d) tracks from the cascade decay of a c hadron from the decay of a b hadron.

that which is observed. The track probabilities for tracks belonging to a specific jet can combined to form a jet probability. Hence $\mathcal{P}_{\text{jet}}$ can be interpreted as the probability of a jet being a uds jet. Figure 3.6 shows distributions of $-\log_{10}(\mathcal{P}_{\text{jet}})$ for various jet flavors from simulated events.

3.3.2 Displaced Vertices

An algorithm is used to search for evidence of displaced secondary vertices in an event. This method was originally developed for b physics analyses at LEP1 [115]. It has been modified slightly to return a jet-by-jet output for an arbitrary number of jets.

The algorithm only uses charged tracks with at least four TPC hits and a χ^2 per degree of freedom of less than four. A χ^2 is calculated when all selected tracks in the jet are assigned to the primary vertex coordinate; this is referred to as χ^2_{PV}. The primary vertex is determined using the method described in Section 3.3.1.

A grid of points is oriented along the jet-axis and centered on the primary vertex. The grid extends 1 cm along the jet-axis in 200 μm steps and $\pm$500 μm along the two orthogonal directions in 20 μm steps. Each point in the grid is considered a candidate secondary vertex, and two χ^2 values are calculated. The first χ^2 is based upon the hypothesis that nearby tracks are assigned to this vertex (referred to as χ^2_{svx}); the second is the new χ^2 of the primary vertex excluding the tracks used in the secondary vertex (referred to as $(\chi^2_{\text{PV}})'$). The quantity $\Delta\chi^2_{\text{svx}} = \chi^2_{\text{PV}} - (\chi^2_{\text{svx}} + (\chi^2_{\text{PV}})')$ is calculated for each grid point,

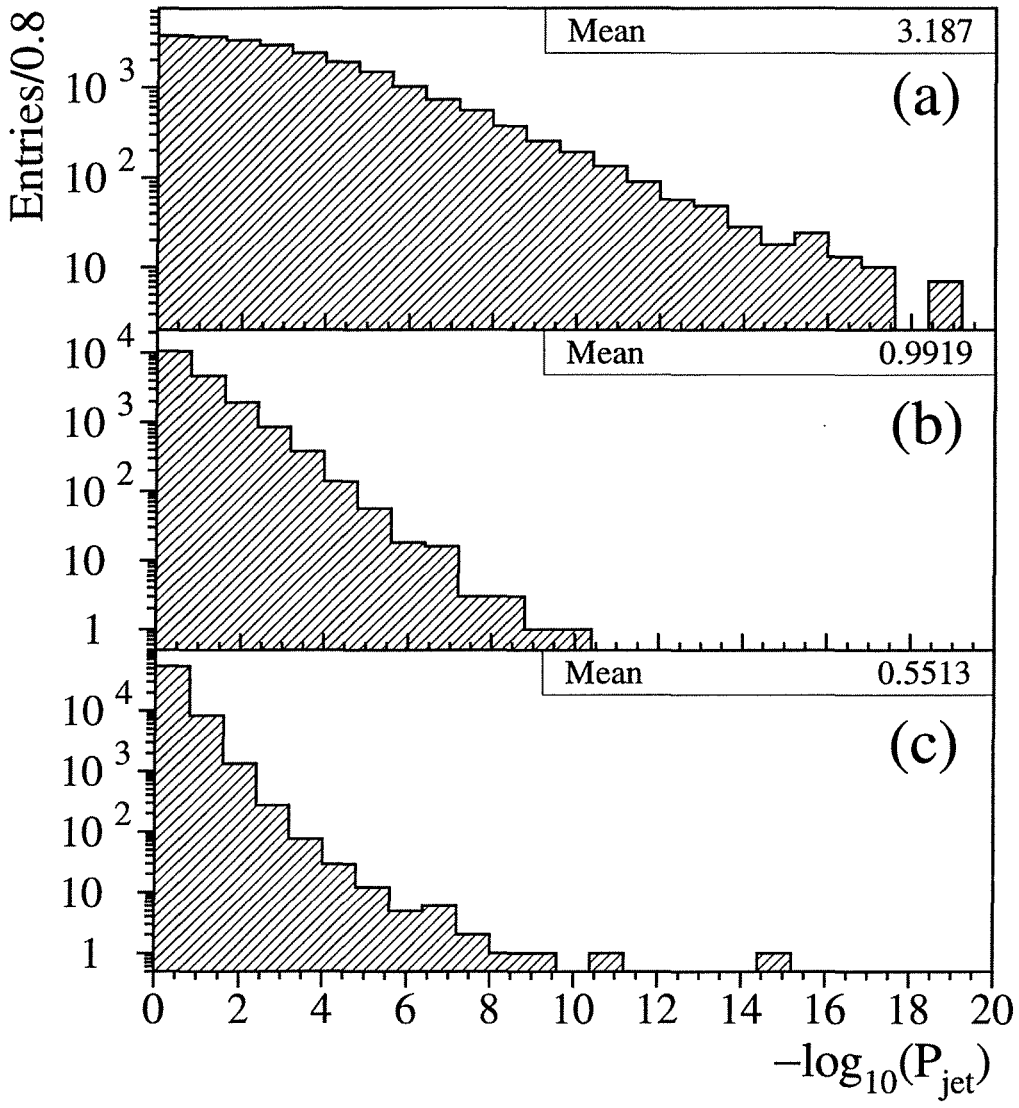

Figure 3.6: Distributions of $-\log_{10}$ of the impact parameter-based $\mathcal{P}_{\text{jet}}$ variable for (a) b jets, (b) c jets, (c) uds jets and gluon jets in simulated events.

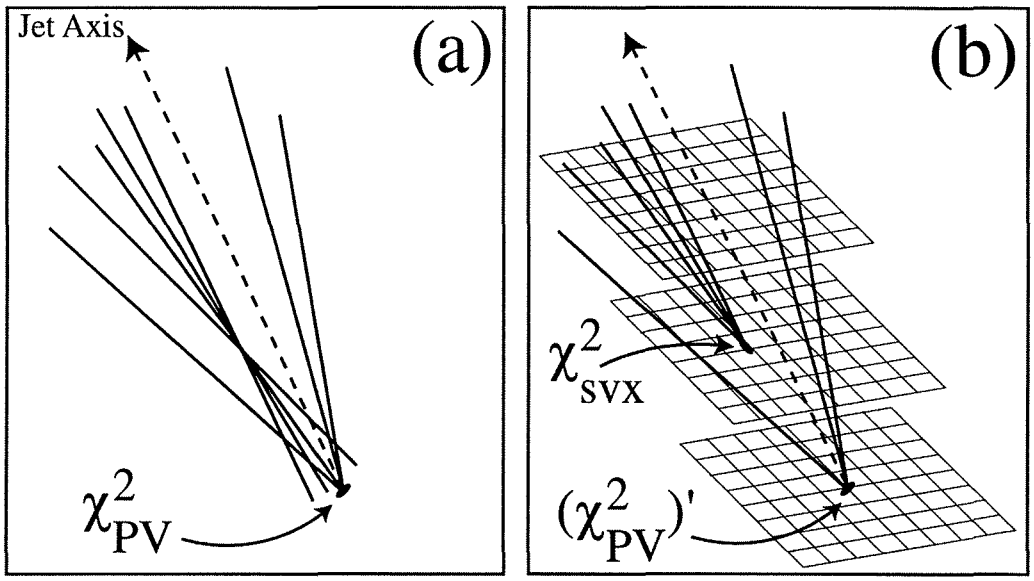

Figure 3.7: An illustration of the displaced vertex algorithm: (a) $\chi^2_{\rm PV}$ is calculated with all good tracks in a jet assigned to the primary vertex, and (b) tracks belonging to a secondary vertex found with a grid search method are used to calculate a $\chi^2_{\rm svx}$ and the other tracks are assigned to the primary vertex for which a new χ^2 is calculated, $(\chi^2_{\rm PV})'$.

and the point with maximal $\Delta\chi^2_{\rm svx}$ is chosen as the secondary vertex. This algorithm is illustrated in Figure 3.7.

For any jet containing usable tracks, this algorithm will always find secondary vertices. However, for uds jets and gluon jets, these are spurious due to the lack of long-lived weakly decaying massive hadrons found in b and c jets; hence uds jets and gluon jets typically have much lower $\Delta\chi^2_{\rm svx}$ values. Figure 3.8 shows $\Delta\chi^2_{\rm svx}$ distributions for various b, c, and uds jets and gluon jets from simulated events.

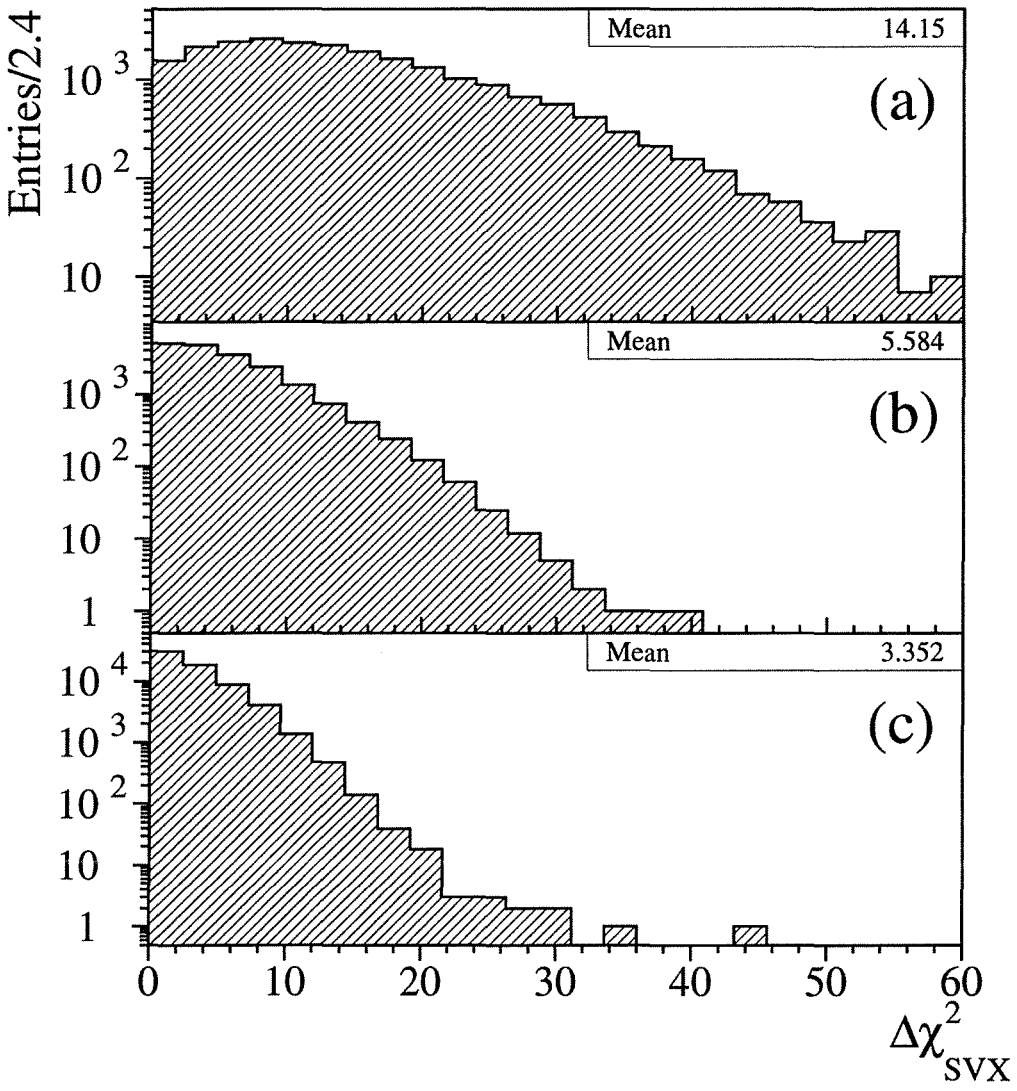

Figure 3.8: The displaced vertex-based $\Delta\chi^2_{\rm svx}$ variable for (a) b jets, (b) c jets, (c) uds jets and gluon jets in simulated events.

3.3.3 Lepton Transverse Momentum

The products of b hadron decay are relatively light and often will have high momenta in the rest frame of the b hadron. The transverse component of the momentum relative to the b hadron flight direction is unaffected by a boost along this direction. The jet axis is a good approximation of this b hadron flight direction. Hence, in the laboratory frame, b hadron decay products will tend to have high transverse momenta with respect to the jet axis compared to particles in light quark jets.

In the absence of lifetime-based information, the lepton[1] transverse momentum with respect to the jet axis provides the best method of tagging b quark jets. Figure 3.9 shows electron p_{T} spectra for leptons from b hadron decay and from other sources; the distribution is dominated by semileptonic b hadron decays for high p_{T}. Unfortunately, as discussed in Section 3.2, the inclusive semileptonic b branching ratio is small, roughly 20% for decays to electrons and muons combined.

Electron and muon identification techniques described below are based upon those developed for ALEPH b physics analysis [116].

Electron Identification

Electron identification relies upon $\mathrm{d}E/\mathrm{d}x$ and track momentum measurements from the TPC combined with the transverse and longitudinal patterns of energy deposited in the ECAL.

[1] In this discussion, the term *lepton* refers to $\mathrm{e}^{\pm}$ and $\mu^{\pm}$.

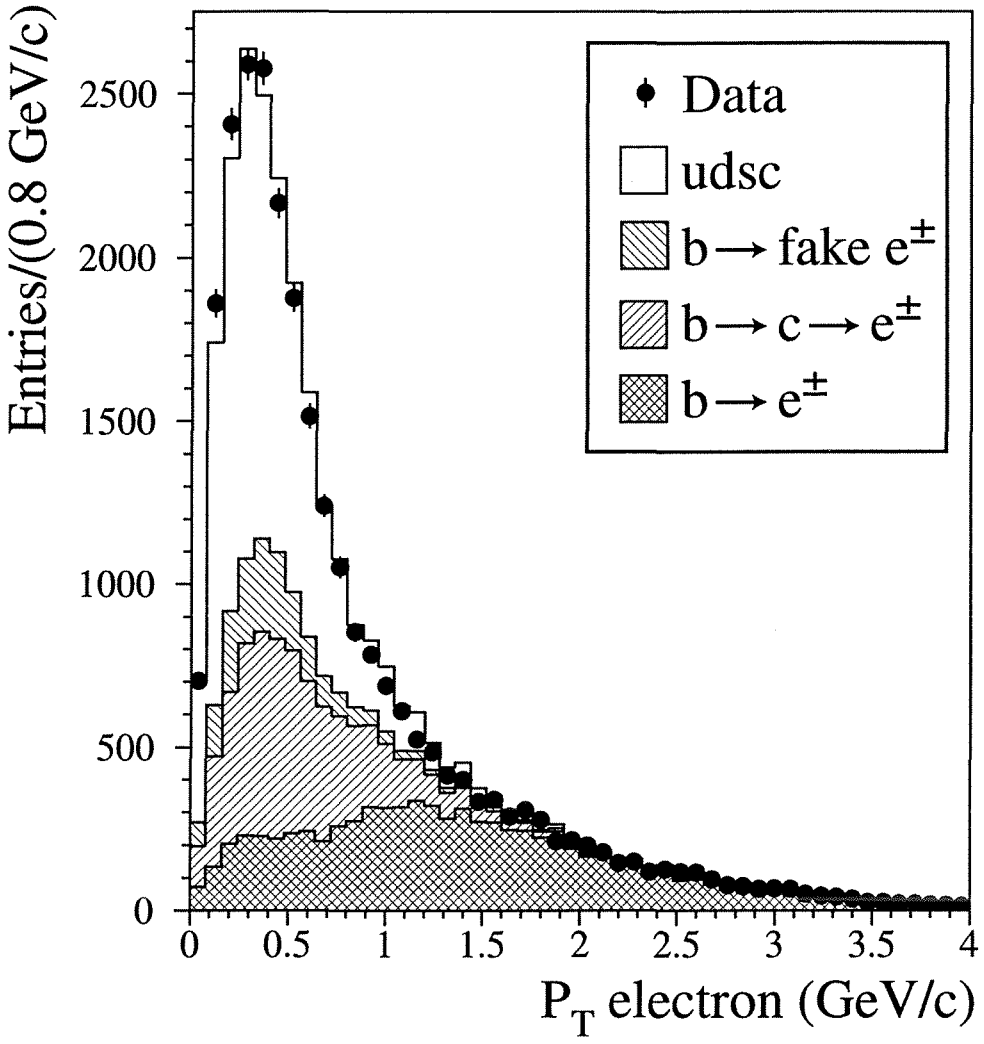

Figure 3.9: Electron p_{T} spectra from data and from simulated events. The different histograms show the contributions from various sources: udsc events, b→fake (misidentified) electrons, cascade decays of b→c→$e^{\pm}$ and direct semileptonic b hadron decay b→$e^{\pm}$. The b jet content of the events has been enhanced with an lifetime-based event cut.

Measurements of $\mathrm{d}E/\mathrm{d}x$ are able to distinguish electrons across a broad momentum spectrum as shown in Figures 2.14 and 2.15. The $\mathrm{d}E/\mathrm{d}x$-based estimator used for electron identification is defined as

$$R_{\mathrm{I}} = \frac{I - \langle I \rangle}{\sigma_I}$$

where I is the measured $\mathrm{d}E/\mathrm{d}x$, $\langle I \rangle$ is the expected $\mathrm{d}E/\mathrm{d}x$ for electrons, and σ_I is the resolution given in Section 2.3.2. A track must have at least 50 isolated TPC wire hits for the R_{I} estimator to be considered reliable; this requirement typically rejects 12% of tracks in a hadronic event.

Electrons which do not traverse a crack region are usually completely absorbed in the ECAL, leaving compact energy deposits. Thus, a second electron identification estimator can be based upon the ratio of energy in adjacent calorimeter storeys to the momentum measured in the TPC. This reflects not only the energy balance between the TPC momentum measurement and the ECAL energy deposit, but also the transverse evolution of the shower in the ECAL.

The four closest ECAL storeys in each stack are determined by extrapolating tracks from the end of the TPC into the ECAL. The four closest storeys do not necessarily belong to the same projective towers since the electron has a curved trajectory in the ECAL due to the magnetic field. The estimator is defined as

$$R_{\mathrm{T}} = \frac{E_4/p - \langle E_4/p \rangle}{\sigma_{E_4/p}}$$

where E_4 is the sum of the energy deposited in the four closest ECAL storeys summed over the three stacks, p is the track momentum measured in the TPC, and $\langle E_4/p \rangle$ is the mean expected energy fraction deposited by an electron in the four central towers. The mean energy fraction has a constant value of 0.85 in the barrel region and 0.89 in the endcap regions for electron momenta greater than 2 GeV/c. The expected resolution on energy-momentum ratio $\sigma_{E_4/p}$ is a function of momentum. Since energy is summed only from the four closest storeys, this R_{T} estimator is a measure of the compactness of an electromagnetic shower; electrons have compact showers while hadrons typically do not.

A third electron identification estimator is based upon longitudinal evolution of electromagnetic showers in the ECAL. The inverse mean depth of energy deposition summed over the four closest storeys in each stack is defined as

$$X_{\mathrm{L}} = \frac{E_4}{\sum_{i=1}^{4}\sum_{j=1}^{3} E_i^j S_j}$$

where E_i^j is the energy deposited in the ith storey of stack j and S_j is the mean depth of energy deposition in that segment for stack j. The estimator is defined as

$$R_{\mathrm{L}} = \frac{X_{\mathrm{L}} - \langle X_{\mathrm{L}} \rangle}{\sigma_{X_{\mathrm{L}}}}.$$

The momentum dependence of $\langle X_{\mathrm{L}} \rangle$ and $\sigma_{X_{\mathrm{L}}}$ is parameterized using high-purity samples of electrons from hadronic events with hard R_{T} and R_{I} requirements and from Bhabha events.

The three estimators R_{I}, R_{T}, and R_{L} are normally distributed and can be used together to identify electrons. The R_{I} estimator is more effective at low momenta while R_{T} and R_{L} are more effective at high momenta. Figure 3.10 shows the behavior of the R_{T} and R_{L} estimators for an electron-enriched and hadron-enriched sample from ALEPH data.

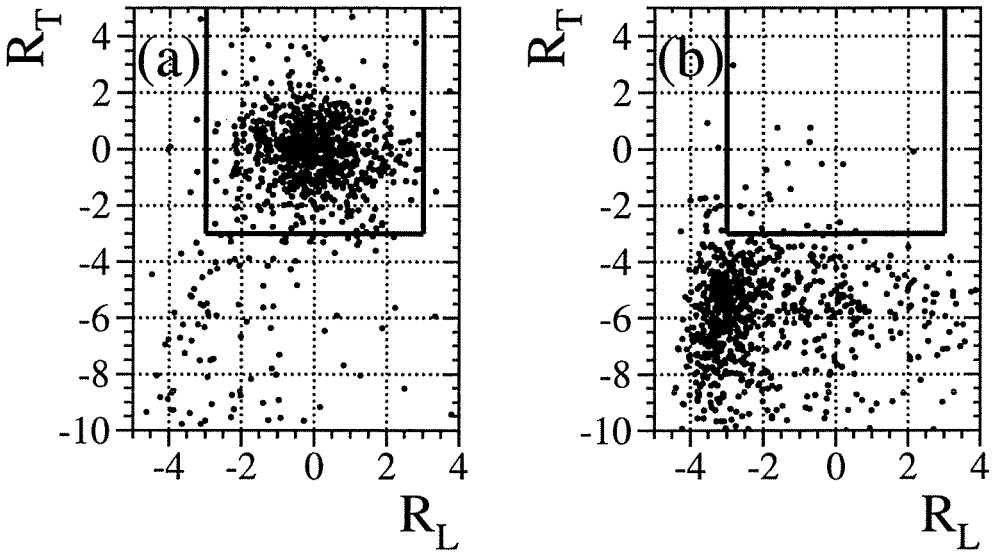

Figure 3.10: A scatter plot of the calorimeter-based electron estimators R_{T} and R_{L} for (a) an electron-enriched sample and (b) a hadron-enriched sample from photon conversions in data. The electron-enriched sample is obtained by requiring R_{I} to be less than 1. The hadron-enriched sample is obtained by requiring R_{I} to be greater than 3.

Good charged tracks with momenta greater than $2\,\mathrm{GeV}/c$ are identified as electrons if they pass the following set of criteria:

$$R_{\mathrm{T}} > -3.0, \quad -3.0 < R_{\mathrm{L}} < 3.0,$$

$$R_{\mathrm{I}} > -2.5.$$

To obtain genuine electrons from the semileptonic decays of heavy quark hadrons, it is necessary to tag and reject unwanted electrons originating from photon conversions in detector material. Dalitz decays (*e.g.*, $\pi^0 \rightarrow e^+e^-\gamma$) also represent a source of unwanted electrons and are especially problematic since these electron/positron pairs originate from the interaction point. Electron candidates are flagged as originating from photon conversions or Dalitz decays if they form a V^0 with an oppositely charged track with a mass of less than $20\,\mathrm{MeV}/c^2$ and pass within 1 cm of that track in either xy and z.

The electron identification efficiency is a function not only of momentum, but also of transverse momentum p_T with respect to a jet axis. It is more difficult to assign unambiguously TPC wire hits to low p_T electrons within a jet due to the proximity of other charged tracks in the congested central part of a jet. This decreases the number of good $\mathrm{d}E/\mathrm{d}x$ measurements. The overall electron identification efficiency ranges from roughly 55% to 70% as a function of p and p_T. Throughout this range, the probability of identifying a hadron as an electron is less than 0.3% [116].

Muon Identification

Muon identification relies upon track information from the TPC together with the digital pattern readout from the HCAL and muon chamber information. Muons penetrate the calorimeter material more than any other charged particle and leave hits in the muon chambers.

Typical HCAL digital hit patterns differ distinctively between charge particle species. This is illustrated in Figure 3.11 for single pions, muons, and

electrons with momenta of 10 GeV/c. Pions deposit their energy in broad showers that do not typically penetrate to the last layers of the HCAL. Muons traverse the entire HCAL leaving hits in each layer. Electrons that are not absorbed in the ECAL would leave short compact showers in the first few layers of the HCAL.

Tracks from the TPC are extrapolated through the calorimeter material based on the muon hypothesis. A road three times the width of the estimated effect of multiple scattering is defined around the extrapolated track path. An HCAL plane is said to be *expected to fire* if the extrapolated track intersects an active region of the plane. This expectation accounts for dead or inefficient regions and cracks between HCAL modules. The plane is said to have *fired* if a digital hit lies within the multiple scattering road. A track is defined to have a muon chamber hit if at least one of the two double-layers has a space point which is less than four times the estimated standard deviation due to multiple scattering from the extrapolated track. The following discriminating variables to distinguish muons are built from this information:

- N_{exp} is the number of expected HCAL planes to have fired,
- N_{fire} is the number of HCAL planes which have fired,
- N_{10} and N_3 are the number of firing HCAL planes within the last ten and three expected for the track respectively,
- N_μ is the number of hits in the muon chambers,
- X_{mult} is the *excess digital hit multiplicity* in the last 10 HCAL lay-

ers defined as the number of digital hits within the extrapolated road divided by the number of firing planes.

Since the HCAL digital hit patterns are two-dimensional projections of hits along a module, there is the possibility of hit-track ambiguities especially when attempting to identify muons contained within high multiplicity hadronic jets. The three-dimensional muon chamber hits can usually resolve such ambiguities.

Good charged tracks with momenta greater than 3 GeV/c are said to have a *good HCAL pattern* and are identified as muons if they pass the following criteria:

$$X_{\text{mult}} < 1.5,$$
$$N_{\text{fire}}/N_{\text{exp}} \geq 0.4, \quad N_3 \geq 1,$$
$$N_{10} \geq 5, \quad N_{\text{exp}} \geq 10$$

Tracks without good HCAL patterns but with one hit in each of the muon chamber layers are identified as muons if

$$X_{\text{mult}} < 1.5,$$
$$d_{\text{hit}} < 0.5\,\text{cm}, \quad \theta_{\text{hits}} < 150\,\text{mrad}$$

where d_{hit} is the minimum distance between a muon chamber hit and the extrapolated track, and θ_{hits} is the angle between the extrapolated track and the track constructed using only the muon chamber hits.

As is the case with electron identification efficiency, muon identification efficiency depends upon p and p_{T} of the muon. However, in this case, the

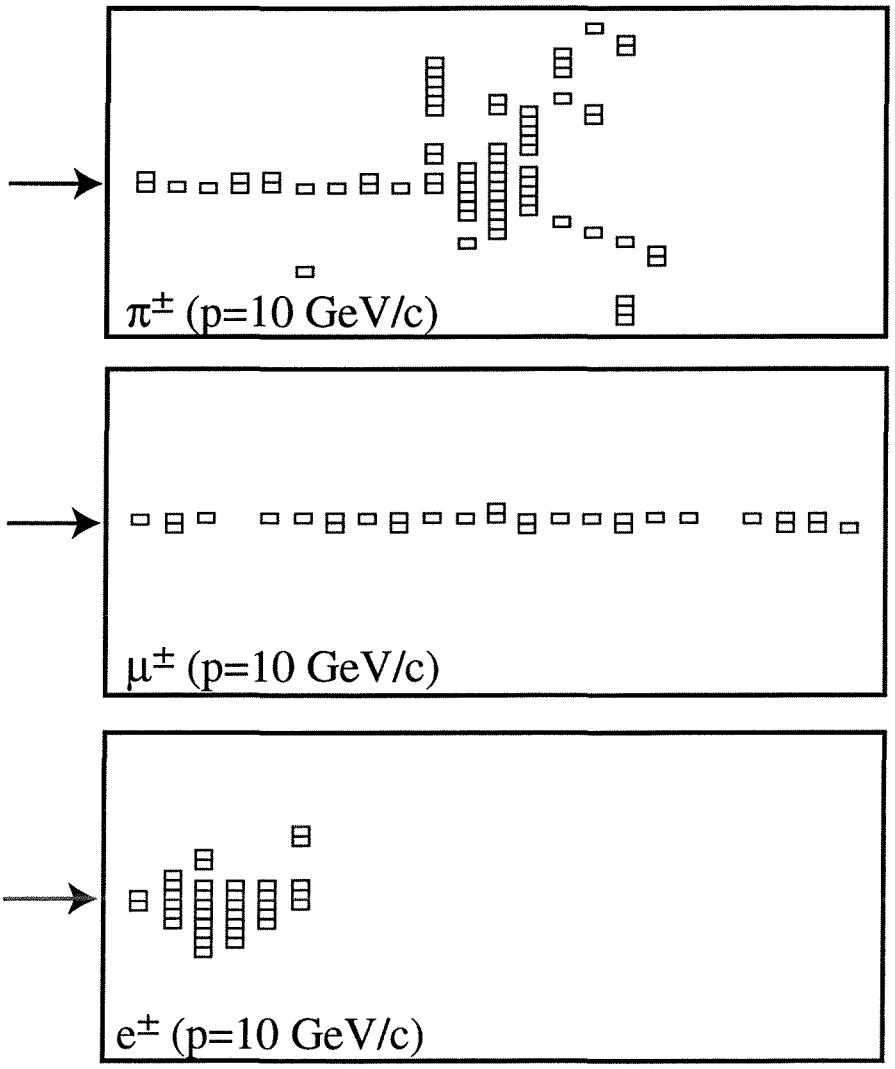

Figure 3.11: An illustration of typical HCAL digital hit patterns for 10 GeV/c pions, muons, and electrons.

dependence upon p_{T} is small and is caused by overlapping and ambiguous track patterns in the HCAL between low p_{T} muons and other particles within a jet. The identification efficiency ranges from 84% to 87%. Throughout this range, the probability to identify a hadron as a muon is less than 0.5% [116].

Lepton Transverse Momentum as a b-Tagging Variable

The transverse momentum of identified electrons and muons with respect to the jet axis is denoted as $p_{\mathrm{T}\ell}$. This variable when available is an effective b-tagging variable. Figure 3.12 shows distributions of $p_{\mathrm{T}\ell}$ for b jets, c jets, and uds jets and gluon jets from simulated events. Not only is a high $p_{\mathrm{T}\ell}$ value indicative of b jets, but so is the fact that a jet has an identified lepton. This is partly due to the fact that leptons from b hadron decay have a harder momentum spectrum and hence pass the lepton identification momentum criteria. In general roughly 30% of b jets have an identified lepton while only 18% of c jets and 7% of uds jets and gluon jets have one.

3.3.4 Jet-shape Variables

A variety of variables have been developed to take into account the broader profile and higher multiplicity of b jets as opposed to udsc jets. This is due to the decay of the massive weakly decaying b hadrons within b jets. Although c jets contain weakly decaying c hadrons, their mass is less than half that of b hadrons; thus c jets more closely resemble uds jets. The situation is different for g jets due to enhanced soft gluon bremsstrahlung in the hadronization process described in Section 3.1.1. Although g jets resemble b jets in all of

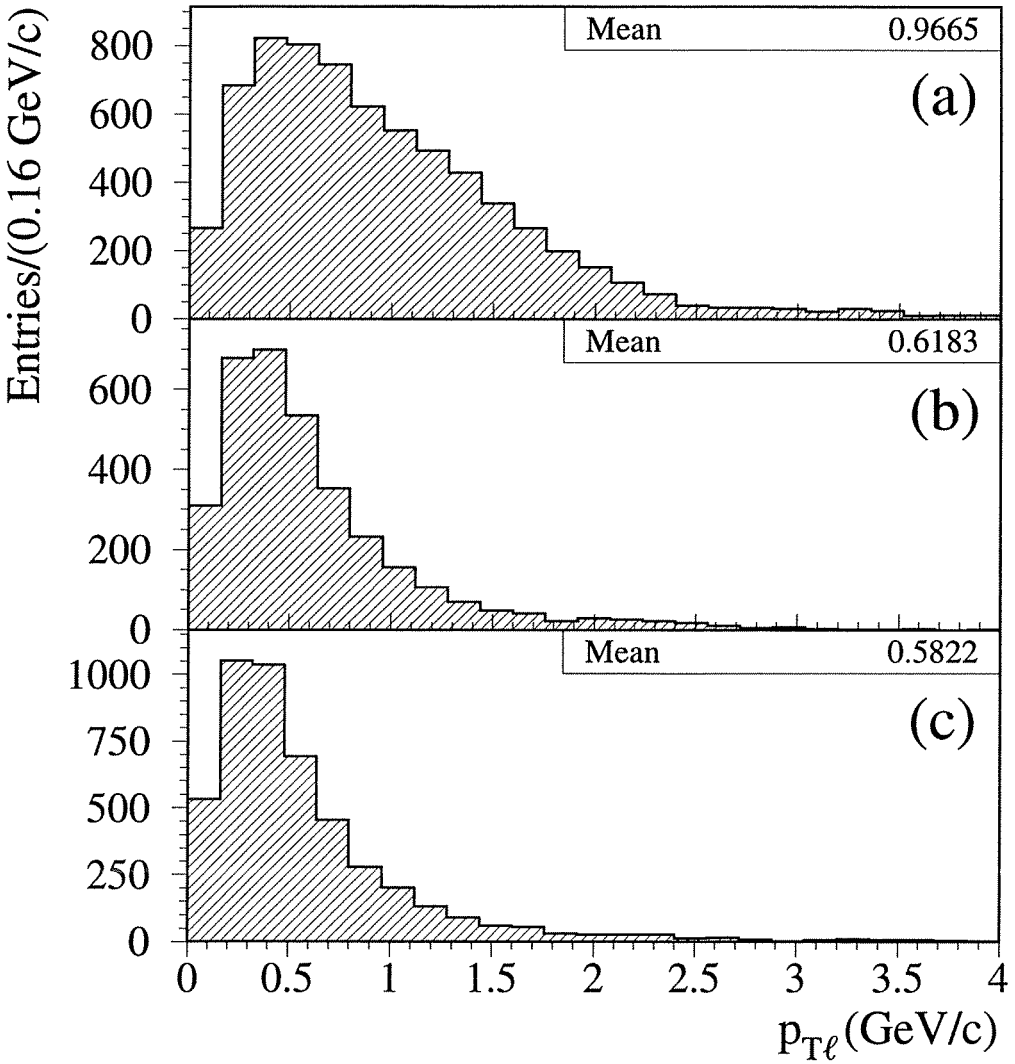

Figure 3.12: Distributions of $p_{T\ell}$ from simulated events for (a) b jets, (b) c jets, and (c) uds jets and gluon jets.

the jet-shape variables described below, these variables are still useful for discriminating between b jets and udsc jets.

Boosted Sphericity

The sphericity of a system of N particles is determined by computing a momentum tensor [117] given as

$$S^{\alpha\beta} = \frac{\sum_{i=1}^{N} p_{i\alpha} p_{i\beta}}{\sum_{i=1}^{N} |\vec{p}_i|^2}$$

where the α and β indices run over the three Cartesian coordinates (x, y, and z) of each three-momentum vector $\vec{p}_i$. The eigenvalues of the momentum tensor are denoted as Q_j $(j = 1, 2, 3)$ and ordered as $Q_1 < Q_2 < Q_3$. Sphericity is defined as

$$S = \frac{3}{2}(Q_1 + Q_2).$$

Traditionally, sphericity has been used to study properties of entire events. For example, two-jet events have a sphericity near zero while multi-jet events or more isotropic events have a sphericity near one. A detailed discussion of sphericity and other event shape variables is given by Wu in Ref. [118].

Boosted sphericity S_{b} is calculated for each jet in an event by boosting all energy flow objects belonging to a jet into the rest frame of the jet. The sum of the momenta and energies of all energy flow objects within a jet defines the boost direction and magnitude. In this manner, each jet can be treated as

a pseudo-event. The sphericity is then calculated using the three-momenta of the boosted energy flow objects. Figure 3.13 shows the boosted sphericity distributions for b, udsc, and g jets in simulated events.

Multiplicity

As discussed in Section 3.2, decays of b hadrons yield on average five charged particles. It is natural to extend this to charged and neutral particles in a jet by examining the energy flow multiplicity of a jet N_{EF}. This quantity is energy dependent, but normalizing by the natural logarithm of the jet energy reduces this dependence. Figure 3.14 shows the distributions of $N_{\mathrm{EF}}/\log E$ for b, udsc, and g jets.

Sum of Transverse Momenta

As is the case for lepton transverse momentum, the transverse momenta for all of the decay products to the b hadron flight direction are unaffected by the boost. Particles in b jets should have higher transverse momenta with respect to the jet axis than light quark jets (with the jet axis approximating the b hadron flight direction within b jets). Hence, the sum of the square of transverse momentum with respect to the jet axis Σp_{T} for energy flow objects in a jet is a good b-tagging variable. Figure 3.15 shows the distributions of Σp_{T}^2 for b, udsc, and g jets.

Other Jet-shape variables

Many other jet-shape variables were developed and studied. These included directed sphericities of the most energetic tracks in a jet, rapidity-based vari-

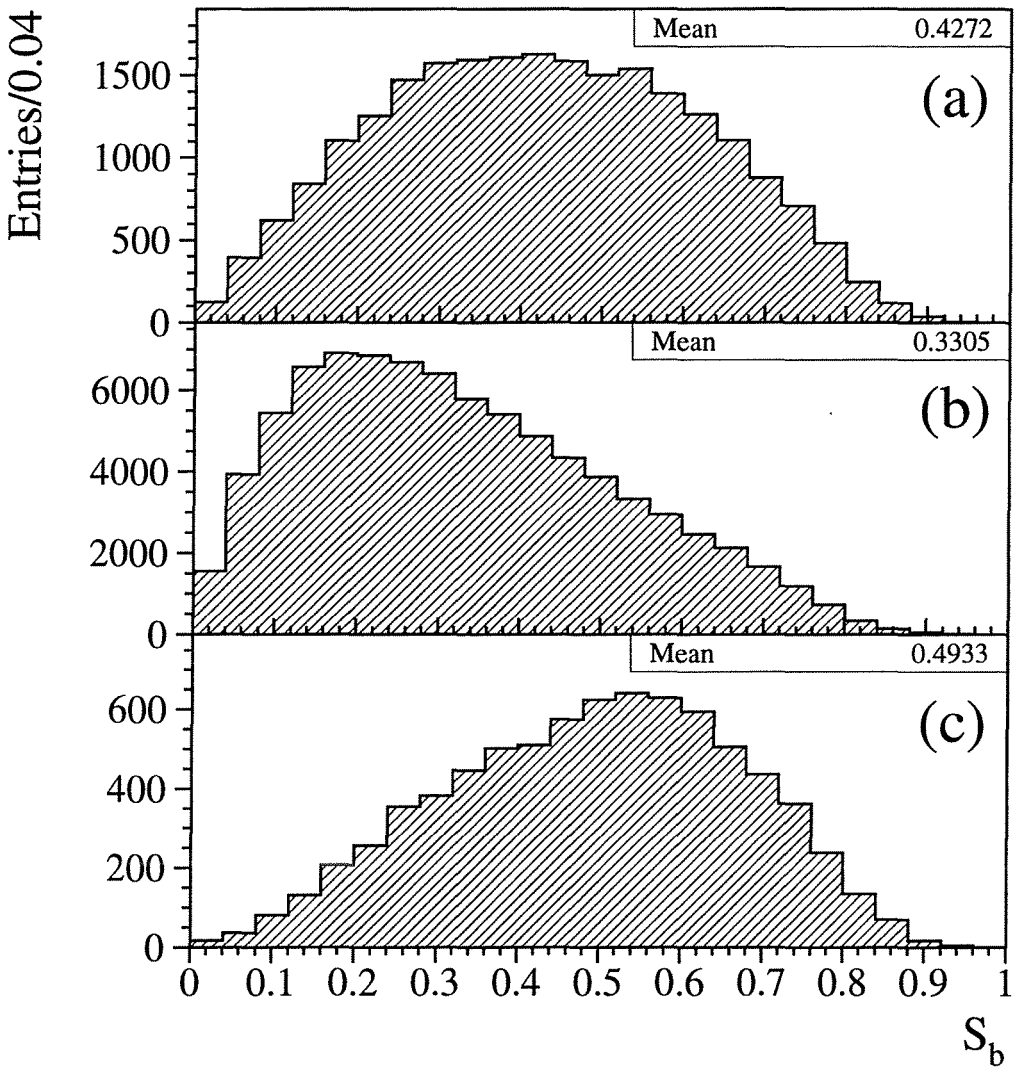

Figure 3.13: Boosted sphericity distributions from simulated events for (a) b jets, (b) udsc jets, and (c) g jets.

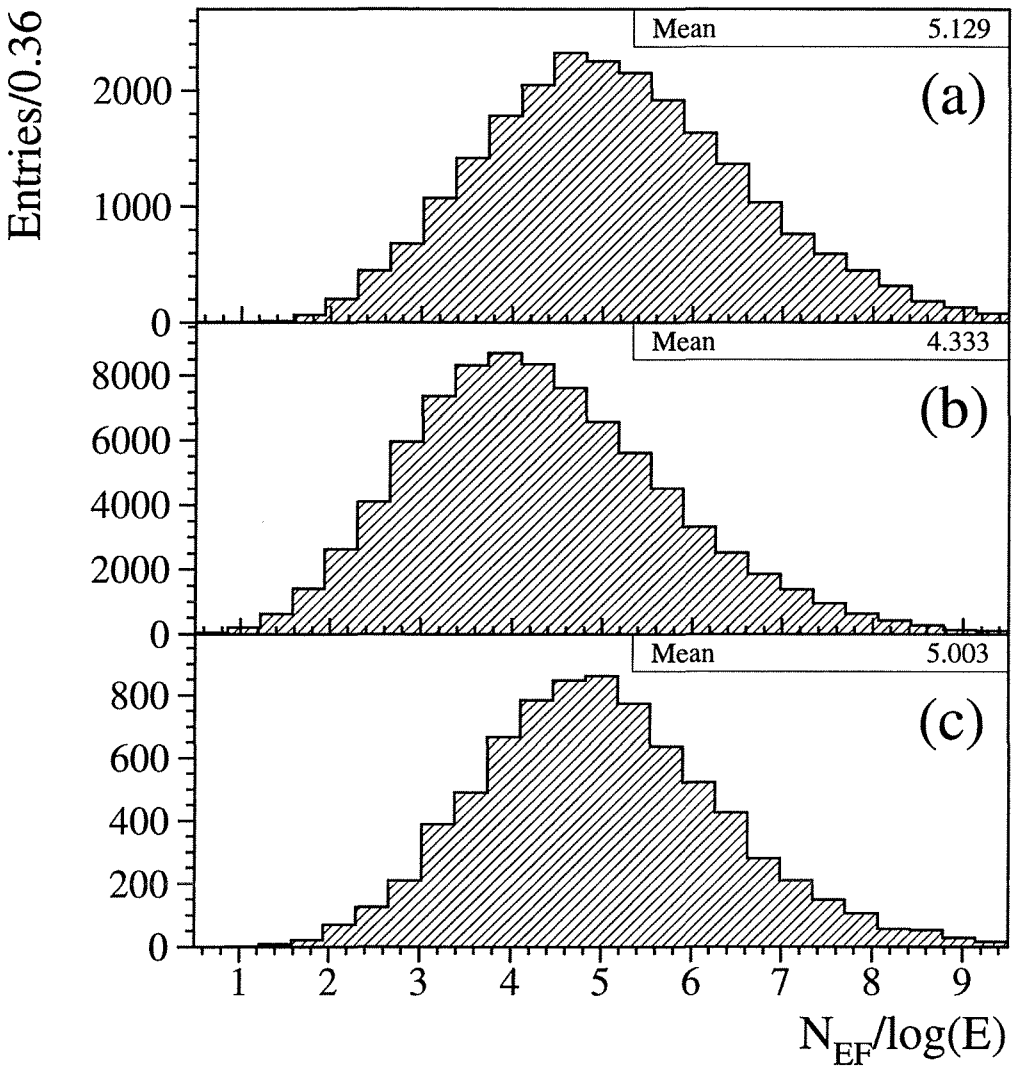

Figure 3.14: Distributions of $N_{\rm EF}/\log E$ from simulated events for (a) b jets, (b) udsc jets, and (c) g jets.

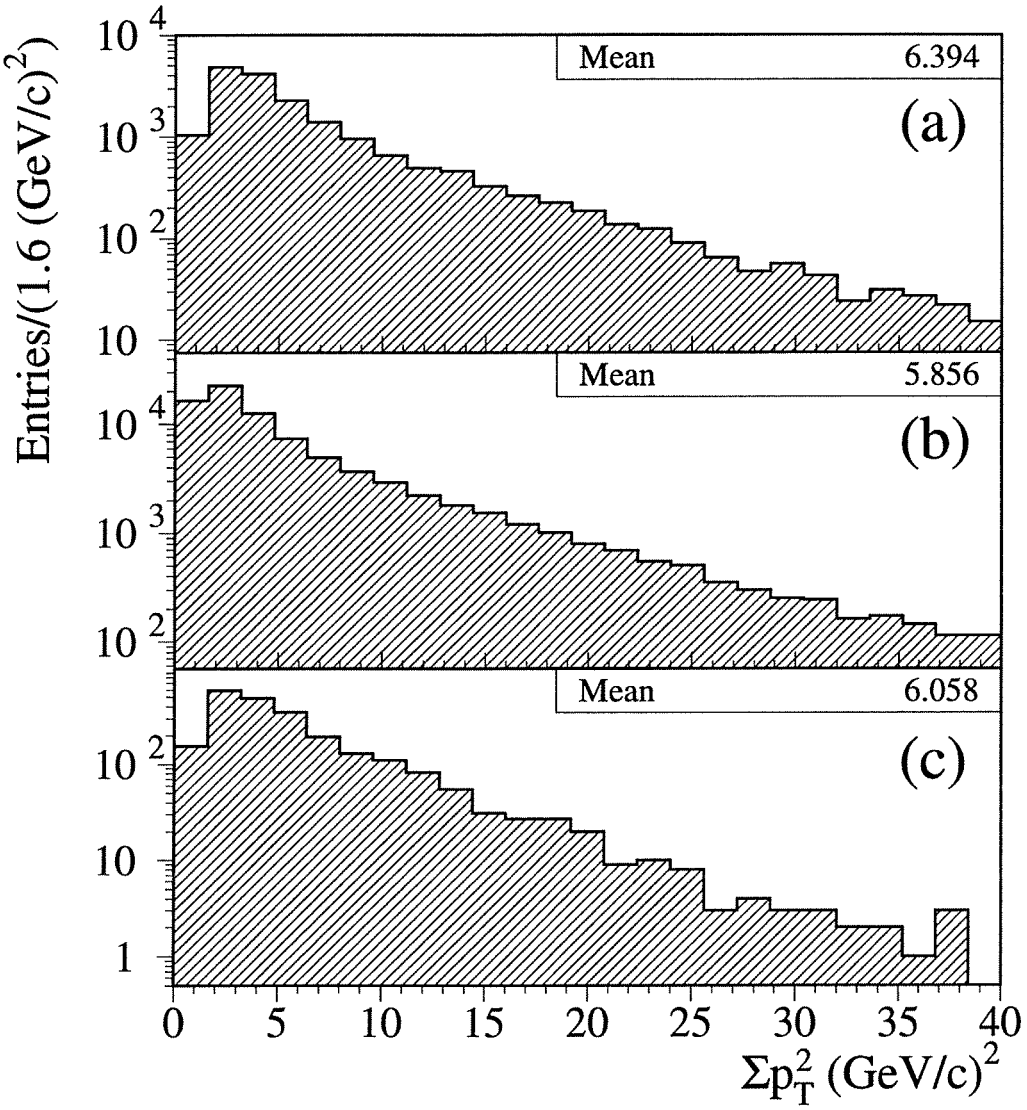

Figure 3.15: Distributions of Σp_T^2 from simulated events for (a) b jets, (b) udsc jets, and (c) g jets.

ables, sums of Fox-Wolfram moments [119], the thrust of the jet, the mass of tracks in a jet with significant impact parameters, etc... When included in a multivariate technique such as the neural network described in Section 3.4, they offered marginal improvement. When evaluated in the context of an analysis designed to search for the Higgs boson, the slight increase in performance (often in uninteresting and unusable efficiency regions) did not justify their inclusion in the b-tag [120].

3.4 A Neural Network b-Tag

3.4.1 Motivation

The six variables described in Section 3.3 demonstrate power to discriminate between b jets and light quark jets; these variables are:

- $\mathcal{P}_{\text{jet}}$: the uds jet probability based upon track impact parameter significance;
- $\Delta\chi^2_{\text{svx}}$: the χ^2 difference based upon a search for secondary vertices in the jet;
- $p_{\text{T}\ell}$: the transverse momentum of an identified electron or muon with respect to the jet axis;
- S_{b}: the boosted sphericity of energy flow objects in the jet;
- $N_{\text{EF}}/\log E$: the energy flow object multiplicity of the jet scaled by the jet energy;

- Σp_{T}^2: the sum of the square of transverse momenta of energy flow objects in the jet with respect to the jet axis.

Each of these six variables could be used alone with various degrees of success. However, some of these variables are not always available for all jets (*e.g.*, if no identified electrons or muons are found, $p_{\mathrm{T}\ell}$ would not be available). None of the variables reflect all aspects of a b jet. For example, although the weakly decaying b hadrons have significant lifetime, they could still decay at or near the primary vertex; however, such a decay might have a high boosted sphericity or multiplicity.

These variables could be used in a traditional cut fashion, but such a method is often cumbersome, and the cut values and combination method would not be well defined. Furthermore, two variables may be partially correlated. For example, a high multiplicity b hadron decay yielding a significantly displaced secondary vertex would enhance both the lifetime-based and jet-shape variables.

An elegant and effective way to deal with this multivariate problem is to use a neural network. Neural networks can be trained to utilize information available from multiple variables. They take into account correlations between variables and learn to rely upon available variables alone when other variables are not available.

Neural networks have been used previously to combine many jet-shape variables together for a single b-tagging variable [121]. The six variable neural network b-tag presented here is unique with respect to its use of

lifetime-based and lepton identification-based variables as well as jet-shape variables.

3.4.2 Architecture and Training

A discussion of the general theory and principles of neural networks is given elsewhere [122]. The neural network used here is a fully-connected multi-layer feed-forward network consisting of four layers based upon the JETNET 3.4 package [123].

The first layer consists of six input nodes for the variables described in the above list. The second and third layers consist of ten hidden nodes each. The fourth layer consists of a single output node yielding the variable used to identify b jets. The structure of this network may be described succinctly as 6-10-10-1 and is illustrated in Figure 3.16. This architecture gives better performance than architectures containing single hidden layers. The performance did not improve with additional hidden neurons and layers, and a reduced network architecture degraded the performance [124].

The neural network is trained on a sample of radiative Z returns extracted from a sample of 400 000 simulated $e^+e^- \rightarrow q\bar{q}(\gamma)$ events generated at $\sqrt{s}$=183 GeV. The radiative Z return process is described in Section 1.3.2. This choice of training sample has several advantages. Neural networks require large training samples to provide sufficient statistically independent exposures to the network during the learning phase. The training sample must also be independent from the sample used for evaluating performance.

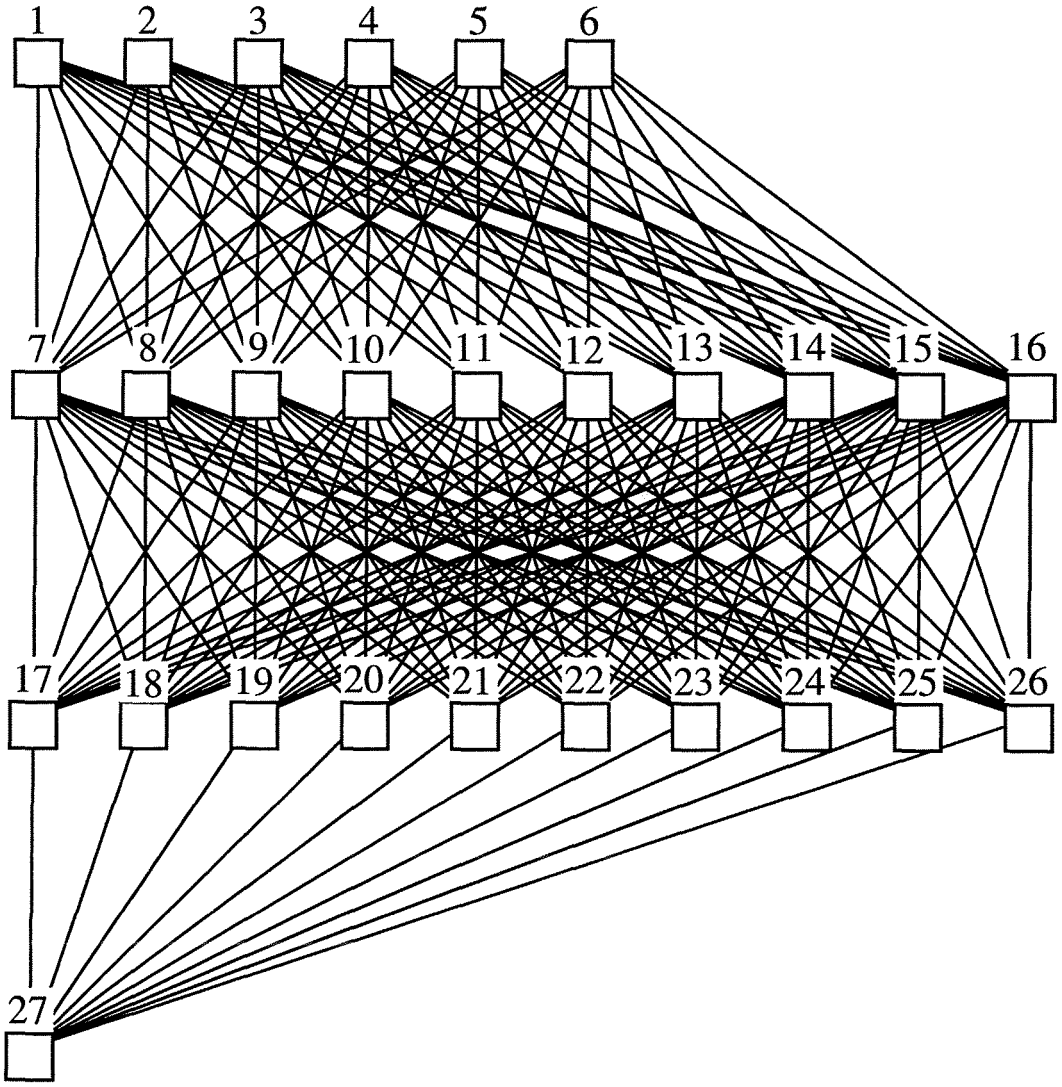

Figure 3.16: A diagram illustrating the architecture of the 6-10-10-1 b-tagging neural network. Neurons are depicted as squares while links are the lines joining the neurons. Neurons 1-6 are the six input nodes. Neurons 7-16 comprise the first 10-node hidden layer. Neurons 17-26 comprise the second 10-node hidden layer. Neuron 27 is the output node.

The analyses designed to search for the Higgs boson effectively reject radiative Z returns at an early preselection stage. Furthermore, radiative Z returns comprise the majority of $e^+e^- \rightarrow q\bar{q}(\gamma)$ cross section, and the jets they contain are similar to those found in Higgs signal and other Standard Model background process events discussed in Section 1.3. Hence, these events provide a large and readily available independent training sample.

The radiative Z return events are selected by requiring that the simulated Z mass be between 70 and 110 GeV/c^2. Energy flow objects which are likely to have been created by an initial state radiation (ISR) photon are flagged, and the remainder of the event is clustered into jets using the Durham algorithm with a $y_{\mathrm{cut}} = 0.0046$. A jet is retained for training if it has a momentum greater than 10 GeV/c and if it has a fraction of electromagnetic energy (using the definition described in Section 4.1) less than 80%. These jets roughly approximate the character of those found in the context of analyses designed to search for the Higgs boson. The resulting training sample from the 400 000 $q\bar{q}(\gamma)$ events consists of roughly 110 000 b jets, 92 000 c jets, 322 000 uds jets, and 38 000 g jets.

The six b-tagging variables are determined for each jet in the training sample. If a variable is not available for a jet, its value is set to a small negative value. The b-tagging variables are scaled such that they have a value between 0.0 and 1.0 when they are available. Hence, a six variable *pattern* is presented to the neural network for each jet in the training sample. The neural network is also presented with the true jet-flavor identity of each pattern. Patterns corresponding to b jets are assigned an ideal output value

of 1.0 while udscg jets are assigned a value of 0.0. The weights between the neurons are adjusted according to the back-propagation training scheme after the network is exposed to 10 patterns which are chosen at random from the training sample. A training *epoch* is defined to be the point when the number of patterns exposed to the neural network is equivalent to the training sample size. The entire training phase consists of 1 000 training epochs; this was chosen on the basis of optimal performance in simulated events.

Attempts were made to use more advanced neural network techniques such as the quick-prop and resilient back-propagation (RPROP) learning schemes as well as non-traditional architectures such as cascade correlation networks and radial basis function (RBF) networks [125]. The simple standard feed-forward back-propagation neural network was found to give similar or better performance in simulated events. Attempts were also made to construct a multiple output neural network where the outputs would correspond to the network response for b jets, c jets, uds jets, and g jets separately. However, this did not result in an enhancement in b-tagging performance.

3.4.3 Performance

A sample of jets from 100 000 simulated radiative Z returns extracted from $q\bar{q}(\gamma)$ events at $\sqrt{s} = 183\,\text{GeV}$ is used to evaluate the performance of the neural network in a stand-alone manner (*i.e.*, outside the context of a specific analysis for the Higgs boson search). This sample is statistically independent from the training sample and is referred to as the *testing sample*.

Figure 3.17 shows distributions of the output of the neural network b-tag for b, c, uds, and g jets from the testing sample. The neural network output distribution is sharply peaked near 1.0 for b jets. For uds jets the output distribution is peaked near 0.0. The distributions for c jets and g jets are also peaked near 0.0 but have larger means due to the presence of weakly decaying c hadrons for c jets and the larger boosted sphericity and higher particle multiplicity for g jets. The rejection of uds, c, and g jets as a function of b jet efficiency is shown in Figure 3.18.[2]

Compared to the single most powerful variable, $\mathcal{P}_{\rm jet}$, the neural network b-tag offers consistently better performance. Figure 3.19 shows the difference in non-b jet rejection between the neural network b-tag and $\mathcal{P}_{\rm jet}$ alone as a function of b jet efficiency.

The inclusion of the three jet-shape variables enhances the rejection power of the neural network b-tag for udsc jets, but, as expected, the rejection of g jets is degraded. This is illustrated by training a neural network consisting of only the $\mathcal{P}_{\rm jet}$, $\Delta\chi^2_{\rm svx}$, and $p_{{\rm T}\ell}$ variables and examining the difference in performance. This is shown in Figure 3.20. Although the g jet rejection is degraded with the full six variable neural network b-tag, the enhanced udsc jet rejection more than compensates for this effect when the neural network b-tag is used in analyses designed to search for the Higgs boson.

It is important to note that the performance studies presented in this section are on a jet-by-jet basis. In analyses designed to search for the Higgs

[2]Throughout this thesis, efficiencies and rejections are denoted as ϵ and ρ respectively. The rejection is defined as $\rho = 1 - \epsilon$.

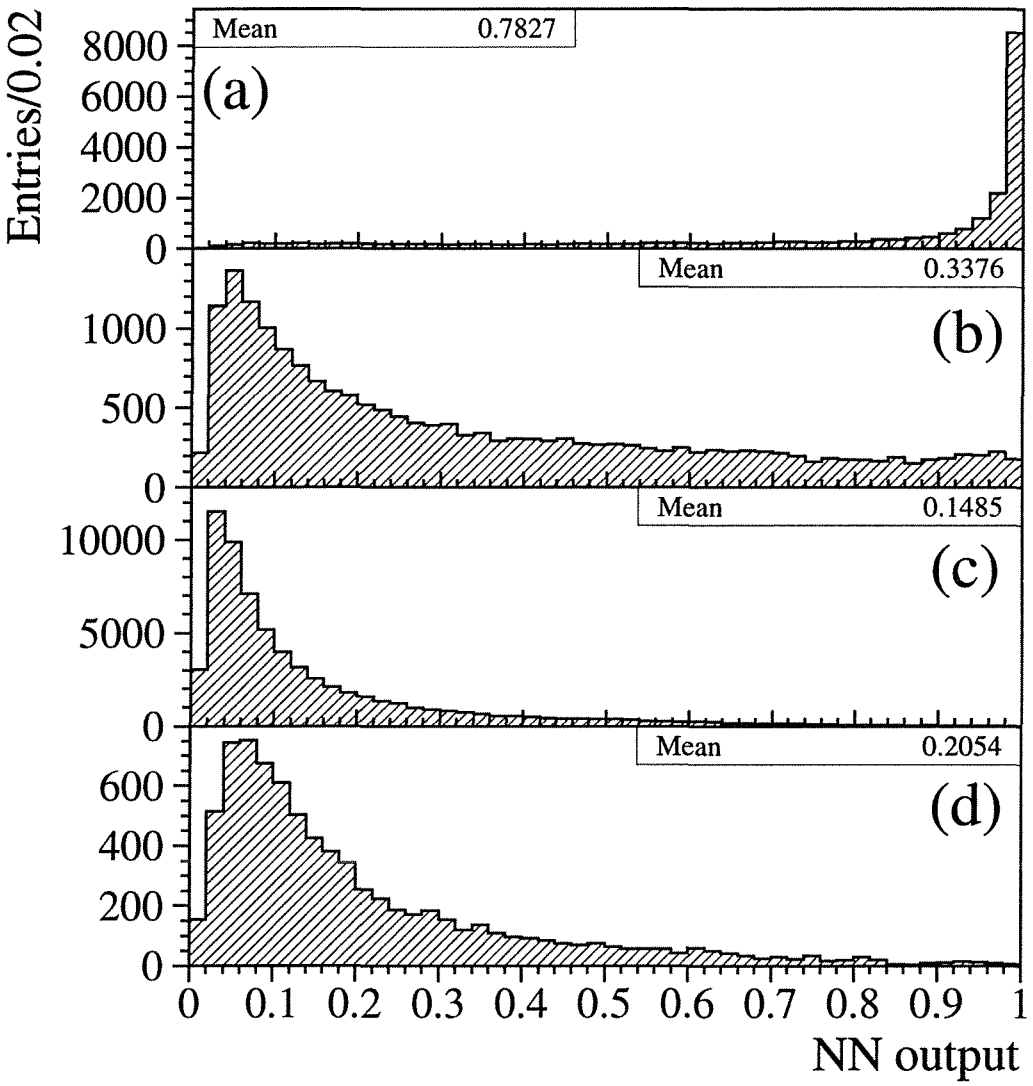

Figure 3.17: Distributions of the neural network b-tag output for (a) b jets, (b) c jets, (c) uds jets, and (d) g jets.

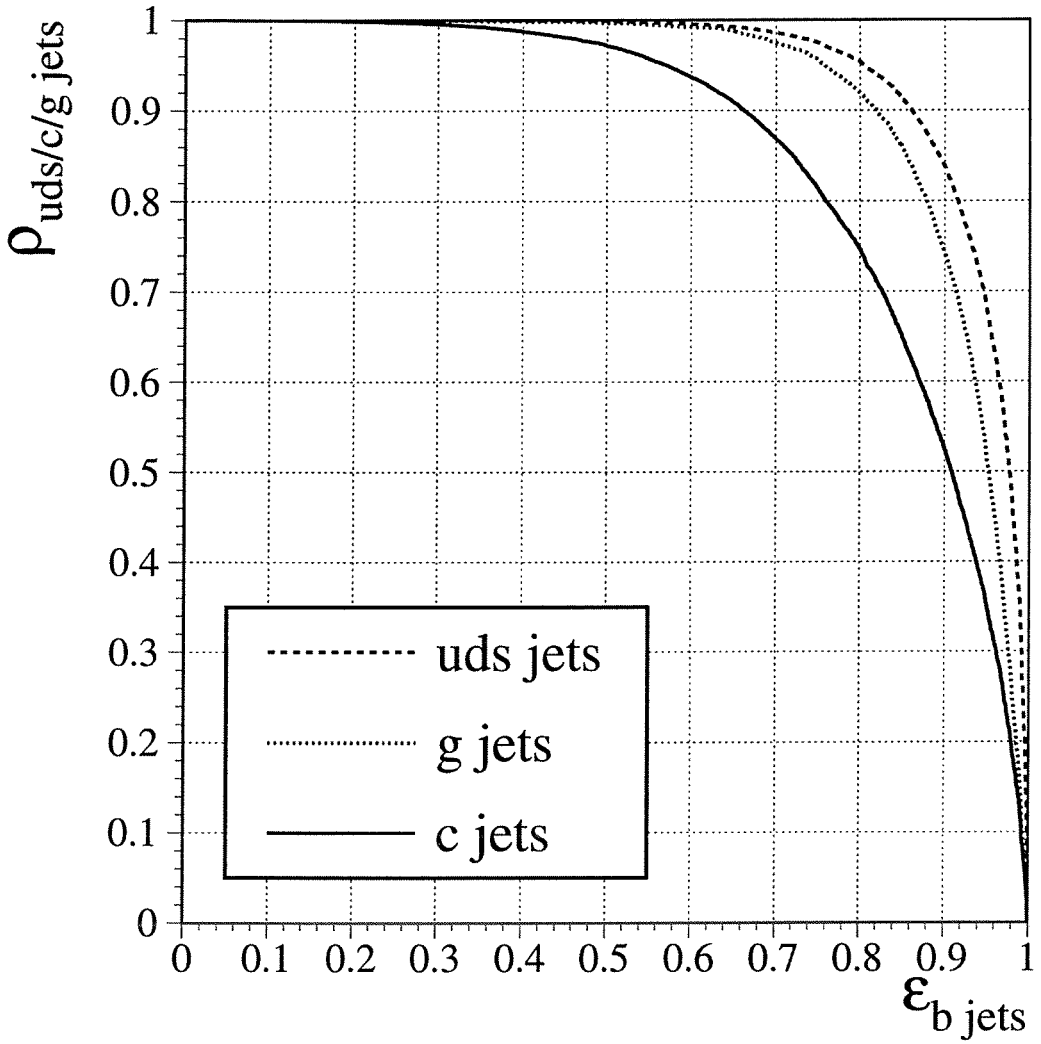

Figure 3.18: The neural network b-tag performance in terms of rejection of non-b jets $\rho_{\mathrm{uds/c/g\ jets}}$ versus efficiency for b jets $\epsilon_{\mathrm{b\ jets}}$ from the testing sample of simulated $\mathrm{q\bar{q}}(\gamma)$ events at $\sqrt{s} = 183\,\mathrm{GeV}$. The solid curve represents the performance for c jets; the dashed curve is for uds jets; the dotted curve is for g jets.

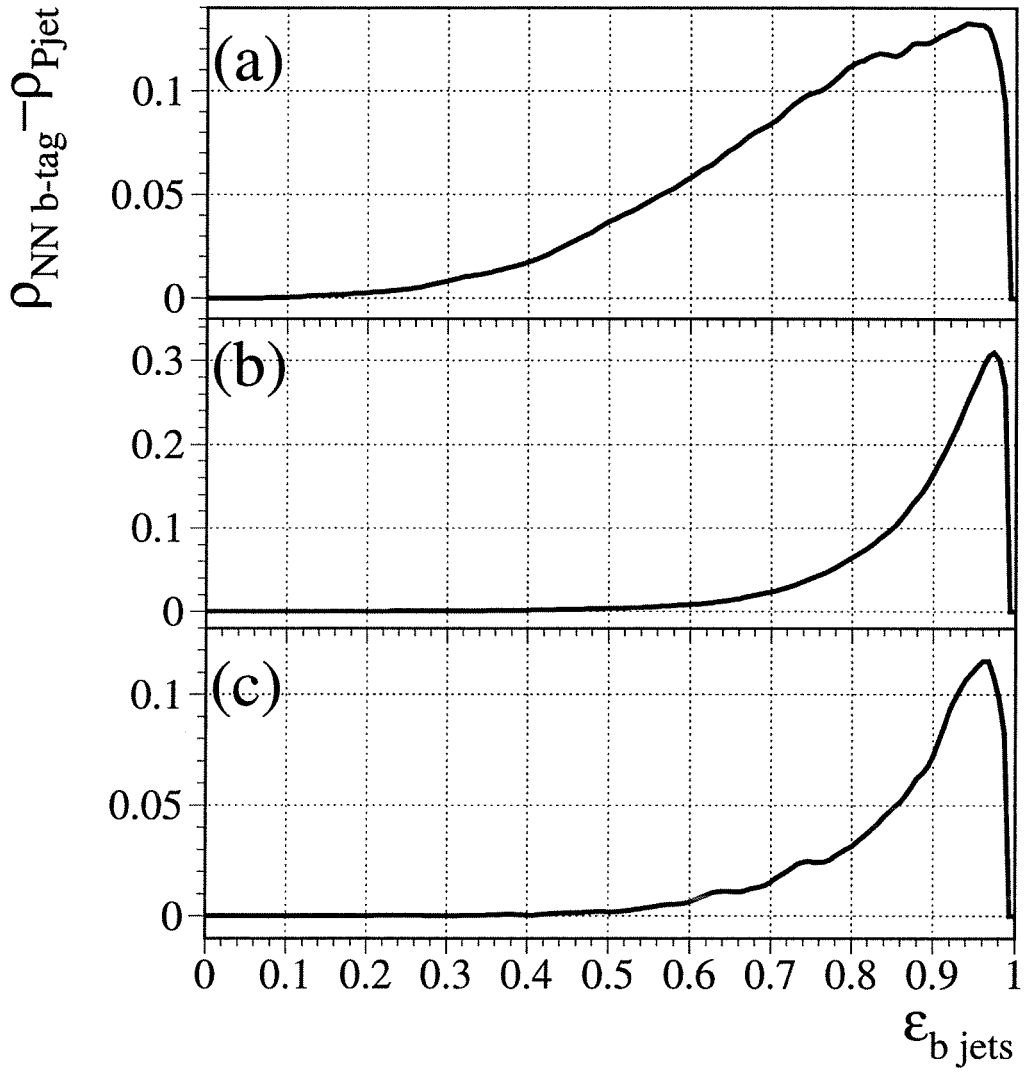

Figure 3.19: Performance differences between a the six variable neural network b-tag and $\mathcal{P}_{\rm jet}$ alone. The performance is given in terms of differences in non-b jet rejection ρ as a function of b jet efficiency $\epsilon_{\rm b\ jets}$ for (a) c jets, (b) uds jets, (c) g jets.

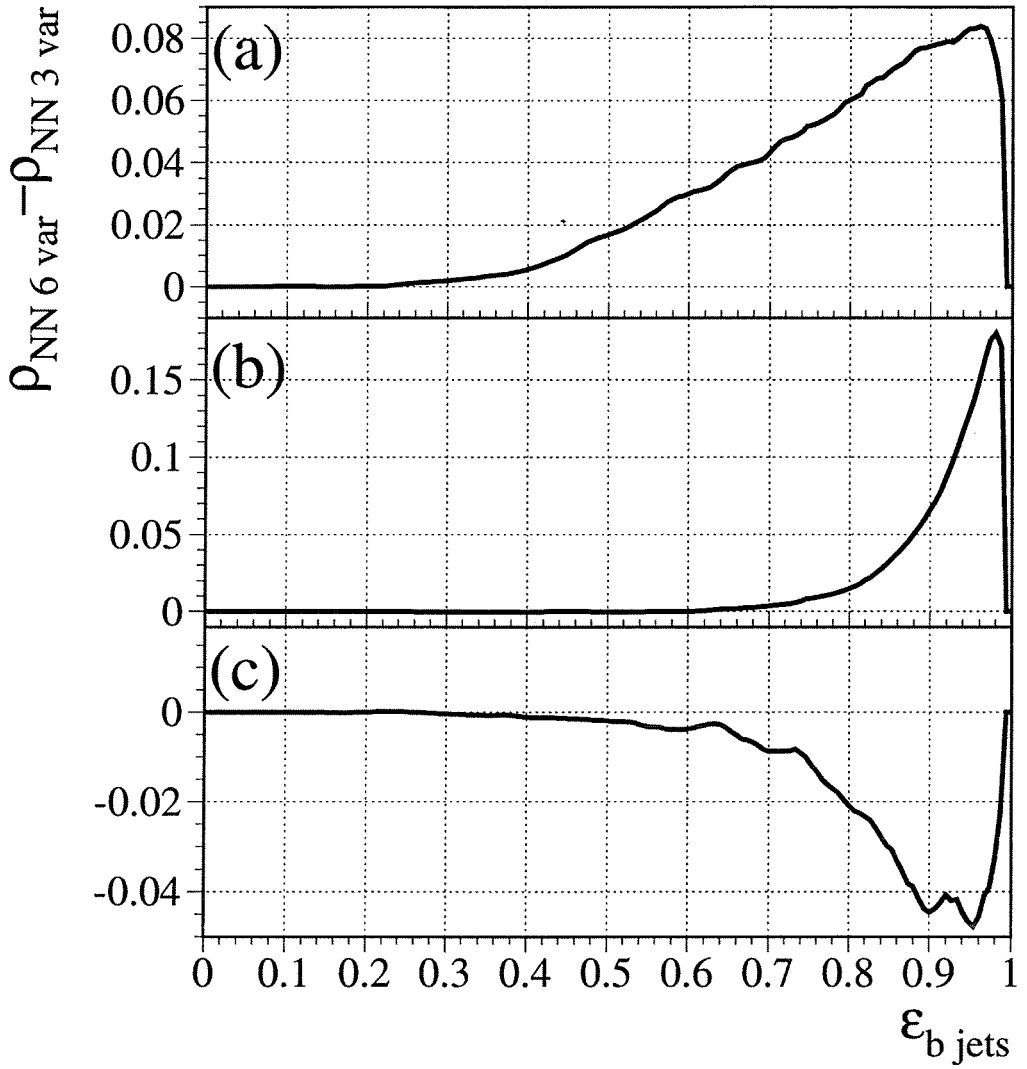

Figure 3.20: Performance differences between the six variable neural network b-tag and a three variable neural network b-tag excluding the three jet-shape variables. The performance is given in terms of differences in non-b jet rejection ρ as a function of b jet efficiency $\epsilon_{\text{b jets}}$ for (a) c jets, (b) uds jets, (c) g jets.

boson, the neural network b-tag is applied to two or four jets in an event. In this context, a small improvement in non-b jet rejection power for a given b jet efficiency can translate into a substantial gain in the performance of the analysis.

3.4.4 Application to Neutral Higgs Searches

The neural network b-tag is structured to provide a jet-by-jet tagging output for an arbitrary number of jets in an event. In this manner, it has been directly applied to and used for all final state LEP2 neutral Higgs boson searches within ALEPH. This includes searches for neutral Higgs bosons predicted by the Minimal Supersymmetric extension to the Standard Model (MSSM) as well as the Standard Model Higgs searches. An earlier implementation of this same neural network b-tag was used for neutral Higgs boson searches conducted at center-of-mass energies of 161 and 172 GeV [126, 127].

3.5 Comparisons between Data and Simulated Events

Since the neural network b-tag uses many variables, one has to worry about introducing large systematic effects associated with discrepancies between the simulated events and the data. There are two sources of discrepancies: the modelling of the detector in the simulated events and the physics parameters used in the event generator (*e.g.*, the average b hadron lifetime,

the free parameter in the Peterson fragmentation function, QCD modelling parameters affecting hadronization).

A number of problems can arise from imperfect modelling of the detector. Since much of the power of the b-tag is derived from the variables based upon displaced vertices and track impact parameters, the behavior of the tracking should agree well between data and simulated events. In fact, problems were observed in the agreement of impact parameter distributions between data and simulated.[3] These problems are ameliorated with a *smearing* of tracks in the simulation. The values of d_0 and z_0 are smeared by 3% for tracks with two VDET hits and 15% for all other tracks [131].

The evaluation of the effect of b-tagging systematic uncertainties on performance is done in the context of analyses designed to search for the Higgs boson; hence a quantitative analysis of these systematics is discussed in Section 4.4. However, a stand-alone study of the general agreement between data and simulated events with respect to b-tagging can be done using the $2.2\,\mathrm{pb}^{-1}$ ALEPH Z-peak data and a comparable sample of simulated Z-peak events. This data sample is chosen since it provides a large sample of hadronic events, nearly 50 000 events, compared to the high energy data.

[3] A problem with the primary vertex was discovered in the simulation of Z-peak events generated after that advent of LEP2 [128]; it has been corrected [129] in the studies presented in this section. A more general problem with the ALEPH simulation of all types of events during 1997 was discovered. This problem is related to VDET alignment parameters in the detector simulation; an $8\,\mu$m correction was applied mistakenly to z coordinates instead of $r\phi$ coordinates [130]. This problem as well as other more minor bugs are present in the simulated event samples used throughout this thesis and are the source of part of the discrepancy between data and simulated events. This is dealt with in a quantitative manner in Section 4.4.

Figures 3.21 through 3.26 show the distributions for Z-peak simulated events with Z-peak data superimposed. It can be seen that the agreement is good. Figure 3.27 shows the distribution of the neural network b-tag output for jets in Z-peak data and simulated Z-peak events.

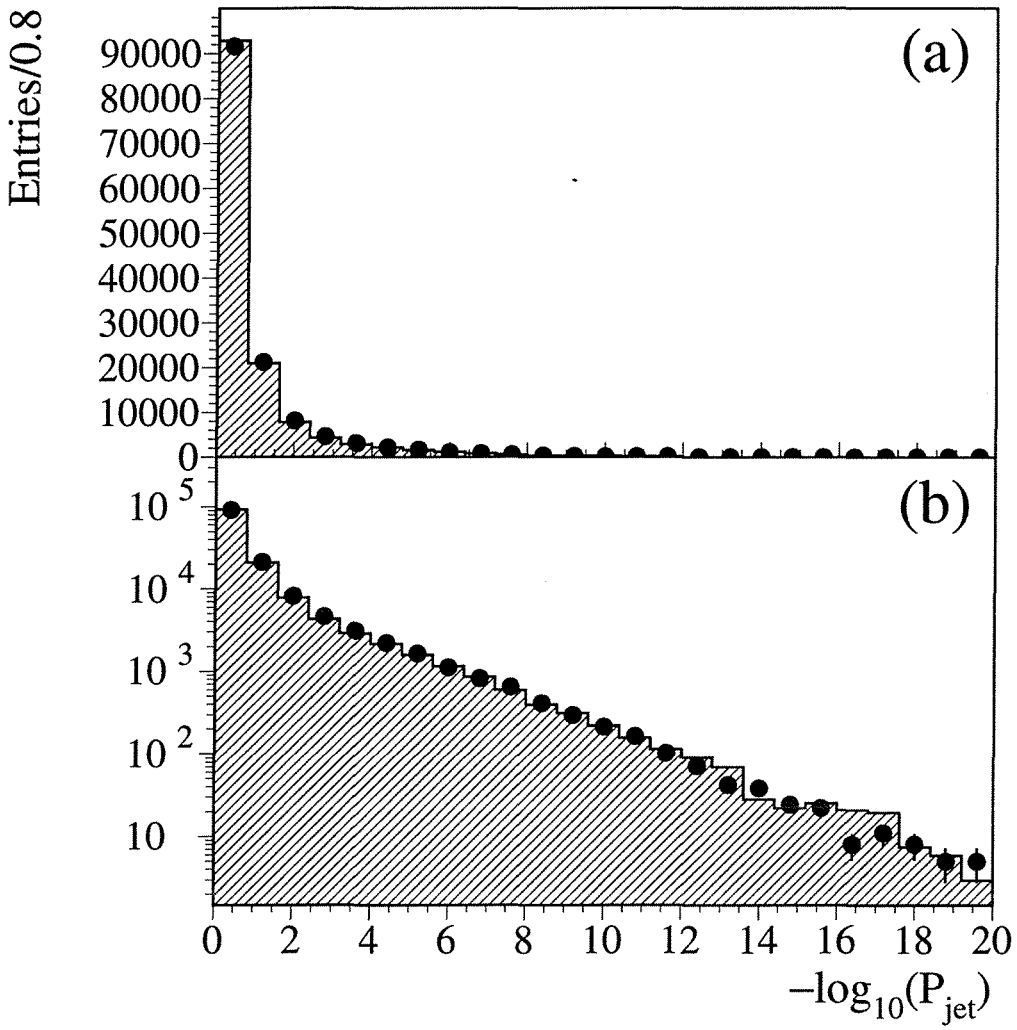

Figure 3.21: Distributions with Z-peak data (points) and simulated events (histogram) of $-\log_{10}\mathcal{P}_{\text{jet}}$: (a) the distribution with a linear y scale to show more clearly any differences in the peak region, (b) the distribution with a logarithmic y scale to show more clearly any differences in the tail region.

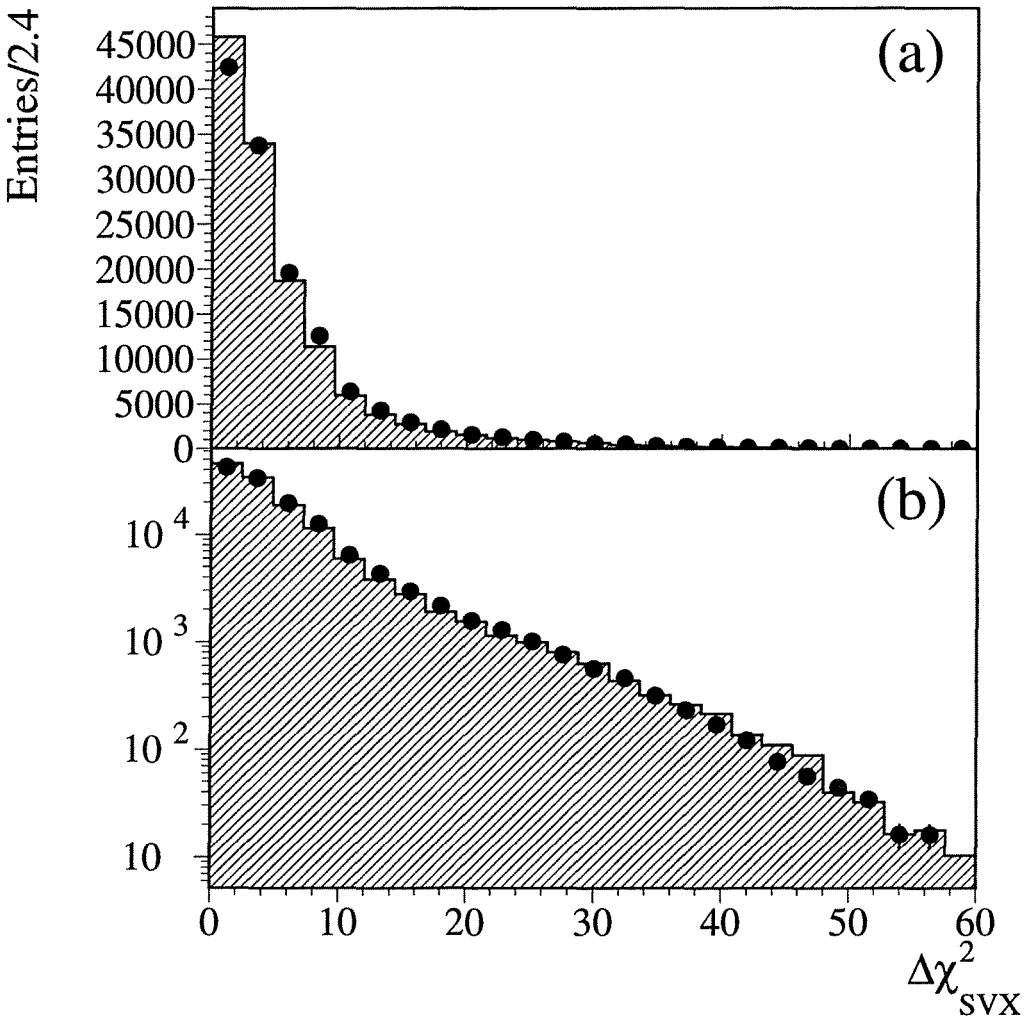

Figure 3.22: Distributions with Z-peak data (points) and simulated events (histogram) of $\Delta\chi^2_{\rm svx}$: (a) the distributions with a linear y scale to show more clearly any differences in the peak region, (b) the distributions with a logarithmic y scale to show more clearly any differences in the tail region.

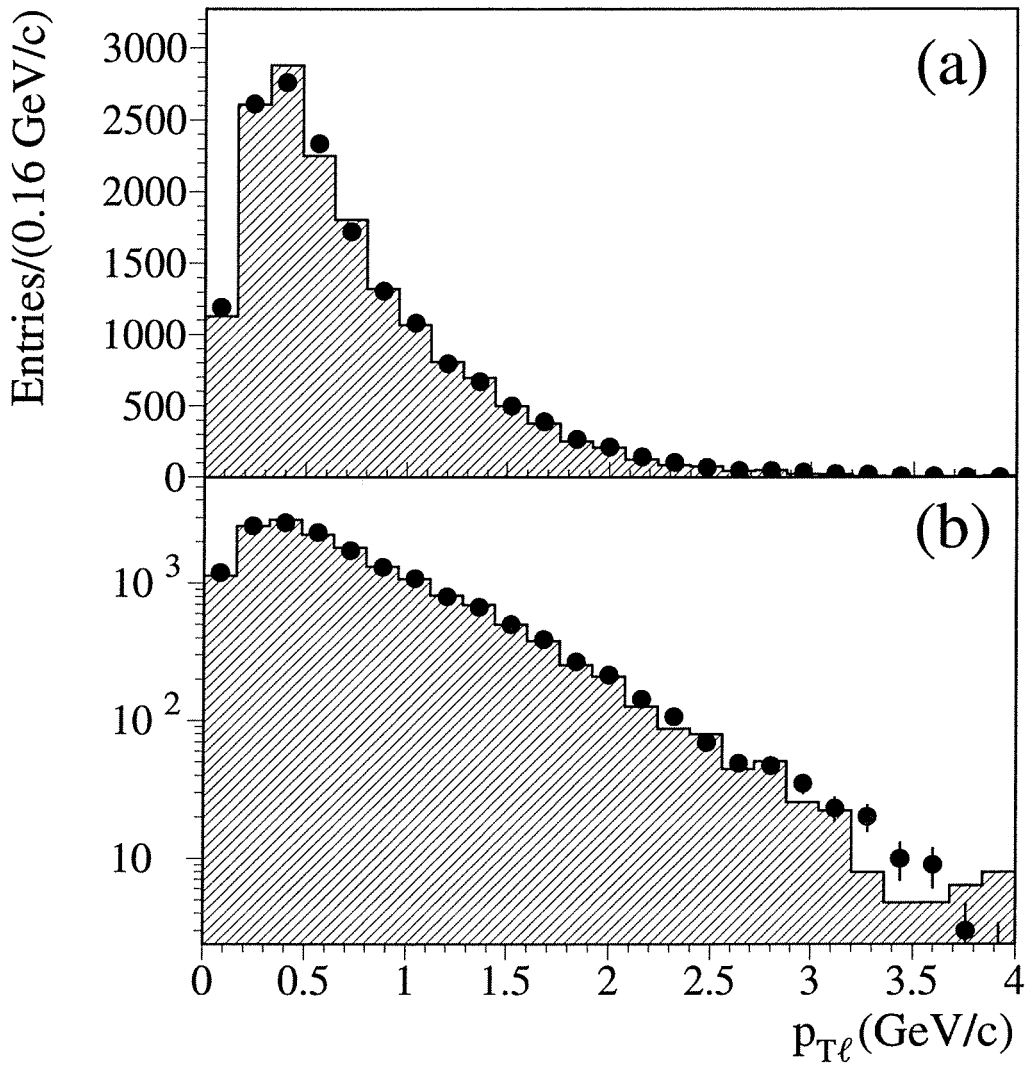

Figure 3.23: Distributions with Z-peak data (points) and simulated events (histogram) of $p_{T\ell}$: (a) the distributions with a linear y scale to show more clearly any differences in the peak region, (b) the distributions with a logarithmic y scale to show more clearly any differences in the tail region.

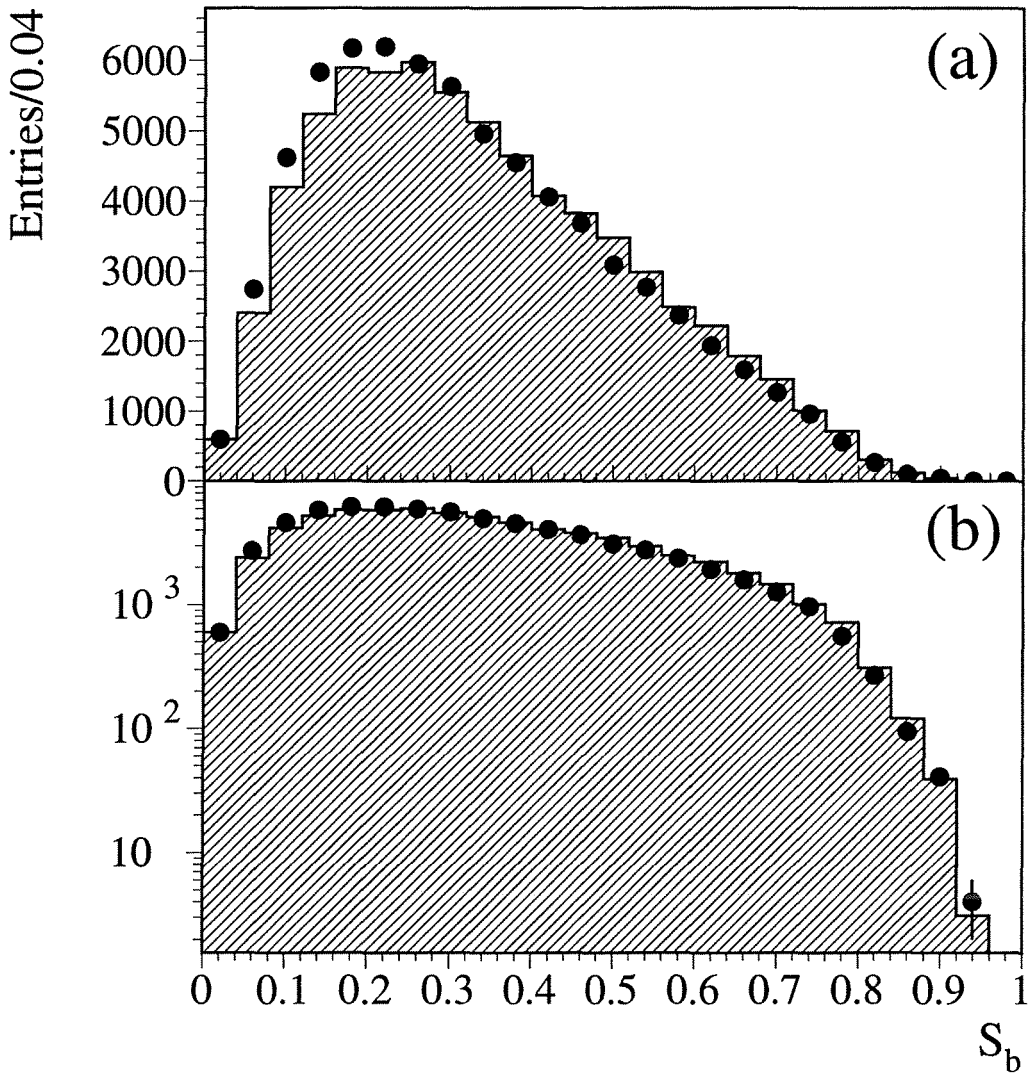

Figure 3.24: Distributions with Z-peak data (points) and simulated events (histogram) of S_b: (a) the distributions with a linear y scale to show more clearly any differences in the peak region, (b) the distributions with a logarithmic y scale to show more clearly any differences in the tail region.

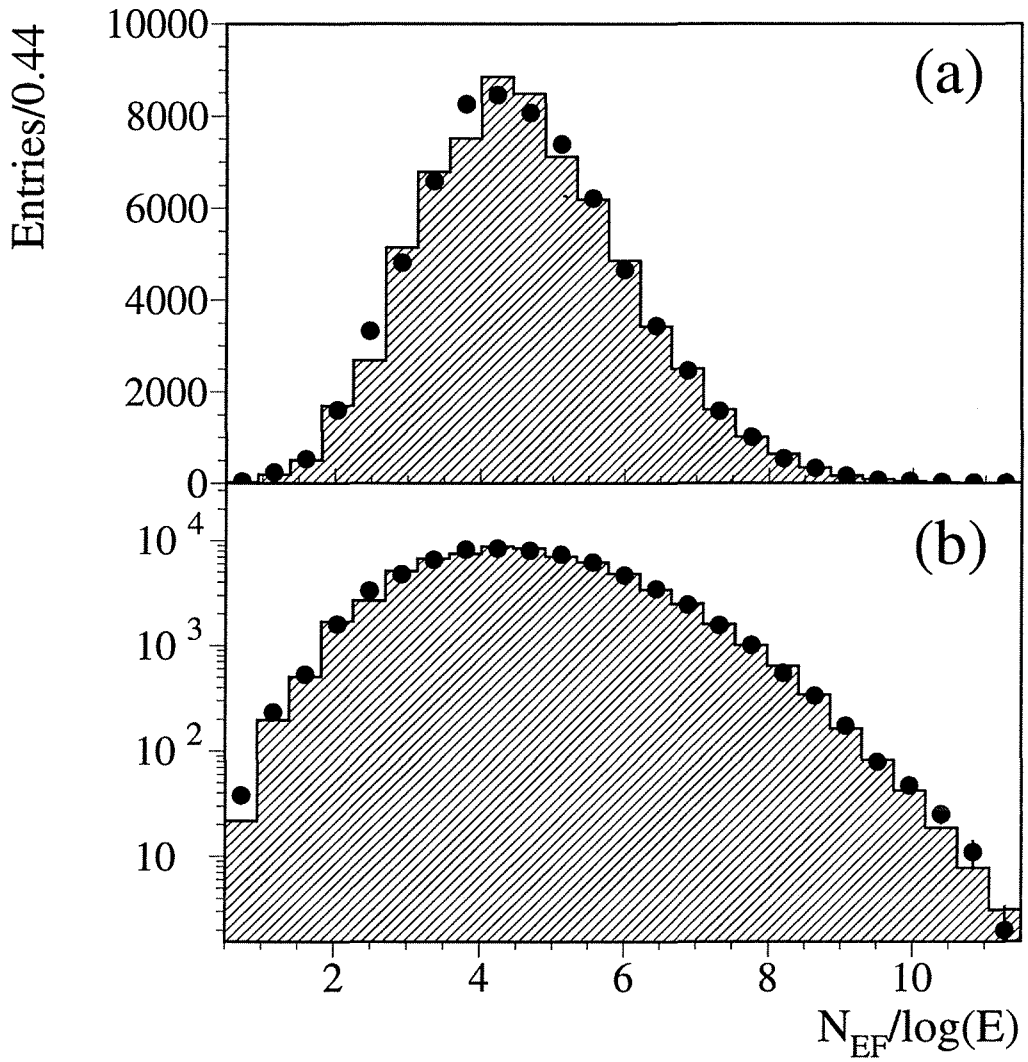

Figure 3.25: Distributions with Z-peak data (points) and simulated events (histogram) of $N_{\mathrm{EF}}/\log(E)$: (a) the distributions with a linear y scale to show more clearly any differences the peak region, (b) the distributions with a logarithmic y scale to show more clearly any differences in the tail region.

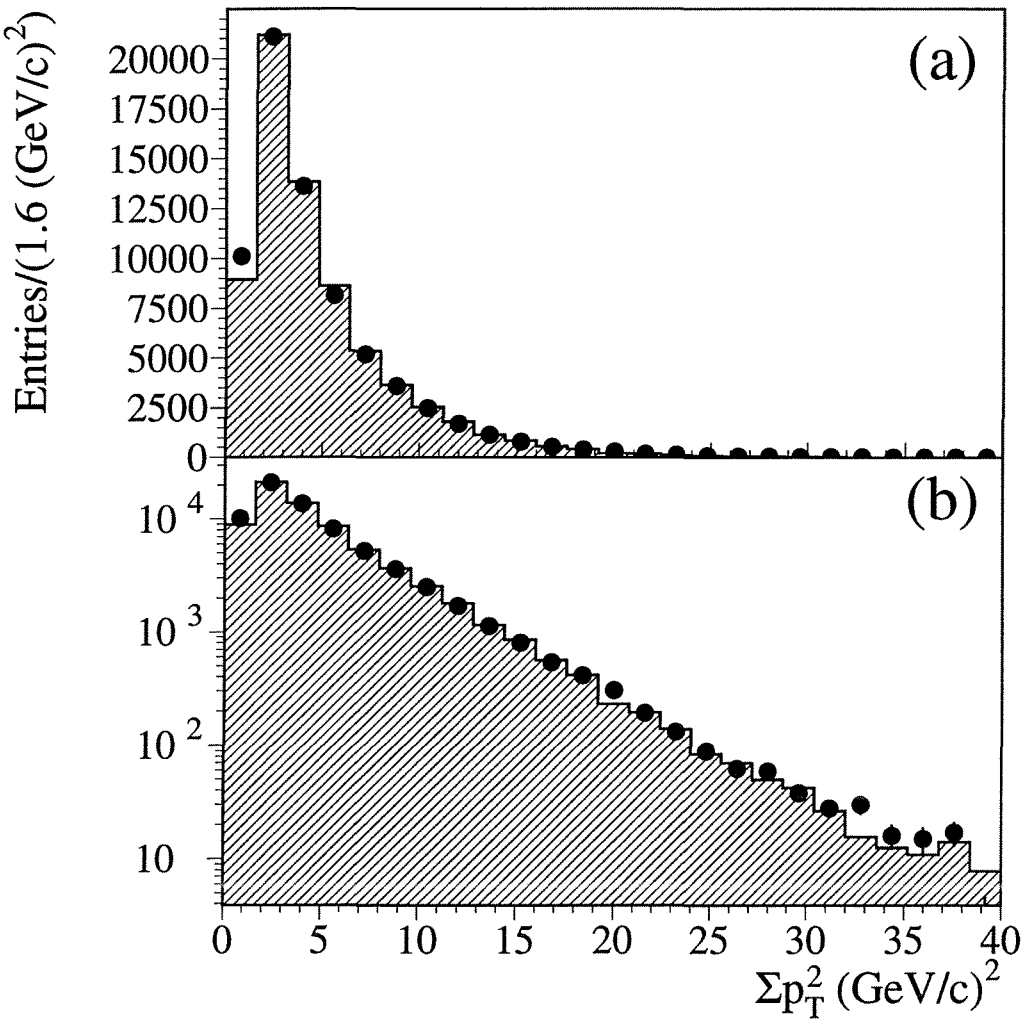

Figure 3.26: Distributions with Z-peak data (points) and simulated events (histogram) of Σp_T^2: (a) the distributions with a linear y scale to show more clearly any differences in the peak region, (b) the distributions with a logarithmic y scale to show more clearly any differences in the tail region.

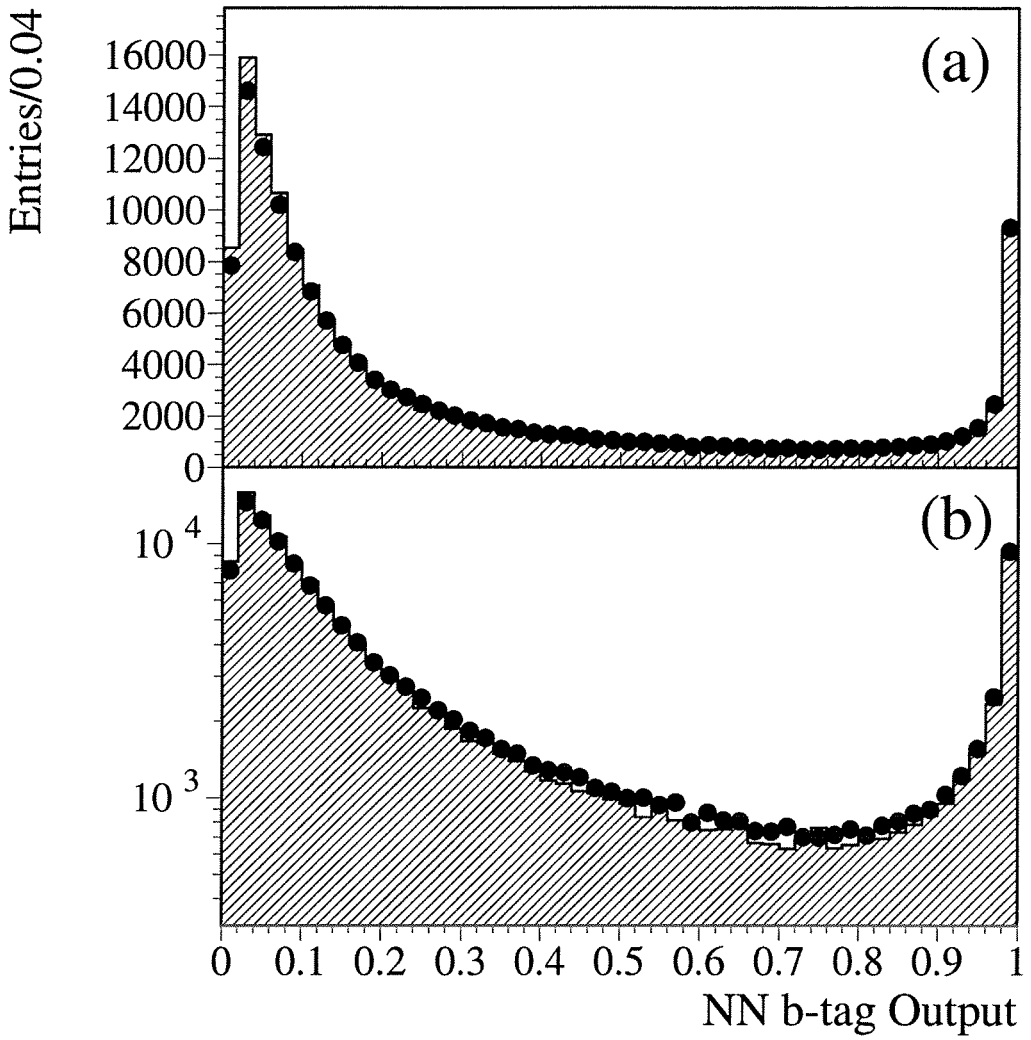

Figure 3.27: Distributions with Z-peak data (points) and simulated events (histogram) of the neural network b-tag output: (a) the distributions with a linear y scale to show more clearly any differences in the peak regions, (b) the distributions with a logarithmic y scale to show more clearly any differences in the tail region.

Chapter 4

Event Selections for the Four-Jet Final State

The event selections described in this chapter are designed to detect evidence of the Higgsstrahlung process in the four-jet final state while rejecting Standard Model background processes. As discussed in Section 1.3.1, the four-jet final state is defined to include the Higgs boson decaying to $b\bar{b}$, $q\bar{q}$, or gg (where $q\bar{q}$ refers to a non-b quark pair) which in total accounts for 64% of the Higgsstrahlung process. The four-jet final state is denoted as $Hq\bar{q}$ and referred to as the *signal*. The dominant case is when the Higgs boson decays to $b\bar{b}$; this accounts for roughly 92% of the total $Hq\bar{q}$ final state for a Higgs boson mass of $85\,\mathrm{GeV}/c^2$. Figure 4.1 shows an ALEPH event display [132] of a simulated signal event.

After an initial set of common selection criteria, described in Section 4.1, two parallel analyses are used to select events. The first analysis, described

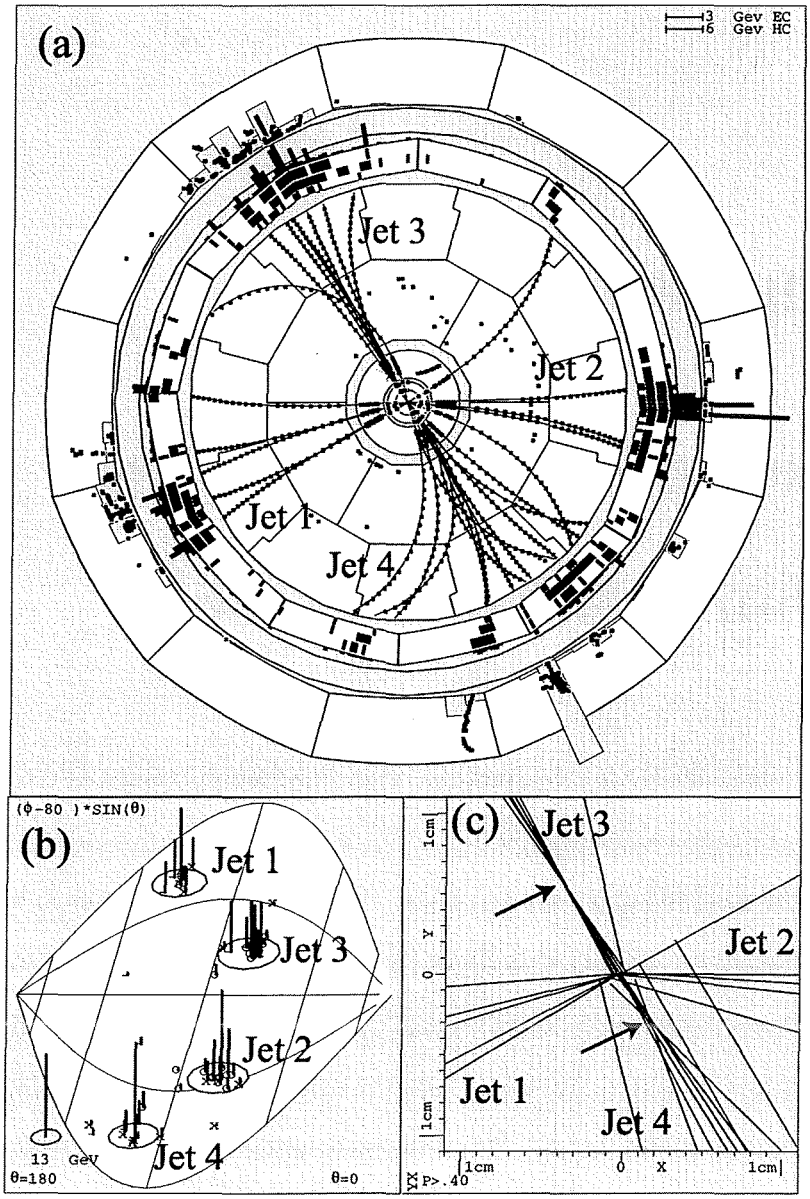

Figure 4.1: An ALEPH event display of a simulated four-jet Higgs signal event at $\sqrt{s} = 183\,\mathrm{GeV}$ and with a Higgs boson mass of $85\,\mathrm{GeV}/c^2$: (a) an xy projection, (b) a $\theta\phi$ projection showing energy flow objects, and (c) an xy projection of the region near the primary vertex (arrows indicate secondary vertices due to b hadron decay). Jets 1 and 2 are light quark jets from the decay of the Z; jets 3 and 4 are b jets from the decay of the Higgs boson.

in Section 4.2, relies upon a series of cuts on various kinematic variables and b-tagging criteria and is referred to as the *cut-based* analysis. A second parallel analysis, described in Section 4.3, relies upon two neural networks which have been trained to recognize the signal process while rejecting the $q\bar{q}$ and W^+W^- background processes. These analyses and their results are combined together using the method described in Chapter 5.

A *reference* Higgs boson mass hypothesis of $M_H = 85\,\mathrm{GeV}/c^2$ for the signal process (corresponding to a production cross section of 0.375 pb at $\sqrt{s} = 183\,\mathrm{GeV}$) is used when discussing analysis performance and showing distributions of discriminating variables; this reference mass is close to the expected experimental sensitivity. Several selection criteria are allowed to vary freely in both the cut-based and neural network analyses. Before the analyses are applied to the data, the values of these criteria are optimized on the basis of the performance (using simulated events) which maximizes the sensitivity to the reference Higgs signal for a combination of all Higgsstrahlung final state analyses; this procedure is described in Chapter 5. The optimized set of event selection criteria is referred to as the *working point*. Despite the optimization for the single reference mass, the event selection criteria are designed to be effective over a sensible range of Higgs boson masses.

The performance quantities (*i.e.*, signal efficiencies and number of events expected from background processes) quoted in this chapter are based upon simulated events samples of 10 000 events for the signal at various Higgs boson masses, 250 000 events for $q\bar{q}(\gamma)$, 150 000 events for W^+W^-, and 30 000

Process	Cross Section (pb)	Sample Size	$\int \mathcal{L}dt$ (fb^{-1})
$e^+e^- \to HZ$ ($M_H = 70\,\mathrm{GeV}/c^2$)	0.821	10 000	12.2
$e^+e^- \to HZ$ ($M_H = 75\,\mathrm{GeV}/c^2$)	0.687	10 000	14.6
$e^+e^- \to HZ$ ($M_H = 80\,\mathrm{GeV}/c^2$)	0.541	10 000	18.5
$e^+e^- \to HZ$ ($M_H = 85\,\mathrm{GeV}/c^2$)	0.375	10 000	26.7
$e^+e^- \to HZ$ ($M_H = 90\,\mathrm{GeV}/c^2$)	0.169	10 000	59.2
$e^+e^- \to q\bar{q}(\gamma)$	102	250 000	2.45
$e^+e^- \to W^+W^-$	15.8	150 000	9.49
$e^+e^- \to ZZ$	2.93	30 000	10.2

Table 4.1: A summary of the samples of simulated events used to evaluate analysis performance. The cross section, number of events in the sample, and the corresponding integrated luminosity are given.

events for ZZ. These samples are summarized in Table 4.1. In the case of the neural network analysis, these samples are independent of the training samples. The analyses are applied to the high energy data sample of $57\,\mathrm{pb}^{-1}$ taken at center-of-mass energies between 181 and 184 GeV described in Section 2.1 and summarized in Table 2.1. The number of expected signal and background events from the simulated samples are normalized to correspond to the integrated luminosity of $57\,\mathrm{pb}^{-1}$ of the data sample.

4.1 Event Preselection, Jet Clustering, and Jet Energy Rescaling

Hadronic events are selected by placing requirements on the number of good charged tracks and the fraction of good charged energy in an event. Events

from the two-photon process have very low particle multiplicity and low visible energy. This is also true of four fermion processes having no hadronic jets. Figure 4.2 shows these quantities for the signal as well as for the background processes. Events are retained if they have at least eight good charged tracks ($N_{\text{charged}} \geq 8$) and if the sum of the energy of all good charged tracks E_{charged} is greater than $0.1\sqrt{s}$. This selection removes virtually all two-photon events and leaves only two- and four-fermion background processes which contain jets from at least two primary quarks.

Radiative Z return ($q\bar{q}\gamma$) events in which initial state radiation (ISR) photons escape into the beam pipe have a large amount of missing momentum along the beam direction P_z and a visible mass M_{vis} near M_Z. Figure 4.3 shows scatter plots of these quantities for the signal process as well as for background processes. Events are required to have $|P_z| < 1.5(M_{\text{vis}} - 90)$ where M_{vis} is in GeV/c^2 and P_z is in GeV/c. This criterion eliminates 72% of the $q\bar{q}\gamma$ background; it is also effective against the remaining four-fermion Zee and Weν background processes which typically have large P_z and lower M_{vis} than signal.

Each event is clustered into jets using the Durham algorithm described in Section 3.1. However, no specific cut on the y_{cut} value is made. Instead the recursive jet clustering algorithm is allowed to proceed until it clusters an event to four jets. Thus the event is said to be *forced* into a four jet topology.

An important quantity is the y_{cut} value for the transition of an event from three to four jets; this is denoted as y_{34} and is a measure of the four-jet character of an event. True two- or three-jet events from the $q\bar{q}(\gamma)$ process

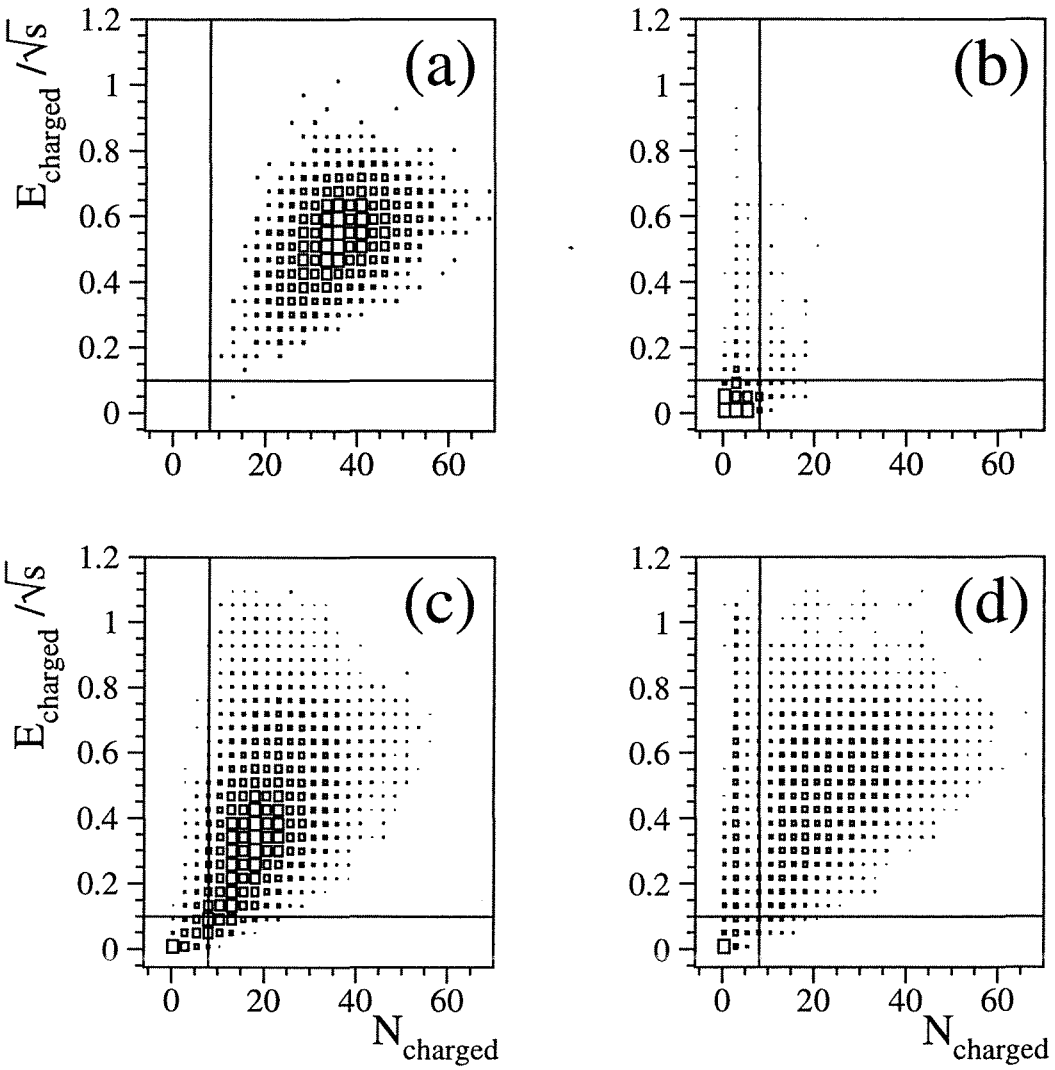

Figure 4.2: Number of good charged tracks N_{charged} versus fraction of good charged energy $E_{\text{charged}}/\sqrt{s}$ in simulated events: (a) signal, (b) $\gamma\gamma$, (c) $q\bar{q}(\gamma)$, (d) four-fermion processes. The solid lines indicate the position of the cuts requiring $N_{\text{charged}} \geq 8$ and $E_{\text{charged}}/\sqrt{s} \geq 0.1$.

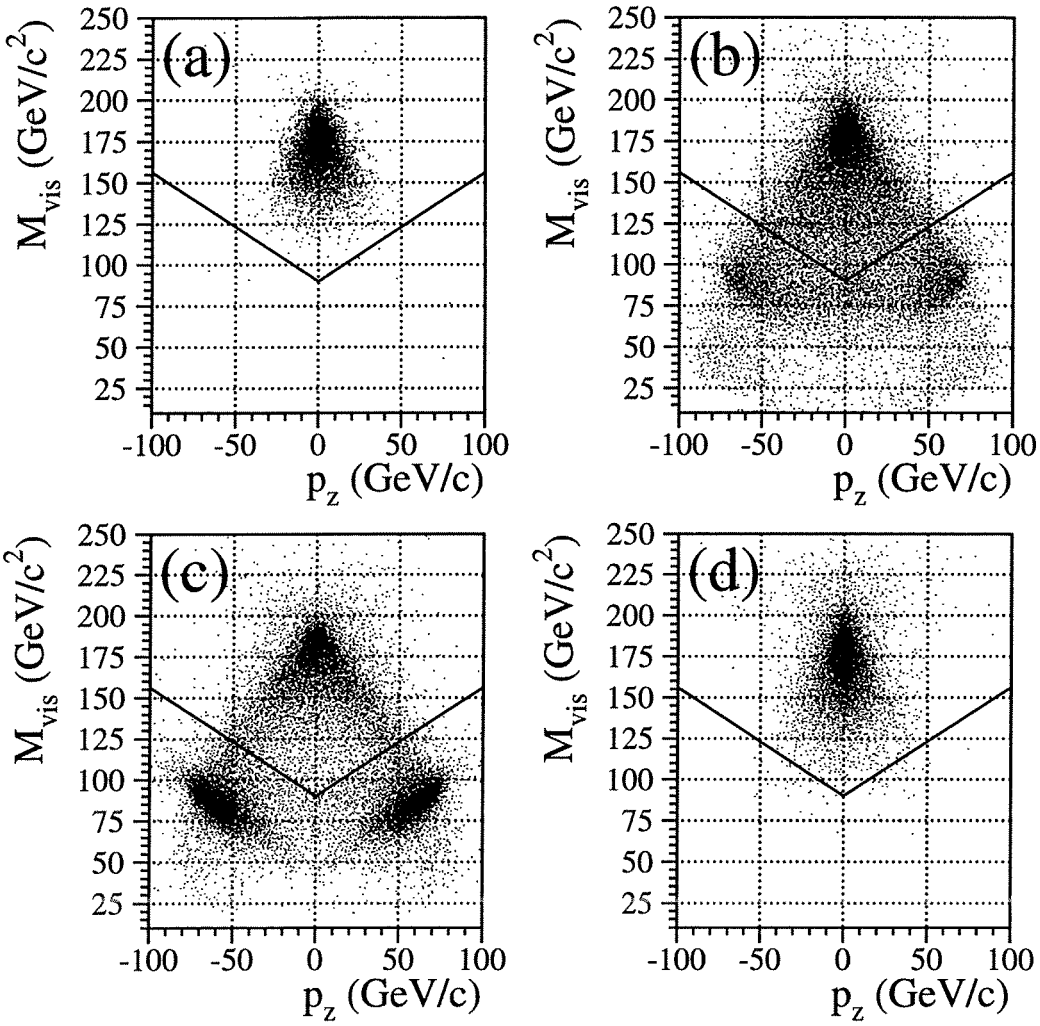

Figure 4.3: Event P_z versus visible mass for (a) signal, (b) four-fermion processes, (c) $q\bar{q}\gamma$, (d) $q\bar{q}$. The solid lines indicate the position of the cut requiring $|P_z| < 1.5(M_{\rm vis} - 90)$.

can be forced to form four jets if the $y_{\rm cut}$ value is small enough; hence, they will have very small y_{34} values. However, events which generally have four energetic primary partons (such as the signal process) are easily forced to form four jets and will have sizeable y_{34} values. Therefore, events with y_{34} values less than 0.004 are rejected. Figure 4.4 shows y_{34} distributions for data and background processes, and the signal. Furthermore, all jets in an event are required to have at least one charged track.

In order to reject remaining $q\bar{q}\gamma$ events in which the ISR photons are detected, the electromagnetic energy content of each jet is determined. Energy flow objects within each jet are flagged as electromagnetic energy if they are identified as electrons, photons, or photon conversions. Furthermore, energy deposits in the ECAL below the TPC acceptance of $|\cos\theta| > 0.95$, LCAL, SiCAL, or HCAL behind ECAL module cracks, are also flagged as electromagnetic energy. The largest value of the fraction of electromagnetic energy with respect to the total jet energy contained in any one degree cone around each energy flow object in a jet $(X_\gamma)_{\rm max}$ must be smaller than 0.80. Distributions of this quantity are shown in Figure 4.5. With the $(X_\gamma)_{\rm max}$ criterion and other requirements described above, $(99.8 \pm 0.1(\text{stat.}))\%$ of the radiative Z return events are eliminated.

The measurements of the jet energies can be improved by using the method of Wu described in Ref. [133] which makes use of energy-momentum conservation within an event. For each jet in a four-jet event, an energy

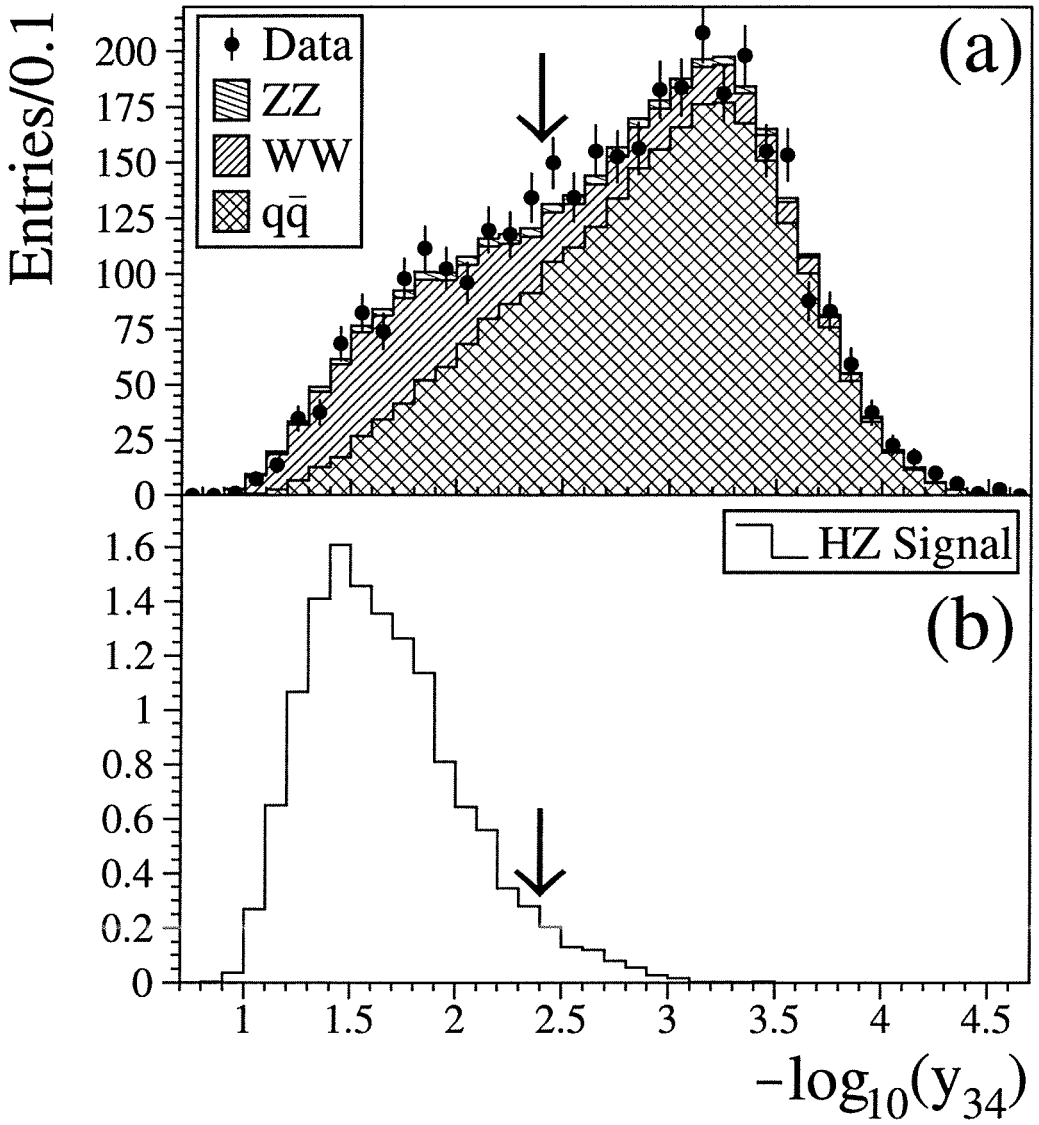

Figure 4.4: Distributions of $-\log_{10} y_{34}$ after the N_{charged}, E_{charged}, $|P_z|$, and M_{vis} criteria are applied: (a) data and simulated background events (b) signal for $M_{\text{H}} = 85\,\text{GeV}/c^2$. The arrows show the position of the cut requiring $y_{34} > 0.004$.

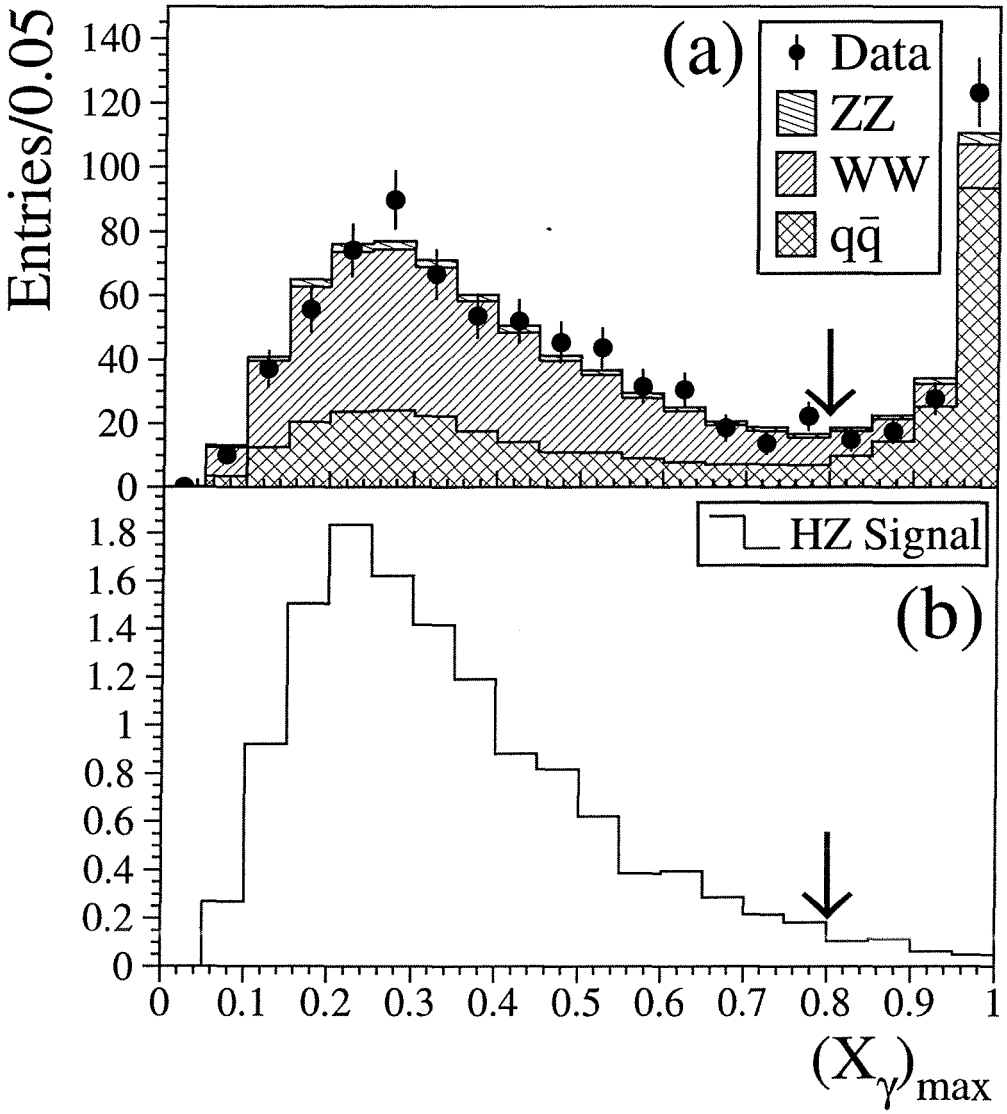

Figure 4.5: Distributions of $(X_\gamma)_{\rm max}$ after the $N_{\rm charged}$, $E_{\rm charged}$, $|P_z|$, and $M_{\rm vis}$ criteria are applied: (a) data and simulated background events (b) signal for $M_{\rm H} = 85\,{\rm GeV}/c^2$. The arrows show the position of the cut requiring $(X_\gamma)_{\rm max} < 0.80$.

rescaling factor α_i is determined:

$$\begin{pmatrix} p_{1x} & p_{2x} & p_{3x} & p_{4x} \\ p_{1y} & p_{2y} & p_{3y} & p_{4y} \\ p_{1z} & p_{2z} & p_{3z} & p_{4z} \\ E_1 & E_2 & E_3 & E_4 \end{pmatrix} \begin{pmatrix} \alpha_1 \\ \alpha_2 \\ \alpha_3 \\ \alpha_4 \end{pmatrix} = \begin{pmatrix} 0 \\ 0 \\ 0 \\ \sqrt{s} \end{pmatrix}$$

where p_{ij} is the jth Cartesian component of the observed momentum for the ith jet, E_i is the observed energy of the ith jet, and α_i is a energy scaling factor for the ith jet. The measured jet velocities (*i.e.*, $\vec{\beta}_i = \vec{p}_i/E_i$) are preserved in this process. In this way, it is possible to compensate partially for intrinsic detector resolutions and any undetected particles (*e.g.*, neutrinos from semileptonic b decays). The procedure fails for roughly 5% of the events due to extreme event energy-momentum imbalance forcing one of α_i values to be negative. In these cases, the original measured jet energies and momenta are used in the analysis.

The selection criteria and procedures discussed above are collectively referred to as the *preselection* throughout this chapter. The efficiency for signal and expected background at various stages of the preselection is presented in Table 4.2.

Criteria	Signal Efficiency (%)	$q\bar{q}(\gamma)$ Total (Z return)	W^+W^-
$E_{ch} \geq 0.1\sqrt{s}$, $N_{ch} \geq 8$	99.9 ± 0.02	5146 ± 5 (3471 ± 4)	799 ± 1
$\|P_z\| < 1.5(M_{vis} - 90)$	98.6 ± 0.1	2623 ± 8 (1083 ± 5)	697 ± 2
$y_{34} > 0.004$	93.4 ± 0.3	283 ± 3 (76 ± 2)	463 ± 2
$(X_\gamma)_{max}$	91.0 ± 0.4	199 ± 3 (7.4 ± 0.5)	393 ± 2

Criteria	ZZ Total (on-shell)	Weν	Zee
$E_{ch} \geq 0.1\sqrt{s}$, $N_{ch} \geq 8$	133 ± 0.4 (13.9 ± 0.1)	21.6 ± 0.2	121 ± 0.7
$\|P_z\| < 1.5(M_{vis} - 90)$	102 ± 0.5 (10.4 ± 0.1)	1.5 ± 0.1	36.5 ± 0.5
$y_{34} > 0.004$	34.9 ± 0.4 (9.1 ± 0.2)	0.28 ± 0.04	9.7 ± 0.3
$(X_\gamma)_{max}$	27.1 ± 0.4 (8.1 ± 0.2)	0.04 ± 0.02	1.3 ± 0.1

Table 4.2: A breakdown of signal efficiency (for $M_H = 85\,\mathrm{GeV}/c^2$) and the number of expected Standard Model background events (for an integrated luminosity of $57\,\mathrm{pb}^{-1}$) at various stages of the preselection. The uncertainties are statistical.

4.2 Event Selection with Cuts

4.2.1 Four-Jet Quality Cuts

After the preselection, almost all of the radiative Z returns ($q\bar{q}\gamma$) have been rejected. A frequent topology from the surviving $q\bar{q}$ background is a "three-against-one" event where gluon bremsstrahlung from one of the primary quarks results in a system of three jets close together in angle recoiling against a single quark jet. An event display of a simulated $q\bar{q}$ event illustrates this topology in Figure 4.6. To eliminate this background, events in which the sum of the smallest four inter-jet angles Θ is less than 350° are rejected. Distributions of this quantity are shown in Figure 4.7.

For Higgs boson masses close to the HZ production threshold of $\sqrt{s} - M_Z$, the characteristic signal topology is two pairs of back-to-back jets. The minimum sum of the cosines of di-jet angles in an event is a good measure of this topology. The quantity $\gamma = \min(\cos\theta_{ij} + \cos\theta_{kl})$ (minimized over all possible permutations of i, j, k, l) tends to -2 as the Higgs boson mass approaches threshold. Events are required to have γ less than -1.3. Figure 4.8 shows the distributions of γ for data and simulated background processes as well as for simulated signal with various Higgs boson masses to illustrate the Higgs boson mass dependence of this quantity.

Table 4.3 shows the number of observed events in data and the number of expected events from background as well as the signal efficiency as the above criteria are applied.

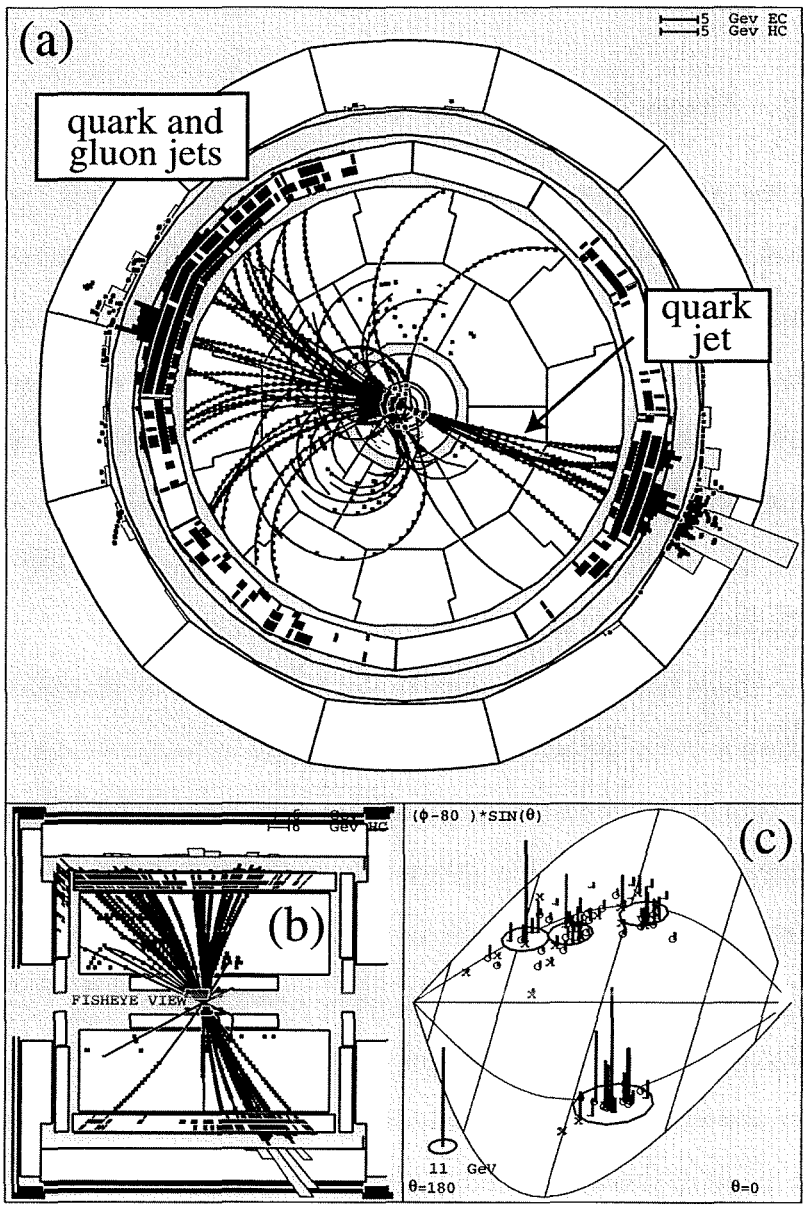

Figure 4.6: An ALEPH event display of a simulated $q\bar{q}$ background event illustrating the "three-against-one" background topology. The event displays show (a) an xy projection, (b) an rz projection, and (c) a $\theta\phi$ projection showing energy flow objects clustered into jets.

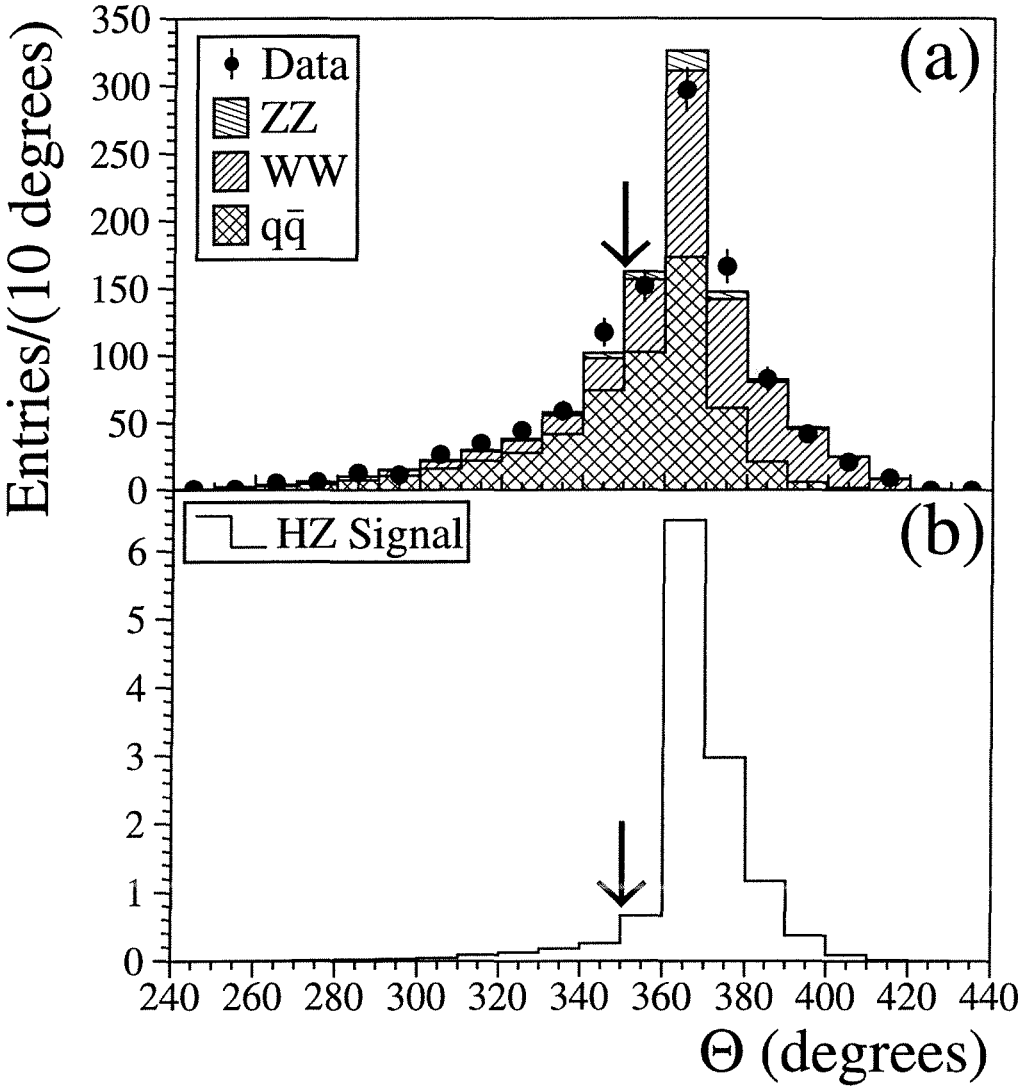

Figure 4.7: Distributions of Θ at the preselection level for (a) data and simulated background processes, and (b) signal for $M_{\mathrm{H}} = 85\,\mathrm{GeV}/c^2$. The arrows show the position of the cut requiring $\Theta > 350°$.

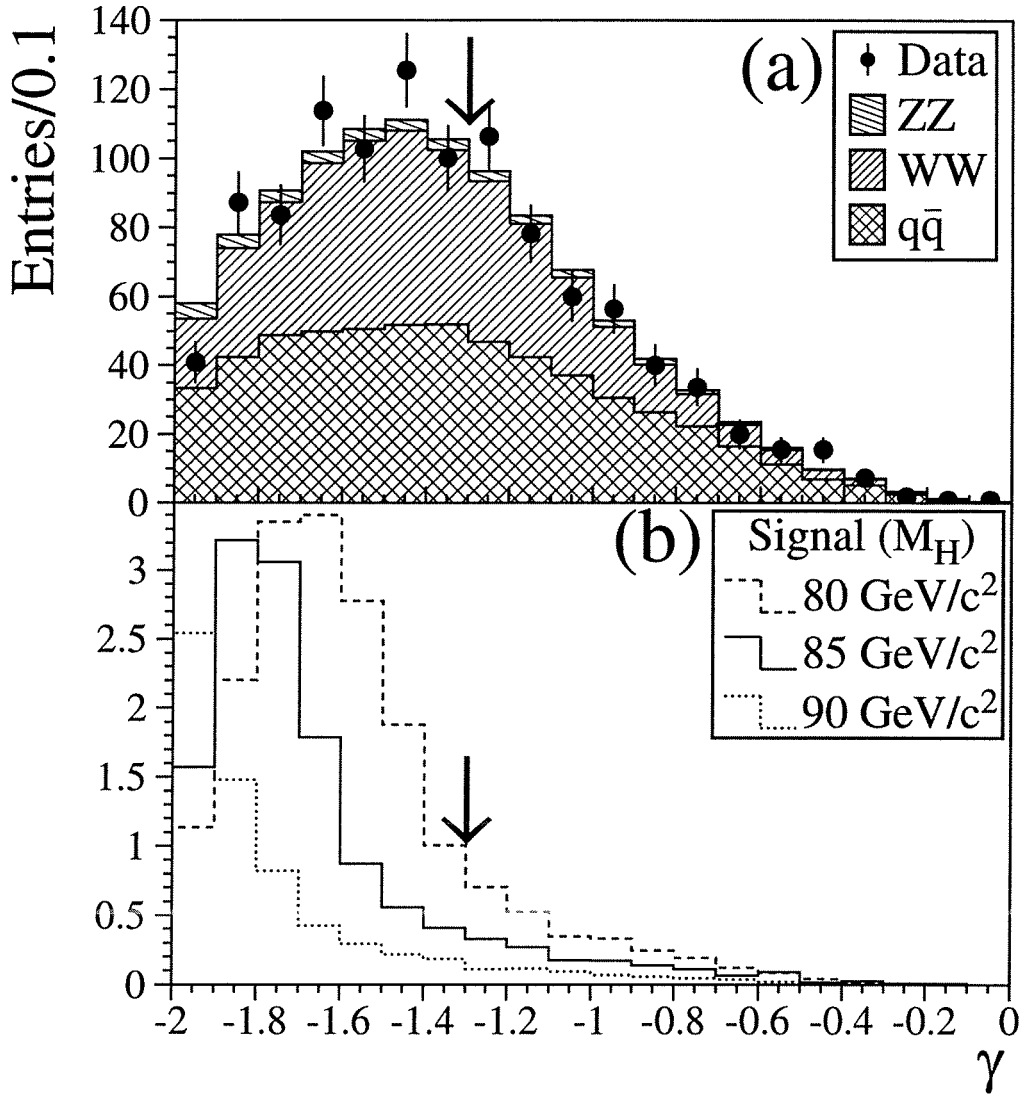

Figure 4.8: Distributions of γ at the preselection level for (a) data and simulated background processes, and (b) signal for $M_{\mathrm{H}} = 80,\ 85,$ and $90\,\mathrm{GeV/c^2}$. The arrows show the position of the cut requiring $\gamma < -1.3$.

Selection Criteria	Number Observed	Number Expected	Signal Efficiency(%)	Number Signal
Preselection	653	620 ± 4	91.0 ± 0.4	12.45 ± 0.05
$+\,\Theta > 350°$	497	478 ± 3	85.2 ± 0.4	11.66 ± 0.05
$+\,\gamma < -1.3$	367	342 ± 2	79.5 ± 0.5	10.88 ± 0.07

Table 4.3: A breakdown of the number of observed events in data, number of expected events from Standard Model background processes, the efficiency for signal and the corresponding number of signal events expected for $M_{\mathrm{H}} = 85\,\mathrm{GeV}/c^2$ at various stages of the cut-based analysis. The uncertainties are statistical only.

4.2.2 b-Tagging and Jet Pairing

The neural network b-tag described in Section 3.4 is applied to the four jets in each event. The output of the neural network b-tag is denoted as η_i for the ith jet in each event. Indices 1 and 2 label jets hypothesized to be from a Z boson candidate while indices 3 and 4 label the jets from a Higgs boson candidate. Figure 4.9(a) shows that, for the correct jet pairing,[1] there is a prominent peak at (1.0, 1.0) in the plane of η_3 versus η_4; this is not the case for the $\mathrm{q\bar{q}}$, $\mathrm{W^+W^-}$, and ZZ background events which survive the preselection and jet quality criteria.

In order to be considered a Higgs boson candidate event, at least one of the six possible jet pairing permutations in an event must pass one of the two following sets of criteria which are labelled A and B. The cut values of the

[1]The term *correct jet pairing* refers to the single permutation which correctly assigns each of the four jets to the Higgs and the Z bosons determined using Monte Carlo truth information. There are six possible jet pairing permutations per event.

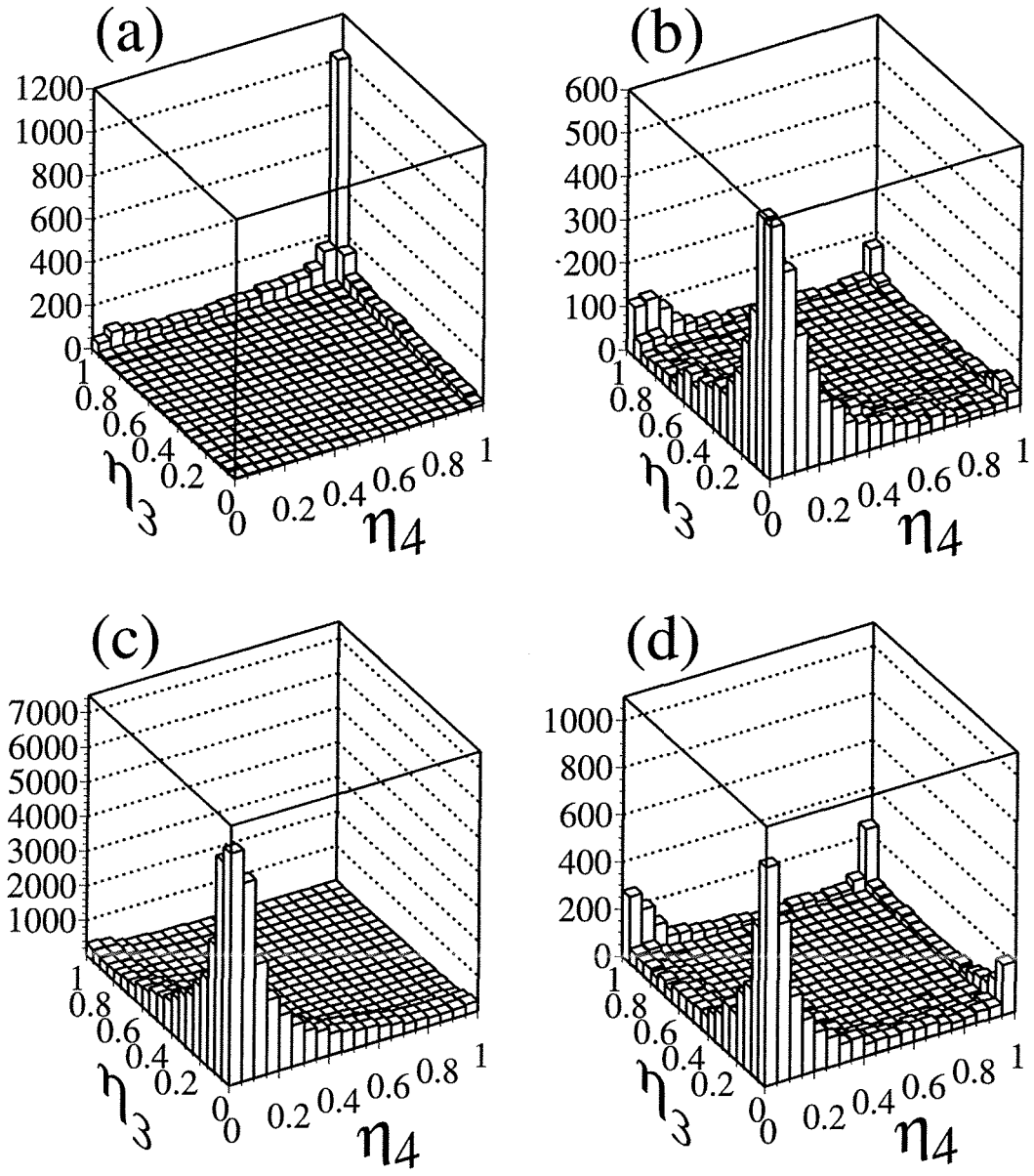

Figure 4.9: Distributions of the neural network b-tag output for the Higgs boson candidate jets (jets 3 and 4) for (a) signal, (b) $q\bar{q}$, (c) W^+W^-, and (d) ZZ.

selection criteria indicated with a dagger (†) below are allowed to vary when determining the best performance of the analysis using simulated events for different signal efficiencies/background rejection points.

(A) The Scenario for Two b jets

This set of criteria is designed to select $HZ \rightarrow b\bar{b}q\bar{q}$ final states where the $q\bar{q}$ pair are not b quarks and the $b\bar{b}$ pair originate from the Higgs boson. This accounts for 72% of the total four-jet final state.

The value of the cut on y_{34} is tightened from its preselection value. Furthermore, requirements are placed on the lower bound for the di-jet invariant mass of the Z candidate jets M_{12} and of the Higgs boson candidate jets M_{34}.

The Higgs boson candidate jets are required to be well-b-tagged. A lower bound is placed on the minimum of the neural network b-tag outputs for the two Higgs boson candidate jets. A requirement is also placed on the product of the b-tag values for the two jets; this allows the b-tagging requirement to be relaxed on one jet when the other jet is extremely well-b-tagged.

The selection criteria are

- $y_{34} > 0.008$;
- $M_{12} > 78\,\mathrm{GeV}/c^2$ (Z candidate);†

- $M_{34} > 55\,\mathrm{GeV}/c^2$ (Higgs boson candidate);
- $\min(\eta_3, \eta_4) > 0.30$;†
- $(1-\eta_3)(1-\eta_4) < 6.0 \times 10^{-3}$.†

Figures 4.10 and 4.11 show the distributions for M_{12} and M_{34} respectively. The signal distributions for both of these quantities are also shown for various Higgs boson masses (*i.e.*, $M_{\mathrm{H}} = 80$, 85, and $90\,\mathrm{GeV}/c^2$). The resolution for both M_{12} and M_{34} degrades slightly as the Higgs boson mass increases; this is due to a threshold effect related to the jet energy rescaling [134].[2]

Distributions of the b-tagging based quantities discussed above are shown in Figures 4.12 and 4.13; their strong discriminating power between signal and background is apparent.

(B) The Scenario for Four-b jets

The $\mathrm{HZ} \rightarrow \mathrm{b\bar{b}b\bar{b}}$ final state accounts for 20% of the total four jet final state. In terms of flavor composition, it has much less background and can be selected by requiring a well-b-tagged *event*. A linear discriminant of the sum of the neural network b-tag for the four jets and the value of y_{34} gives better separation between signal and background than cutting on these quantities individually.

[2]Near threshold, di-jet pairs are back-to-back; hence the resulting four-jet system occupies a plane. This effectively causes the loss of one of the constraints in the rescaling procedure.

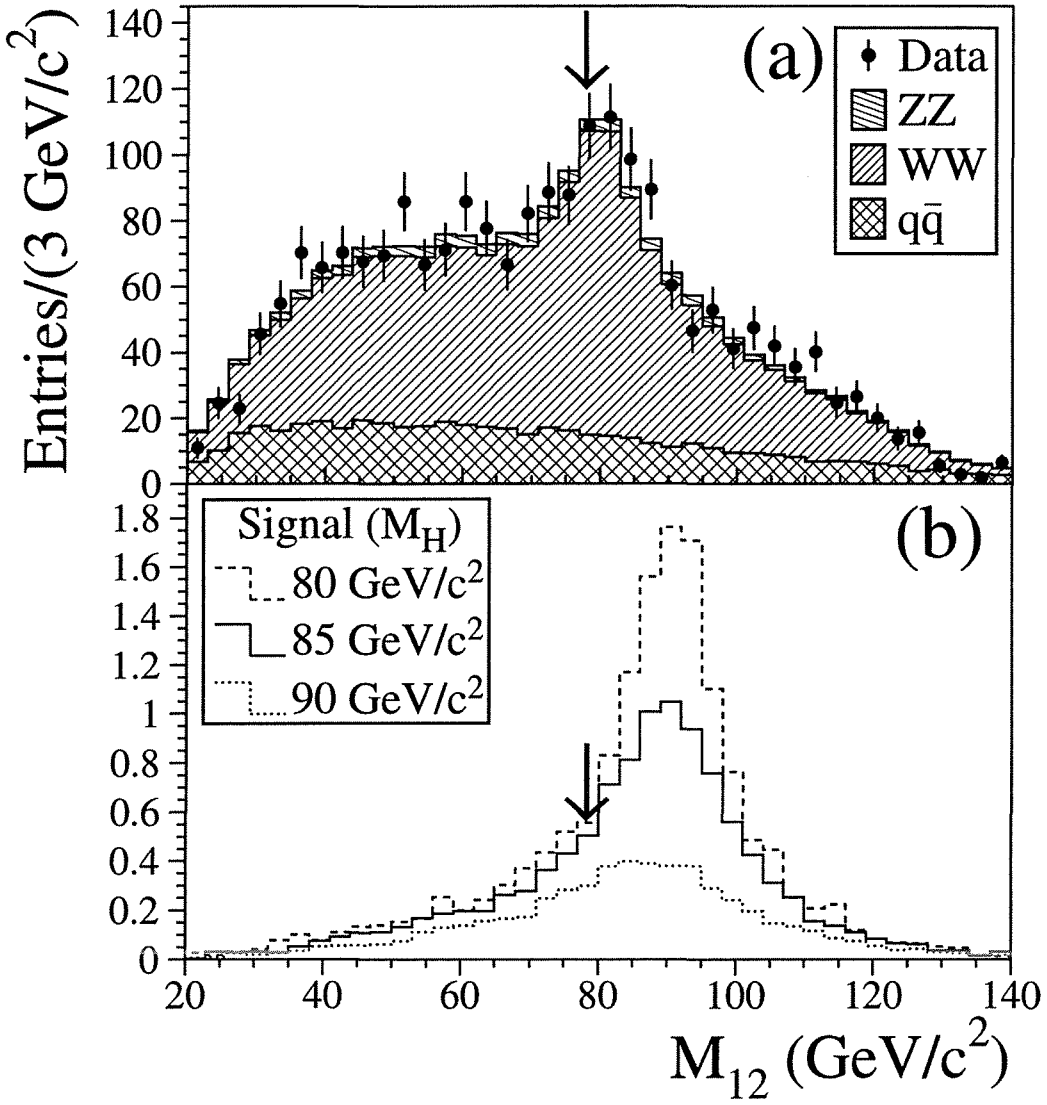

Figure 4.10: Distributions of M_{12} (Z candidate mass) at the preselection level for (a) data and simulated background processes, and (b) signal for $M_{\mathrm{H}} = 85\,\mathrm{GeV}/c^2$. The arrows show the position of the cut requiring $M_{12} > 78\,\mathrm{GeV}/c^2$. All six jet pairing combinations per event are used for the distributions for data and simulated background; only the correct jet pairing is used for the signal.

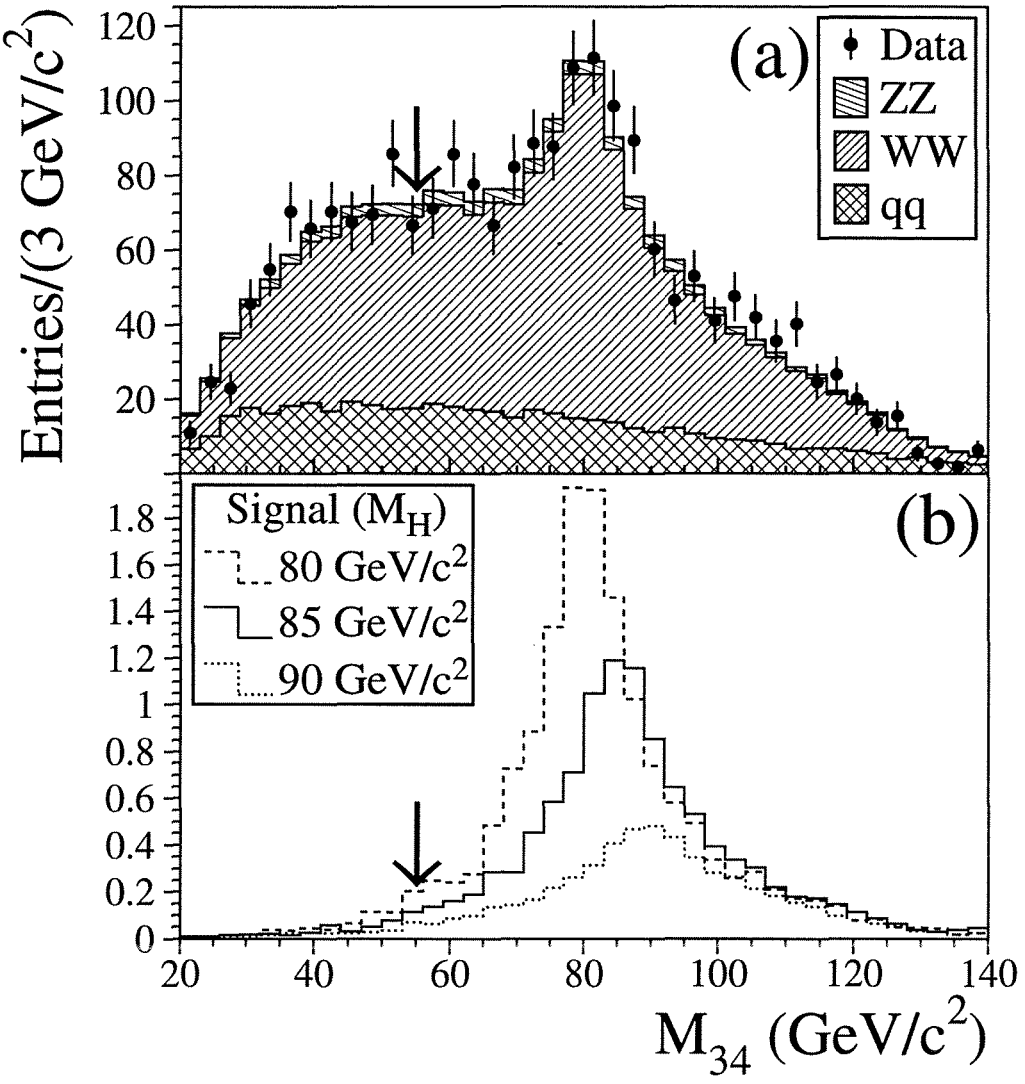

Figure 4.11: Distributions of M_{34} (Higgs boson candidate mass) at the preselection level for (a) data and simulated background processes, and (b) signal for $M_{\mathrm{H}} = 80, 85,$ and $90\,\mathrm{GeV}/c^2$. The arrows show the position of the cut requiring $M_{34} > 55\,\mathrm{GeV}/c^2$. All six jet pairing combinations per event are used for the distributions for data and simulated background; only the correct jet pairing is used for the signal.

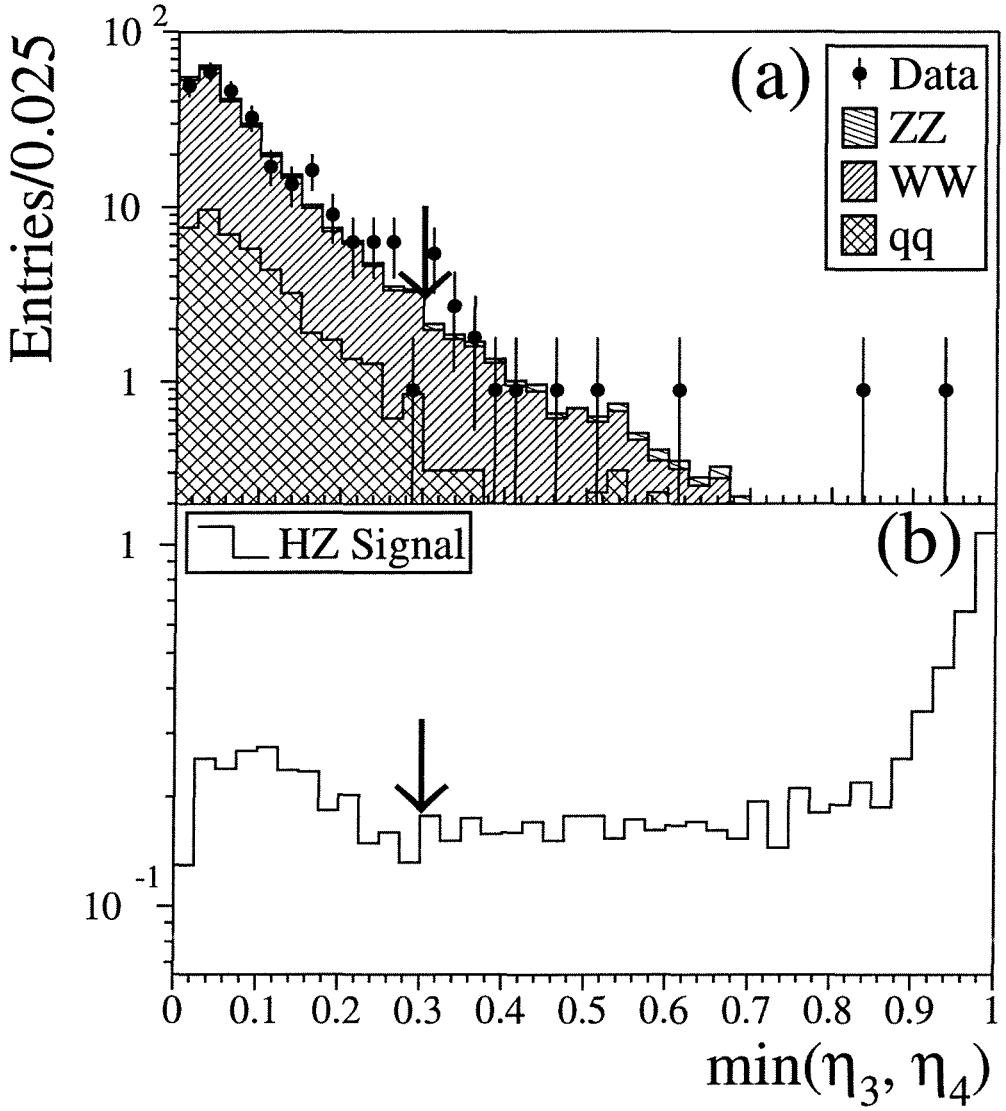

Figure 4.12: Distributions of $\min(\eta_3, \eta_4)$ at the preselection level for (a) data and simulated background processes, and (b) signal for $M_{\mathrm{H}} = 85\,\mathrm{GeV}/c^2$. The arrows show the position of the cut requiring $\min(\eta_3, \eta_4) > 0.30$. All six jet pairing combinations per event are used for the distributions for data and simulated background; only the correct jet pairing is used for the signal.

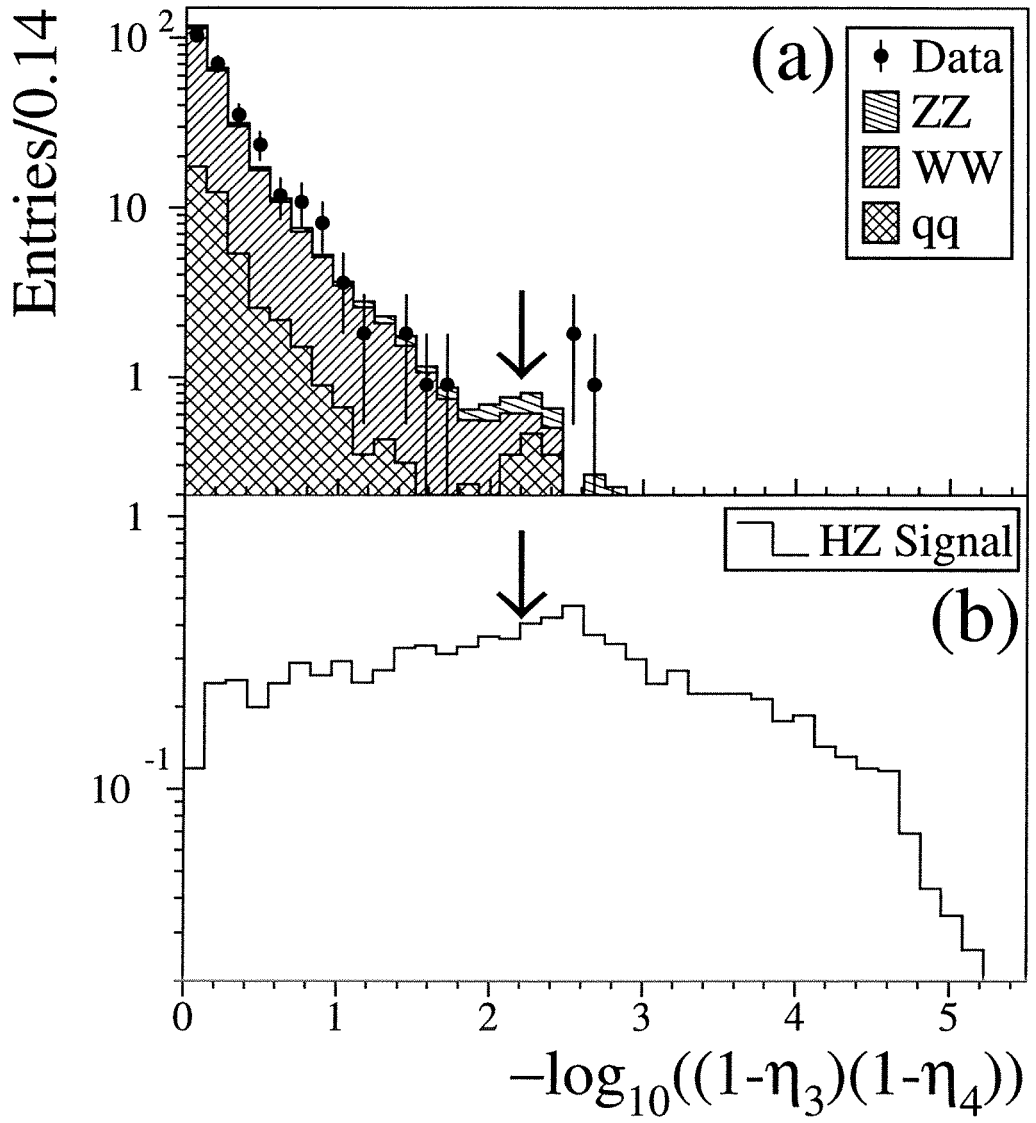

Figure 4.13: Distributions of $-\log_{10}((1-\eta_3)(1-\eta_4))$ at the preselection level for (a) data and simulated background processes, and (b) signal for $M_{\mathrm{H}} = 85\,\mathrm{GeV}/c^2$. The arrows show the position of the cut requiring $(1-\eta_3)(1-\eta_4) < 6.0 \times 10^{-3}$. All six jet pairing combinations per event are used for the distributions for data and simulated background; only the correct jet pairing is used for the signal.

Background events are concentrated at low values of y_{34} and the discriminant will impose a tighter b-tagging cut on $\sum_{i=1}^{4}\eta_i$ than for higher values of y_{34}. The coefficients in the linear discriminant are chosen on the basis of the Fisher linear discriminant method [135]. Hence, the selection consists of a single criterion:

- $\kappa = 9.5y_{34} + \sum_{i=1}^{4}\eta_i > 2.9.^{\dagger}$

Figure 4.14 shows distributions of κ for simulated background and signal events.

Jet pairing permutations are selected if they pass either of the two sets of selection criteria (A or B). If more than one jet pairing of a given event passes this selection, the one with M_{12} closest to $91.2\,\mathrm{GeV}/c^2$ is chosen.

4.2.3 Performance

As described in Section 4.2.2, several selection criteria are allowed to vary to determine the performance of the analysis. A scan over a four-dimensional grid of selection criteria is performed to find the minimal expected background for a given efficiency for the signal. This grid corresponds to the requirements placed on the four free selection criteria denoted with (†) in Section 4.2.2; the scan range corresponds to cut values of 62 to $88\,\mathrm{GeV}/c^2$ for M_{34}, 0.05 to 0.95 for $\min(\eta_3, \eta_4)$, 2.5×10^{-4} to 1.025×10^{-2} for $(1-\eta_3)(1-\eta_4)$, and 2.5 to 4.25 for κ.

The signal efficiency is defined as the number of simulated Higgsstrahlung

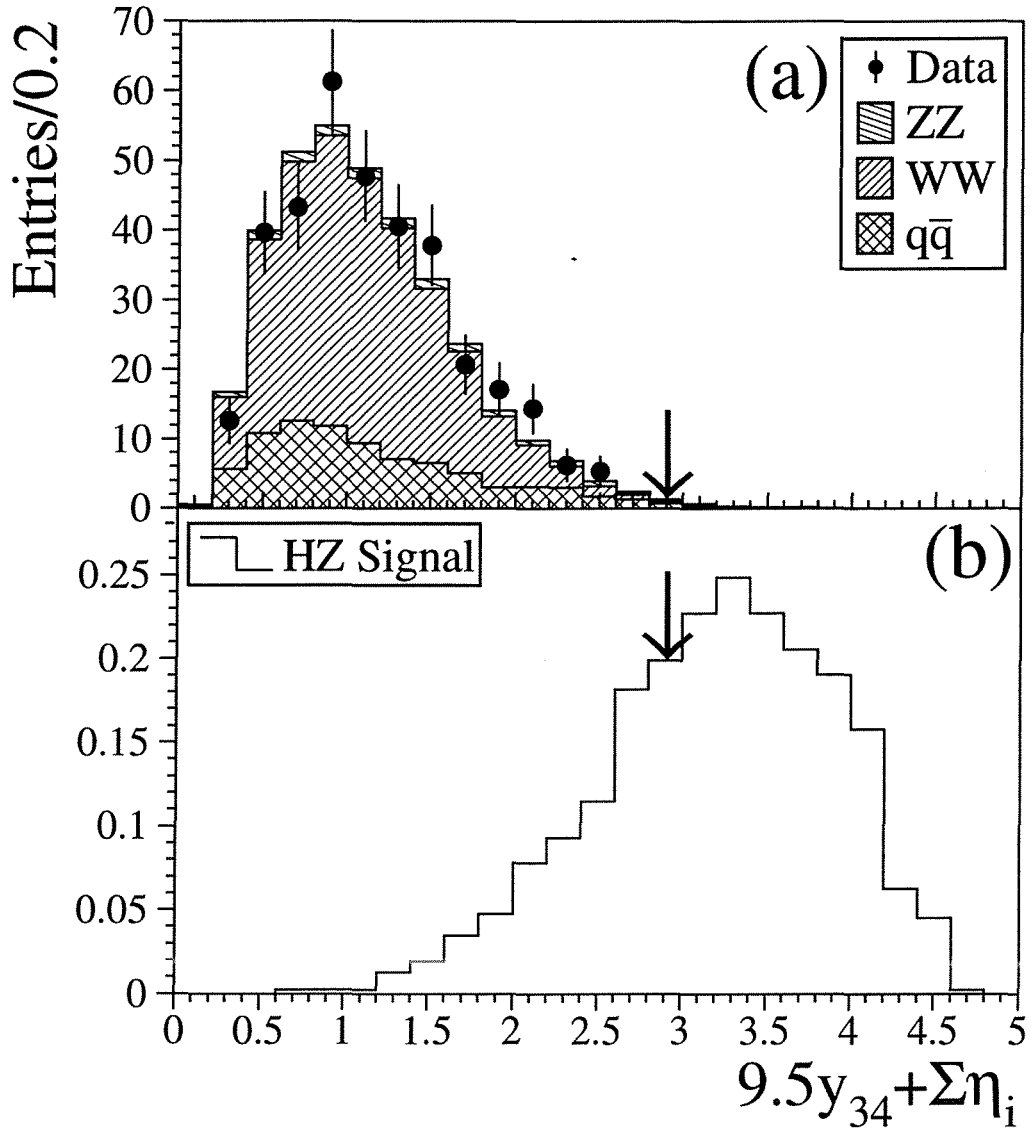

Figure 4.14: Distributions of $9.5y_{34} + \sum_{i=1}^{4} \eta_i$ at the preselection level for (a) simulated background processes, and (b) signal with $M_{\mathrm{H}} = 85\,\mathrm{GeV}/c^2$. The arrows show the position of the cut requiring $\kappa = 9.5y_{34} + \sum_{i=1}^{4} \eta_i > 2.9$. All six jet pairing combinations per event are used for the distributions for data and simulated background; only the correct jet pairing is used for the signal.

events passing the selection criteria which have both the Higgs boson decaying to hadrons (*i.e.*, $H \rightarrow b\bar{b}$, $q\bar{q}$, or gg) and the Z boson decaying to hadrons (*i.e.*, $Z \rightarrow b\bar{b}$ or $q\bar{q}$) divided by the total number of simulated Higgsstrahlung events in the sample which have both the Higgs and Z bosons decaying to hadrons. The number of expected background events is determined using the efficiency for simulated background events to pass the selection criteria multiplied by the integrated luminosity of the data sample of $57\,\mathrm{pb}^{-1}$ and the production cross section for each of the background processes described in Section 1.3.2.

Figure 4.15 shows the performance of the cut-based analysis in terms of efficiency for a signal with $M_{\mathrm{H}} = 85\,\mathrm{GeV}/c^2$ versus the number of events expected from Standard Model background processes. The expected background is broken down into its contribution from $q\bar{q}$, W^+W^-, and ZZ processes. An arrow denotes the working point determined using the method summarized in Chapter 5. This working point corresponds to a signal efficiency of $(34.0 \pm 0.6)\%$ (*i.e.*, 4.65 ± 0.08 signal events expected) for $M_{\mathrm{H}} = 85\,\mathrm{GeV}/c^2$ and an expected background of 3.45 ± 0.22 events (1.52 ± 0.19 $q\bar{q}$, 0.53 ± 0.05 W^+W^-, and 1.40 ± 0.09 ZZ);[3] the uncertainties are statistical only. The flavor composition of the background is given in Table 4.4.

The signal efficiency is dependent upon the Higgs boson mass hypoth-

[3]No events survive the selection criteria from the simulated samples of Weν and Zee. A 95% confidence level upper limit on the expected number of events can be set at 0.02 events for each process.

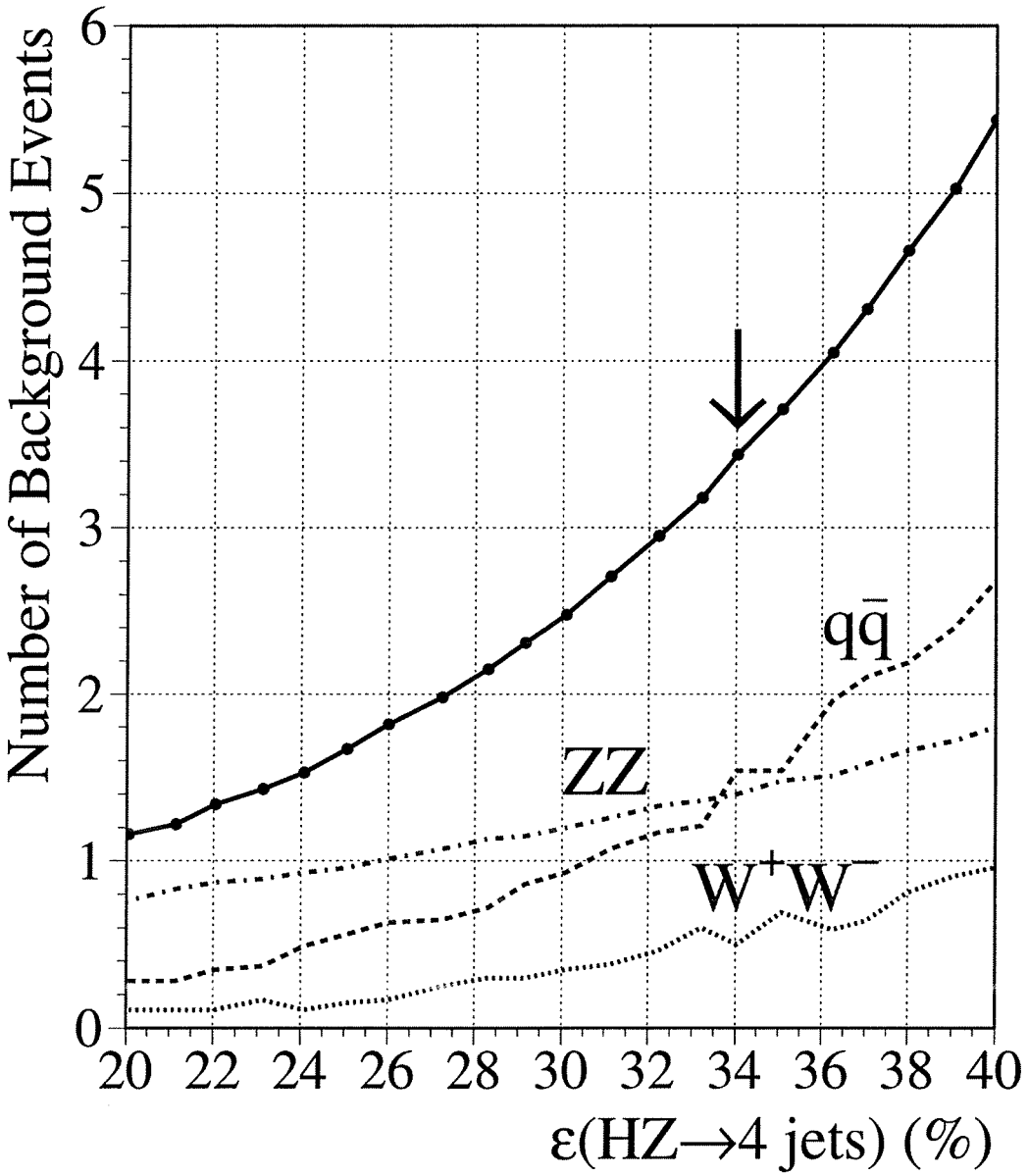

Figure 4.15: The performance of the cut-based analysis in terms of efficiency for a signal with $M_{\mathrm{H}} = 85\,\mathrm{GeV}/c^2$ versus the number of events expected from Standard Model background processes for an integrated luminosity of $57\,\mathrm{pb}^{-1}$. The background is broken down into its contribution from $\mathrm{q\bar{q}}$, $\mathrm{W^+W^-}$, and ZZ processes. The arrow denotes the working point determined using the method summarized in Chapter 5.

Background Composition					
$q\bar{q}$		W^+W^-		ZZ	
1.52 ± 0.19 Events		0.53 ± 0.05 Events		1.40 ± 0.09 Events	
$b\bar{b}gg$	53%	$c\bar{s}\bar{c}s$	53%	$b\bar{b}q\bar{q}$	53%
$b\bar{b}q\bar{q}$	22%	$c\bar{s}u\bar{d}$	27%	$b\bar{b}c\bar{c}$	23%
$b\bar{b}c\bar{c}$	12%	$c\bar{s}\bar{c}d$	5%	$b\bar{b}b\bar{b}$	20%
$b\bar{b}b\bar{b}$	5%	$c\bar{s}\bar{c}b$	4%	$c\bar{c}c\bar{c}$	2%
$c\bar{c}gg$	5%	$c\bar{b}u\bar{d}$	4%	$c\bar{c}q\bar{q}$	1%
Other	3%	Other	7%	Other	1%

Table 4.4: A breakdown of the flavor composition of the expected Standard Model background processes after the cut-based selection criteria are applied. Charge-conjugation is implied for the W^+W^- modes.

esis used for the simulated events. Figure 4.16 shows the signal efficiency evaluated using several simulated samples with different Higgs boson mass hypotheses. As the Higgs boson masses decreases, the selection criteria for γ and M_{34} begin to eliminate more of the signal and the efficiency is reduced. As the Higgs boson mass approaches the HZ production threshold, the degraded M_{12} and M_{34} resolutions cause some of the signal to fall below the M_{12} and M_{34} requirements, thus reducing the efficiency slightly.

Roughly 50% of the signal events pass through the two b-jet scenario (A) branch only, 33% pass through the four b-jet scenario (B) branch only, and the remaining events (roughly 17%) pass both branches (A and B). A detailed breakdown in terms of four-jet final state composition and event selection branches is given in Table 4.5.

A large fraction of events, roughly 94%, which pass only the two b jet sce-

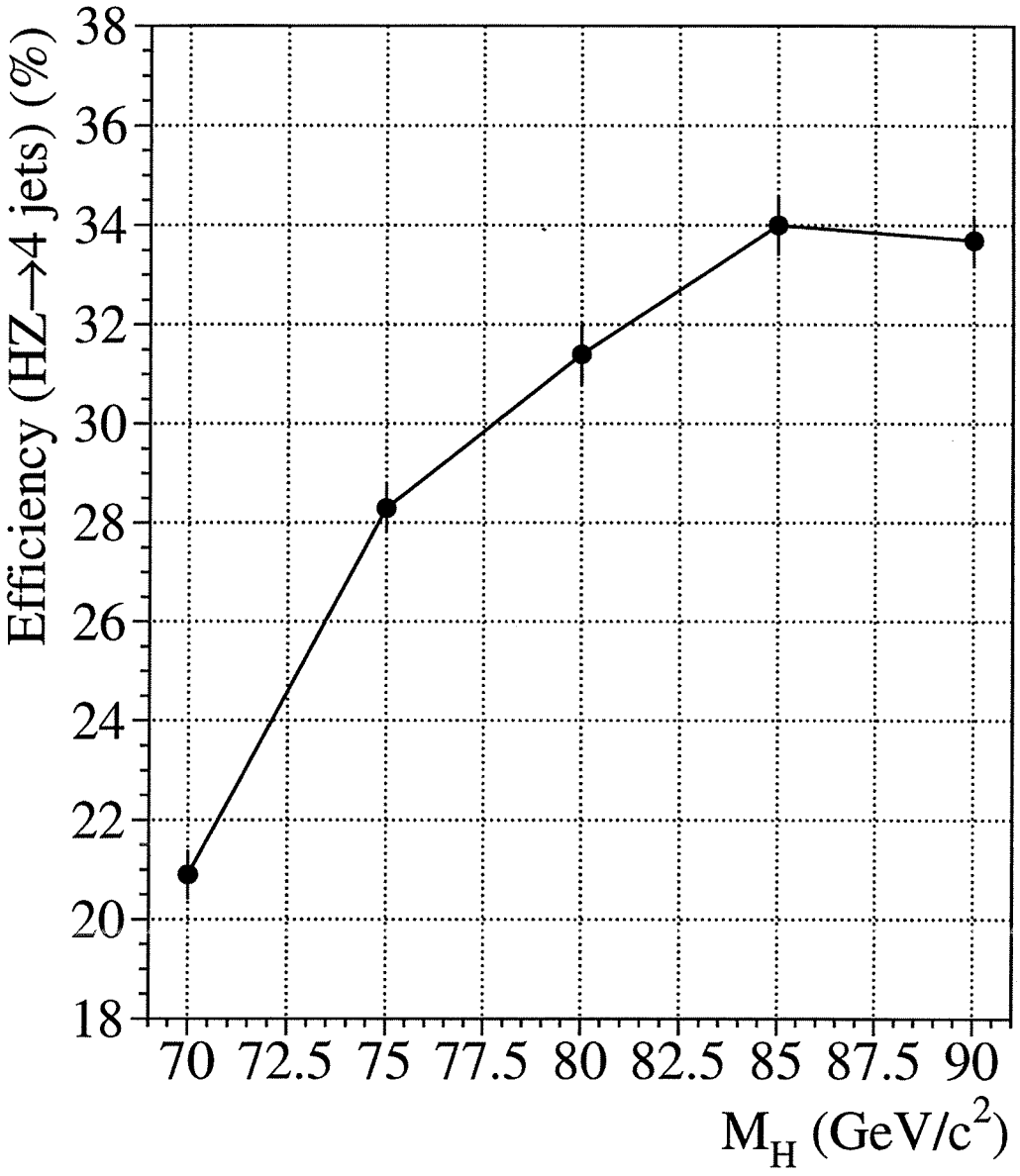

Figure 4.16: The working point signal efficiency for various Higgs boson mass hypotheses. The error bars indicate the statistical uncertainty.

Branch	$\epsilon(HZ \to 4jets)$	$\epsilon(HZ \to b\bar{b}q\bar{q})$	$\epsilon(HZ \to b\bar{b}b\bar{b})$	$\epsilon(HZ \to (q\bar{q}, gg)(q\bar{q}, b\bar{b}))$
A Only	16.4 ± 0.4	15.0 ± 0.4	1.1 ± 0.1	0.3 ± 0.1
B Only	11.1 ± 0.4	4.2 ± 0.3	6.6 ± 0.3	0.3 ± 0.1
A and B	6.5 ± 0.3	2.2 ± 0.2	4.2 ± 0.3	0.08 ± 0.04
A or B	34.0 ± 0.6	21.4 ± 0.5	11.9 ± 0.4	0.7 ± 0.1

Table 4.5: A breakdown of signal efficiency in percent for the cut-based analysis in terms of four-jet final state composition (where $q\bar{q}$ refers to a non-b quark pair) and two branches of the analysis (*i.e.*, the two b jet scenario branch A and the four b jet scenario branch B). The uncertainties are statistical only.

nario branch (A) have only one jet-pairing combination which satisfies the selection criteria; the remaining 6% of the selected events have two jet-pairing combinations. All six possible jet pairing combinations are selected for events passing only the four b jet scenario branch (B) since none of the selection criteria are based upon jet pairings. This is also true for events passing both of the two branch criteria. As described in Section 4.2.2, if more than one jet pairing of a given event passes this selection, the one with M_{12} closest to $91.2\,\mathrm{GeV}/c^2$ is chosen. The overall correct jet pairing[4] fraction is 58%; the fraction is 86%, 19%, and 52% for events passing only the two b jet scenario (A) branch, only the four b jet scenario (B) branch, and both of the branches, respectively.

[4]The rigorous assignment of quarks from the Higgs and Z bosons at the Monte Carlo truth level to reconstructed jets is not possible. The criterion used here is the jet closest in angle to a given quark; however, gluon bremsstrahlung before the hadronization process can result in changes in the trajectories of primary quarks and subsequent jet-quark misassignment. This results in a usable but not a perfect tag of the correct jet pairing.

For the correct jet-pairing in simulated signal events, the di-jet mass of the Higgs boson candidate jets M_{34} is centered around the nominal Higgs boson mass used in the simulation, but the resolution is poor. The correct jet-pairing M_{34} distribution has an RMS of $8.3\,\mathrm{GeV}/c^2$. A better measure of the Higgs boson mass is the quantity $M_{34} + M_{12} - 91.2\,\mathrm{GeV}/c^2$. This quantity is referred to as the *reconstructed* Higgs boson mass and is used in the confidence level calculation method described in Chapter 5; the RMS for correct jet-pairings is $5.1\,\mathrm{GeV}/c^2$. This is due to the anti-correlated nature of M_{34} and M_{12} and the jet energy rescaling procedure. Distributions of M_{34} and the reconstructed Higgs boson mass are shown in Figure 4.17.

4.3 Event Selection with Neural Networks

The b-tagging scheme described in Chapter 3 demonstrates that neural networks are able to combine multiple discriminating variables together in an effective and efficient manner. It is natural to extend this approach to an entire event selection in which multiple variables are available but are often difficult to incorporate into a cut-based analysis.

The strategy for this event selection is to train and use neural networks to identify signal while rejecting the $q\bar{q}$ and W^+W^- backgrounds. Two neural networks in tandem are used, each incorporating differing sets of variables designed to reject specific backgrounds. Some of the variables used for the neural networks are also used in the cut-based selection. One network is designed to reject $q\bar{q}$ events while the other is designed to reject W^+W^- events;

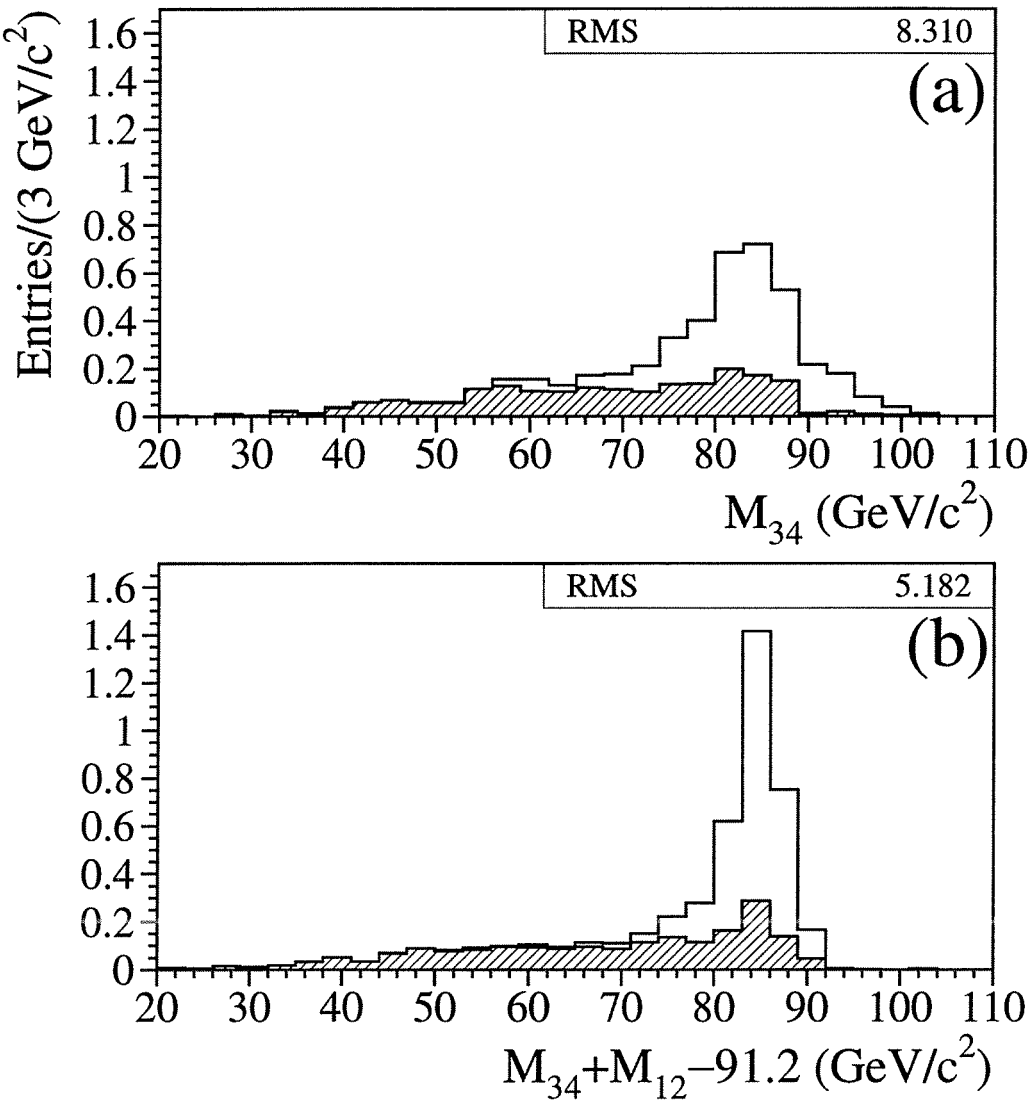

Figure 4.17: Distributions of (a) M_{34} and (b) the reconstructed Higgs boson mass $M_{12} - M_{34} - 91.2\,\mathrm{GeV}/c^2$. In both distributions the hatched histogram shows the contribution from incorrect jet-pairings. The quoted RMS is for correct jet-pairings only.

hence they are referred to as the *anti*-$q\bar{q}$ and *anti*-W^+W^- neural networks respectively. The use of a neural network to reject ZZ events deteriorates the overall analysis performance for Higgs boson masses approaching M_Z due to the irreducible component $ZZ \rightarrow b\bar{b}q\bar{q}$.

Individual patterns composed of sets of input variables are presented to the neural networks. During the training phase, the network weights are optimized to produce an output near one for signal patterns and near zero for background patterns. The basic elements used for patterns are the six possible four-jet pairings or combinations per event. Only the correct jet pairing in signal events is presented to the neural network as signal pattern. However, all six jet pairings in $q\bar{q}$ and W^+W^- events are used as background patterns.

As is the case for the b-tagging neural network, the performance of a neural network is not only a function of the discriminating power of the input variables but also of proper handling of the input variables, the network architecture, and the internal parameters used during training [122]. Unfortunately clearly defined rules for determining most of these parameters do not exist. Hence they must be chosen on the basis of optimal performance on an independent testing sample of simulated signal and background processes.

4.3.1 The Input Variables

The anti-$q\bar{q}$ and anti-W^+W^- neural networks share many variables with the cut-based analysis. Several additional variables have been added to each

which increase performance. Most of these additional discriminating variables show only marginal separation between signal and total background distributions; however, often there is significant separation between one background component (*i.e.*, $q\bar{q}$ or W^+W^-) and signal. This motivates the construction of separate neural networks for discrimination against the different background types.

The additional discriminating variables can be grouped into two classes: *topological/kinematic* variables and *b-tagging* variables.

Additional Topological/Kinematic Variables

The additional set of topological/kinematic variables includes the following:

- An *event broadening* variable B is calculated by dividing the event into hemispheres based on the thrust axis [136]. The thrust axis is defined as the vector $\hat{n}$ which maximizes the quantity

$$T = \frac{\sum_{i=1}^{N} |\vec{p}_i \cdot \hat{n}|}{\sum_{i=1}^{N} |\vec{p}_i|}$$

  where N is the number of energy flow objects in the event, $\vec{p}_i$ is the three-momentum vector of the ith energy flow object, and T is the

thrust. A quantity B_{hemi} is calculated for each hemisphere:

$$B_{\text{hemi}} = \frac{\sum_{j=1}^{N} |p_{\text{T}j}|}{\sum_{j=1}^{N} |p_j|}$$

where N is the number of energy flow objects in the hemisphere, p_j is the momentum of the jth energy flow, and p_{Tj} is the transverse momentum of the jth energy flow with respect to the thrust axis. The quantity B is the minimum of B_{hemi} for the two hemispheres. The distributions for this quantity are shown in Figure 4.18(a).

- The average four-jet QCD matrix element $\langle \mathcal{M} \rangle$ is determined by using the four-momenta of the four jets in the event and calculating the first-order transition amplitude for $e^+e^- \rightarrow q\bar{q}q\bar{q}$ and $e^+e^- \rightarrow q\bar{q}gg$. This quantity is described in detail elsewhere [137]. Figure 4.18(b) shows the distributions of this variable.

- $(E_{\text{jet}})_i$ is the energy of the ith jet in the event. The two smallest and the largest jet energies are used. Figure 4.18(c) shows distributions for the lowest energy jet.

- $(M_{\text{jet}})_i$ is the mass of the ith jet in the event. The two lowest jet masses are used.

- $\cos\theta_{\not p}$ is cosine of the polar angle of the event missing momentum vector.

- $\min(\theta_{ij})$: the minimum di-jet angle. Figure 4.18(d) shows distributions of this variable.

Additional b-Tagging Variables

The neural network b-tag presented in Chapter 3 offers improved performance over single b-tagging variables by combining multiple variables together. It was developed in an analysis-independent manner so that it could be applied in a uniform manner to many final state analyses designed to search for neutral Higgs bosons. It can be complemented with additional b-tagging variables to enhance performance for the four-jet final state. The flexibility of the neural network framework allow this to be done relatively easily.

The variables listed below show discriminating power between jet flavors. They are evaluated for each jet in the event and included as input variables to the analysis neural networks in various forms.

- A *charm rejection* variable μ_i is based upon the impact-parameter-based probability $(\mathcal{P}_{jet})_i$ described in Section 3.3.1. This new quantity μ_i is the ith jet probability recalculated using only tracks which have a rapidity with respect to the jet axis of less than 4.9. This modification was developed for ALEPH heavy flavor analyses at LEP1 to enhance identification of c jets and is described in detail elsewhere [138]. There is a substantial component of background from W^+W^- events with one or two charm jets. Figure 4.19(a) and (b) show distributions of this variable.

- The *boosted aplanarity* of a jet is calculated in a manner similar to that of boosted sphericity described in Section 3.3.4. Energy flow objects comprising jet i are boosted into the rest-frame of the jet, and the momentum tensor $S^{\alpha\beta}$ and its eigenvalues Q_j $(j = 1, 2, 3)$ are calculated. The aplanarity is defined as $3/2\,Q_1$ where $Q_1 < Q_2 < Q_3$. Figure 4.19(c) shows the distributions of this variable.

- The boosted sphericity of a jet, described in Section 3.3.4.

- The multiplicity of good charged tracks in a jet with rapidity (with respect to the jet axis) greater than 1.6 is calculated. Figure 4.19(d) shows distributions of this variable.

These additional b-tagging variables are applied to the Z candidate jets in the anti-$q\bar{q}$ neural network in order to reduce the $b\bar{b}gg$ component of the $q\bar{q}$ background process. The charm rejection variable is applied to the Higgs boson candidate jets in the anti-W^+W^- neural network in order to reduce the component of the W^+W^- background process having two c jets.

4.3.2 The Neural Networks

The anti-$q\bar{q}$ neural network uses a 22-10-10-1 fully-connected feed-forward architecture [122]. The 22 input variables are listed in Table 4.6.

The anti-W^+W^- neural network uses a 14-12-10-2 fully-connected feed-forward architecture. The 14 input variables are listed in Table 4.7.

During the training phase, both networks are exposed to patterns derived

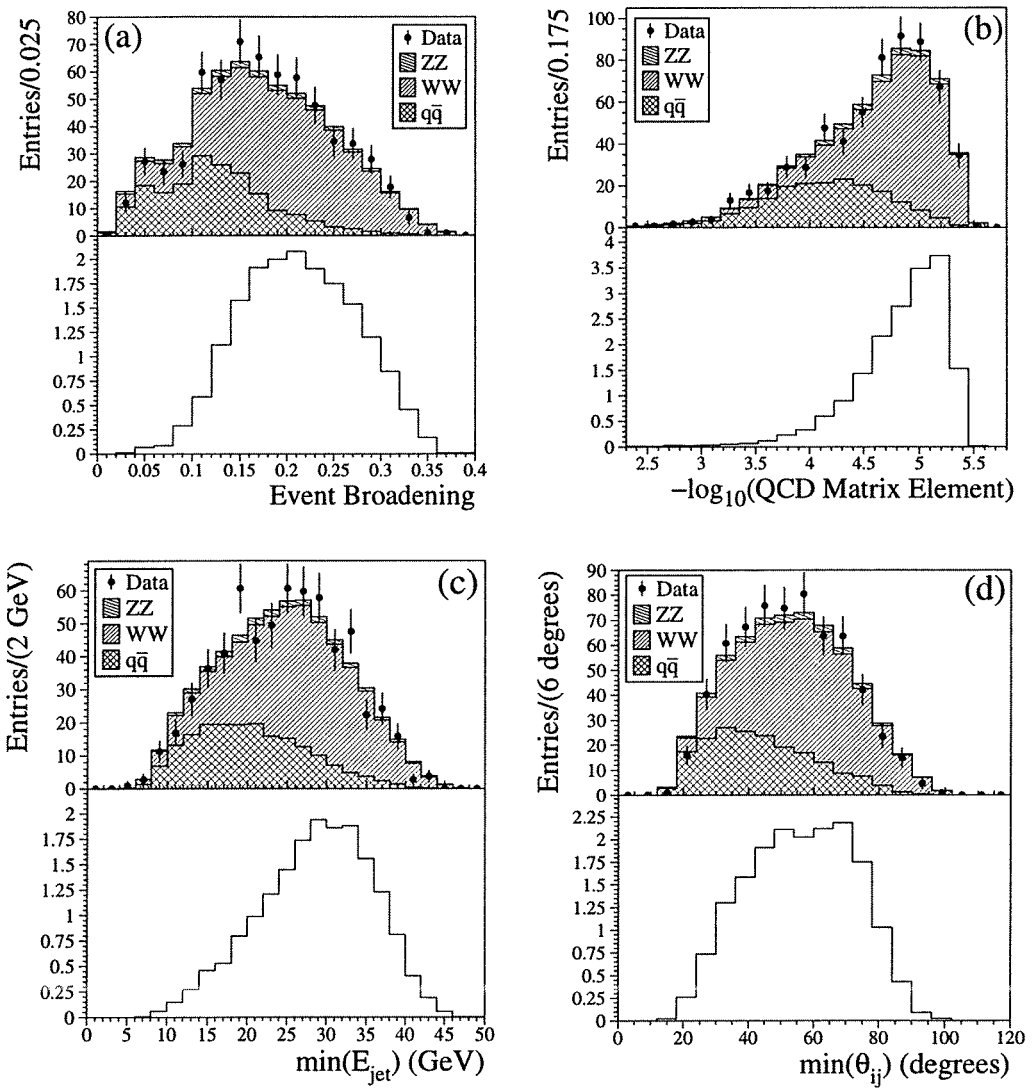

Figure 4.18: Distributions of some of the additional topological/kinematic discriminating variables used in the neural network selection at the preselection level: (a) the event broadening, (b) $-\log_{10}$ of the average QCD matrix element, (c) the minimum jet energy, and (d) $\min(\theta_{ij})$. Distributions for simulated background events and data are shown in the upper half of each plot while the signal with $M_{\mathrm{H}} = 85\,\mathrm{GeV}/c^2$ is given in the lower half. All six jet pairings are shown in distributions of data and simulated background; only the correct pairing is shown for signal.

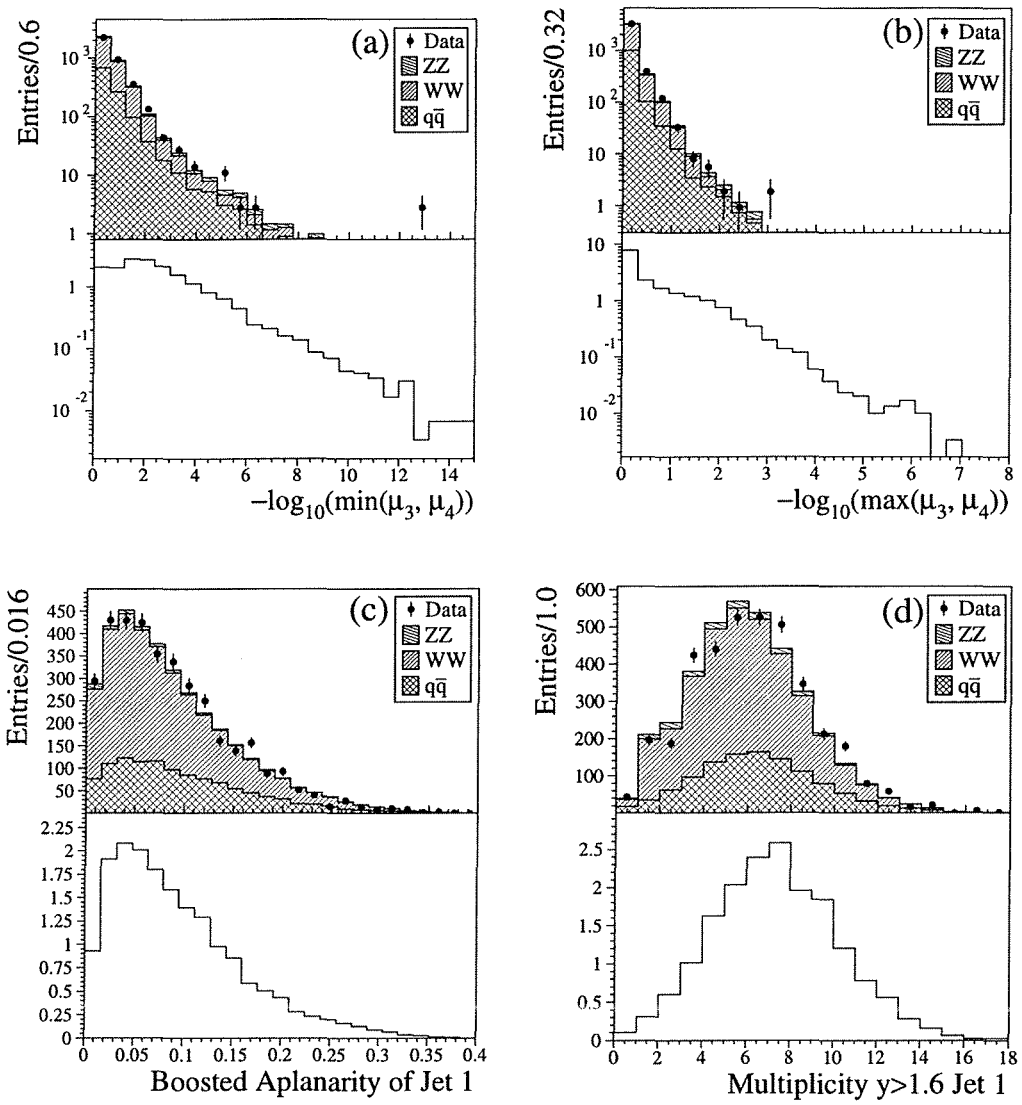

Figure 4.19: Distributions of some of the additional b-tagging discriminating variables used in the neural network selection at the preselection level: (a) $-\log_{10}(\min(\mu_3, \mu_4))$, (b) $-\log_{10}(\max(\mu_3, \mu_4))$, (c) boosted aplanarity of the most energetic Z candidate jet, and (d) multiplicity of tracks with rapidity greater than 1.6 of the most energetic Z candidate jet. Distributions for simulated background events and data are shown in the upper half of each plot while the signal with $M_{\mathrm{H}} = 85\,\mathrm{GeV}/c^2$ is given in the lower half. All six jet pairings are shown in distributions of data and simulated background; only the correct pairing is shown for signal.

Variable	
1.	y_{34} ‡
2.	γ ‡
3.	M_{12} ‡
4.	$\min(\eta_3, \eta_4)$ ‡
5.	$(1-\eta_3)(1-\eta_4)$ ‡
6.	$\sum_{i=1}^{4} \eta_i$ ‡
7.	Θ ‡
8.	$\langle \mathcal{M} \rangle$, average four-jet QCD matrix element
9–10.	Boosted aplanarity of Z candidate jets
11–12.	Boosted sphericity of Z candidate jets
13–14.	Multiplicity of tracks with rapidity larger than 1.6, in the Z candidate jets
15.	$\min(\theta_{ij})$, lowest interjet angle
16.	$\cos\theta_{\not p}$, cosine of the polar angle of the event missing momentum vector
17.	$\min(M_{ij} + M_{kl})$, lowest di-jet mass sum
18–19.	M_{min}, M_{min2}, the two lowest jet masses
20–21.	E_{min}, E_{min2}, the two lowest jet energies
22.	E_{max}, largest jet energy

Table 4.6: The complete list of inputs to the anti-$q\bar{q}$ neural network. The variables marked with ‡ are in common with cut-based selection described in Section 4.2.

from simulated events which pass extended preselection requirements. The preselection criteria are identical to those described in Section 4.1 with the exception of requirements that the sum of the four neural network b-tag outputs be greater than 1.0 and that M_{34} be greater than $45\,\mathrm{GeV}/c^2$.

The anti-$q\bar{q}$ and anti-W^+W^- are trained on dedicated training samples which are summarised in Tables 4.8 and 4.9. Both neural networks are trained using pre-existing packages [125, 139]. The number of training epochs is

Variable	
1.	y_{34} ‡
2.	γ ‡
3.	M_{12} ‡
4–5.	$\min(\eta_3, \eta_4)$ ‡, $\max(\eta_3, \eta_4)$
6.	$(1-\eta_3)(1-\eta_4)$ ‡
7.	$\sum_{i=1}^{4} \eta_i$ ‡
8–9.	$\min(\eta_1, \eta_2)$, $\max(\eta_1, \eta_2)$
10–11.	$\min(\mu_3, \mu_4)$, $\max(\mu_3, \mu_4)$
12.	B, event broadening
13.	$E_{\min}$, lowest jet energy
14.	$\min(M_{ij})$, lowest di-jet mass

Table 4.7: The complete list of inputs to the anti-W^+W^- neural network. The variables marked with ‡ are in common with the cut-based variables described in Section 4.2.

1 000 and 1 500 for the anti-$q\bar{q}$ and anti-W^+W^- neural networks respectively. Figure 4.20 shows distributions of the outputs of the neural networks from independent testing samples.

4.3.3 Performance

The performance curve for the neural network analysis is obtained by allowing the selection cuts on the anti-W^+W^- and anti-$q\bar{q}$ neural network outputs to vary freely. The working point is determined using the method described in Chapter 5. Figure 4.21 shows the performance of the neural network analysis in terms of number of expected events from background processes versus efficiency for a signal with $M_H = 85\,\mathrm{GeV}/c^2$. An arrow denotes the working point which corresponds to requiring the anti-$q\bar{q}$ neural network

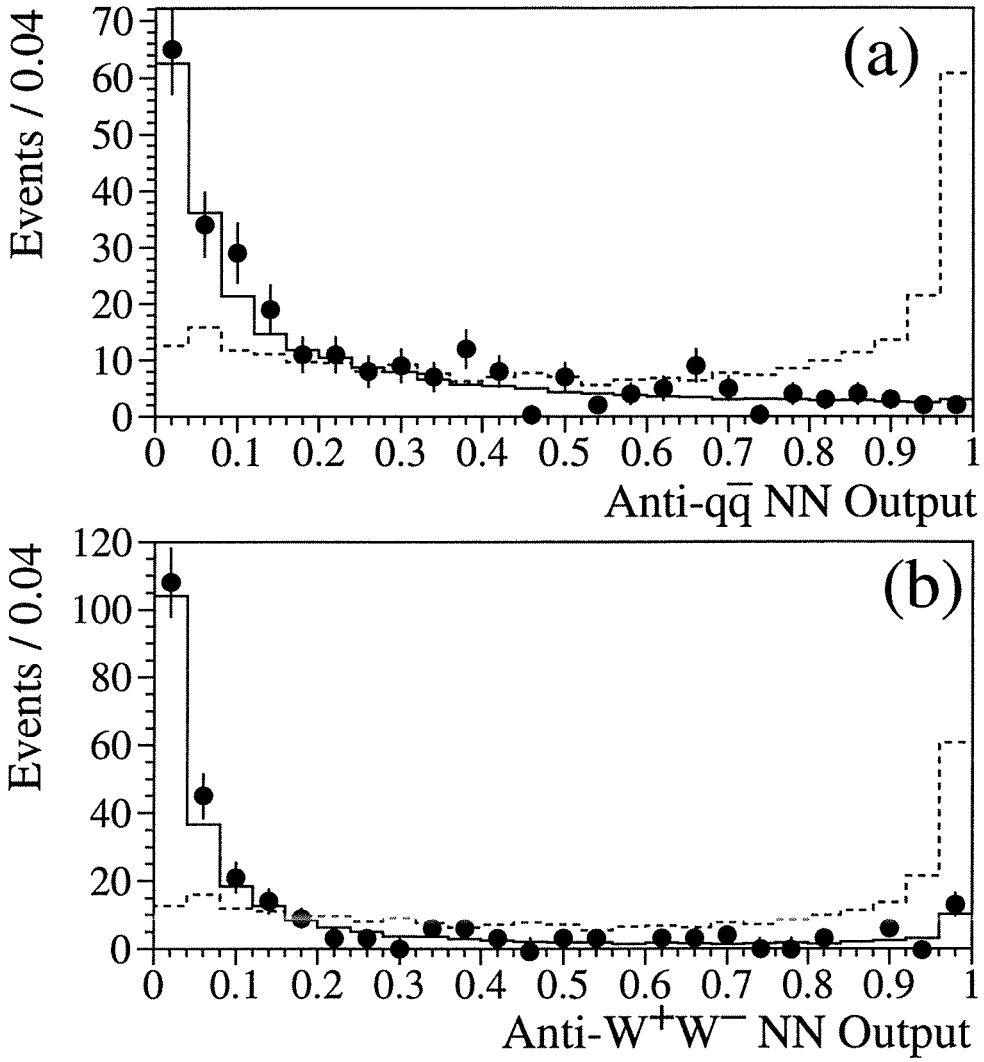

Figure 4.20: The neural network outputs for (a) anti-W^+W^- , and (b) anti-$q\bar{q}$ network. The solid lines indicate the response for background processes normalized to $57\,pb^{-1}$ while the dashed line in each plot indicates the response for signal with a Higgs mass of $85\,GeV/c^2$ which has an arbitrary normalization. The points show the distributions obtained from data.

Process	Number Events before presel.	Number Combinations after presel.
HZ signal ($M_{\mathrm{H}} = 70\,\mathrm{GeV}/c^2$)	19 995	12 380
HZ signal ($M_{\mathrm{H}} = 80\,\mathrm{GeV}/c^2$)	20 000	12 920
HZ signal ($M_{\mathrm{H}} = 85\,\mathrm{GeV}/c^2$)	19 990	15 110
$\mathrm{q\bar{q}}(\gamma)$	1 109 729	62 772

Table 4.8: The training sample composition for the anti-$\mathrm{q\bar{q}}$ neural network.

Process	Number Events before presel.	Number Combinations after presel.
HZ signal ($M_{\mathrm{H}} = 80\,\mathrm{GeV}/c^2$)	20 000	9 443
$\mathrm{W^+W^-}$	26 000	21 213

Table 4.9: The training sample composition for the anti-$\mathrm{W^+W^-}$ neural network.

output to be greater than 0.940 and the anti-$\mathrm{W^+W^-}$ neural network output to be greater than 0.964. This yields a signal efficiency of $(31.4 \pm 0.6)\%$ (4.24 ± 0.08 signal events expected for $M_{\mathrm{H}} = 85\,\mathrm{GeV}/c^2$) and an expected background of 2.36 ± 0.15 events (0.70 ± 0.11 $\mathrm{q\bar{q}}$, 0.38 ± 0.05 $\mathrm{W^+W^-}$, and 1.28 ± 0.08 ZZ); the uncertainties are statistical only. The contribution from $\mathrm{q\bar{q}}$, $\mathrm{W^+W^-}$, and ZZ is also shown as well as the performance curve for the cut-based analysis. It is apparent that the neural network analysis offers consistently better performance than the cut-based analysis; for example, at a signal efficiency of 34%, there is roughly a 15% reduction in background using the neural network analysis.

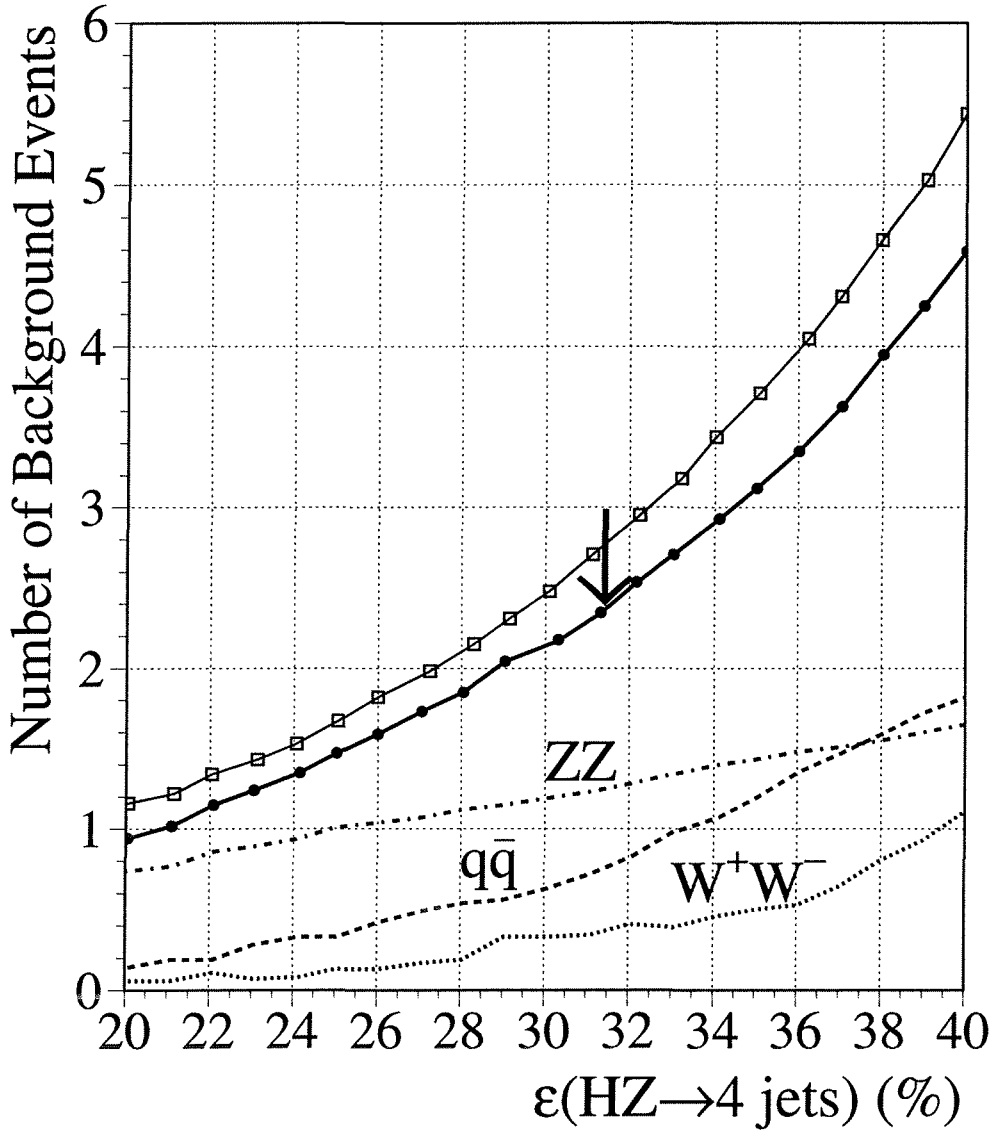

Figure 4.21: The performance of the neural network analysis in terms of efficiency for a signal with $M_{\mathrm{H}} = 85\,\mathrm{GeV}/c^2$ versus the number of events expected from Standard Model background processes for an integrated luminosity of $57\,\mathrm{pb}^{-1}$. The background is broken down into its contribution from $\mathrm{q\bar{q}}$, $\mathrm{W^+W^-}$, and ZZ processes. The arrow denotes the working point determined using the method summarized in Chapter 5. The thin line with open squares denotes the performance curve from the cut-based analysis shown in Figure 4.15.

4.4 Systematic Studies

Studies of uncertainties due to b-tagging, jet angle resolution, and discrepancies between data and simulated events are presented in this section. Systematic effects are quantified with respect to variations of the signal efficiency ($M_{\mathrm{H}} = 85\,\mathrm{GeV}/c^2$) at the working point, ϵ_{WP} defined as:

$$\Delta\epsilon_{\mathrm{relative}} = \frac{\epsilon' - \epsilon_{\mathrm{WP}}}{\epsilon_{\mathrm{WP}}}$$

where ϵ' is the new signal efficiency determined from a given systematic variation. Some systematic uncertainties are treated as symmetric when calculating the total.

4.4.1 b-Tagging

Since b-tagging is the most powerful selection criterion in both the cut-based and neural network analyses, systematic effects related to the detector tracking simulation in simulated events and generator-level b physics parameters must be carefully studied.

In the simulation, the b quark fragmentation is modelled with the Peterson function [99] described in Section 3.1.3. An average from experimental measurements [140] of the value of the free parameter in the fragmentation function ϵ_{b} is 0.0045 ± 0.0014. In order to estimate the uncertainty on the signal selection efficiency arising from the uncertainty on ϵ_{b}, signal events are reweighted to a harder ($\epsilon_{\mathrm{b}} = 0.0031$) and a softer ($\epsilon_{\mathrm{b}} = 0.0059$) frag-

mentation. As expected, the signal selection efficiency increases (decreases), due to the average increase (decrease) in the boost of b hadrons. The difference between the nominal and reweighted sample efficiencies is taken as the systematic uncertainty due to our limited knowledge of the fragmentation process. Using this technique, a relative working point signal efficiency change of $\pm 1.6\%$ is observed.

In the samples of simulated events the average b hadron lifetime is set to 1.50 ps. A recent fit for this quantity from experimental measurements is 1.55 ± 0.02 ps [141]. The uncertainty due to this discrepancy is quantified by reweighting simulated events from 1.50 ps to 1.55 ps and reevaluating the working point signal efficiency. A relative $+1.1\%$ shift in working point signal efficiency is seen for both the cut-based and neural network analyses.

As discussed in Section 3.5, a smearing of the d_0 and z_0 of 3% for tracks in simulated events with two VDET hits and 15% for all other tracks is performed in order to account for modelling uncertainties of the tracking. To estimate conservatively the systematic uncertainty due to this smearing, the working point signal efficiency is reevaluated without this smearing. Relative shifts of -0.27% and -1.1% in working point signal efficiency are seen for the cut-based and neural network analyses respectively.

Uncertainties due to further problems in the modelling of the tracking in the simulation by reevaluating the working point signal efficiency with a new sample of simulated signal events generated for which some of these problems have been corrected. A relative signal efficiency shift of $+5.0\%$ is observed

in the cut-based analysis and +5.6% in the neural network analysis.[5]

In order to account for uncertainties on the average b hadron multiplicity, simulated signal events were reweighted so as to increase the average charged b hadron track multiplicity by 0.4 for the weakly-decaying b hadron species. This results in a relative working point signal efficiency change of +3.7% for the cut-based analysis and a relative change +2.1% for the neural network analysis.

The b-tagging related systematic uncertainties are summarised in Table 4.10.

Source	$\Delta\epsilon_{\text{relative}}$ (%) Cut-based	$\Delta\epsilon_{\text{relative}}$ (%) Neural Network
b Fragmentation	± 1.6	± 1.6
b Lifetime	$+1.1$	$+1.1$
b Multiplicity	$+3.7$	$+2.1$
Track Smearing	-0.27	-1.1
Different Tracking	$+5.0$	$+5.6$
Total	$^{+6.5}_{-1.6}$	$^{+6.3}_{-1.9}$

Table 4.10: A summary of the b-tagging related systematics for the cut-based and neural network analyses in terms of relative signal efficiency changes.

4.4.2 Jet Angle

In these analyses, most kinematic variables are calculated using the directions and rescaled energies of the jets. Hence uncertainties in the jet direction can

[5]Part of this error includes statistical uncertainties due to the limited sample sizes of the new and old samples (10 000 events in each case).

contribute an additional systematic error.

The jet angular resolutions of the ALEPH detector have been estimated to be $\Delta\theta = 17.7\,\text{mrad}$ and $(\sin\theta)\Delta\phi = 19.4\,\text{mrad}$ at LEP1 [72]. Here, at LEP2, these jet resolutions are conservatively assumed to be 10% worse, and the jet angles are smeared by $8.1\,\text{mrad}$ in θ, and $8.9/\sin\theta\,\text{mrad}$ in ϕ respectively. The relative change in working point signal efficiency is -0.8%.

4.4.3 Neural Network Variables

Since the neural network analyses use a large set of discriminating variables, there is the danger of introducing systematic uncertainties due to discrepancies between the simulation and data. Therefore, the systematic effect of each variable used as input to the neural networks must be studied. It should be noted that since the neural network analysis shares seven variables with the cut-based analysis, some of these systematic concerns apply to the cut-based analysis also.

In order to quantify any possible discrepancies between data and simulated events for each of the kinematic and jet shape input variables to the neural networks, the working point efficiency and expected background is reevaluated with a reweighting technique. At the preselection level, a smooth X_i distribution is found for each input variable i. The ratio $R(X_i) = X_i(\text{DATA})/X_i(\text{MC})$ is calculated. Each of the signal events is reweighted by a factor $(R(X_i) + 1)/2$. All selection cuts are applied, and the reweighted efficiency ϵ' is calculated. The change relative to the work-

ing point signal efficiency is determined for each variable and summarized in Table 4.11. The total relative uncertainty is $\Delta\epsilon_{\text{relative}} = ^{+1.0}_{-2.2}$ %.

Variable	$\Delta\epsilon_{\text{relative}}$ (%)
Θ	0.1
γ	0.0
y_{34}	0.0
M_{12}	−1.6
$\min(M_{ij})$	0.2
B	0.2
$\cos\theta_{\not p}$	−1.0
$\langle\mathcal{M}\rangle$	0.0
$\min(\theta_{ij})$	−0.1
Largest E_{jet}	−0.1
Smallest E_{jet}	0.0
Second smallest E_{jet}	−0.1
Smallest M_{jet}	0.2
Second smallest M_{jet}	0.4
Boosted Aplanarity of jet 1	0.0
Boosted Aplanarity of jet 2	0.1
Boosted Sphericity of jet 1	−0.1
Boosted Sphericity of jet 2	−1.1
Multiplicity for $y > 1.6$ of jet 1	−0.4
Multiplicity for $y > 1.6$ of jet 2	0.8
TOTAL	$^{+1.0}_{-2.2}$

Table 4.11: Relative changes in working point signal efficiency due to systematic reweighting of discriminating variables in the neural network analysis.

4.4.4 Summary of Systematics

Systematic uncertainties related to b-tagging, jet angle resolution, and discrepancies between data and Monte Carlo simulations of the kinematic vari-

ables used in the neural network are studied. The uncertainties due to b-tagging result in a relative signal efficiency uncertainty of $\Delta\epsilon_{\text{relative}} = ^{+6.5}_{-1.6}$ % and $\Delta\epsilon_{\text{relative}} = ^{+6.3}_{-1.9}$ % in the cut-based and neural network analyses respectively. The uncertainties due to jet angle resolution result in a relative signal efficiency uncertainty of -0.8%. Finally, uncertainties derived from reweighting the kinematic variables used in the neural network analysis result in a relative working point signal efficiency uncertainty of $\Delta\epsilon_{\text{relative}} = ^{+1.0}_{-2.2}$ %.

All of the combined systematic uncertainties are less than statistical uncertainty due to the limited size of the simulated event sample. Variations in the expected background were also studied and were also found to be less than the statistical uncertainty.

These systematic uncertainties are incorporated into the final result presented in Chapter 5 (*i.e.*, the lower limit on the mass of the Higgs boson) using the method of Cousins and Highland described in Ref. [142].

Chapter 5

Limit Setting Methods and Results

The analyses described in Chapter 4 and Appendix A are designed to search for evidence of the production Higgs boson via the Higgsstrahlung process. No evidence of a significant excess is observed in the ALEPH data sample in each of the individual final state analyses.

A confidence level calculation method is used to determine a lower limit on the mass of the Higgs boson. For this purpose, the different final state analyses are combined together using a technique which weights each analysis according to its intrinsic ability. Before the final state analyses are applied to the data, their expected combined performance in the absence of signal is determined; the resulting average combined confidence level is maximized with respect to the most relevant event selection criteria using a reference signal with a Higgs boson mass of $85\,\mathrm{GeV}/c^2$. This establishes a *working*

point for each analysis. These methods are summarized in Section 5.1.

Events from the data sample which pass the optimized selection criteria are discussed in Section 5.2. Systematic uncertainties are incorporated, and a final combined lower limit at a 95% confidence level on the mass of the Higgs boson is determined. This is presented in Section 5.3.

5.1 Limit Setting Method

5.1.1 The Confidence Levels

This section summarizes the confidence level calculation methods used within ALEPH. These methods are based upon and described in detail in Refs. [143, 144]. An *estimator* (often also referred to as a *test statistic*) is defined as

$$\xi = \sum_{i=0}^{n} e^{-s} \frac{s^i}{i!} P_i^n \left(x_1, \ldots, x_n\right)$$

where n is the number of candidate events and s is the number of expected events from the Higgs boson signal process. The first part of each term of the estimator is the standard Poisson probability that i events are from signal when s signal events are expected. The summation over this quantity alone gives the probability that n events or fewer are from signal when s are expected.

The term P_i^n in the estimator represents an important and powerful extension of a confidence level calculation based only on Poisson statistics. This term is a measure of how signal-like the i most signal-like events are; specif-

ically it is the probability for the i most signal-like events to be as or less signal-like than observed according to the values of a discriminating variable for each event $x_{(1,\ldots,n)}$.

In practice there are multiple sets of discriminating variables for some analyses. The reconstructed Higgs boson mass is a discriminating variable for all final state analyses (*i.e.*, the $Hq\bar{q}$ analyses described in Chapter 4 and the $H\nu\bar{\nu}$, $H\ell^+\ell^-$, $H\tau^+\tau^-$, and $\tau^+\tau^-q\bar{q}$ analyses described in Appendix A). For some of the final state analyses, the power of the confidence levels is improved by including more discriminating variables in the test statistic. These new variables are

- the b-tagging sum $(\eta_1 + \eta_2)$ of the two hemispheres in the $H\nu\bar{\nu}$ final state cut-based analysis;
- the neural network output in the $H\nu\bar{\nu}$ final state neural network analysis;
- the b-tagging sum $(\eta_1 + \eta_2)$ of the two jets for the $H\ell^+\ell^-$ final state analysis.

The construction of the P_i^n quantity involves several steps. For a given single discriminating variable x, the probability densities as a function of x are determined from simulated events. This probability density is denoted as $p_s(x)$ for signal and $p_b(x)$ for background processes. These probability

densities are converted to

$$\eta(x) = \frac{p_s(x) - p_b(x)}{p_s(x) + p_b(x)}.$$

which reflects the signal-likeness of an event having a discriminating variable value x.

A probability density for signal events only $\rho_s(\eta)$ is calculated based upon the $\eta(x)$ distribution. A cumulative probability distribution $R(\eta)$ is calculated based on $\rho_s(\eta)$ for each event:

$$R(\eta) = \int_{-1}^{\eta} d\eta' \, \rho_s(\eta').$$

Hence R ranks each event, indicating how signal-like an event which has a discriminating variable value x is.

In the case of multiple discriminating variables, there are multiple cumulative probability distributions for the signal (*i.e.*, one for each discriminating variable). The ranking variable $R(\eta_1, \ldots, \eta_{n_{\text{disc}}})$ is the product of the integrals of each different $\eta(x_j)$ distribution where x_j is the jth discriminating variable out a total of n_{disc}.

For a given set of n events, the events are ordered according to their R values. The R values for the i most signal-like events are combined according to the standard prescription for multiple cumulative probability distributions to determine P_i^n.

Multiple hypothesized Higgs masses are denoted $\hat{m}_{\text{H}}$ and are considered

in the confidence level calculation. The shapes of the distributions of the discriminating variables are fed into a toy Monte Carlo program; one set of distributions corresponds to the background processes for the given working point (see Section 5.1.3) while multiple sets of signal distributions are used each corresponding to a specific value of $\hat{m}_{\mathrm{H}}$ [145]. These signal distributions are evaluated at $5\,\mathrm{GeV}/c^2$ intervals using samples of simulated Higgs boson events. An interpolation method is used to obtain the distributions at $0.5\,\mathrm{GeV}/c^2$ intervals in $\hat{m}_{\mathrm{H}}$ for the confidence level determinations.

A large number of *gedanken* experiments using signal only is performed for specific values of $\hat{m}_{\mathrm{H}}$ using the toy Monte Carlo program. Expected distributions of ξ as a function of $\hat{m}_{\mathrm{H}}$ are obtained. These expected distributions are denoted as $\rho(\xi)$, and their areas are normalized to one.

The confidence level on a given signal hypothesis $\hat{m}_{\mathrm{H}}$ is defined as the fraction of all possible experiments with signal only that would have an estimator value ξ less than or equal to the observed value from the data ξ_{obs} [144]:

$$c(\hat{m}_{\mathrm{H}}, \xi_{\mathrm{obs}}) = \int_{\xi_{\mathrm{min}}}^{\xi_{\mathrm{obs}}} \rho(\xi) d\xi.$$

The traditional definition of confidence level is simply $1 - c$ (*i.e.*, 95% confidence level corresponds to a value of c of 0.05).

An expected confidence level for the null hypothesis is calculated. This null hypothesis assumes that the Higgs boson is too heavy to be produced at LEP and the expected confidence level is denoted as $\langle c \rangle_{\infty}(\hat{m}_{\mathrm{H}})$.

5.1.2 Combination of Confidence Levels

Since there are multiple final state analyses, it is necessary to merge them together when determining the confidence levels and hence the final result. The *elitist* prescription of Ref. [144] is used to accomplish this. This prescription is an extension of a *democratic* prescription which would combine the confidence levels of n different analyses together in an equal way regardless of their intrinsic capability to search for the Higgs boson

$$f(\hat{m}_{\mathrm{H}}) = \prod_{i=1}^{n} c_i(\hat{m}_{\mathrm{H}})$$

where f can be interpreted as a new estimator from which to derive a combined confidence level. The new combined confidence level would be the fraction of all possible experiments that would have a value f less than or equal to the measured one.

The elitist prescription weights each analysis so that superior ones contribute more to the combined confidence level than inferior analyses:

$$f(\hat{m}_{\mathrm{H}}) = \prod_{i=1}^{n} c_i^{a_i(\hat{m}_{\mathrm{H}})}(\hat{m}_{\mathrm{H}})$$

where $a_i(\hat{m}_{\mathrm{H}})$ is the weight assigned to the ith analysis for a given hypothesized Higgs boson mass $\hat{m}_{\mathrm{H}}$. These weights are determined during an optimization procedure which minimized the combined expected confidence level $\langle c \rangle_{\infty}(\hat{m}_{\mathrm{H}})$. During this procedure, the weights corresponding to the AND of the cut-based and neural network analyses for the Hq$\bar{\mathrm{q}}$ final state are fixed to

1.0; all other weights are allowed to vary during the optimization procedure. The complete details and derivation of this procedure are non-trivial and are described in detail in Ref. [144].

5.1.3 Working Point Determination

The value of the combined $\langle c \rangle_\infty$ at $\hat{m}_{\mathrm{H}} = 85\,\mathrm{GeV}/c^2$ is minimized with respect to the position of the cuts on the most relevant selection criteria for each of the final state analyses. These most relevant selection criteria are:

- the three selection criteria based upon b-tagging information and the invariant mass of jets from the Z boson in the $\mathrm{Hq\bar{q}}$ cut-based analysis;
- the neural network outputs in the $\mathrm{Hq\bar{q}}$ neural network analysis;
- the b-tag sum $(\eta_1 + \eta_2)$ and the event acoplanarity in the $\mathrm{H}\nu\bar{\nu}$ cut-based analysis;
- the neural network output in the $\mathrm{H}\nu\bar{\nu}$ neural network analysis;
- the reconstructed Z mass in the $\mathrm{H}\ell^+\ell^-$ analysis;
- the neural network outputs in the $\mathrm{H}\tau^+\tau^-$ and $\tau^+\tau^-\mathrm{q\bar{q}}$ analyses.

Technically the resulting working points may not correspond to the most optimal selection; however, this procedure has the notable advantage of providing a well-defined and unbiased way to determine the most relevant selection criteria.

Two selections exist for the $Hq\bar{q}$ and $H\nu\bar{\nu}$ final states: the cut-based analyses and the neural network analyses. In each case, the two original analyses are separated into three statistically independent *subselections*. The first subselection, corresponding to the overlap of the cut-based and neural network analyses, is very pure. Two less pure exclusive subselections (*i.e.*, cut-based only and neural network only) contain additional information and are combined with the first, decreasing further the overall expected confidence level. The gain from this procedure is significant since, when two analyses are aimed at selecting the same signal and have similar performance, they often have a large overlap in signal efficiency but not so large an overlap in terms of background. Signal events are, unlike reducible background events, signal-like in *many* variables. The selection of a background event by both selections is therefore less probable: it depends on the specific choice of variables in each of the selections.

Systematic uncertainties related to the knowledge of the residual background shape and normalization do not affect the results since no background subtraction is performed.

5.2 Results from Data

Seven events are selected in the data by the various optimized selections, in agreement with the 7.2 events expected from all Standard Model background processes. Four of these events are selected in the four-jet final state; these candidates are discussed in Section 5.2.1. The other three candidate

M_H (GeV/c^2)	$H\ell^+\ell^-$	$H\nu\bar{\nu}$			$Hq\bar{q}$			$H\tau^+\tau^-$	$\tau^+\tau^-q\bar{q}$
		AND	Cuts	NN	AND	Cuts	NN		
60	79.6	8.8	8.7	4.7	9.3	5.4	8.1	18.1	0.93
70	77.8	15.8	4.4	7.9	12.4	8.6	9.0	22.9	2.9
80	78.3	20.9	2.8	10.9	23.5	7.4	5.2	22.7	9.8
85	76.2	17.9	4.0	12.2	26.1	7.8	5.2	20.7	12.6
90	71.9	11.1	5.2	7.0	24.6	9.4	4.6	17.4	13.6
95	31.1	9.5	2.6	7.2	19.1	7.6	6.0	12.7	11.6
100	4.0	6.0	1.7	5.7	14.2	6.6	6.9	6.8	5.7
Number of events									
n_b	2.0	0.16	0.08	0.18	1.4	2.1	1.00	0.17	0.16
n_{obs}	3	0	0	0	1	2	1	0	0
n_s	1.1	0.82	0.18	0.56	3.6	1.1	0.71	0.14	0.16

Table 5.1: A summary of all the final state analyses. Signal detection efficiencies are given in percent for different Higgs boson mass values. For the $Hq\bar{q}$ and $H\nu\bar{\nu}$ channels three independent sub-selections are used: events selected by both the cut-based and the neural network-based selections (summarized in the column labelled "AND"), and events selected exclusively by either of them. The number of expected background events (n_b), the number of events selected in the data (n_{obs}), and the number of expected signal events for $M_H = 85\,GeV/c^2$ (n_s) are also given.

events are found in the leptonic final state and are discussed in Section 5.2.2. Table 5.1 summarizes the efficiencies of the analyses and subselections for various hypothesized Higgs masses, the number of expected background, the number of candidates observed in the data, and the number of expected signal events. Figure 5.1 shows the reconstructed Higgs boson mass distribution for the candidates in all channels and the expected distributions from background and signal.

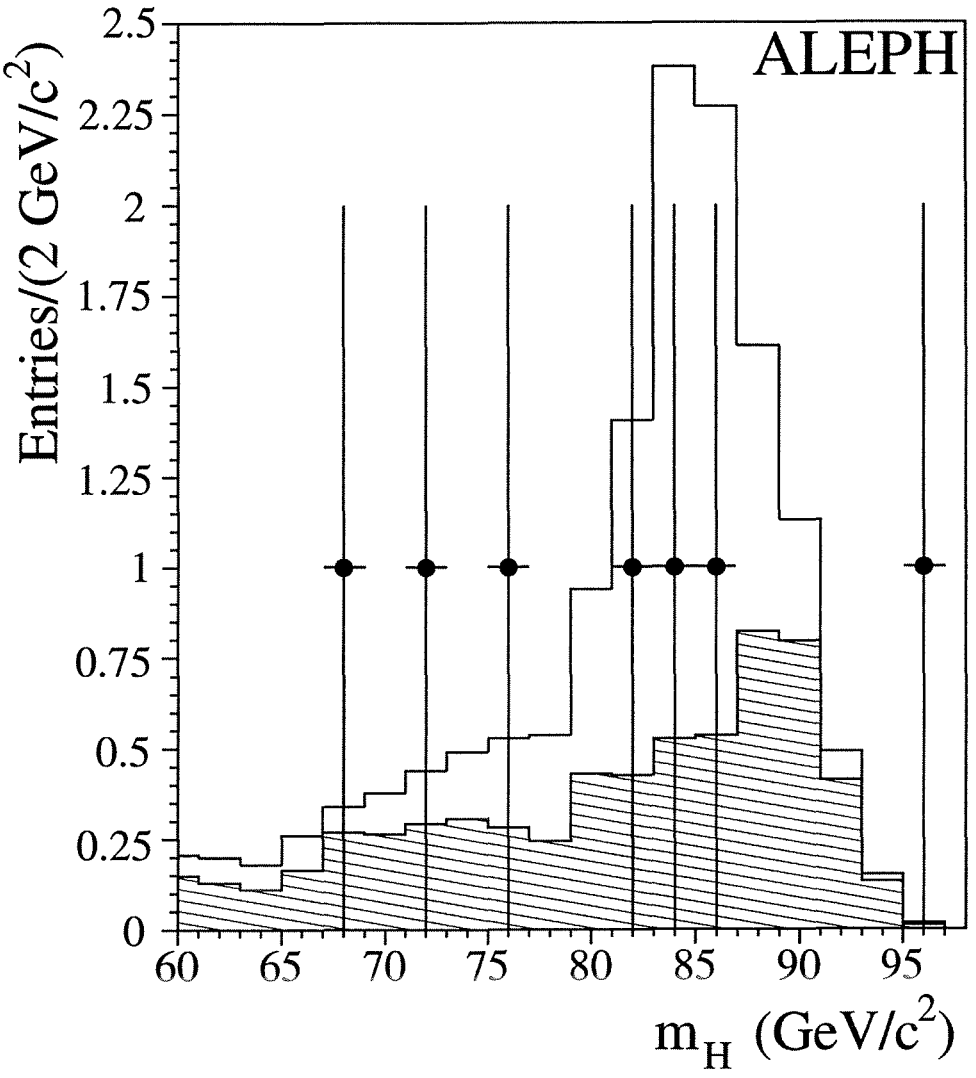

Figure 5.1: Distributions of the reconstructed Higgs boson mass of selected events in all search channels [146, 147]. The histogram shows the expected distribution from signal and background processes, with the contribution from background processes shown in the hatched histogram. The signal distribution is for a Higgs boson mass of $85\,\mathrm{GeV}/c^2$. The data events are shown with the points. The events selected in different channels do not have equal weights in the combination procedure but have been plotted here with unit weight for convenience.

5.2.1 Results from the Four-Jet Analyses

Four events from data are selected. One candidate event is selected by the cuts and neural network subselection and has a reconstructed Higgs boson mass of $71.5\,\mathrm{GeV}/c^2$. Two events are selected by the cut only subselection and have masses of 76.1 and $85.0\,\mathrm{GeV}/c^2$. One event is selected by the neural network only subselection and has a mass of $85.2\,\mathrm{GeV}/c^2$. The properties of these events are summarized in Table 5.2. Figures 5.2 through 5.5 show event displays of these candidate events in various views.

5.2.2 The Other Final State Analyses

Three candidates are selected in the dilepton channel with reconstructed Higgs boson masses of 67.0, 82.2, and $96.5\,\mathrm{GeV}/c^2$. The properties of these candidates are summarized in Table 5.3. An event display of one of these candidates is shown in Figure 5.6. No events are selected from data using the $\mathrm{H}\nu\bar{\nu}$, $\mathrm{H}\tau^+\tau^-$, and $\tau^+\tau^-\mathrm{q}\bar{\mathrm{q}}$ final state analyses.

5.3 Combined Results and Limits

Figure 5.7 shows the expected and observed confidence levels as a function of the hypothesized Higgs boson mass for the three independent subselections of the four-jet analyses and the combined confidence levels. The corresponding confidence levels for the other Higgsstrahlung final state analyses are shown in Figure 5.8. A lower limit on the Higgs boson mass of $85.7\,\mathrm{GeV}/c^2$ at 95%

Higgs Boson Candidates from Data in the Four-Jet Final State				
Run	44220	44830	44681	44253
Event	9376	2048	3559	6449
m_H	85.0	76.1	71.5	85.2
η_3	0.992	0.993	0.998	0.784
η_4	0.553	0.547	0.537	0.998
η_1	0.985	0.073	0.165	0.132
η_2	0.253	0.090	0.193	0.051
M_{34}	94.1	63.7	69.1	103.0
M_{12}	82.1	103.5	93.6	73.5
y_{34}	0.0120	0.0120	0.0206	0.0137
Θ	364	365	363	373
γ	-1.80	-1.74	-1.83	-1.72
$NN_{W^+W^-}$	0.866	0.938	0.994	0.971
$NN_{q\bar{q}}$	0.999	0.897	0.970	0.946

Table 5.2: A summary of the four Higgs boson candidate events in the four-jet final state analyses. The events in the first two columns are selected by the cut only subselection. The event in the third column is selected by the cut and neural network subselection. The event in the fourth column in selected by the neural network only subselection

Higgs Boson Candidates from Data in the Dilepton Final State				
Run	Event	Z Mass (GeV/c^2)	Higgs Mass (GeV/c^2)	$(\eta_1 + \eta_2)$
44128	409	91.3	82.2	0.94
44577	9277	85.0	96.5	1.89
44728	3975	91.4	67.0	1.07

Table 5.3: A summary of the three Higgs boson candidates in the dilepton final state analysis.

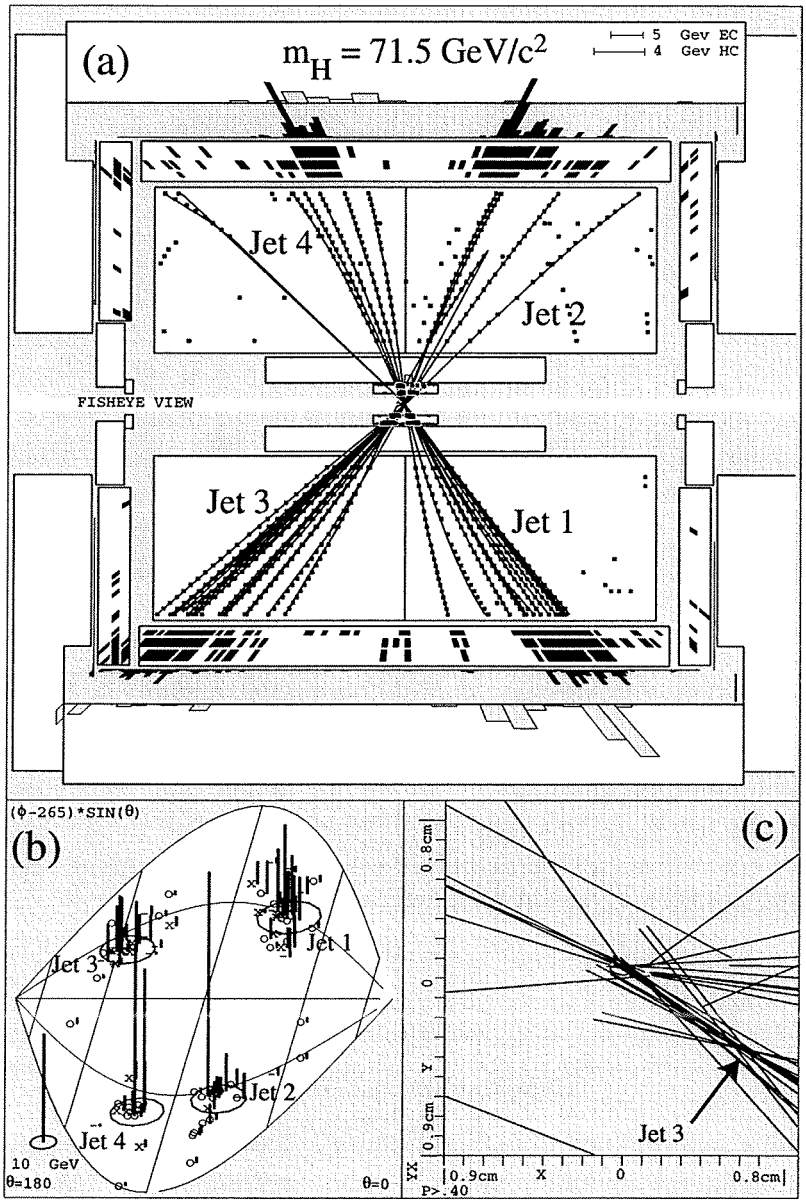

Figure 5.2: An event display of a Higgs boson candidate event (Run 44681, Event 3559) selected by both the neural network and cut-based four-jet final state analyses. The event displays show (a) an rz projection, (b) a $\theta\phi$ projection showing energy flow objects clustered into jets, and (c) an xy projection of the region near the primary vertex (the arrow indicates an apparent secondary vertex in one of the jets of the Higgs boson candidate).

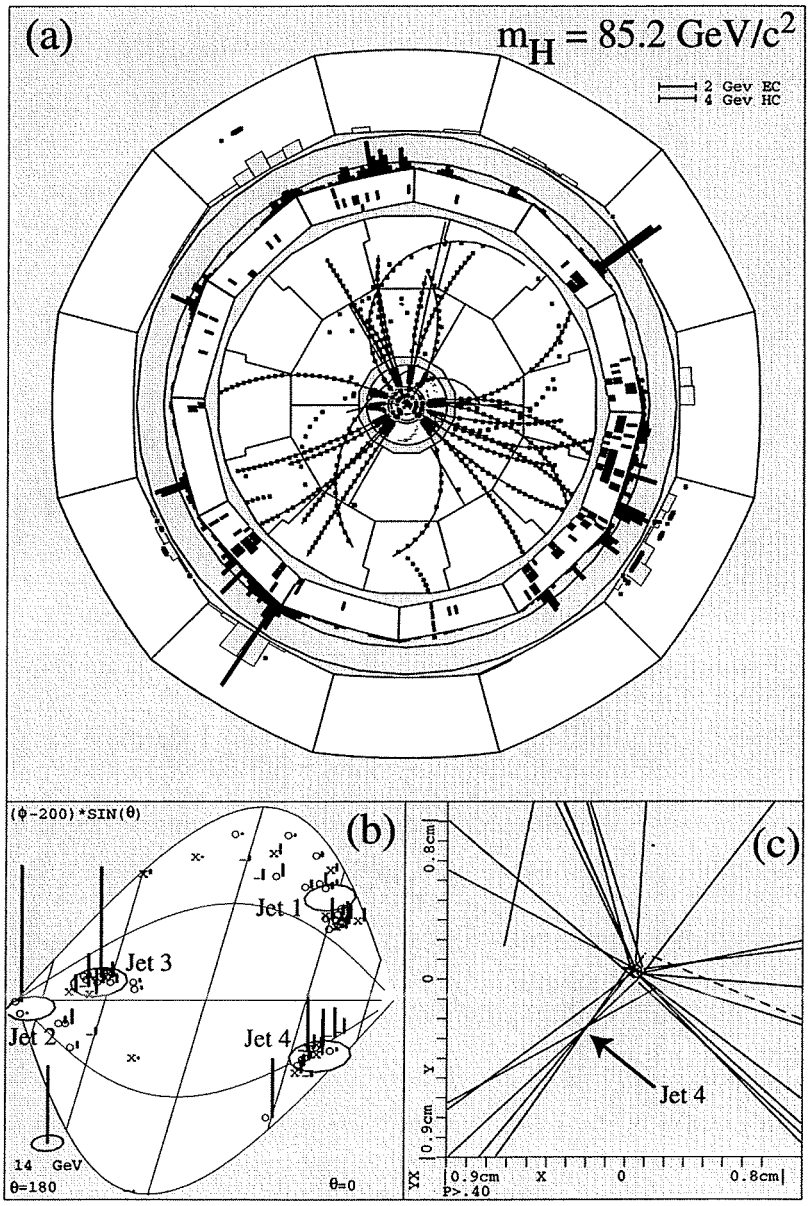

Figure 5.3: An event display of a Higgs boson candidate (Run 44253, Event 6449) selected only by the neural network four-jet final state analysis. The event displays show (a) an xy projection, (b) a $\theta\phi$ projection showing energy flow objects clustered into jets, and (c) an xy projection of the region near the primary vertex (the arrow indicates an apparent secondary vertex in one of the jets of the Higgs boson candidate).

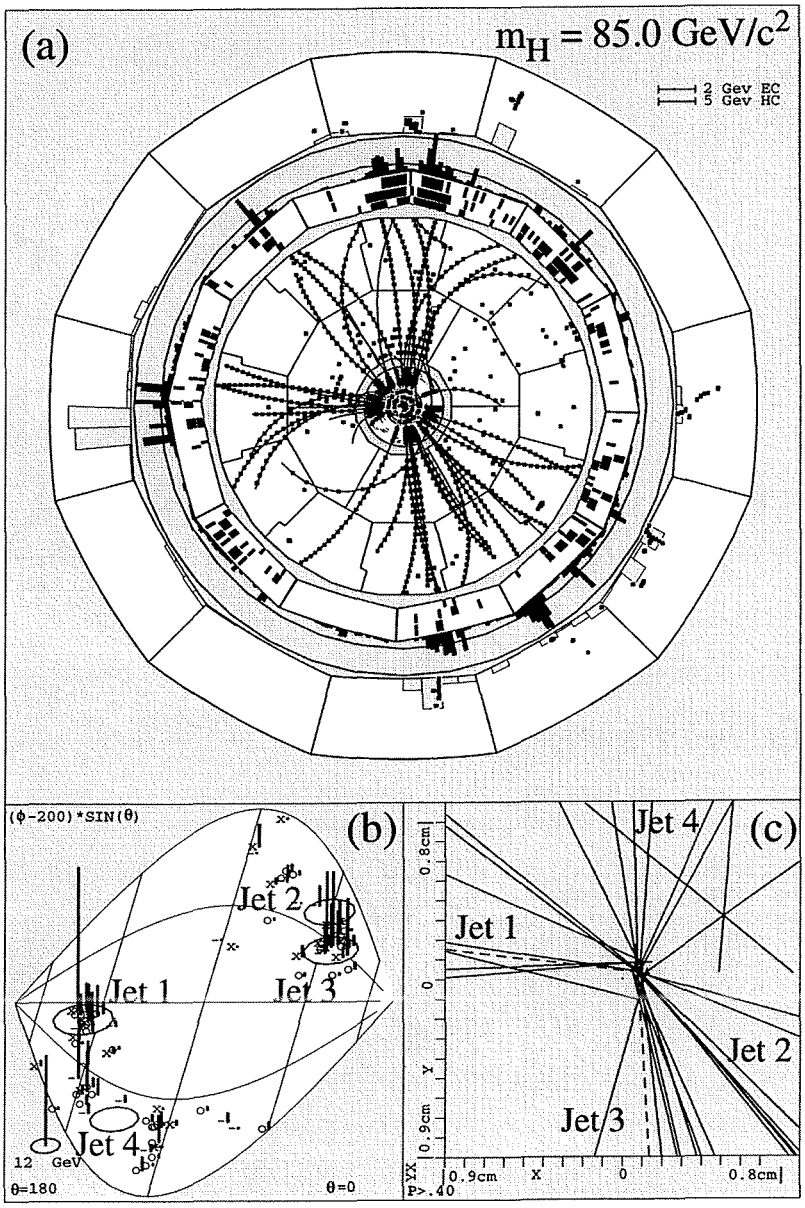

Figure 5.4: An event display of a Higgs boson candidate (Run 44220, Event 9376) selected only by the cut-based four-jet final state analysis. The event displays show (a) an xy projection, (b) a $\theta\phi$ projection showing energy flow objects clustered into jets, and (c) an xy projection of the region near the primary vertex.

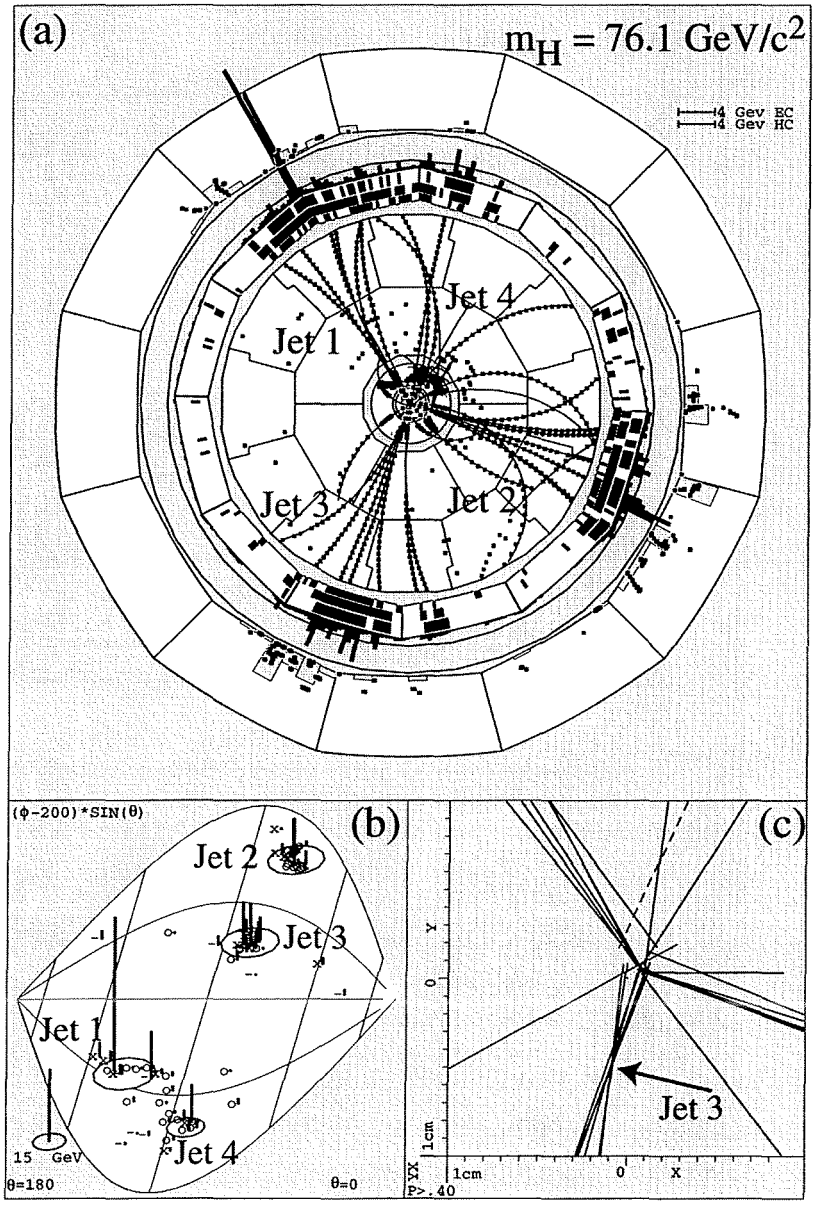

Figure 5.5: An event display of a Higgs boson candidate event (Run 44830, Event 2048) selected only by the cut-based four-jet final state analysis. The event displays show (a) an xy projection, (b) a $\theta\phi$ projection showing energy flow objects clustered into jets, and (c) an xy projection of the region near the primary vertex (the arrow indicates an apparent secondary vertex in one of the jets of the Higgs boson candidate).

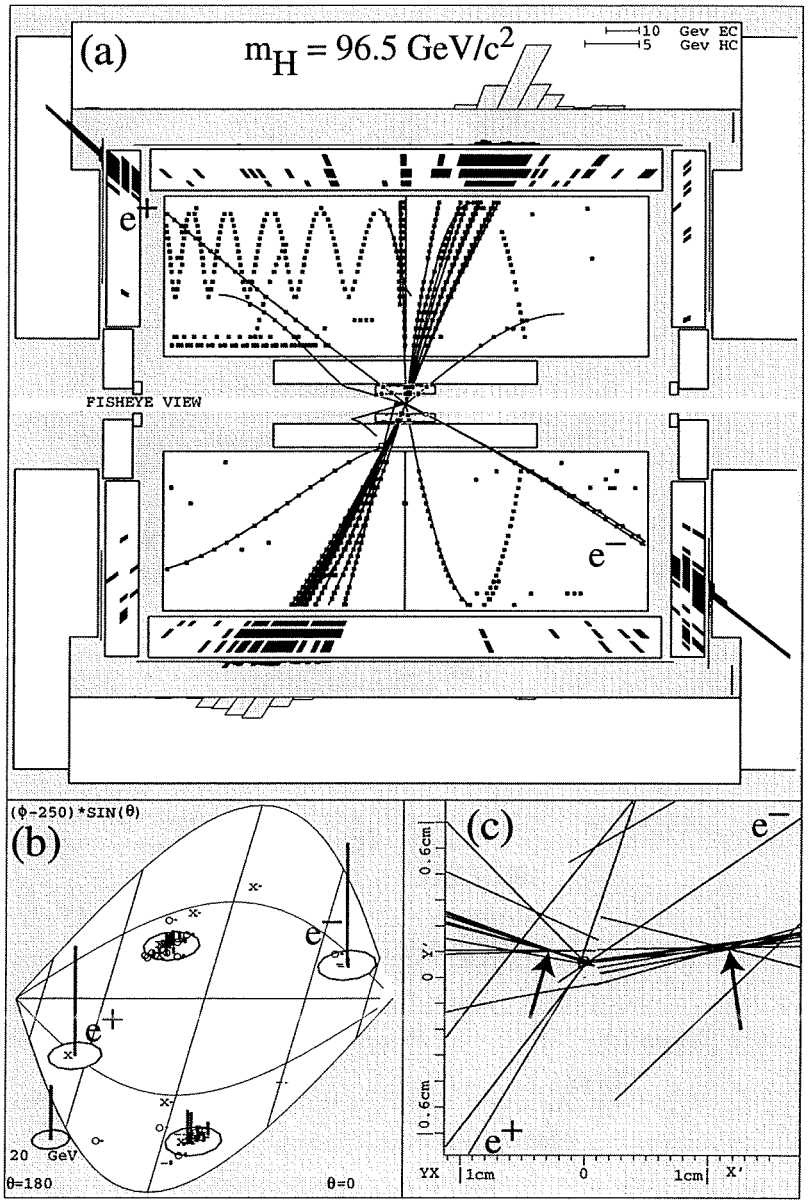

Figure 5.6: An event display of a Higgs boson candidate event (Run 44577, Event 9277) selected by the dilepton final state analysis. This event has an e^+e^- pair from the Z boson candidate and two well b-tagged jets from the Higgs boson candidate. The event displays show (a) an rz projection, (b) a $\theta\phi$ projection showing energy flow objects clustered into jets, and (c) an xy projection of the region near the primary vertex (the arrows indicate apparent secondary vertices in each of the jets).

confidence level is set using the combined confidence levels of the three four-jet subselections. It is not possible to set lower limits greater than 60 GeV/c^2 on the Higgs boson mass at the 95% confidence level using any of the other final state analyses alone.

The result obtained when all subselections are combined using the 57 pb^{-1} of high energy data is displayed in Figure 5.9. The lower limit on the Higgs boson mass at the 95% confidence level is 88.2 GeV/c^2.

Three events were selected by ALEPH Higgs boson searches from the LEP1 data in the H$\mu^+\mu^-$ final state with reconstructed Higgs masses of 49.7, 51.5, and 66.9 GeV/c^2 [36]. No events were selected by ALEPH Higgs boson searches in the $\sqrt{s} = 161, 170$, and 172 GeV data [126]. The corresponding confidence level curves combining the lower energy data results and the results with the data near 183 GeV are shown in Figure 5.10. These lower energy data results only have an impact on the confidence levels for mass values lower than roughly 75 GeV/c^2 and do not change the 88.2 GeV/c^2 lower limit at 95% confidence level.

The values of the LEP energy have been determined by the LEP energy working group [148] to be consistently 0.280 GeV lower than the values used to calculate all of the confidence levels quoted. The cross sections are reevaluated at these new energies which translates into a decrease of the mass limit by 0.2 GeV/c^2.

Incorporating this systematic LEP energy shift, the Higgsstrahlung searches exclude all Higgs boson masses below 88.0 GeV/c^2 at the 95% confidence level. The average limit expected in the absence of signal is

85.3 GeV/c^2. With this expected limit, the probability to observe a limit at least as high as 88.0 GeV/c^2 is 22%.

As explained in Chapter 4 and Appendix A, a number of systematic effects are studied and their impacts evaluated. The uncertainties related to the selection procedure and to the inadequacies of the simulation of events dominate, translating into uncertainties on the selection efficiencies ranging from roughly 0.5% to 7%, depending on the final state. Following the method of Ref. [142], a small decrease of the confidence level results. This corresponds to a change in the mass limit of $-0.1\,\mathrm{GeV}/c^2$.

The mass of the Standard Model Higgs boson therefore exceeds 87.9 GeV/c^2 at the 95% confidence level. This is significantly higher than the previous lower limit on the mass of the Higgs boson of 70.7 GeV/c^2 at 95% confidence level which used the ALEPH data taken at center-of-mass energies of 161 and 172 GeV and the ALEPH LEP1 data.

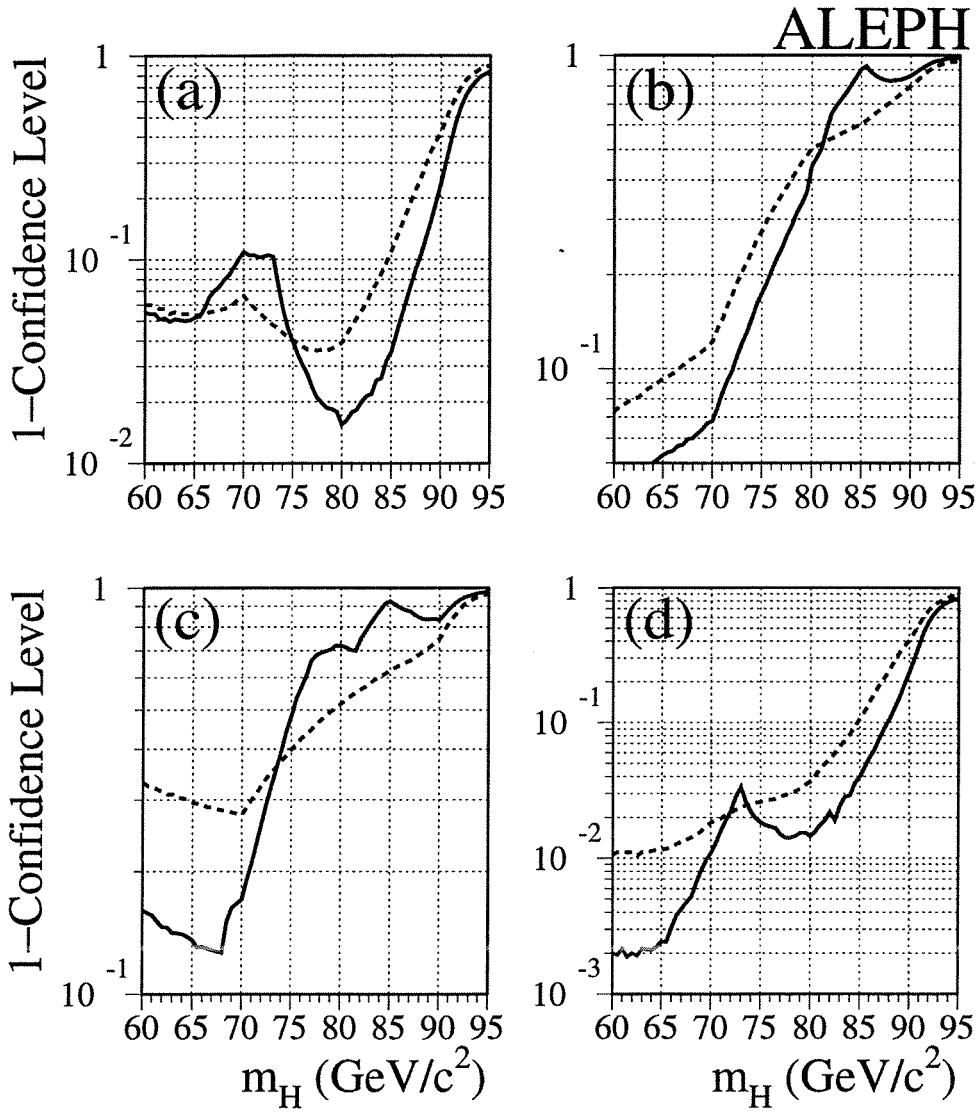

Figure 5.7: The observed (solid line) and expected (dashed line) confidence levels as a function of the Higgs boson mass for combinations of the four-jet final state analyses: (a) the cut-based *AND* neural network subselection, (b) the neural network only subselection, (c) the cut-based only subselection, (d) the combination of these three subselections [146, 147].

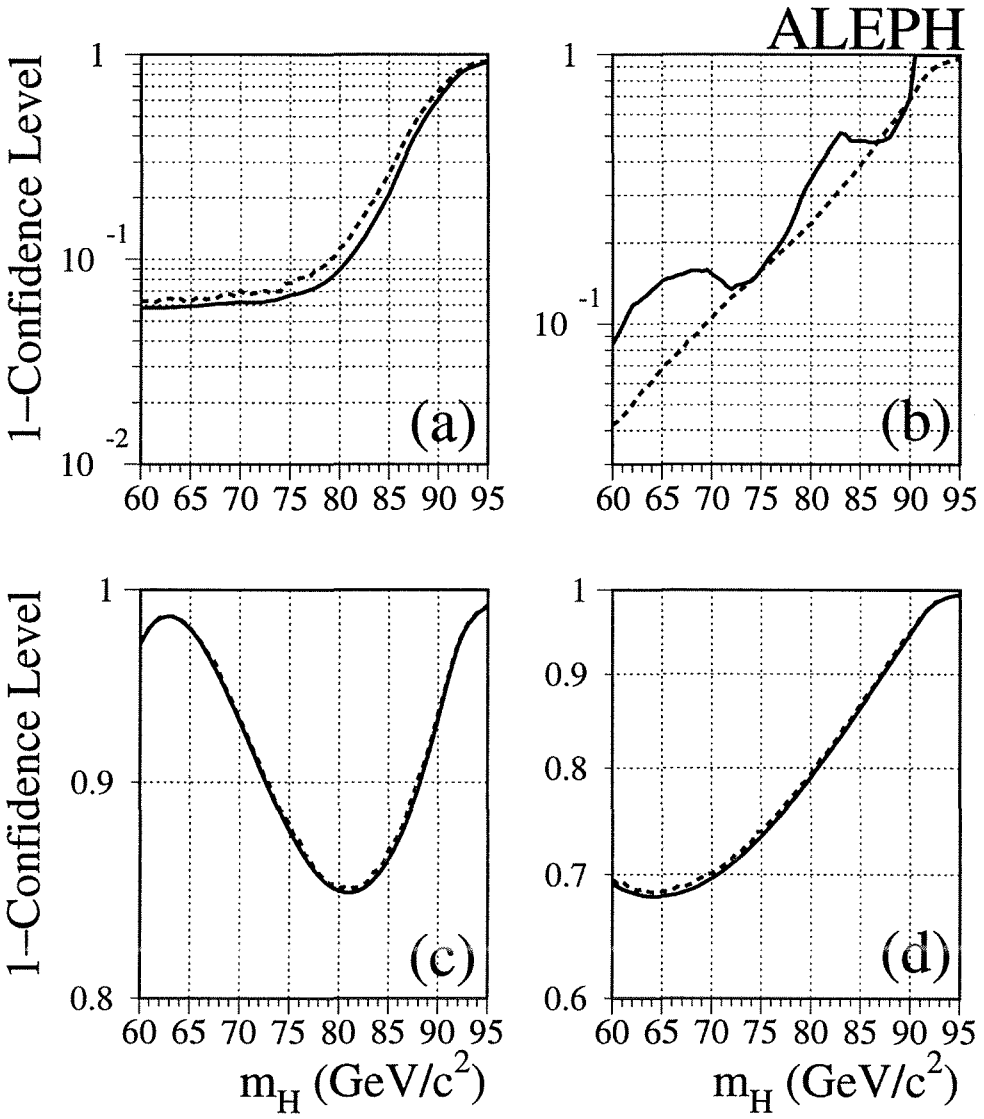

Figure 5.8: The observed (solid line) and expected (dashed line) confidence levels as a function of the Higgs boson mass for the the final states other than four-jets: (a) the combination of the cut-base and neural network selections for $H\nu\bar{\nu}$, (b) $H\ell^+\ell^-$, (c) $\tau^+\tau^-q\bar{q}$, (d)$H\tau^+\tau^-$ [146, 147].

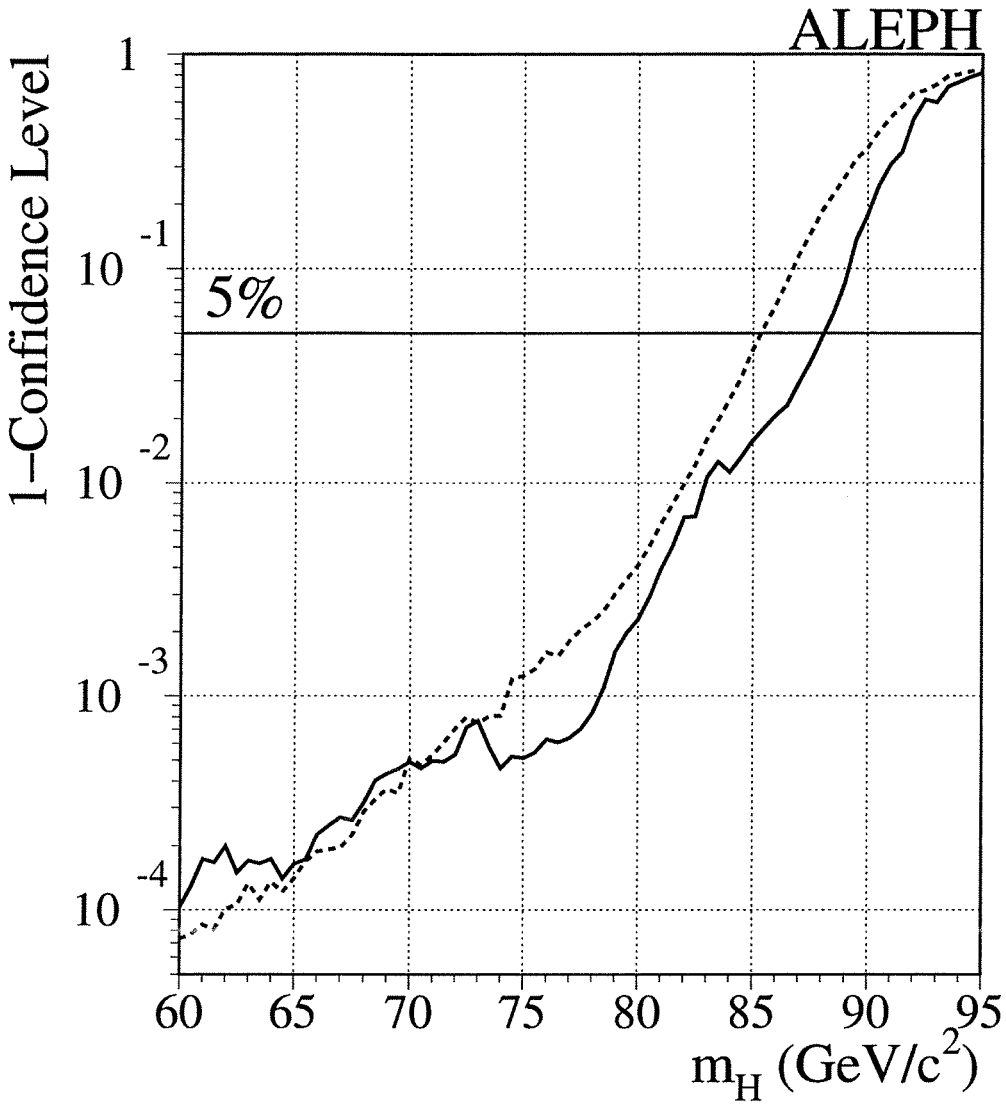

Figure 5.9: The observed (solid line) and expected (dashed line) confidence levels as a function of the Higgs boson mass after all channels are combined, using only the $57\,\mathrm{pb}^{-1}$ of ALEPH data taken at center-of-mass energies near 183 GeV [146, 147]. The solid horizontal line denotes an exclusion confidence level of 95%.

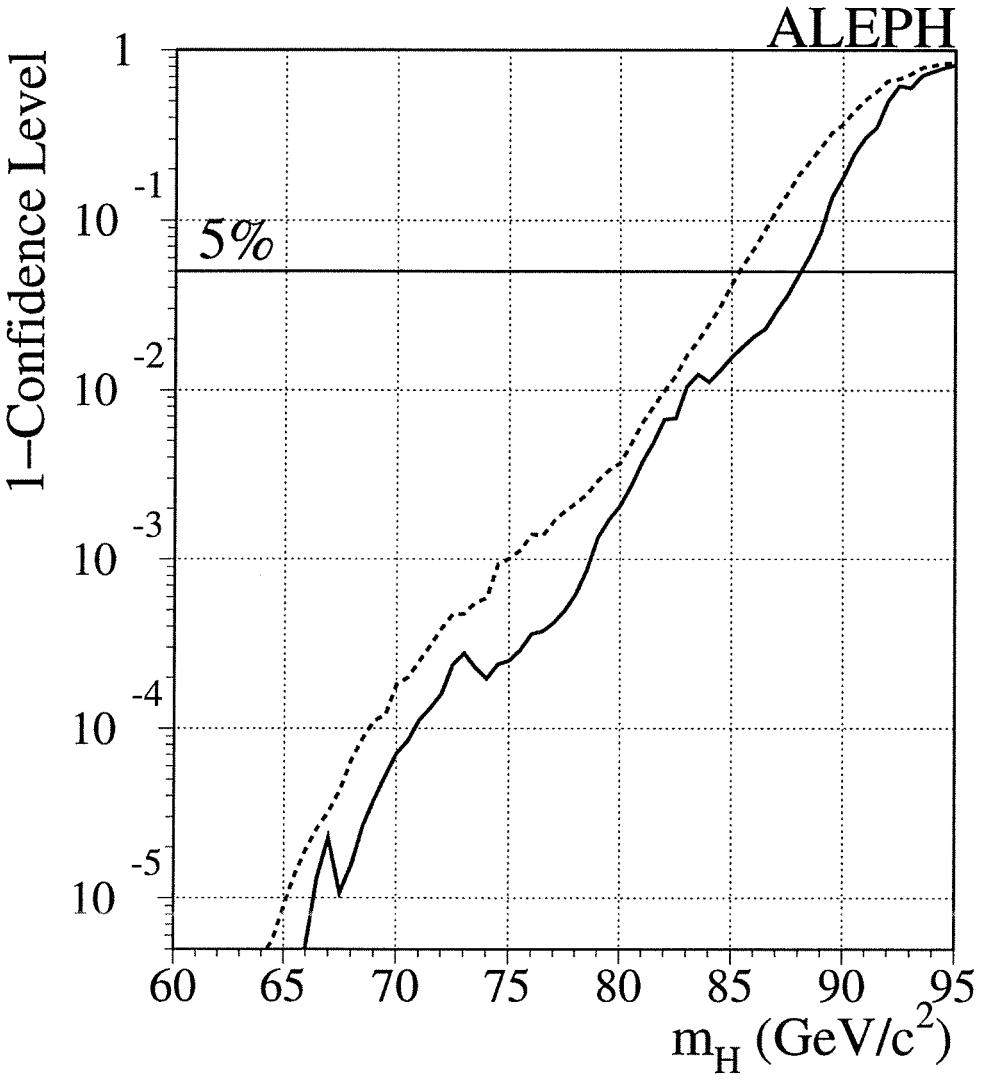

Figure 5.10: The observed (solid line) and expected (dashed line) confidence levels as a function of the Higgs boson mass using all ALEPH data (LEP1 and LEP2) [146, 147]. The solid horizontal line denotes an exclusion confidence level of 95%.

Chapter 6

Summary, Outlook, and Conclusion

6.1 Summary

The results from the ALEPH Higgs boson searches show no evidence for the production of the Higgs boson in the data collected at center-of-mass energies near 183 GeV; a 95% confidence level lower limit of 87.9 GeV/c^2 is set. The other LEP experiments also conducted searches for the Standard Model Higgs boson. Their data also show no evidence of Higgs boson production, and lower limits on the Higgs boson mass of 85.7, 87.6, and 88.3 GeV/c^2 at the 95% confidence level are obtained by DELPHI, L3, and OPAL respectively [149]. These results are summarized in Table 6.1. Combining these four results, a preliminary combined 95% confidence level lower limit on the mass of the Higgs boson is determined to be 89.8 GeV/c^2 [150].

LEP Higgs Boson Searches at $\sqrt{s}$=183 GeV				
	Experiment			
	ALEPH	DELPHI	L3	OPAL
Observed Events	7	6	18	9
Expected Background	7.2	6.5	24.2	8.9
Observed Limit at 95% C.L. (GeV/c^2)	87.9	85.7	87.6	88.3
Expected Limit at 95% C.L. (GeV/c^2)	85.5	86.5	85.0	86.2

Table 6.1: A summary of results of Higgs boson searches conducted by the four LEP experiments. The lower limits use LEP2 data collected at $\sqrt{s}$ = 161, 172, and 183 GeV and the LEP1 data [150].

6.2 Outlook for the Future

Although the existence of the Higgs boson has not been experimentally confirmed, there is still a wide range of Higgs masses that remain unexplored. These unexplored ranges will be probed by the increasing center-of-mass energies at LEP2, the upgraded Tevatron collider, the approved future Large Hadron Collider (LHC), and possibly a future high energy e^+e^- collider.

6.2.1 Future LEP Higgs Boson Searches

In 1998, LEP will have delivered an integrated luminosity of roughly 200 pb^{-1} to each of the four LEP experiments at a center-of-mass energy of 189 GeV. The same or similar analyses designed to search for the Higgs boson at center-of-mass energies near 183 GeV can be applied to these higher energy data. During the summer of 1998, LEP had already delivered roughly 35 pb^{-1}, and each of the four LEP experiments performed preliminary searches using this

Preliminary LEP Higgs Boson Searches at $\sqrt{s}$=189 GeV				
	Experiment			
	ALEPH	DELPHI	L3	OPAL
Observed Events	10	4	22	4
Expected Background	8.0	4.8	18.0	8.6
Observed Limit at 95% C.L. (GeV/c^2)	88.0	89.6	89.0	93.6
Expected Limit at 95% C.L. (GeV/c^2)	87.5	89.5	88.6	89.3

Table 6.2: A summary of preliminary results of Higgs boson searches conducted by the four LEP experiments. The lower limits use LEP2 data collected at $\sqrt{s}$ = 161, 172, 183, and 189 GeV and the LEP1 data [150].

data sample. The results of these searches are summarized in Table 6.2.1. Preliminary lower limits were set on the mass of the Higgs boson at 95% confidence level of 88.0, 89.6, 89.0, and 93.6 GeV/c^2 by ALEPH, DELPHI, L3, and OPAL respectively [151].

During 1999 and 2000, LEP should be able to achieve center-of-mass energies approaching 200 GeV, increasing the sensitivity to the Higgs boson mass up to roughly 105 GeV/c^2. If the Higgs boson is not discovered at LEP2, this task will be taken up by experimentalists at future colliders.

6.2.2 Future Higgs Searches at the Tevatron

The main injector upgrade will increase the Tevatron's center-of-mass energy to 2 TeV from 1.8 TeV and luminosity to $2 \times 10^{32}\,\mathrm{cm}^{-2}\mathrm{s}^{-1}$ from $10^{31}\,\mathrm{cm}^{-2}\mathrm{s}^{-1}$. This will offer the CDF and D0 experiments the possibility to explore a Higgs boson mass range from 80 to around 120 GeV/c^2 if a sufficiently large integrated luminosity is collected [152].

The primary Higgs production process considered is $q\bar{q} \rightarrow W^{\pm}H$ with $H \rightarrow b\bar{b}$ and $W^{\pm} \rightarrow \ell\nu_{\ell}$, where ℓ denotes either an electron or a muon. At a center-of-mass energy of 2 TeV and a Higgs mass of 80 GeV/c^2, this process has a cross section of 500 fb (which must be multiplied by the branching ratio of roughly 21% for $W^{\pm} \rightarrow e\nu_e$, $\mu\nu_{\mu}$). Searches for this process could be supplemented with searches for the Higgs production process $q\bar{q} \rightarrow (W^{\pm}, Z)H$ with $H \rightarrow \tau^{+}\tau^{-}$ and $(W^{\pm}, Z) \rightarrow q\bar{q}$.

Studies indicate that with a data sample of 5 fb^{-1} it should be possible to discover a Higgs boson in the mass range from 60 to 90 GeV/c^2. To explore the mass range up to 120 GeV/c^2 would require more integrated luminosity, on the order of roughly 25 fb^{-1} [152].

6.2.3 Future Higgs Searches at the LHC

The LHC will be a pp collider with a center-of-mass energy of 14 TeV and a peak design luminosity of $10^{34}\,\mathrm{cm}^{-2}\mathrm{s}^{-1}$ [153]. With the advent of the LHC, it will be possible to search for the Higgs boson with a mass up to 1 TeV/c^2 with the two main LHC detector experiments: A Toroidal LHC ApparatuS (ATLAS) [154] and the Compact Muon Solenoid (CMS) [155].

The dominant Higgs boson production mechanism at the LHC will be the gluon fusion process $pp \rightarrow gg \rightarrow H$ with a cross section ranging between 100 to 0.1 pb for Higgs boson masses between 100 GeV/c^2 and 1 TeV/c^2. Fusion processes involving $W^{\pm}$ and Z bosons lead to the next most prevalent production process: $qq \rightarrow Hqq$ with a cross section between 10 and 0.1 pb.

Diagrams contributing to Higgs boson production at the LHC are shown in Figure 6.1. Production cross sections are shown in Figure 6.2.

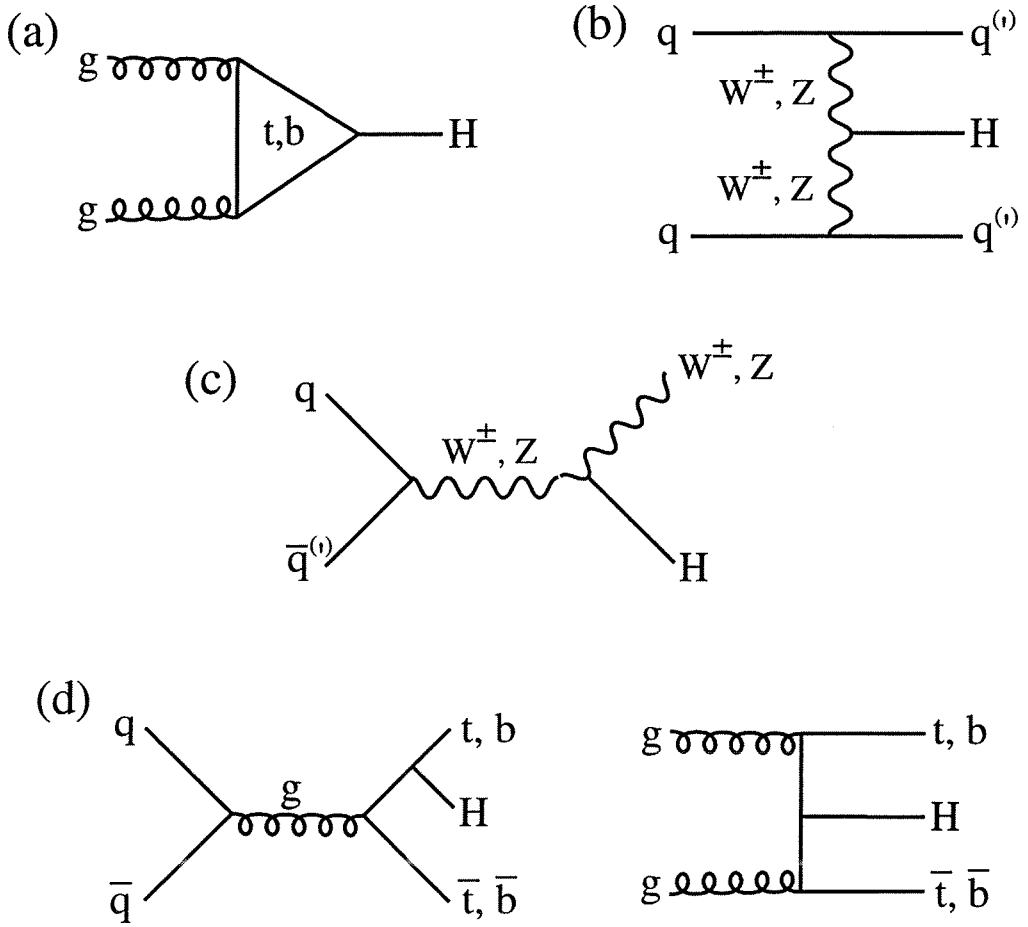

Figure 6.1: Diagrams contributing to Higgs boson production at the LHC: (a) $gg \rightarrow H$, (b) $qq \rightarrow Hqq$, (c) $q\bar{q}^{(\prime)} \rightarrow H(W^{\pm}, Z)$, and (d) $q\bar{q}/gg \rightarrow H(b\bar{b}, t\bar{t})$.

Despite the LHC impressive center-of-mass energy and luminosity, the LEP2 and Tevatron Higgs boson searches will still be important since the mass range from 90 to 140 GeV/c^2 is the most difficult for the LHC exper-

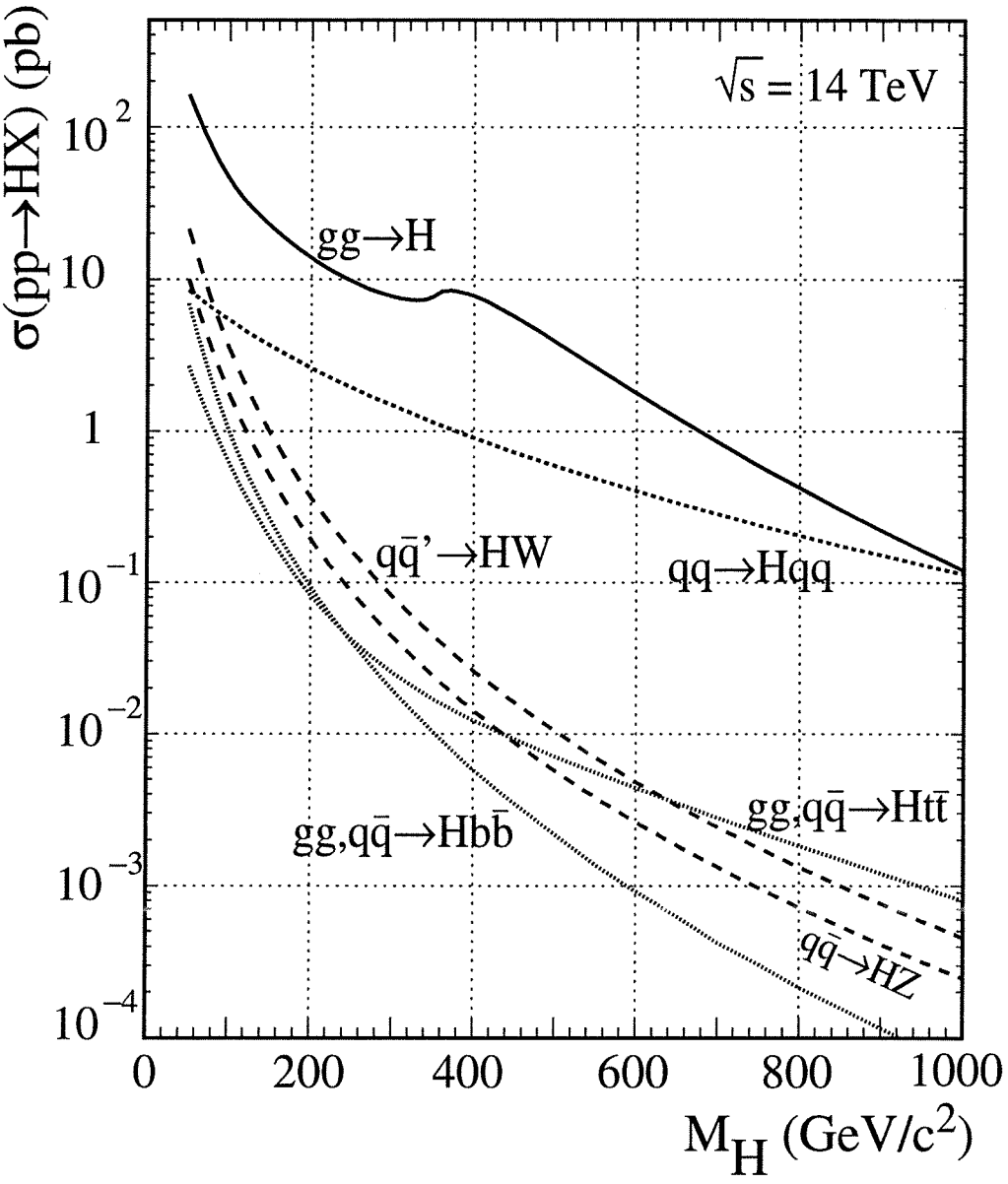

Figure 6.2: Higgs boson production cross sections at the LHC from Ref. [156].

iments [152]. As discussed in Section 1.2.2, in this mass range the Higgs boson decays predominantly to $b\bar{b}$. Unfortunately, at the LHC, QCD background processes will overwhelm this signal. Other backgrounds render the $H \rightarrow \tau^+\tau^-$ mode infeasible. The most promising mode to use is the rare $H \rightarrow \gamma\gamma$ decay mode for light Higgs boson searches. For a $100\,fb^{-1}$, CMS will be able discover (*i.e.*, the signal significance would exceed the 5σ level) the Higgs boson in the mass range from 90 to $140\,GeV/c^2$ utilizing its high-resolution, high-granularity crystal calorimeter [155]. With the same integrated luminosity ATLAS can search in the range 110 to $140\,GeV/c^2$ but would need on the order of $400\,fb^{-1}$ to reach down to $90\,GeV/c^2$ [154, 157].

The situation for Higgs boson masses from 140 to roughly $800\,GeV/c^2$ is different. In this mass regime, the Higgs boson decays predominantly to W^+W^- and $ZZ^{(*)}$. A *gold-plated* mode exists with very low background: $H \rightarrow ZZ^{(*)} \rightarrow \ell^+\ell^-\ell^+\ell^-$. It is possible to use decays modes of the dominant $H \rightarrow W^+W^-$, but the background is larger [154, 155, 156]. A discovery for a Higgs boson in the mass range for the gold-plated signal would need only a very small integrated luminosity, perhaps as little as $10\,fb^{-1}$ [155].

For Higgs boson masses between $800\,GeV/c^2$ and 1 TeV, the total width of the Higgs boson becomes large, between 100 and $600\,GeV/c^2$. Due to this broad resonance, the gold-plated signal channel becomes insufficient and must be supplemented with or abandoned in favor of higher rate channels such as $H \rightarrow (ZZ,\ W^+W^-) \rightarrow \ell\ell\nu\nu$ [154, 155].

6.2.4 Future Higgs Searches at e^+e^- Linear Colliders

Several preliminary proposals exists for future high luminosity and high energy e^+e^- colliders: the Next Linear Collider (NLC) [158] and the Compact (or CERN) Linear Collider (CLIC) [159]. The first such collider will probably have a center-of-mass energy around 500 GeV with the potential to increase it to 1.5 GeV [160].

The Higgs production mechanisms are similar to those at LEP2: the Higgsstrahlung, W^+W^-, and ZZ fusion processes discussed in Section 1.2.1. As shown in Figure 6.3, the W^+W^- fusion process dominates at high energies. There is the additional production mechanism of radiation off of top quarks $e^+e^- \rightarrow (\gamma,\ Z) \rightarrow t\bar{t} + H$, but the cross section for this is very small [157]. There is also the possibility that these future e^+e^- machines could be run in a $\gamma\gamma$ or $e^{\pm}\gamma$ collider mode, in which case the Higgs could be produced via $\gamma\gamma \rightarrow H$, $e\gamma \rightarrow \nu W^{\pm}H$, and $e\gamma \rightarrow eH$ processes [161].

Studies indicate that in e^+e^- collisions at a center-of-mass energy of 500 GeV an integrated luminosity of $5\,fb^{-1}$ would be needed to discover the Higgs boson with mass up to $180\,GeV/c^2$. To extend the discovery range up to $300\,GeV/c^2$ would require roughly $50\,fb^{-1}$ [162].

6.3 Conclusion

While the search for the Higgs boson presented in this thesis reveals no evidence of its existence, there is still an ample range of experimentally un-

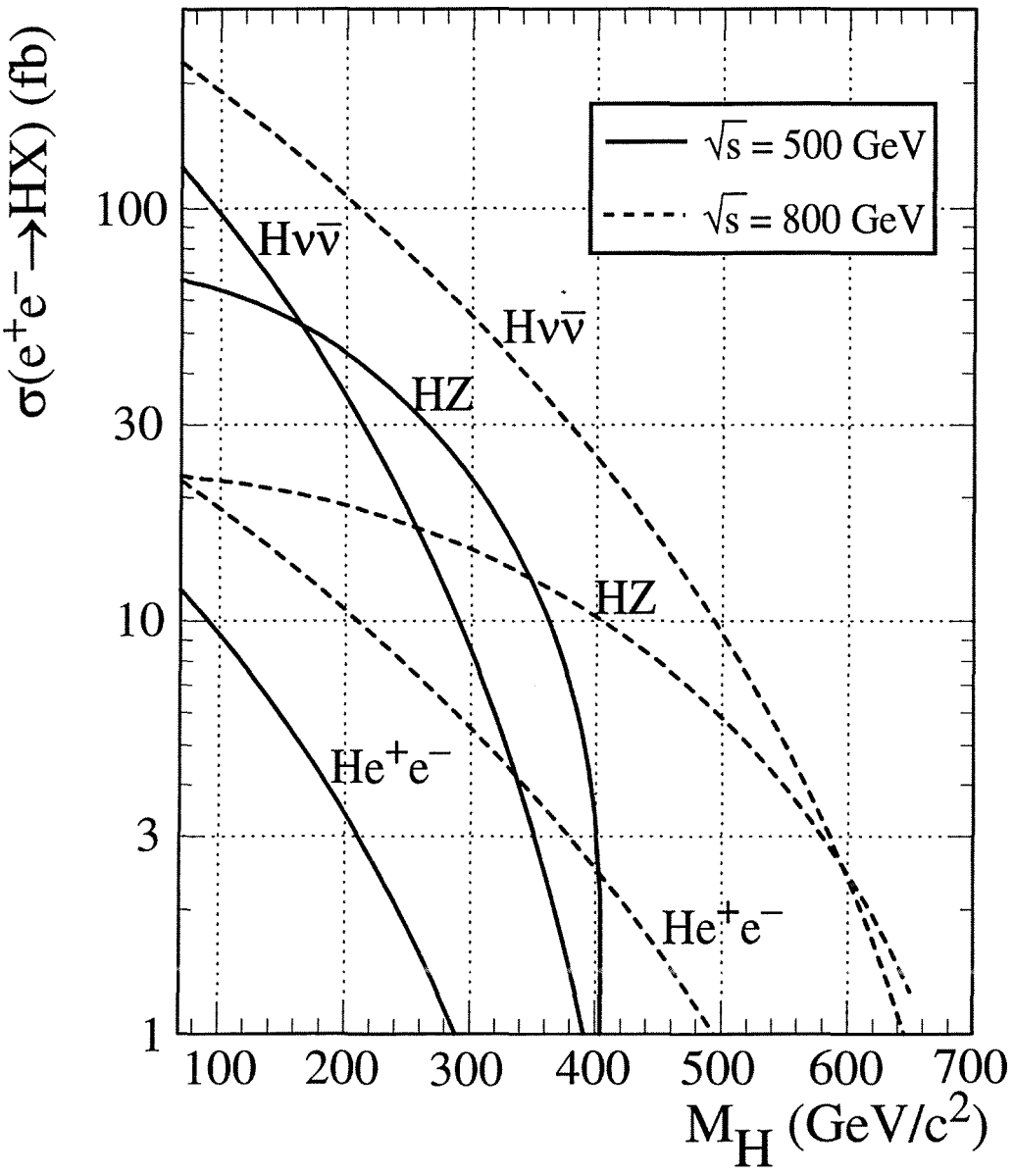

Figure 6.3: Higgs boson production cross sections in high energy e^+e^- collisions from Ref. [161]. The solid curves are for a center-of-mass energy of 500 GeV while the dashed curves are for a center-of-mass energy of 800 GeV. The HZ, $H\nu\bar{\nu}$, and He^+e^- curves refer to the Higgsstrahlung, W^+W^- fusion, and ZZ fusion processes respectively.

explored masses. If this Higgs boson exists, there is an excellent discovery potential for it at present and future colliders. If the Higgs boson has not been discovered by the end of the LHC era, the Higgs mechanism for spontaneous electroweak symmetry breaking may have to be reevaluated and possibly replaced by another theory which in turn will need experimental verification.

Appendix A

Other Higgsstrahlung Final State Event Selections

This appendix briefly describes the event selections used for other possible $e^+e^- \to HZ$ final states: the leptonic channel $H\ell^+\ell^-$ [147, 163], the missing mass channel $H\nu\bar{\nu}$ [147, 164], and final states with τ leptons $H\tau^+\tau^-$ and $\tau^+\tau^-q\bar{q}$ [147, 165]. The $\tau^+\tau^-\tau^+\tau^-$ and $\tau^+\tau^-\nu\bar{\nu}$ final states are not explicitly considered. All of these analyses rely upon the neural network b-tagger described in Chapter 3 with the exception of the $\tau^+\tau^-\ell^+\ell^-$ and $\tau^+\tau^-q\bar{q}$ analyses. The results of these analyses are combined together with the $Hq\bar{q}$ analyses described in Chapter 4 using the methods described in Chapter 5.

A.1 The Dilepton Final States

The $H\ell^+\ell^-$ channel represents 6.7% of the Higgsstrahlung cross-section where ℓ refers to either an electron or a muon. The signal events are characterized by two leptons with an invariant mass close to M_Z and a recoil mass equal to the Higgs mass. The case in which the Higgs boson decays to $\tau^+\tau^-$ is also considered. Although the branching ratio of this channel is small, the experimental signature is very clear and the Higgs boson mass can be reconstructed with high resolution.

Figure A.1 shows an exemplary simulated Higgs signal event in this final state at $\sqrt{s} = 183\,\text{GeV}$ and with a Higgs boson mass of $85\,\text{GeV}/c^2$. The event has two energetic muons from the Z and two b jets from the Higgs boson. One jet has an apparent secondary vertex indicated with an arrow in Figure A.1(c).

A.1.1 Selection Criteria

Events are required to have at least four good tracks with $|\cos\theta| < 0.95$ with a total charged energy larger than $0.1\sqrt{s}$.

The selection procedure reconstructs the Z boson by finding pairs of oppositely charged particles, hereafter referred to as *leptons*. To be considered as lepton candidates, charged particles must either be identified as electrons or muons, or else must be isolated from other particles by more than 10°. The isolation angle of a particle is defined as the half-angle of the largest cone around the particle direction containing less than 5% of the total energy

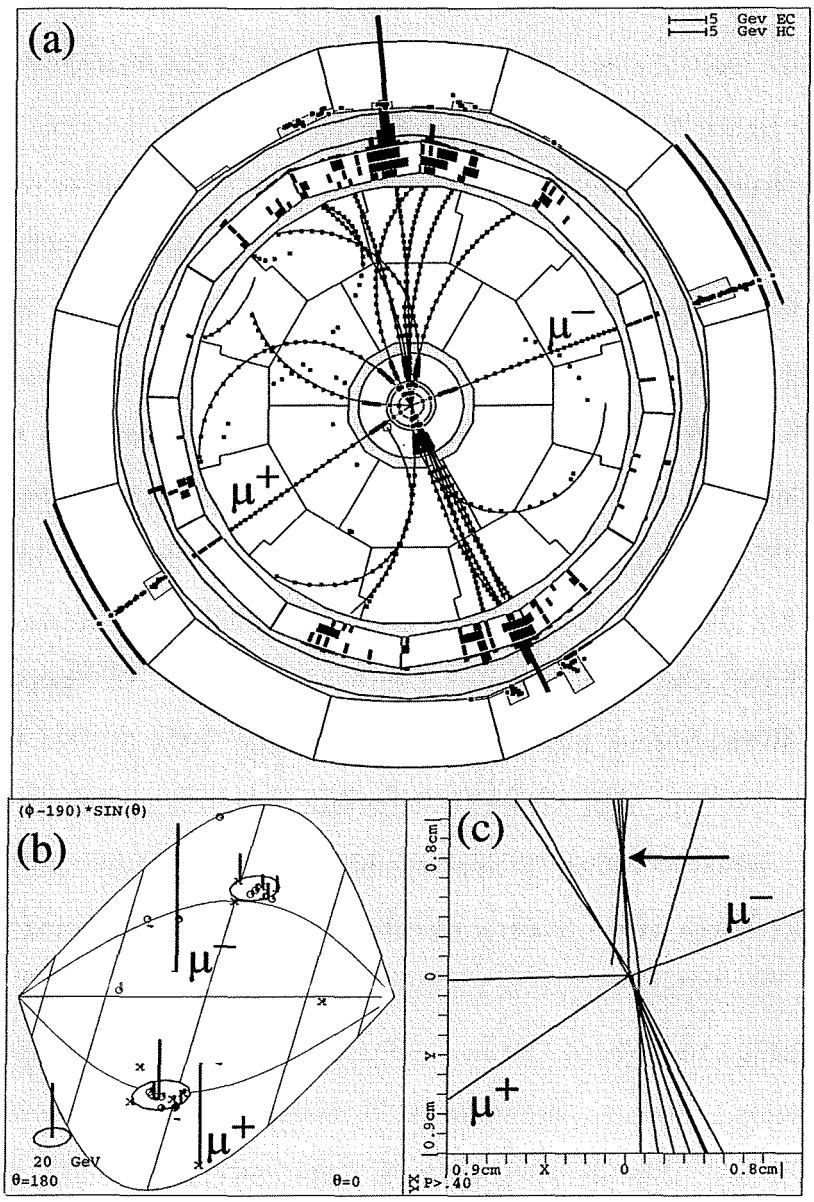

Figure A.1: An ALEPH event display of a simulated dilepton ($\mu^+\mu^-$) channel Higgs signal event at $\sqrt{s} = 183\,\text{GeV}$ and with a Higgs boson mass of $85\,\text{GeV}/c^2$: (a) an xy projection, (b) a $\theta\phi$ projection showing energy flow objects, and (c) an xy projection of the region near the primary vertex (the arrow indicates a secondary vertex due to b hadron decay).

of the other particles in the event. To account for possible bremsstrahlung photons, neutral energy-flow objects within 2° of the directions of the lepton momenta are excluded from the isolation calculation. In events with an identified electron, the energy of these neutral objects is added to the electron energy. All accepted combinations of oppositely charged lepton candidates must have at least one identified lepton. Mixed e-μ pairs are not considered.

Low angle muons are identified down to 7.5° from the beam line by finding hit patterns in the hadronic calorimeter consistent with a muon. The momentum of such a low angle muon is calculated from an over-constrained fit to the event using energy and momentum conservation. Low angle electrons are identified down to 12.4° from the beam line by finding large isolated energy deposits in the electromagnetic calorimeters. To separate these electrons from photons, an electron candidate must have at least two consistent hits in the ITC. This expanded definition of lepton candidates improves the $H\ell^+\ell^-$ signal efficiency by approximately 4% for the same purity.

The Higgs boson mass is calculated as the mass recoiling to the lepton pair. Final state radiation photons off the Z decay products are identified and added to isolated lepton candidates to improve the Higgs boson mass resolution. Such a photon must be isolated and have an energy greater than 2 GeV. The isolation angle is determined in the same way as above, but excluding the leptons from the calculation. If more than one photon is identified, the photon which forms with the leptons the invariant mass closest to M_Z is chosen. The reconstructed $\ell^+\ell^-(\gamma)$ mass is allowed to vary according to the procedure described in Chapter 5. The working point corresponds to

requiring this quantity to be greater than $82.75\,\mathrm{GeV}/c^2$.

To reject events with an energetic photon from a radiative Z return, the most energetic isolated photon must have an energy less than 75% of the most probable energy of the photon in $q\bar{q}(\gamma)$ events.

After selection of the lepton pair, the remaining particles are clustered into two jets using the Durham algorithm. To reject $q\bar{q}(\gamma)$ events where the leptons are close to the jets, the sum of the transverse momenta of the leptons with respect to their nearest jet is required to be greater than $20\,\mathrm{GeV}/c$. The visible mass, excluding the particles attributed to the Z decay, must be larger than $15\,\mathrm{GeV}/c^2$. This rejects $e^+e^- \to \gamma^*$ and $Z\gamma^*$ processes with a low γ^* mass. The background from $W^+W^- \to q\bar{q}'\ell\nu$ events is rejected by explicitly reconstructing the $W^\pm$ bosons. The missing four-momentum (neutrino) and the lepton are assigned to the leptonic W. Events with exactly four good tracks are candidates for $(H \to \tau^+\tau^-)\ell^+\ell^-$ and are required to have a missing energy of at least $0.1\sqrt{s}$. Although requirements on the neural network b-tag output for the two jets are not explicit event selection criteria, this information is used in the limit setting procedure described in Chapter 5.

Figure A.2 shows the performance of this analysis in terms of number of expected background events versus signal efficiency; the performance curve is obtained by varying the reconstructed $\ell^+\ell^-(\gamma)$ mass. The $H\ell^+\ell^-$ working point corresponds to a selection efficiency is 76.2% for $M_H = 85\,\mathrm{GeV}/c^2$. The total background expected is 2.0 events, dominated by the topologically indistinguishable backgrounds from the ZZ and Zee processes. Results from the data are presented in Section 5.2.2.

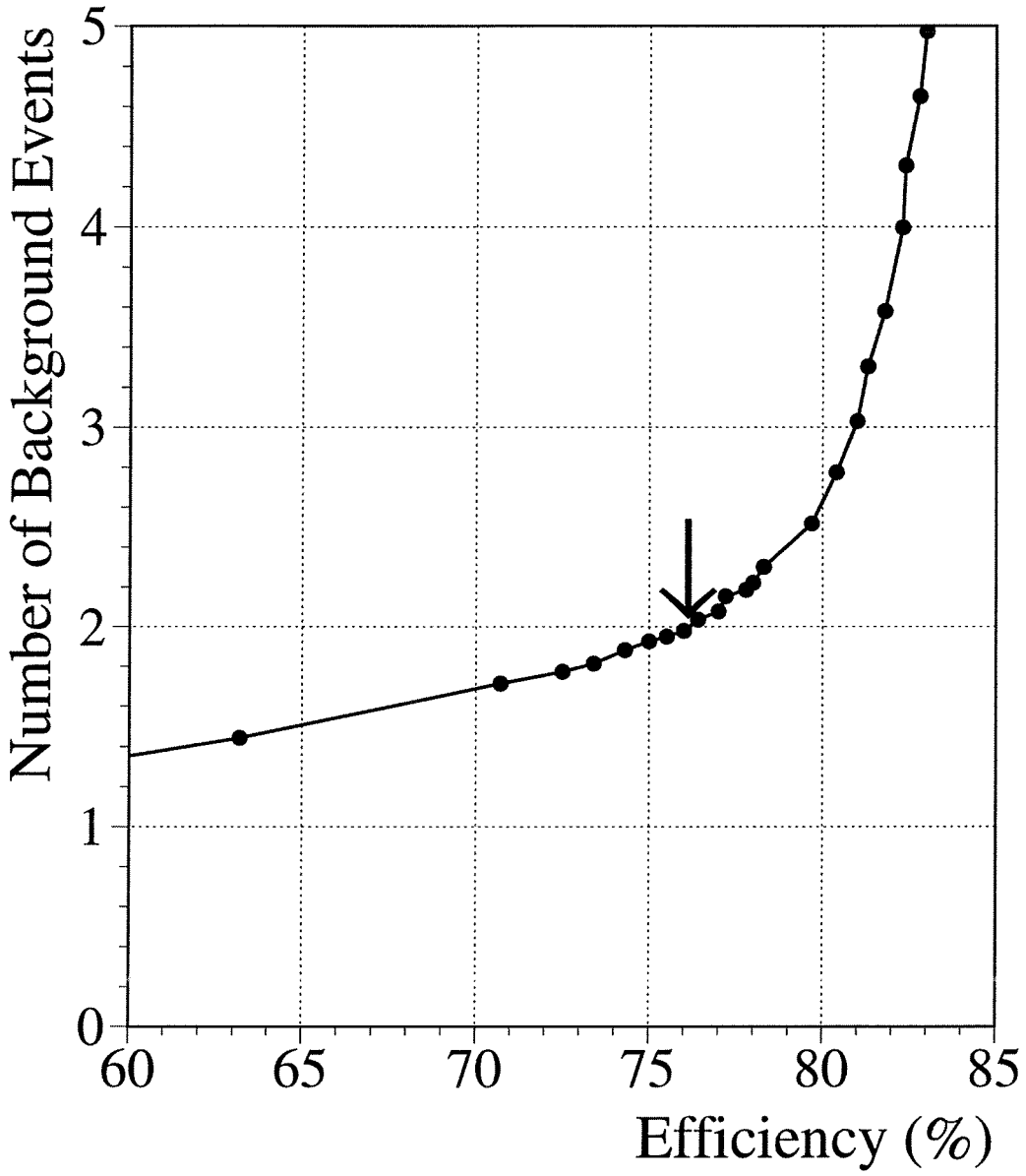

Figure A.2: The performance of the $H\ell^+\ell^-$ analysis in terms of efficiency for a signal with $M_H = 85\,\mathrm{GeV}/c^2$ versus the number of events expected from Standard Model background processes for an integrated luminosity of $57\,\mathrm{pb}^{-1}$. The arrow denotes the working point determined using the method summarized in Chapter 5.

A.1.2 Systematic Uncertainties

Several potential sources of systematic uncertainty are investigated. These include the identification of electrons and muons, the isolation criterion, and the simulation of the energy and momentum resolution of jets and leptons. Some limitations are found in the simulation of the background to low angle electrons which, however, do not contribute any systematic effect. The total relative systematic uncertainty in the signal detection efficiency is 0.4%.

A.2 The Missing Mass Final State

The HZ final state where the Z decays invisibly to two neutrinos constitutes 20% of the total Higgsstrahlung cross section. A large missing mass and two b jets from the Higgs boson decay characterize this final state. Figure A.3 shows an ALEPH event display of an exemplary simulated Higgs signal event in this final state at $\sqrt{s} = 183\,\mathrm{GeV}$ and with a Higgs boson mass of $85\,\mathrm{GeV}/c^2$. The neutrino and anti-neutrino from the decay of the Z escape undetected; thus the event exhibits missing mass and two acoplanar jets. The two b jets from the Higgs exhibit displaced vertices indicated by arrows in Figure A.3(c).

As is the case for the $\mathrm{Hq\bar{q}}$ final state, two independent analyses are used to search for a signal in this final state: a cut-based analysis and an analysis based on a neural network.

Both analyses share a common hadronic event preselection; events must contain five or more good charged particles and a total charged energy greater

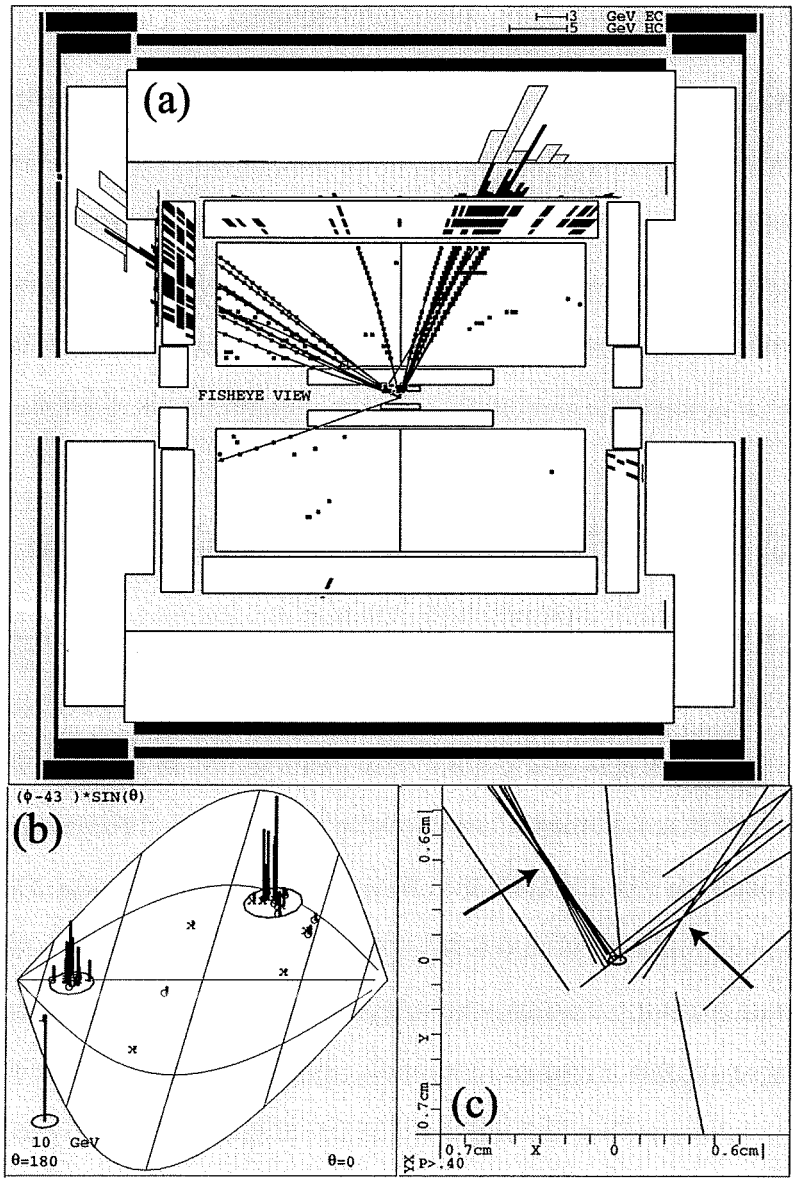

Figure A.3: An ALEPH event display of a simulated missing energy channel Higgs signal event at $\sqrt{s} = 183\,\text{GeV}$ and with a Higgs boson mass of $85\,\text{GeV}/c^2$: (a) an rz projection, (b) a $\theta\phi$ projection showing energy flow objects, and (c) an xy projection of the region near the primary vertex (arrows indicate secondary vertices due to b hadron decay).

than $0.1\sqrt{s}$. The plane perpendicular to the thrust axis is used to divide the event into two hemispheres. All energy flow particles in a hemisphere are considered to belong to a jet, and both jets are required to have non-zero energy. To reduce background from $\gamma\gamma$ interactions, the preselection requires either $P_{\mathrm{T}} > 0.05\sqrt{s}$ or $M_{\mathrm{vis}} > 0.3\sqrt{s}$, where P_{T} is the total transverse momentum of the event and M_{vis} is the visible mass. Finally, the missing mass of the event must be larger than $80\,\mathrm{GeV}/c^2$.

A.2.1 Cut-based Event Selection

In order to reject radiative Z returns, the missing momentum vector is required to point into the detector ($\theta_{\not p} > 20°$), and its component along the beam line is not allowed to be large ($|P_z| < 26\,\mathrm{GeV}/c$). The energy deposited within a 12° cone around the beam axis is required to be small ($E_{12} < 0.012\sqrt{s}$) to reject Weν and Zee events with a very energetic electron deflected at a low angle into the detector.

A modified event acoplanarity $\tilde{A}$ further reduces the contamination from radiative Z return events. This is defined as $\tilde{A} = (\hat{j}_1 \times \hat{j}_2) \cdot \hat{z}$ where $\hat{j}_i$ is the unit vector pointing along the direction of the sum of the momenta of all energy flow objects in the ith hemisphere and z is the beam direction.

Events are required to be well b-tagged. Jets are formed by forcing the event to two jets, and the sum of the output of the neural network btag for these two jets $\eta_1 + \eta_2$ is determined. For this final state, the neural network b-tag has been slightly modified. The value of the transverse lepton momentum

$p_{T\ell}$ is ignored if it is greater than $1.5\,\mathrm{GeV}/c$. This requirement is necessary due to events of the type $W^+W^- \to \tau\nu_\tau q\bar{q}'$. In this case, an electron or muon from a single-prong τ decay is clustered with one of the quark jets and typically has an extremely large $p_{T\ell}$ which mistakenly enhances the neural network b-tag output. Distributions of $\eta_1 + \eta_2$ are shown in Figure A.4.

Finally, in order to suppress background from $W^+W^- \to q\bar{q}'\tau\nu$ decays, the whole event is reclustered into τ-minijets (see Section A.3), and the most isolated jet is required to have a low energy ($E_\tau < 7\,\mathrm{GeV}$).

The acoplanarity and $\eta_1 + \eta_2$ requirements are allowed to vary in determining analysis performance and the working point. The working point corresponds to requiring the acoplanarity to be greater than 0.13 and that $\eta_1 + \eta_2$ be greater than 1.1.

A.2.2 Neural Network Event Selection

The analysis described above is complemented with a neural network selection based using the six variables of the cut selection and five additional ones. The new variables include the fraction of the energy deposited beyond 30° of the beam line, the total energy within a 30° wedge around the missing momentum direction, the acolinearity of the jets, and an additional combination of the b-tagging variables, $\log_{10}(1 - \eta_1\eta_2/2)$. The isolation angle of the most isolated track (with $p > 1\,\mathrm{GeV}/c$), θ_{iso}, provides additional discriminating power against $W^+W^- \to q\bar{q}'\tau\nu$ background.

The neural network is a fully-connected multi-layer feed-forward net-

work trained with Resilient Backpropagation (RPROP) algorithm using the Stuttgart Neural Network Simulator (SNNS) [125]. The architecture is 11-20-3 with the three output nodes corresponding to $H\nu\bar{\nu}$ signal, W^+W^-, and $q\bar{q}$. The network weights are trained to produce an output near one for $H\nu\bar{\nu}$ signal and near zero for background patterns. The architecture and training parameters are chosen based upon optimal performance in simulated events. The training sample consists of simulated Higgs boson signal for masses of 80 and 85 GeV/c^2 and $q\bar{q}$ and W^+W^- background processes. The events used for training are required to pass the preselection criteria. Only the neural network output corresponding to the $H\nu\bar{\nu}$ signal is used to discriminate between signal and background.

Figure A.5 shows the neural network output. Events are selected if the neural network response exceeds 0.983.

The limit setting technique uses the fitted mass and the neural network output as discriminating variables. The requirement on the analysis neural network output is allowed vary in determining the performance and the working point.

A.2.3 Results

Figure A.6 shows the performance of the cut-based and neural network analyses in terms of number of expected background events. The working point for the cut-based analysis corresponds to a signal efficiency of 21.9% with 0.24 events expected from background processes; the neural network analysis

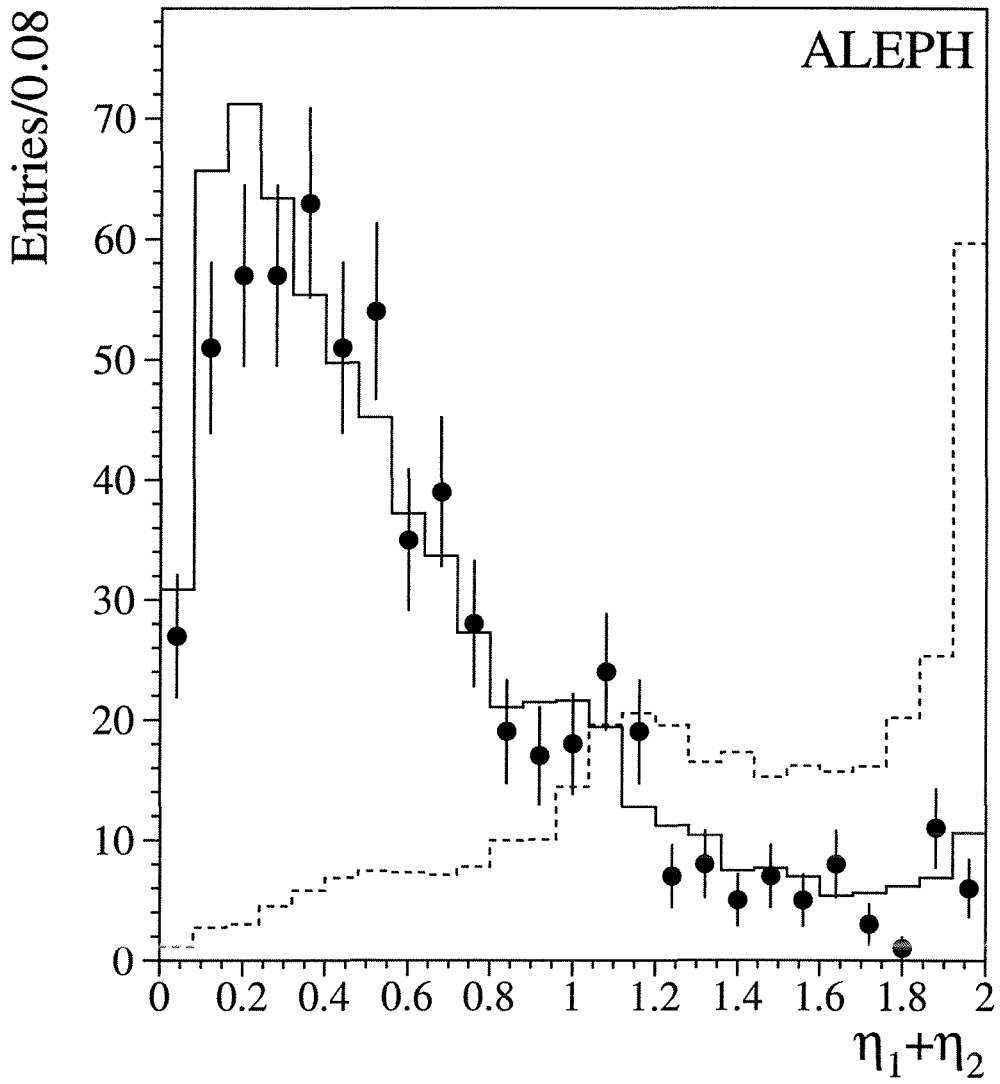

Figure A.4: The distribution in the missing energy channel of the sum of the two neural network b-tag outputs. The distribution is shown for the data (points), the total simulated background (solid line), and the reference signal sample (dashed line) after the preselection cuts. The signal distributions have an arbitrary normalization.

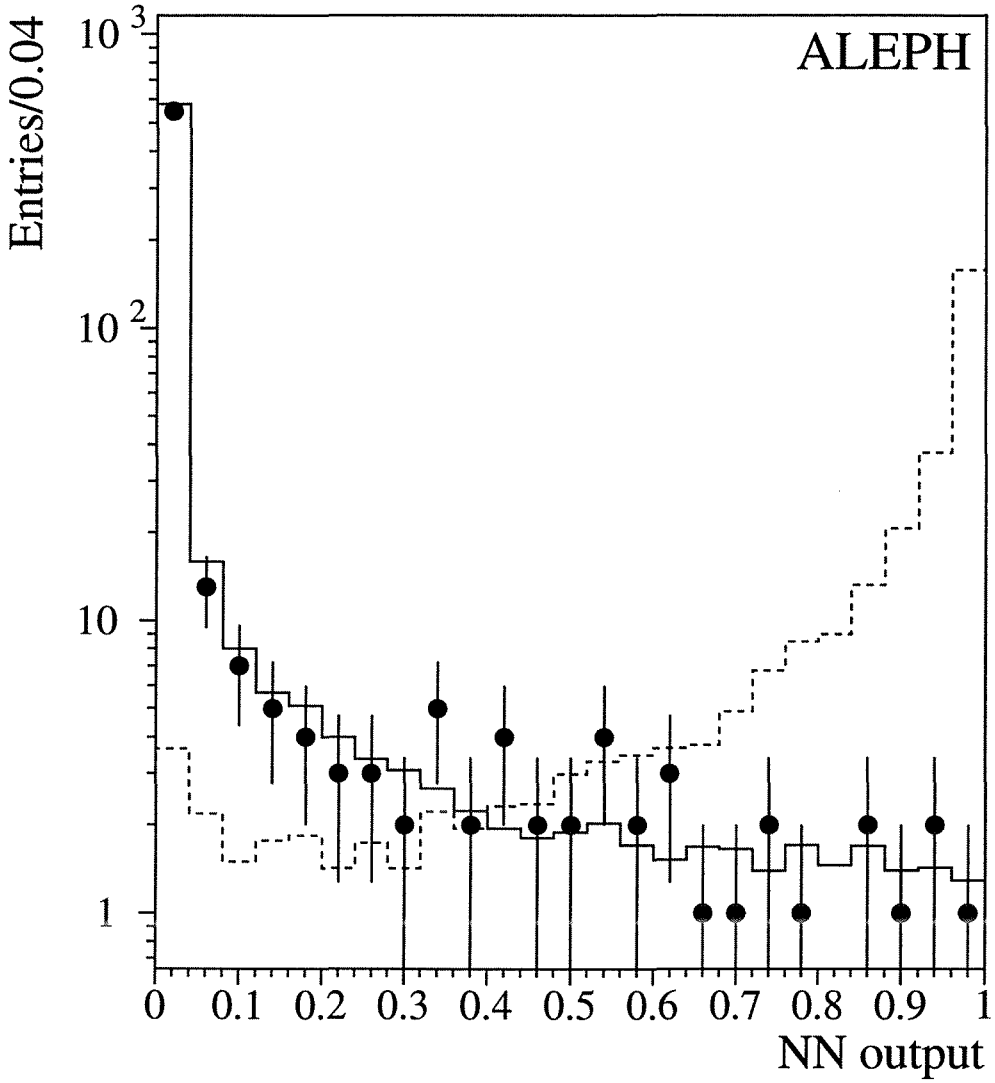

Figure A.5: The distribution in the missing energy channel of the output of the neural network used for event selection. The distributions are shown for the data (points), the total simulated background (solid line), and the reference signal sample (dashed line) after the preselection cuts. The signal distributions have an arbitrary normalization.

working point corresponds to a signal efficiency of 30.4% and 0.34 events expected from background processes. Results from the data are presented in Section 5.2.2.

A.2.4 Systematic Uncertainties

Based on deviations between data and simulated events of the kinematic variable distributions, a relative systematic uncertainty of 2.4% is determined. The simulated HZ signal events are reweighted to simulate changes in the b-lifetime, b-multiplicity, and b-fragmentation, giving a total systematic uncertainty of 3.0%. The relative systematic uncertainty from discrepancies between the tracking in the simulated data and real data is 6.1%. The total relative systematic uncertainty of the selection efficiency is 7.2%.

A.3 Final States with τ Leptons

Three signal channels contribute to final states with at least one $\tau^+\tau^-$ pair. The process $HZ \rightarrow H\tau^+\tau^-$ corresponds to 3.4% of the total Higgsstrahlung process, and $H \rightarrow \tau^+\tau^-, Z \rightarrow q\bar{q}$ corresponds to an additional 5.5%. These events are expected to have two oppositely charged low multiplicity jets in association with missing energy from the τ decays. The case of $H \rightarrow \tau^+\tau^-$ and $Z \rightarrow \ell^+\ell^-$ is the third Higgsstrahlung final state with τ leptons, but it is grouped together with the analysis for $H\ell^+\ell^-$ final state discussed in Section A.1.

Figure A.7 shows an exemplary simulated $H\tau^+\tau^-$ signal event at $\sqrt{s} =$

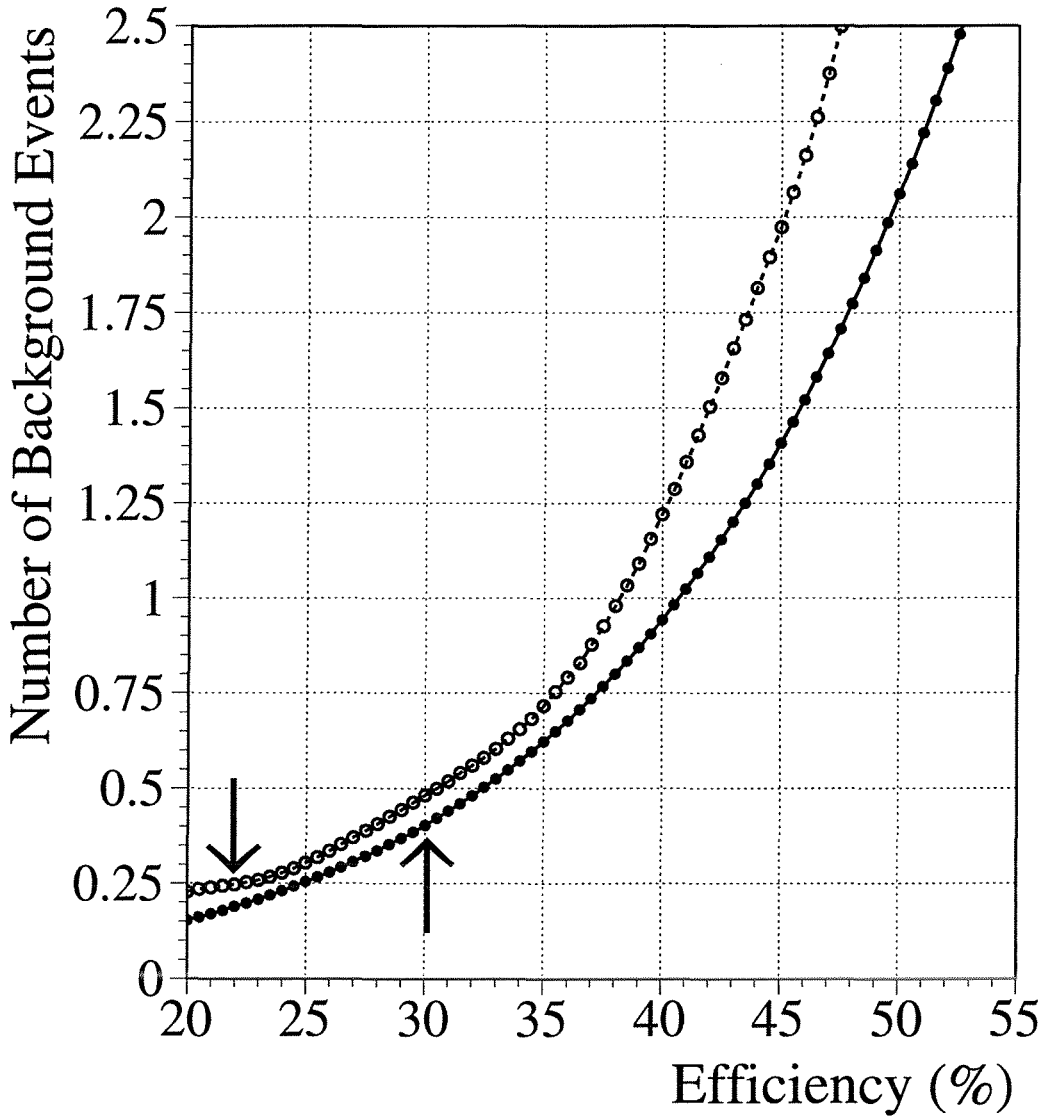

Figure A.6: The performance of the H$\nu\bar{\nu}$ analyses in terms of efficiency for a signal with $M_{\mathrm{H}} = 85\,\mathrm{GeV}/c^2$ versus the number of events expected from Standard Model background processes for an integrated luminosity of $57\,\mathrm{pb}^{-1}$. The dashed line with open circles shows the cut-based analysis performance while the solid line with filled circles shows the neural network analysis performance. The arrows denote the working points determined for each analysis using the method summarized in Chapter 5.

183 GeV and with a Higgs boson mass of 85 GeV/c^2. The decay products of one τ has a three-prong topology (*i.e.*,$\tau^+ \rightarrow a_1^+ \bar{\nu}_\tau$ with $a_1^+ \rightarrow \pi^+\pi^+\pi^-$) and the decay of the other τ has a one-prong topology (*i.e.*,$\tau^- \rightarrow \nu_\tau e^- \bar{\nu}_e$). There are two b jets in the event from the decay of the Higgs boson. One jet has an apparent secondary vertex indicated with an arrow in Figure A.7(c).

A.3.1 Event Selection

Hadronic events are selected by requiring at least eight good tracks. The total charged energy in the event is required to exceed 20% of the center-of-mass energy. Events from radiative Z returns are rejected by requiring $|P_z| + E_{\mathrm{miss}} < 1.8\gamma_{\mathrm{peak}}$. Here, P_z and E_{miss} are the total longitudinal momentum of the event and its missing energy. The mean of the ISR photon spectrum peak is denoted as γ_{peak} and is defined as $\gamma_{\mathrm{peak}} = \sqrt{s}/2 - M_Z^2/2\sqrt{s}$. In addition, $|P_z|$ is required not to exceed $0.6\gamma_{\mathrm{peak}}$. In order to exploit the missing energy expected in this final state, the total missing transverse momentum of the event is required to be at least $0.025\sqrt{s}$.

The event is clustered into a large number of jets, referred to as *minijets*, with mass consistent with M_τ. The τ candidates are then selected from these minijets.

Events with at least two oppositely charged τ candidates are selected. At least one of the candidates has to be single-prong. The remainder of the event is forced to form two jets using the Durham clustering algorithm. Events which have more than one τ pair candidate yield multiple $\tau^+\tau^-q\bar{q}$

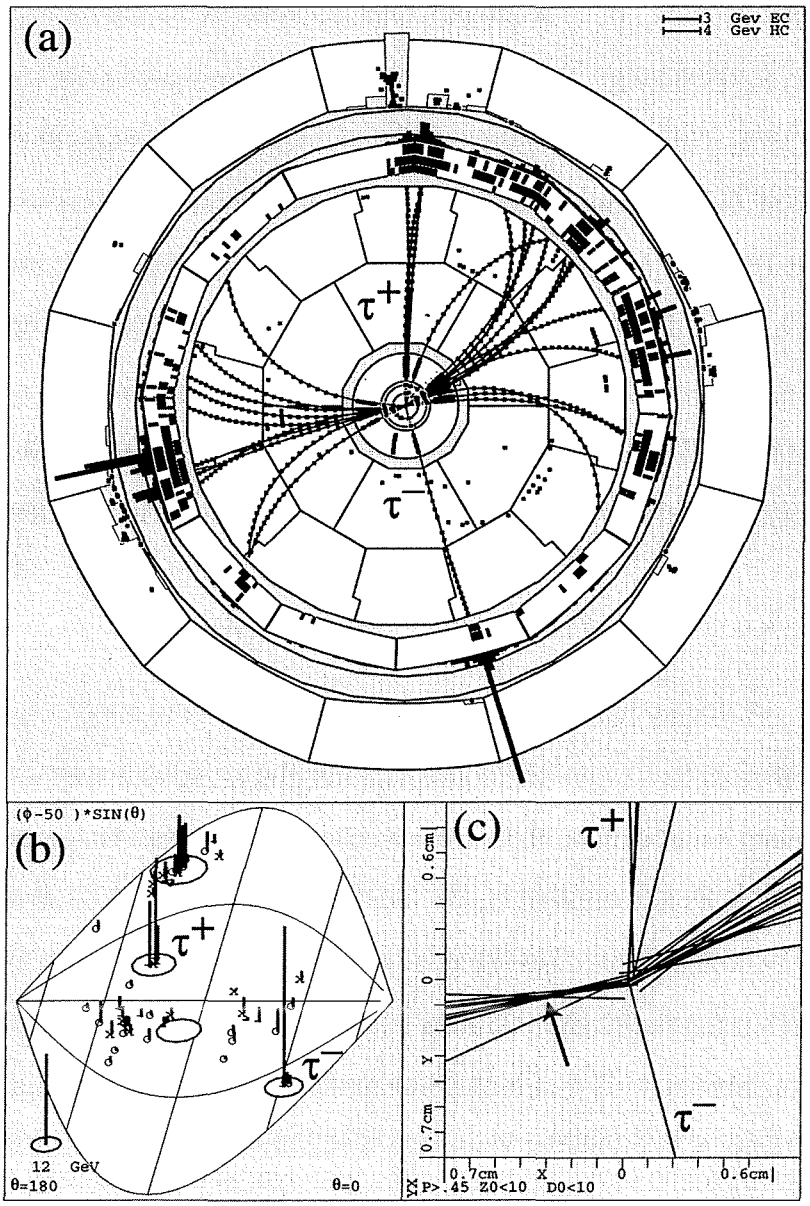

Figure A.7: An ALEPH event display of a simulated $H\tau^+\tau^-$ signal event at $\sqrt{s} = 183\,\text{GeV}$ and with a Higgs boson mass of $85\,\text{GeV}/c^2$: (a) an xy projection, (b) a $\theta\phi$ projection showing energy flow objects, and (c) an xy projection of the region near the primary vertex (the arrow indicates a secondary vertex due to b hadron decay). The τ^+ exhibits as three-prong decay while the τ^- exhibits a one-prong decay.

combinations. A χ^2 is determined for each event combination with a kinematic consistency fit. This fit requires energy-momentum conservation while keeping the four jet directions fixed. In the fit, the mass of the candidate τ jets is fixed to the nominal τ lepton mass, and the energy resolution of the two non-τ jets is taken into account. The invariant mass of either the $\tau^+\tau^-$ or the $q\bar{q}$ pair is constrained to be compatible with the M_Z, depending on the channel. In addition, the non-τ jet momenta are constrained to be larger than 75% of the measured value. The combination with the lowest χ^2 is chosen and presented to the neural networks described below.

A.3.2 The HZ→H$\tau^+\tau^-$ Final State

To discriminate between H$\tau^+\tau^-$ and background events, a neural network is used with five input variables: the total missing transverse momentum of the event, the sum of the two τ jet isolation angles, the sum of the fitted transverse momentum of the τ jets with respect to their nearest hadronic jet, the kinematic consistency χ^2, and $(\eta_1 + \eta_2)$. The jet isolation angle definition for the second variable is the same as for the H$\ell^+\ell^-$ selection. The last variable reflects the b quark content of the two non-τ jets.

Figure A.8 shows the response of the H$\tau^+\tau^-$ neural network in the data and in simulated signal and background events. The neural network output is allowed to vary in determining analysis performance and the working point. The performance of this analysis is shown in Figure A.10. The working point corresponds to neural network output values larger than 0.979. This yields

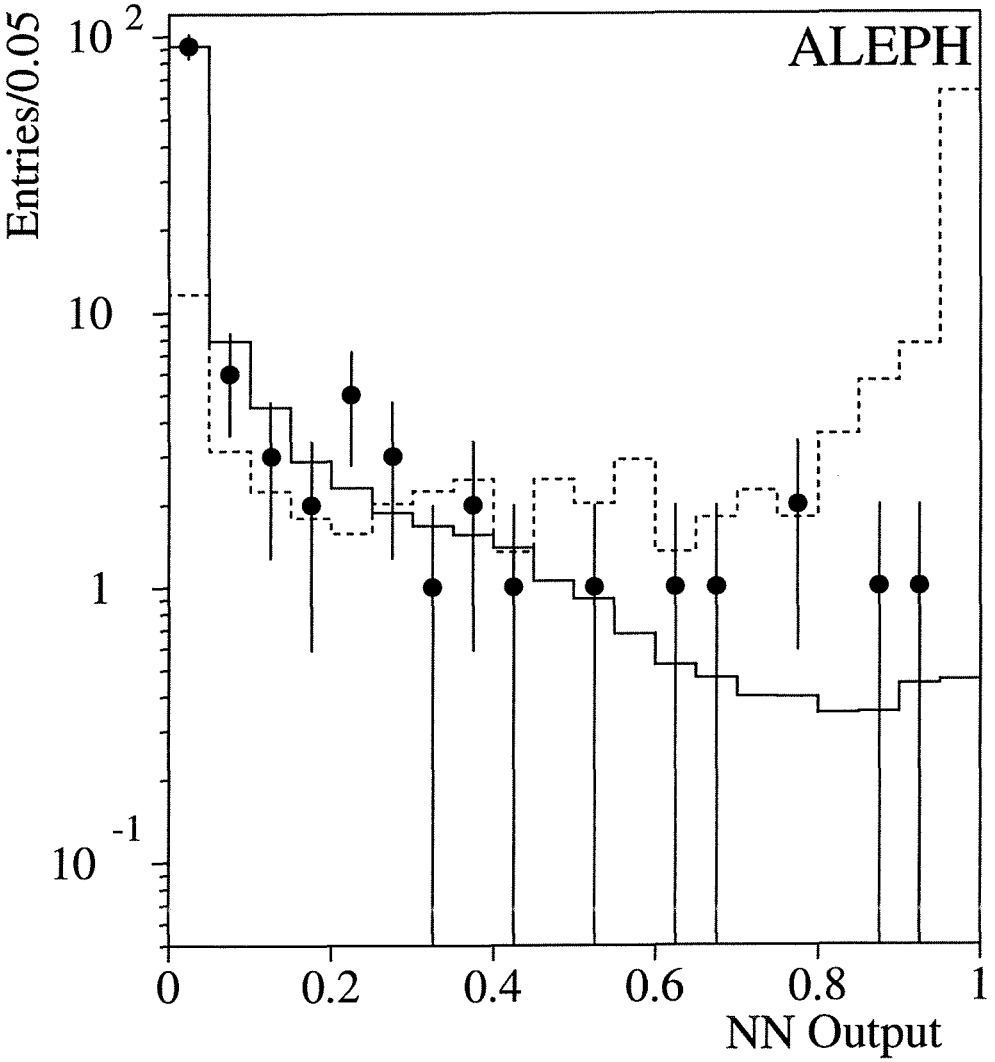

Figure A.8: The distributions of the neural network outputs for the $H\tau^+\tau^-$ channel. The distributions are shown for the data (points), the total simulated background (solid line), and the reference signal sample (dashed line) after the preselection cuts. The signal distributions have an arbitrary normalization.

a signal detection efficiency of 20.7% with 0.17 background events expected. Results from the data are presented in Section 5.2.2.

A.3.3 The HZ→$\tau^+\tau^-q\bar{q}$ Final State

A neural network is also used to select HZ → $\tau^+\tau^-q\bar{q}$ events. The input variables to this neural network are identical to those described in the previous subsection except that the b-tagging variable is not used. This is a limiting factor in the performance of the selection. Figure A.9 shows the neural network output in the data and simulated signal and background events.

Again the neural network output is allowed to vary in determining analysis performance and the working point. The performance of this analysis is shown in Figure A.10. The working point corresponds to requiring events to have a neural network output larger than 0.980. This results in a signal selection efficiency of 12.6% and 0.16 events expected from background processes. Results from the data are presented in Section 5.2.2.

A.3.4 Systematic Uncertainties

The main sources of systematic uncertainty in the final states with τ leptons are the reconstruction of the kinematic variables, the clustering of jets and the tagging of jets containing b quarks.

From a comparison of multihadronic events with an identified lepton, in the data and in simulated events, a discrepancy in the total transverse momentum is observed which translates into an absolute uncertainty of 0.3%

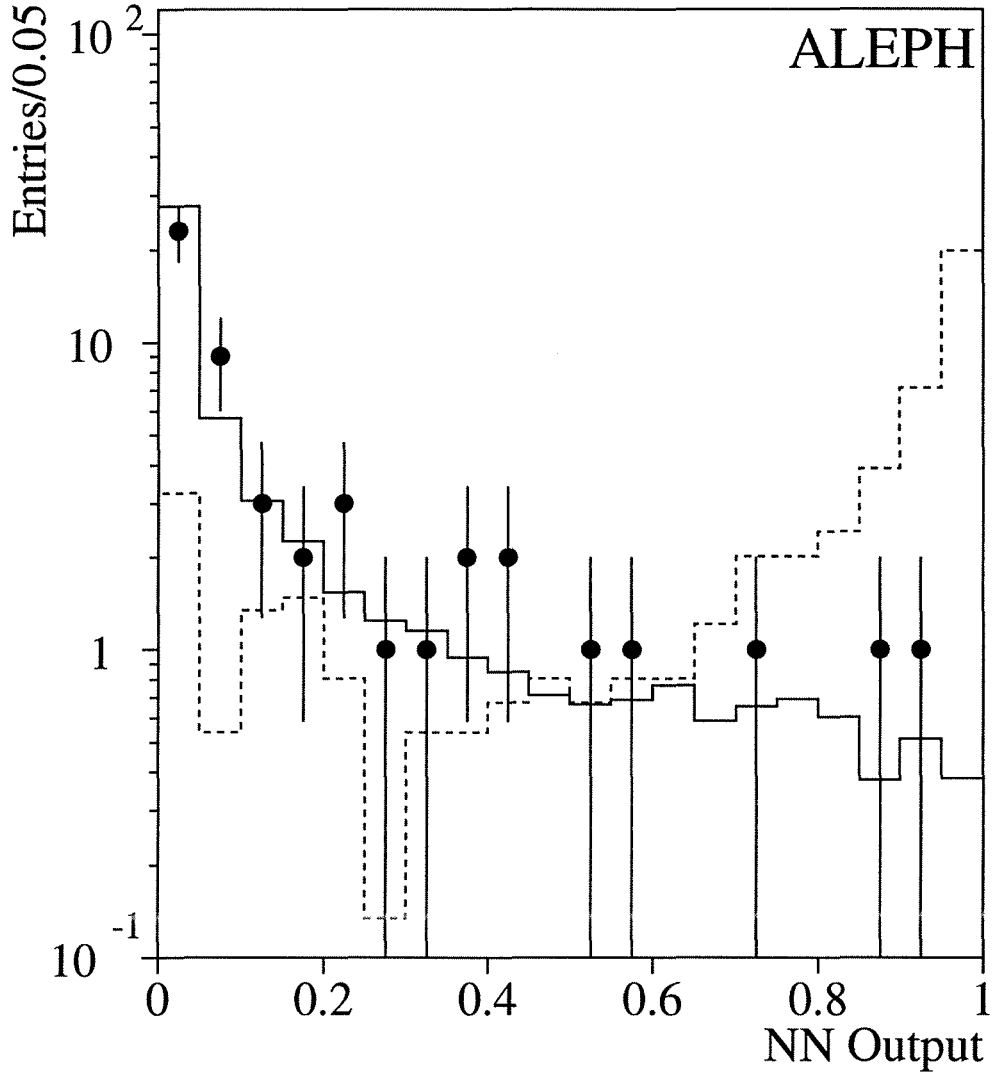

Figure A.9: The distributions of the neural network outputs for the $\tau^+\tau^-\mathrm{q\bar{q}}$ channel. The distributions are shown for the data (points), the total simulated background (solid line), and the reference signal sample (dashed line) after the preselection cuts. The signal distributions have an arbitrary normalization.

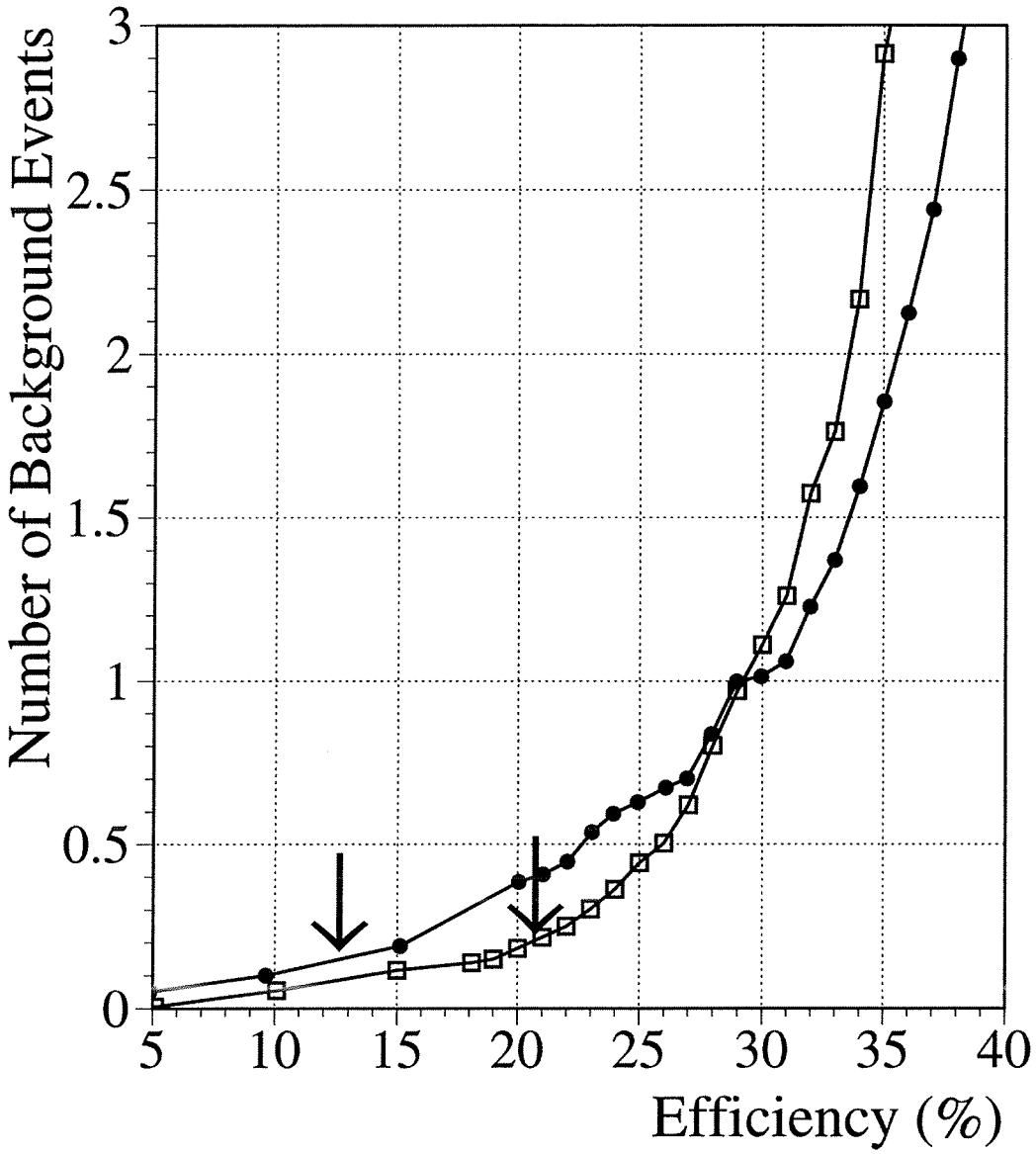

Figure A.10: The performance of the $H\tau^+\tau^-$ and $\tau^+\tau^-q\bar{q}$ analyses in terms of efficiency for a signal with $M_H = 85\,\mathrm{GeV}/c^2$ versus the number of events expected from Standard Model background processes for an integrated luminosity of $57\,\mathrm{pb}^{-1}$. The line with filled circles shows the $\tau^+\tau^-q\bar{q}$ analysis performance while the line with open squares shows the $H\tau^+\tau^-$ analysis performance. The arrows denote the working points of each analysis.

(0.2%) in the signal detection efficiency for the $H\tau^+\tau^-$ ($\tau^+\tau^-q\bar{q}$) final state. The effects from jet reconstruction are evaluated by conservatively smearing the reconstructed jet angles and energies according to the expected measurement errors. The systematic effect on the detection efficiency is 0.4% (0.1%) from the jet directions and 0.1% (0.1%) from the jet energies, in absolute terms. Uncertainties arising from the tagging of b jets affect only the $H\tau^+\tau^-$ selection and are evaluated to total 0.9%. Therefore, total relative systematic uncertainties of 5.6% and 1.9% are respectively assigned to the $H\tau^+\tau^-$ and $\tau^+\tau^-q\bar{q}$ signal detection efficiencies.

Bibliography

[1] S.L. Glashow, *Nucl. Phys.* **A22** (1961) 579; S. Weinberg, *Phys. Rev. Lett.* **19** (1967) 1264; A. Salam, *"Elementary Particle Theory,"* ed. N. Svarthold, Stockholm, Almquist, and Wiksel (1968) 367.

[2] D. Decamp *et al.* (ALEPH Collaboration), *Phys. Lett.* **B235** (1990) 399.

[3] C. Caso *et al.* (PDG group), *Eur. Phys. J.* **C3** (1998) 1.

[4] F. Englert and R. Brout, *Phys. Rev. Lett.* **13** (1964) 321; P.W. Higgs, *Phys. Lett.* **12** (1964) 132, *Phys. Rev. Lett.* **13** (1964) 508, *Phys. Rev.* **145** (1966) 1156; G.S. Guralnik, C.R. Hagen, and T.W.B. Kibble, *Phys. Rev. Lett.* **13** (1964) 585; T.W.B. Kibble, *Phys. Rev. Lett.* **155** (1967) 1554.

[5] S. Weinberg, *Phys. Rev.* **D19** (1979) 1277; L. Susskind, *ibid.* **D20** (1979) 2619.

[6] W.A. Bardeen, C.T. Hill, and M. Lindner, *Phys. Rev.* **D41** (1990) 1647; R. Sekhar Ckivukula, B.A. Dobrescu, H. Georgi, and C.T. Hill, FERMILAB-Pub-98/284-T (hep-ph/9809470).

[7] E. Noether, *Nachr. Kgl. Ges. Wiss. Göttingen* (1918) 235.

[8] C.N. Yang and R.L. Mills, *Phys. Rev.* **96** (1954) 191.

[9] G. 't Hooft, *Nucl. Phys.* **B33** (1971) 173.

[10] G. Arnison *et al.* (UA1 Collaboration), *Phys. Lett.* **B122** (1983) 103; M. Banner *et al.* (UA2 Collaboration), *ibid.* **B122** (1983) 476.

[11] J. Goldstone, *Nuovo Cimento* **19** (1961) 154.

[12] Y. Nambu, *Phys. Rev. Lett.* **4** (1960) 380.

[13] E. Fermi, *Z. Phys.* **88** (1934) 161.

[14] H. Becquerel, *Comptes-rendu de l'Academie des Sciences*, **122** (1896), 420.

[15] T.D. Lee and C.N. Yang, *Phys. Rev.* **104** (1956) 254.

[16] C.S. Wu, E. Ambler, R.W. Hayward, D.D. Hoppes, and R.P. Hudson, *Phys. Rev.* **105** (1957) 1413; M. Goldhaber, L. Grodzins, and A.W. Sunyar, *ibid.* **109** (1958) 1015; R.L. Garwin, L.M. Ledermann, and M. Weinrich, *ibid.* **105** (1957) 1415; J.I. Friedmann and V.L. Telegdi, *ibid.* **105** (1957) 1681.

[17] `http://www.phys.hawaii.edu/~jgl/neutrino_news.html`

[18] N. Cabibbo, *Phys. Rev. Lett.* **10** (1963) 531.

[19] M. Kobayashi and T. Maskawa, *Prog. Theor. Phys.* **49** (1973) 652.

[20] S.L. Wu and G. Zobernig, *Z. Phys.* **C2** (1979) 107; S.L. Wu and G. Zobernig, TASSO Note 84 (1979); TASSO Collaboration, *Phys. Lett.* **B86** (1979) 243.

[21] E. Leader and E. Predazzi, *An Introduction to Gauge Theories and Modern Particle Physics* (Cambridge University Press, 1996) Vol. 1.

[22] P. Janot, *"The HZHA Generator"* in *Physics at LEP2* (edited by G. Altarelli, T. Sjöstrand and F. Zwirner), CERN 96-01 (1996) 309.

[23] M. Spira and P.M. Zerwas, CERN-TH/97-379 (1997).

[24] V.D. Barger and R.J.N. Phillips, *Collider Physics* (Addison-Wesley Publishing Company, Redwood City, 1987).

[25] J.F. Gunion, H.E. Haber, G. Kane, and S. Dawson, *The Higgs Hunter's Guide* (Addison-Wesley, Redwood City, 1990).

[26] P.B. Arnold, *Phys. Rev.* **D40** (1989) 613.

[27] J.R. Espinosa and M. Quirós, *Phys. Lett.* **B353** (1995) 257.

[28] G. Quast, *Electroweak Physics*, LEPC talk 15 September 1998 (unpublished).

[29] M.W. Grünewald, *"Combined Analysis of Precision Electroweak Results"* to appear in *Proceedings of the XXIX International Conference on High Energy Physics* (Vancouver, 1998).

[30] D. Kohler, B.A. Watson, and J.A. Becker, *Phys. Rev. Lett.* **33** (1974) 1628; N.C. Mukhopadhyay, P.F.A. Goudsmit, and A. Barroso, *Phys. Rev.* **D29** (1984) 565; S.J. Freedman *et al.*, *Phys. Rev. Lett.* **52** (1984) 240; R. Barbieri and T.E.O. Ericson, *Phys. Lett.* **B57** (1975) 270; S. Alder, R. Dashen, and S. Treiman, *Phys. Rev.* **D10** (1974) 3728.

[31] M. Davier and H. Nguyen Ngoc, *Phys. Lett.* **B229** (1989) 150; D. Decamp *et al.* (ALEPH Collaboration), *ibid.* **B245** (1990) 289.

[32] S. Egli *et al.* (SINDRUM Collaboration), *Phys. Lett.* **B222** (1989) 533.

[33] G.D. Barr *et al.*, *Phys. Lett.* **B235** (1990) 356; N.J. Baker *et al.*, *Phys. Rev. Lett.* **59** (1987) 2832.

[34] A. Snyder *et al.* (Mark II Collaboration), *Phys. Lett.* **B229** (1989) 169; M.S. Alam *et al.* (CLEO Collaboration), *Phys. Rev.* **D40** (1989) 712.

[35] J. Lee-Franzini, *"Update on Light Higgs' Searches"* in *Proceedings of the XXIV International Conference on High Energy Physics* (Munich, 1988) 1432; H. Albrecht *et al.* (ARGUS Collaboration), *Z. Phys.* **C42** (1989) 349.

[36] D. Buskulic *et al.* (ALEPH Collaboration), *Phys. Lett.* **B384** (1996) 427.

[37] P. Abreu *et al.* (DELPHI Collaboration), *Nucl. Phys.* **B421** (1994) 3.

[38] M. Acciarri *et al.* (L3 Collaboration), *Phys. Lett.* **B385** (1996) 454.

[39] G. Alexander *et al.* (OPAL Collaboration), *Z. Phys.* **C73** (1997) 189.

[40] The ALEPH, DELPHI, L3, and OPAL Collborations, CERN-EP/98-046 (1998).

[41] L. Groer, HEP-EX/9707034 (1997).

[42] F. Abe *et al.* (CDF Collaboration), *Phys. Rev. Lett.* **79** (1997) 3819.

[43] J. Valls, *"MSSM and Higgs Search at the Tevatron,"* presentation at the *XXIX International Conference on High Energy Physics* (Vancouver, 1998).

[44] G. Altarelli, T. Sjöstrand, and F. Zwirner (eds.), *Physics at LEP2*, CERN 96-01 (1996).

[45] T. Sjöstrand, *The PYTHIA 5.7 and JETSET 7.4 Manual*, LU-TP.95/20, CERN-TH.7112/93, and *Comput. Phys. Commun.* **82** (1994) 74.

[46] M. Skrzypek, S. Jadach, W. Placzek, and Z. Was, *Comput. Phys. Commun.* **94** (1996) 216; M. Skrzypek, S. Jadach, M. Martinez, W. Placzek, and Z. Was, *Phys. Lett.* **B372** (1996) 289.

[47] J.A.M. Vermaseren in *Proceedings of the IVth International Workshop on Gamma Gamma Interactions*, Eds. G. Cochard and P. Kessler (Springer Verlag, 1980).

[48] This generator is based on the differential cross section published in: S. Ambrosanio and B. Mele, *Nucl. Phys.* **B374** (1992) 3.

[49] ALEPH Collaboration, *"Study of Fermion Pair Production in e^+e^- Collisions at 130-183 GeV,"* contributed paper #906, XXIX International Conference on High Energy Physics (ICHEP98), Vancouver 23-29 July 1998; DELPHI Collaboration, *"Results on Fermion-Pair Production at LEP energies up to 183 GeV,"* contributed paper #441, *ibid.*; L3 Collaboration, *"Measurement of Hadron and Lepton-Pair Production above the Z Resonance,"* contributed paper #510, *ibid.*; OPAL Collaboration, *"Tests of the Standard Model and Constraints on New Physics from Measurements of Fermion-pair Production at 183 GeV at LEP,"* contributed paper #264, *ibid.*

[50] L3 Collaboration, *"Cross section of hadron production in $\gamma\gamma$ collisions at LEP,"* contributed paper #519, XXIX International Conference on High Energy Physics (ICHEP98), Vancouver 23-29 July 1998; OPAL Collaboration, *"Total Hadronic Cross Section for Photon-Photon Interactions at LEP,"* contributed paper #199, *ibid.*

[51] ALEPH Collaboration, *"Measurement of WW cross section and W branching ratios at LEP2 with the ALEPH detector,"* contributed paper #915, XXIX International Conference on High Energy Physics (ICHEP98), Vancouver 23-29 July 1998; DELPHI Collaboration, *"W-pair Production cross-section and W branching ratios in e^+e^- interactions at 183 GeV,"* contributed paper #290, *ibid.*; L3 Collaboration, *"Measurement of W-Pair Cross Sections and W-Decay Branching Fractions at LEP,"* contributed paper #501, *ibid.*; OPAL Collaboration, *"Measurement of the W^+W^- Production Cross-section and W-boson Decay Branching Fractions at $\sqrt{s} = 183\,GeV$,"* contributed paper #393, *ibid.*

[52] DELPHI Collaboration, *"Neutral current four-fermion production in e^+e^- collisions at $\sqrt{s} = 130$-183 GeV,"* contributed paper #230, XXIX International Conference on High Energy Physics (ICHEP98), Vancouver 23-29 July 1998; L3 Collaboration, *"Four-Fermion Events and Observation of Resonant ZZ Production at LEP,"* contributed paper #488, *ibid.*; OPAL Collaboration, *"Study of Z Boson Pair Production in e^+e^- Collisions at $\sqrt{s}$ =183 and 189 GeV,"* contributed paper #267, *ibid.*

[53] D. Zerwas, *Energie manquante à LEP2 : Boson W et Physique nouvelle*, Ph.D. Thesis, Université Paris-Sud - LAL (1998); M. Acciarri *et al.* (L3 Collaboration), *Phys. Lett.* **B436** (1998) 417; P. Abreu *et al.* (DELPHI Collaboration), *Phys. Lett.* **B423** (1998) 194.

[54] *Large Electron-Positron Storage Ring Technical Notebook*, CERN (1989).

[55] D. Boussard, CERN SL/96-016-RF (1996).

[56] `http://nicewww.cern.ch/sl/opnews/Lep/Lep96.html`

[57] B. Goddard *et al.*, CERN SL/97-02(AP) (1997).

[58] W. Herr, CERN SL/94-06(DI) (1994).

[59] J.P. Koutchouk, CERN SL/92-29(DI) (1992).

[60] A.A. Sokolov and I.M. Ternov, *Sov. Phys. Dokl.* **8** (1964) 1203.

[61] L. Arnaudon *et al.*, CERN SL/94-07(BI) (1994).

[62] J. Wenninger, CERN SL/94-06(DI) (1994).

[63] The LEP Energy Working Group, LEP Energy Group/97-01 (1997).

[64] J. Wenninger, CERN SL/95-21(OP) (1995).

[65] P. Bright-Thomas, ALEPH/97-029 (1997).

[66] D. Buskulic *et al.* (ALEPH Collaboration), *Z. Phys.* **C71** (1996) 179.

[67] Compiled from the minutes of the ALEPH Echenevex meetings during 1997.

[68] N. Qi, Report from the LEP Energy Working Group, 6 March 1998.

[69] ALEPH Collaboration (edited by C. Bowdery), *The ALEPH Handbook 1995* Volumes 1 and 2.

[70] ALEPH Collaboration (edited by D. Schlatter, P. Perrodo, O. Schneider, and A. Wagner), *"ALEPH in Numbers"* Internal ALEPH Report.

[71] D. Decamp *et al.* (ALEPH Collaboration), *Nucl. Instrum. Methods* **A294** (1990) 121.

[72] D. Decamp *et al.* (ALEPH Collaboration), *Nucl. Instrum. Methods* **A360** (1995) 481.

[73] A. Schwarz, *Phys. Rep.* **238** (1994) 1.

[74] W.R. Leo, *Techniques for Nuclear and Particle Physics Experiments: A How-to Approach* (Springer-Verlag, Berlin, 1992).

[75] D. Creanza *et al.*, *"Construction and Performance of the New ALEPH Vertex Detector,"* to appear in *Proceedings of the Conference on Advanced Technology and Particle Physics* (Como, Italy, 1996).

[76] A. Bonissent, D. Rousseau, M. Thulasidas, and K. Trabelsi, ALEPH/97-116 (1997).

[77] A. Wagner and H. Dietl, ALEPH/97-006 (1997).

[78] E. Iarocci, *Nucl. Instrum. Methods* **A217** (1983) 30.

[79] D. Buskulic *et al.* (ALEPH Collaboration), *Z. Phys.* **C62** (1994) 539.

[80] B. Bloch-Devaux (private communication).

[81] B. Bloch-Devaux, ALEPH 97-070 (1997).

[82] P. Hansen (private communication).

[83] An extrapolation of the statistical error reported in R. Barate *et al.* (ALEPH Collaboration), *Phys. Lett.* **B401** (1997) 347.

[84] R. Frühwirth, *Nucl. Instrum. Methods* **A262** (1987) 444.

[85] R. Barate *et al.* (ALEPH Collaboration), *Phys. Lett.* **B412** (1997) 155.

[86] G. Altarelli, T. Sjöstrand, and F. Zwirner (eds.), *Physics at LEP2: Volume 2, Event Generators*, CERN 96-01 (1996).

[87] `http://wwwcn.cern.ch/asdoc/geant/GEANTMAIN.html`.

[88] H.C. Fesefeldt, PITHA/85-02 (1985).

[89] G. Hanson *et al.*, *Phys. Rev. Lett.* **35** (1975) 1609.

[90] X. Artru and G. Mennessier, *Nucl. Phys.* **B70** (1974) 93; A. Casher, H. Neuberger, and S. Nussinov, *Phys. Rev.* **D20** (1979) 179; B. Anderson, G. Gustavson, G. Ingelman, and T. Sjöstrand, *Phys. Rep.* **97** (1983) 31.

[91] T. Sjöstrand, *Comput. Phys. Commun.* **82** (1994) 74.

[92] B.R. Webber, *Nucl. Phys.* **B238** (1984) 492; G.C. Fox and S. Wolfram, *ibid.* **B168** (1980) 285; R.D. Field and S. Wolfram, *ibid.* **B213** (1983) 65; T.D. Gottschalk, *ibid.* **B239** (1984) 325.

[93] G. Marchesini *et al.*, *Comput. Phys. Commun.* **67** (1992) 465.

[94] R. Barate *et al.* (ALEPH Collaboration), *Z. Phys.* **C76** (1997) 1.

[95] D. Buskulic *et al.* (ALEPH Collaboration), *Phys. Lett.* **B384** (1996) 353; R. Barate *et al.* (ALEPH Collaboration), *Z. Phys.* **C76** (1997) 191.

[96] W. Bartel *et al.*, *Phys. Lett.* **B101** (1981) 129.

[97] S. Bethke, Z. Kunszt, D.E. Soper, and W.J. Stirling, *Nucl. Phys.* **B370** (1992) 310.

[98] S. Catani *et al.*, *Phys. Lett.* **B269** (1991) 432; W.J. Stirling, *J. Phys. G: Nucl. Part. Phys.* **17** (1991) 1567.

[99] C. Peterson, D. Schlatter, I. Schmitt, and P.M. Zerwas, *Phys. Rev.* **D27** (1983) 105.

[100] R. Akers *et al.* (OPAL Collaboration), *Z. Phys.* **C61** (1994) 209.

[101] P. Abreu *et al.* (DELPHI Collaboration), *Phys. Lett.* **B425** (1998) 399.

[102] M. Acciarri *et al.* (L3 Collaboration), *Phys. Lett.* **B416** (1998) 200.

[103] J.J. Aubert *et al.*, *Phys. Rev. Lett.* **33** (1974) 1404; J.E. Augustin *et al.*, *ibid.* **33** (1974) 1406.

[104] S. Herb *et al.*, *Phys. Rev. Lett.* **39** (1974) 252.

[105] M.K. Gaillard, B.W. Lee, and J.L. Rosner, *Rev. Mod. Phys.* **47** (1975) 277; J. Ellis, M.K. Gaillard, and D.V. Nanopoulos, *Nucl. Phys.* **B100** (1975) 313; J. Ellis, M.K. Gaillard, D.V. Nanopoulos, and S. Rudaz, *Nucl. Phys.* **B131** (1977) 285.

[106] J.H. Kühn and P.M. Zerwas, *"Heavy Flavours"* in *"Z Physics at LEP 1"* (edited by G. Altarelli, R. Kleiss, and C. Verzegnassi), CERN 89-08 (1989) 267.

[107] H. Albrecht *et al.* (ARGUS Collaboration), *Z. Phys.* **C54** (1992) 20.

[108] P. Abreu *et al.* (DELPHI Collaboration), *Phys. Lett.* **B347** (1995) 447.

[109] R. Giles *et al.* (CLEO Collaboration), *Phys. Rev.* **D30** (1984) 2279.

[110] D. Brown and M. Frank, ALEPH/92-135 (1992); D. Buskulic *et al.* (ALEPH Collaboration), *Phys. Lett.* **B313** (1993) 535.

[111] Modifications to the ALEPH impact parameter routine (QIPBTAG) were made by John Carr.

[112] D. Brown, ALEPH/92-47 (1992).

[113] S. Wasserbaech, ALEPH/95-054 (1995).

[114] S. Wasserbaech (private communication).

[115] T. Mattison, ALEPH/92-173 (1992). D. Buskulic *et al.* (ALEPH Collaboration), *Phys. Lett.* **B322** (1994) 441.

[116] D. Buskulic *et al.* (ALEPH Collaboration), *Nucl. Instrum. Methods* **A346** (1994) 461.

[117] J.D. Bjorken and S.J. Brodsky, *Phys. Rev.* **D1** (1970) 1416.

[118] S.L. Wu, *Phys. Rep.* **107** (1984) 59.

[119] G.C. Fox and S. Wolfram, *Nucl. Phys.* **B149** (1979) 413.

[120] S.R. Armstrong, presentation in the ALEPH Higgs Task Force, 4 February 1998 (unpublished).

[121] L. Bellantoni *et al.*, *Nucl. Instrum. Methods* **A310** (1991) 618.

[122] C. Peterson and T. Rögnvaldsson, *"An Introduction to Artificial Neural Networks,"* in *1991 CERN School of Computing* (edited by C. Verkerk) (1991) 113; L. Lönnblad, C. Peterson, and T. Rögnvaldsson, *Comput. Phys. Commun.* **70** (1992) 167; S.R. Amendolia, *"Neural Networks,"* in *1993 CERN School of Computing* (edited by C.E. Vandoni and C. Verkerk) (1993) 1.

[123] L. Lönnblad, C. Peterson, and T. Rögnvaldsson, *"JETNET 3.0 : A Versatile Artificial Neural Network Package,"* CERN-TH 7135/94 (1994).

[124] S.R. Armstrong, presentation in the ALEPH Higgs Task Force, 1 October 1996 (unpublished).

[125] A. Zell *et al.*, *"SNNS - Stuttgart Neural Network Simulator User Manual, Version 4.0,"* University of Stuttgart, Institute for Parallel and Distributed High Performance Computing (IPVR), Department of Computer Science, Report 6/95 (1995).

[126] R. Barate *et al.* (ALEPH Collaboration), *Phys. Lett.* **B412** (1997) 155.

[127] R. Barate *et al.* (ALEPH Collaboration), *Phys. Lett.* **B412** (1997) 173.

[128] S.R. Armstrong, presentation in the ALEPH Offline Software Meeting, 4 February 1998 (unpublished).

[129] S. Wasserbaech (private communication); A. Ealet and N. Konstantinidis, presentation in the ALEPH Higgs Task Force, 24 June 1998 (unpublished).

[130] S.R. Armstrong, *"Minutes of the ALEPH Offline Software Meeting"*, 15 October 1997 (unpublished).

[131] M. Thulasidas (private communication).

[132] All of the event displays in this thesis rely upon the DALI event display program: H. Drevermann, D. Kuhn, B.S. Nilsson, *"Event Display: Can We See What We Want to See?"* in *1995 CERN School of Computing*, CERN 95-05 (1995) 17.

[133] S.L. Wu, *Z. Phys.* **C9** (1981) 329; T.L. Barklow, *A Search for the Production of Charged Higgs and Technipions with Large Hadronic Branching Ratios in* e^+e^- *Annihilation at 34.5 GeV Center-of-Mass Energy*, Ph.D. Thesis, University of Wisconsin-Madison (1983).

[134] S.R. Armstrong *et al.*, ALEPH 98-041 (1998).

[135] R.A. Fisher, *Annals of Eugenics* **7** (1936) 179.

[136] E. Fahri, *Phys. Rev. Lett.* **39** (1977) 1587.

[137] D. Danckaert *et al.*, *Phys. Lett.* **B114** (1982) 203.

[138] E. Martin, ALEPH/95-137 (1995).

[139] J. Proriol, *Nucl. Instrum. Methods* **A337** (1994) 566.

[140] D. Buskulic *et al.* (ALEPH Collaboration), *Phys. Lett.* **B357** (1995) 699; F. Thomson and A. Halley, ALEPH/97-027 (1997); ALEPH Collaboration, *"Inclusive Heavy Flavour Lifetime and Mixing Measurements at ALEPH,"* paper #596 submitted to the International Europhysics Conference on High-Energy Physics (EPS-HEP97), Jerusalem (1997).

[141] R.M. Barnett *et al.* (Particle Data Group), *Phys. Rev.* **D54** (1996) 1.

[142] R.D. Cousins and V.L. Highland, *Nucl. Instrum. Methods* **A320** (1992) 331.

[143] J.F. Grivaz and F. Le Diberder, *Nucl. Instrum. Methods* **A333** (1993) 320.

[144] P. Janot and F. Le Diberder, *Nucl. Instrum. Methods* **A411** (1998) 449.

[145] P. Janot, presentation in the ALEPH Higgs Task Force, 21 January 1997 (unpublished).

[146] The ALEPH Higgs Task Force, ALEPH 98-029 (1998).

[147] R. Barate *et al.* (ALEPH Collaboration), CERN-EP/98-114 (1998) (*accepted for publication in Physics Letters B*).

[148] The LEP energy working group, LEP Energy Working Group Internal Note 98-01 (1998).

[149] DELPHI Collaboration, *"Search for neutral Higgs bosons in e^+e^- collisions at $\sqrt{s}$ =183 GeV,"* contributed paper #200, XXIX International Conference on High Energy Physics (ICHEP98), Vancouver 23-29 July 1998; OPAL Collaboration, *"Search for Higgs Bosons in e^+e^- Collisions at $\sqrt{(s)}$=183 GeV,"* contributed paper #353, *ibid.*; M. Acciarri *et al.* (L3 Collaboration), *Phys. Lett.* **B431** (1998) 437.

[150] P. Bock *et al.* (The LEP Working Group for Higgs Boson Searches), ALEPH 98-069/DELPHI 98-114/L3 2310/OPAL TN-558 (1998).

[151] P.A. McNamara, *"Standard Model Higgs at LEP,"* to appear in *Proceedings of the XXIX International Conference on High Energy Physics* (Vancouver, Canada, 1998).

[152] D. Amidei and R. Brock (eds.), *Future Electroweak Physics at the Fermilab Tevatron: Report of the tev2000 Study Group*, Fermilab-PUB-96/082 (1996).

[153] The LHC Study Group (P. Lefèvre and T. Pettersson eds.), *The Large Hadron Collider: Conceptual Design*, CERN/AC/95-05(LHC) (1995).

[154] W.W. Armstrong *et al.* (ATLAS Collaboration), *ATLAS Technical Proposal*, CERN/LHCC/94-43 (1994).

[155] G.L. Bayatian *et al.* (CMS Collaboration), *CMS Technical Design Report*, CERN/LHCC-94-38 (1994).

[156] M. Spira, *Fortsch. Phys.* **46** (1998) 203.

[157] A. Djouadi, PM-97-32 (hep-ph/9710439) (1997).

[158] C. Adolphsen *et al.* (NLC Design Group), *Zeroth-Order Design Report for the Next Linear Collider*, SLAC-474 (1996).

[159] J.P. Delahaye *et al.*, CERN/PS 97-23(LP) (1997).

[160] J.Ellis, E. Keil, and G. Rolandi, CERN-EP/98-03 (1998).

[161] E. Accomando *et al.* (ECFA/DESY LC Physics Working Group), DESY 97-100 (hep-ph/9705442) (1997).

[162] S. Kuhlman *et al.* (NLC Accelerator Design Group and NLC Physics Working Group), *Physics and Technology of the Next Linear Collider*, FERMILAB-PUB-96/112 (1996).

[163] T. Greening and the ALEPH Higgs Task Force, ALEPH 98-003 (1998).

[164] M. Kado *et al.* and the ALEPH Higgs Task Force, ALEPH 98-009 (1998).

[165] F. Badaud *et al.* and the ALEPH Higgs Task Force, ALEPH 98-010 (1998).